Efficient Localization in a Dispersive Waveguide: Applications in Terrestrial Continental Shelves and on Europa

by

Sunwoong Lee

Submitted to the Department of Mechanical Engineering
in partial fulfillment of the requirements for the degree of

Doctor of Philosophy in Mechanical Engineering

at the

MASSACHUSETTS INSTITUTE OF TECHNOLOGY

May 2006
[June 2006]

Author .....
Department of Mechanical Engineering
May 5, 2006

Certified by .....
Nicholas C. Makris
Associate Professor of Mechanical and Ocean Engineering
Thesis Supervisor

Accepted by .....
Lallit Anand
Chairman, Department Committee on Graduate Students

Efficient Localization in a Dispersive Waveguide: Applications in Terrestrial Continental Shelves and on Europa

by

Sunwoong Lee

Submitted to the Department of Mechanical Engineering
on May 5, 2006, in partial fulfillment of the
requirements for the degree of
Doctor of Philosophy in Mechanical Engineering

Abstract

Methods are developed for passive source localization and environmental parameter estimation in seismo-acoustic waveguides by exploiting the dispersive behavior of guided wave propagation. The methods developed are applied to the terrestrial continental shelf environment and the Jovian icy satellite Europa. The thesis is composed of two parts. First, a method is derived for instantaneous source-range estimation in a horizontally-stratified ocean waveguide from passive beam-time intensity data obtained after conventional plane-wave beamforming of acoustic array measurements. The method is advantageous over existing source localization methods, since (1) no knowledge of the environment is required except that the received field should not be dominated by purely waterborne propagation, (2) range can be estimated in real time with little computational effort beyond plane-wave beamforming, and (3) array gain is fully exploited. Second, source range estimation and environmental parameter inversion using passive echo-sounding techniques are discussed and applied to Europa. We show that Europa's interior structure may be determined by seismo-acoustic echo sounding techniques by exploiting natural ice fracturing events or impacts as sources of opportunity. A single passive seismic sensor on Europa's surface may then be used to estimate the thickness of its ice shell and the depth of its subsurface ocean. To further understand the seismo-acoustic characteristics of natural sources on Europa, a fracture mechanics model is developed for the initiation and propagation of a crack through a porous ice layer of finite thickness under gravitational overburden. It is found that surface cracks generated in response to a tidally induced stress field may penetrate through the entire outer brittle layer if a subsurface ocean is present on Europa. While Europa's ice is likely highly porous and fractured, our current caculations show that porosity-induced scattering loss of ice-penetrating radar waves should not be significant.

Thesis Supervisor: Nicholas C. Makris
Title: Associate Professor of Mechanical and Ocean Engineering

Acknowledgments

First and foremost, I would like to thank my advisor, Prof. Nicholas Makris, for his support, encouragement, and inspiration. He has been an excellent mentor who has guided me with extreme patience throughout the years. It was my great pleasure working with him.

I would like to thank the members of my thesis committee. Prof. Robert Pappalardo at University of Colorado guided me through Europa research with his thorough knowledge in planetary science. Prof. Tomasz Wierzbicki helped me with his expertise in fracture mechanics. Prof. Rainer Weiss gave me numerous invaluable comments on my thesis.

Thanks are also due to Prof. Henrik Schmidt, Prof. Arthur Baggeroer, and Prof. George Frisk for their excellent teaching at MIT, and their encouragement. Dr. Torrence Johnson at JPL and Dr. Louise Prockter at JHU/APL have also encouraged me constantly.

Financial support for this work has been provided by Prof. Makris via funds from the ONR Geoclutter Program and the ONR Graduate Traineeship Award. I'd like to thank Dr. Jeffrey Simmen and Dr. Ellen Livingston at ONR for their financial support.

I am indebted to many colleagues in the Acoustics Group for their helpful comments and inspiring conversations. I would like to thank Yi-san Lai, Purnima Ratilal, Joshua Wilson, Tianrun Chen, Deanelle Symonds, Ioannis Bertsatos, Srinivasan Jagannathan, Michele Zanolin, Luiz Souza, Irena Veljkovic, Joe Edwards, Ding Wang, Andrew Poulsen, and Hyun Joe Kim. Yi-san Lai, Purnima Ratilal, and Michele Zanolin were also great teachers from whom I have learned many different aspects of acoustics.

I thank Lillie Ruhlmann, Eddie Scheer, and Keith von der Heydt for their technical assistance. I am grateful to Geoff Fox for his administrative help.

I would like to thank former and current Korean colleagues in the department. They are Wonjoon Cho, Yonghwan Kim, Jae Auh, Kwanghee Ko, Sungjoon Kim,

Young Woong Lee, and Kwang Hyun Lee.

I am deeply grateful to Areti Kiara, who has been motivating me to continue my work with great confidence.

My parents and sisters have been supporting me with endless love. None of these would have been possible without them.

I have made this letter longer than usual, because I lack the time to make it short.

– BLAISE PASCAL

Contents

List of Figures

List of Tables

Chapter 1

Introduction

Sonar systems have long been employed as the most important means of charting, ranging, navigating, and communicating in ocean waveguides [10]. Passive and active sonar systems have been extensively used in Navy surface ships, submarines, and marine fishery ships to detect, localize, and identify noise sources, targets, and fish schools using array beamforming in continental shelves, deep ocean basins, and ice-covered Arctic Ocean [134]. Localization of sources or targets in waveguides is one of the most important goals in these applications. The depth and composition of oceans and sub-ocean layers are widely mapped using echo-sounding techniques that measure time-of-flight and reflection amplitude of seismo-acoustic waves using ray-tracing [86]. Deep interior structure of the Earth is estimated using seismo-acoustic waves emanating from natural earthquakes, and using worldwide seismic stations around the globe that measure travel times of multiple reflections from seismo-acoustic interfaces [2]. Localization of sources in these applications is also important since accurate source location is required for estimating environmental parameters.

In free-space, where there is no dispersion, only the bearing of a source can be estimated using array beamforming. In waveguides, however, multi-modal dispersion allows passive localization of a source in range. On the other hand, this same effect degrades the bearing estimation of a receiving line array when standard free-space planewave beamforming is employed. Therefore, both range and bearing have to be estimated simultaneously to properly account for multi-modal wave propagation in a

waveguide.

The thesis is composed of two parts. First, we discuss efficient source localization techniques in terrestrial shallow-water waveguides typical of continental shelves. In shallow-water, acoustic waves form normal modes that are trapped in a waveguide and propagate efficiently over long-range with different frequency-dependent group velocities and elevation angles. This dispersive multi-modal wave propagation behavior is of crucial importance in shallow-water acoustics and enables passive localization of the source. Receiver line arrays towed by surface ships or submarines are typically employed for source localization.

The array invariant method is derived in Chap. 2 for instantaneous source-range estimation in a horizontally-stratified ocean waveguide from passive beam-time intensity data obtained after conventional plane-wave beamforming of acoustic array measurements. The method has advantages over existing source localization methods such as matched field processing or the waveguide invariant. First, no knowledge of the environment is required except that the received field should not be dominated by purely waterborne propagation. Second, range can be estimated in real time with little computational effort beyond plane-wave beamforming. Third, array gain is fully exploited. The method is applied to data from the Main Acoustic Clutter Experiment of 2003 for source ranges between 1 to 8 km, where it is shown that simple, accurate, and computationally efficient source range estimates can be made. In Chap. 3, the array invariant method is further developed to instantaneously and simultaneously localize multiple broadband noise sources in a horizontally stratified ocean waveguide. It is shown that the cross-correlation of instantaneous beam-time intensity asymptotically reaches the array invariant. Both range and bearing of the source can then be determined instantaneously without knowledge of the environmental parameters. It is shown that multiple uncorrelated noise sources can be simultanesouly localized in a horizontally stratified ocean waveguide without ambiguity using this method.

Second, source range estimation and environmental parameter inversion using echo-sounding techniques with a single receiver is discussed, and applied to Jupiter's moon Europa in Chap. 4. Europa is covered with an ice shell, the thickness of which

is poorly constrained. It is hypothesized that Europa possesses a liquid ocean below the ice shell, however, there is no conclusive evidence to support this, and the depth of the potential ocean is unknown. The surface of Europa is believed to fracture in response to tidal forcing due to Jupiter providing natural acoustic sources. We show that the seismo-acoustic waves emanating from the fractures and numerous multiple reflections from the environmental interfaces may enable us to probe its interior structure using ocean-acoustic echo-sounding techniques with a single passive seismic sensor on Europa's surface. The multitude of natural source events at various ranges over the operational period of a surface sensor will enable us to efficiently estimate environmental parameters such as ice shell thickness and subsurface ocean depth. Quantitative analysis is presented with full-field seismo-acoustic modeling of the Europan environment. This includes models for Europan ambient noise and conditions on signal-to-noise ratio necessary for the proposed technique to be feasible. The possibility of determining Europa's ice layer thickness by surface wave and modal analysis with a single seismic sensor is also investigated. In Chap. 5, a fracture mechanics model is developed for the initiation and propagation of a crack through a porous ice layer of finite thickness under gravitational overburden. It is found that surface cracks generated in response to a tidally induced stress field may penetrate through the entire outer brittle layer if a subsurface ocean is present on Europa. Such penetration is found to be very unlikely in the absence of an ocean. A cycloidal crack would then form as a sequence of near instantaneous discrete failures, each extending roughly the brittle layer thickness in range, linked with a much lower apparent propagation speed set by the moving tidal stress field. The implications of this porous ice fracture model for ice-penetrating radar scattering loss and seismic activity are quantified.

Chapter 2

The array invariant

It has long been known that multi-modal dispersion in a shallow water waveguide degrades the performance of bearing estimates by conventional plane-wave beamforming. This is due to the advent of spurious effects unique to the waveguide environment such as multiple peaks and beam spreading in the beamformer output [24, 131, 137, 82]. Attempts, on the other hand, have been made to localize sources submerged in ocean waveguides by exploiting multi-modal interference using methods such as matched field processing (MFP) [19, 7, 119]. Apart from being computationally expensive, MFP techniques require accurate knowledge of the wave propagation environment. They are susceptible to large systematic errors from mismatch when adequate environmental information is not available [36, 124].

The range of a source in a horizontally stratified ocean waveguide can sometimes also be estimated by the much simpler waveguide invariant method [22, 18, 32, 69], which employs only incoherent processing of acoustic intensity data as a function of range and bandwidth. The waveguide invariant method, however, requires knowledge of certain "invariant" parameters, which unfortunately often vary significantly with ocean sound speed structure. It also requires a sufficiently large number of waveguide modes to significantly contribute to the measured field because these cause the interference structure necessary to produce a unique solution. Sufficiently dense sampling of the intensity data in source-receiver range is also necessary to provide an unambiguous solution. When the application involves single-sensor measurements,

joint ambiguity in source-receiver range and velocity is an inherent limitation of the waveguide invariant method. This ambiguity can disappear when spatial sensor arrays of sufficient horizontal aperture are used. None of the usual benefits of increased signal-to-noise ratio at the array output appear, however, because only incoherent processing of the spatial samples can be performed.

Here we show that instantaneous source range estimation is possible in a horizontally stratified ocean waveguide by a computationally inexpensive method that has significant advantages over the waveguide invariant because it requires neither *a priori* knowledge of environmental parameters nor multiple modes in the received field, and fully exploits the coherent gain possible with receivers of finite spatial aperture [72]. Since the new approach takes advantage of invariant properties of passive beam-time intensity data obtained after conventional plane-wave beamforming of underwater acoustic array measurements, we call it the *array invariant* method. We show that maximum beam-time intensity migrates along an angle that is invariant to environmental parameters but follows a known and unique dependence on source-receiver range. Horizontal source localization is also achieved when the receiving array has sufficient horizontal aperture to resolve source bearing. The formulation introduced here is specifically for broadband transient source signatures. A more general but involved formulation that can treat continuous broadband noise signatures is possible [73].

The array invariant method is derived in Sec. 2.1. Illustrative examples are presented in Sec. 2.2. In Sec. 2.3, source localization by the array invariant method is experimentally demonstrated using data from the Main Acoustic Clutter 2003 Experiment. Comparisons between the array invariant method and other acoustic techniques for source range estimation in the ocean, such as the waveguide invariant method and MFP, are presented in Sec. 2.4.

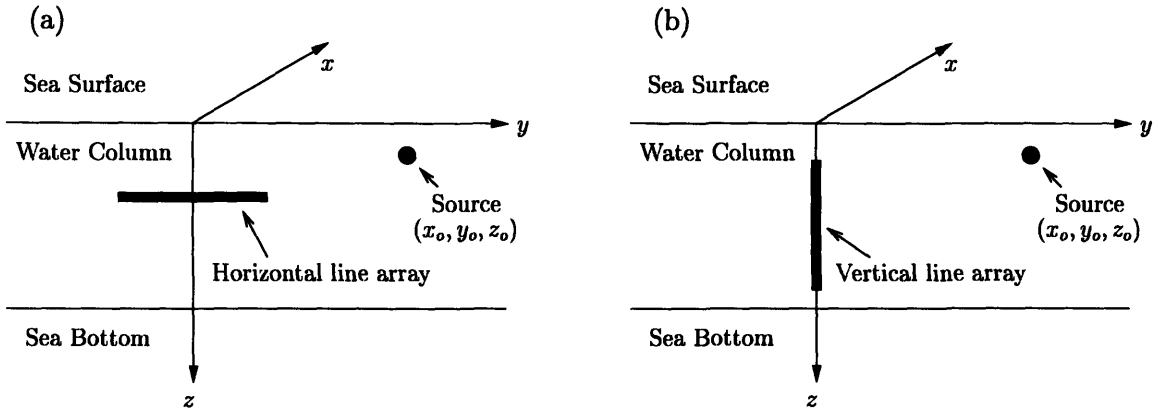

Figure 2-1: The geometry of the coordinate system for a horizontal line array (a), or a vertical line array (b). The horizontal line array is aligned parallel to the y-axis. The vertical line array is located along the z-axis. A source is located at (x_o, y_o, z_o).

2.1 Derivation of the array invariant

Analytic expressions are derived for the migration of peak intensity through a beam-time intensity image generated from acoustic array measurements made in an ideal waveguide. It is then shown that the expressions are approximately valid for typical horizontally stratified ocean waveguides, where they can be used for instantaneous source localization.

2.1.1 Beam-time migration for horizontal arrays in stratified waveguides

The measurement and coordinate geometry of Fig. 2-1 (a) shows a horizontal line array parallel to the y-axis, with array center at $(0, 0, z)$, and source at (x_o, y_o, z_o). We define $\mathbf{r} = x\hat{\imath}_x + y\hat{\imath}_y$, and $r = |\mathbf{r}|$, where $\hat{\imath}_x$ and $\hat{\imath}_y$ are unit vectors in the x and y directions, respectively. The wavenumber vector $\mathbf{k}$ is decomposed into $k_x = -k \sin\phi \cos\theta$, $k_y = -k \sin\phi \sin\theta$, and $k_z = -k \cos\phi$, where $k = |\mathbf{k}|$, and elevation angle ϕ and bearing θ are shown in Fig. 2-2.

The pressure P at frequency f due to a source at $(\mathbf{r_o}, z_o)$ can be expressed using

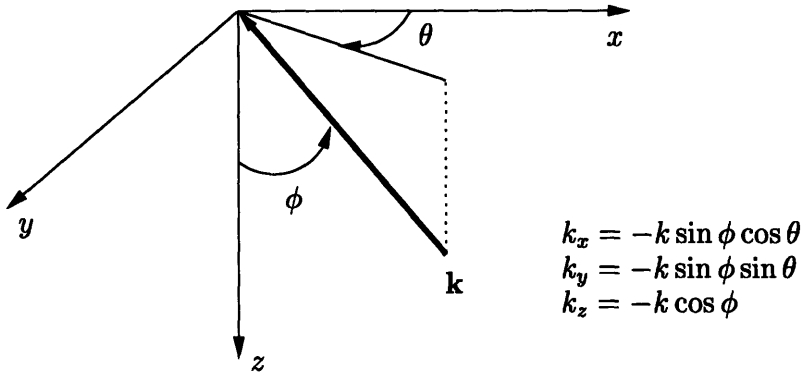

Figure 2-2: Definition of the elevation angle ϕ and the bearing θ of plane waves. The angles are defined in the "coming from" direction.

normal mode theory as

$$P(\mathbf{r}, z, f) = 4\pi Q(f) \frac{i}{\sqrt{8\pi}\rho(z_o)} e^{-i\pi/4} \sum_n u_n(z_o) u_n(z) \frac{e^{ik_{rn}|\mathbf{r}-\mathbf{r_o}|}}{\sqrt{k_{rn}|\mathbf{r}-\mathbf{r_o}|}}, \tag{2.1}$$

where $Q(f)$ is the source spectrum, ρ is the density, k_{rn} is the horizontal wavenumber of the n^{th} mode, and u_n is the mode shape of the n^{th} mode which satisfies

$$\int_0^\infty \frac{u_m(z) u_n^*(z)}{\rho(z)}\, dz = \delta_{mn}.$$

Using the far-field approximation

$$|\mathbf{r} - \mathbf{r_o}| \simeq r_o - y \sin\theta_o,$$

where θ_o is source bearing, the beamformed pressure P_B can be expressed as a function of array scan angle θ,

$$\begin{aligned} P_B(s, f) &= \int_{-\infty}^{\infty} T(v) P(v, z, f) e^{i2\pi v \sin\theta}\, dv \\ &= 4\pi Q(f) \frac{i}{\sqrt{8\pi}\rho(z_o)} e^{-i\pi/4} \sum_n u_n(z_o) u_n(z) \frac{e^{ik_{rn}r_o}}{\sqrt{k_{rn}r_o}} B(s - s_n), \end{aligned} \tag{2.2}$$

where $s = \sin\theta$, $v = ky/2\pi$, $s_n = \sin\phi_n \sin\theta_o$, and $\sin\phi_n = k_{rn}/k$. For evanescent

modes, $\phi_n = \pi/2 - i\phi'_n$, where $\phi'_n = \ln[k_{rn}/k + \{(k_{rn}/k)^2 - 1\}^{(1/2)}]$. The beam pattern $B(s)$ is the spatial Fourier transform of the array taper function $T(v)$ [64, 16]. This far-field formulation is valid when $r_o \gg L^2/\lambda$, where L is the array aperture, and $\lambda = 2\pi/k$.

The time-domain expression for the beamformed pressure $P_B(s,t)$ is obtained by taking the inverse Fourier transform of Eq. (2.2),

$$P_B(s,t) = 2\,\mathrm{Re}\left\{\int_0^\infty P_B(s,f)e^{-i2\pi ft}\,df\right\} = 2\,\mathrm{Re}\left\{P_{B+}(s,t)\right\}, \tag{2.3}$$

where $\mathrm{Re}\{\cdot\}$ represents the real part. The complex beamformed pressure $P_{B+}(s,t)$ can then be approximated using the method of stationary phase [34, 89, 82, 110] when $k_{rn}r_o \gg 1$, as given in Eq. (A.10) in Appendix A. The stationary phase approximation for Eq. (2.3) simplifies to Eq. (A.12) if the relative phase shifts between the different frequency components of the source spectrum are negligible, which occurs when $Q(f) = |Q(f)|$, such as in an impulsive or Gaussian signal. This is the simplifying approximation that limits the present formulation to the domain of transient signals, which is clearest for introducing the concepts. A more general formulation for continuous broadband noise is possible [73]. The complex beamformed pressure in Eq. (2.3) can then be approximated as

$$P_{B+}(s,t) \;\simeq\; \frac{4\pi i}{\sqrt{8\pi\rho(z_o)}}e^{-i\pi/4}\sum_n |Q(\tilde{f})|\tilde{u}_n(z_o)\tilde{u}_n(z)\frac{\tilde{B}(s-\tilde{s}_n)}{\sqrt{\tilde{k}_{rn}r_o}}F_n(\tilde{f}), \tag{2.4}$$

where $\tilde{f}$ is the frequency component within the source band that satisfies

$$t = \frac{r_o}{v_{gn}(\tilde{f})}, \tag{2.5}$$

v_{gn} is the group velocity of the n^{th} mode, and $\tilde{u}_n, \tilde{k}_{rn}, \tilde{B}, \tilde{s}_n, \tilde{v}_{gn}, \tilde{\phi}_n$ are the corresponding values of $u_n, k_{rn}, B, s_n, v_{gn}, \phi_n$ at $f = \tilde{f}$. The function $F_n(\tilde{f})$ in Eq. (2.4) is given in Eq. (A.13) of Appendix A. The bearing of peak beamformed pressure for

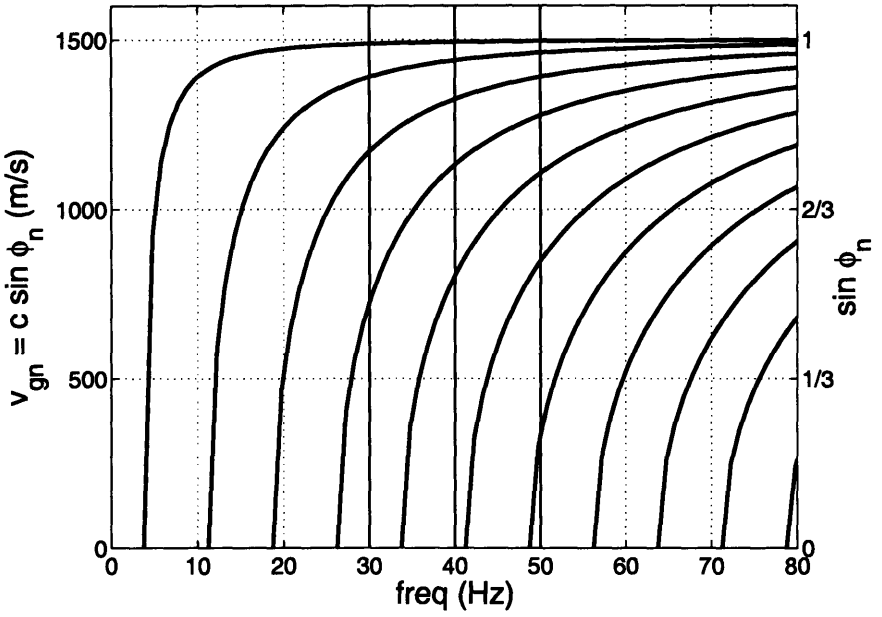

Figure 2-3: Group velocity v_{gn} and modal elevation angle $\sin\phi_n$ as a function of frequency in an ideal waveguide. The water depth and the sound speed are 100 m and 1500 m/s, respectively, and the boundaries are assumed to be pressure release. The vertical lines at 30, 40, and 50 Hz will be referred to in Fig. 2-5

the n^{th} mode at time t is specified by

$$\tilde{s}_n(t) = \sin\tilde{\phi}_n(t) \sin\theta_o, \tag{2.6}$$

which is the zero of the argument of the beam pattern $\tilde{B}(s - \tilde{s}_n)$ in Eq. (2.4). Equations (2.5) and (2.6) enable the temporal migration of the maximum beamformer output angle to be determined in any horizontally stratified ocean waveguide. These equations are significant because they lead directly to source localization in an ocean waveguide by the new array invariant method.

2.1.2 Array invariant for horizontal arrays in ideal waveguides

Here we show that the bearing of peak beamformed pressure $\tilde{s}_n(t)$, given in Eq. (2.6) for any given mode at any time, is an observable from which source range can be

estimated. This is done by first noting that group velocity and modal elevation angle are related by

$$[v_{gn}]^{-1} = \frac{1}{2\pi}\frac{d}{df}\sqrt{k^2 - k_{zn}^2} = \frac{1}{2\pi}\frac{dk}{df}\frac{k}{k_{rn}} = [c\sin\phi_n]^{-1} \tag{2.7}$$

for an ideal isovelocity waveguide with pressure-release or rigid boundaries since the vertical wavenumber of the n^{th} mode k_{zn} is not a function of f. This is illustrated in Fig. 2-3. Then Eqs. (2.5) and (2.7) can be used to express Eq. (2.6) as

$$\tilde{s}_n(t) \equiv \tilde{s}(t) = \frac{r_o}{ct}\sin\theta_o, \tag{2.8}$$

which shows that the $\tilde{s}_n(t)$ merge to a single beamformer migration line $\tilde{s}(t)$ for all mode numbers if the source bandwidth is sufficiently large. For fixed source bearing, the beamformer migration line changes only as a function of source range as can be seen in Eq. (2.8) and as illustrated in Fig. 2-4.

If the bandwidth of the source signal is not sufficiently large, $\tilde{s}_n(t)$ may appear as discrete line segments along the trajectory described by the right-hand side of Eq. (2.8). This is due to the discrete nature of the waveguide modes. An example is shown in Fig. 2-5 (a) for a source signal in the 30 to 40-Hz band. For a given frequency band, the length of an $\tilde{s}_n(t)$ segment is greater for higher order modes. This is because they exhibit more dispersion than lower order modes, as can be deduced from Fig. 2-3 by noting that the change in group velocity across the band increases with mode number.

For a given mode and $\tilde{s}_n(t)$ segment, the $\tilde{s}_n(t)$ will migrate to a different part of the $\tilde{s}(t)$ curve when the frequency band of the source signal changes. This is because both the group velocity and elevation angle of the given mode change as a function of frequency. This is illustrated in Fig. 2-4 (b) where the source frequency is now in the 40 to 50-Hz band. Comparison of Figs. 2-5 (a) and (b) shows that the $\tilde{s}_n(t)$ for a given mode migrates to an earlier segment with greater scan angle because both group velocity v_{gn} and elevation angle ϕ_n for that mode have increased with the positive shift in the bandwidth. This migration is constrained to occur within the $\tilde{s}(t)$ curve

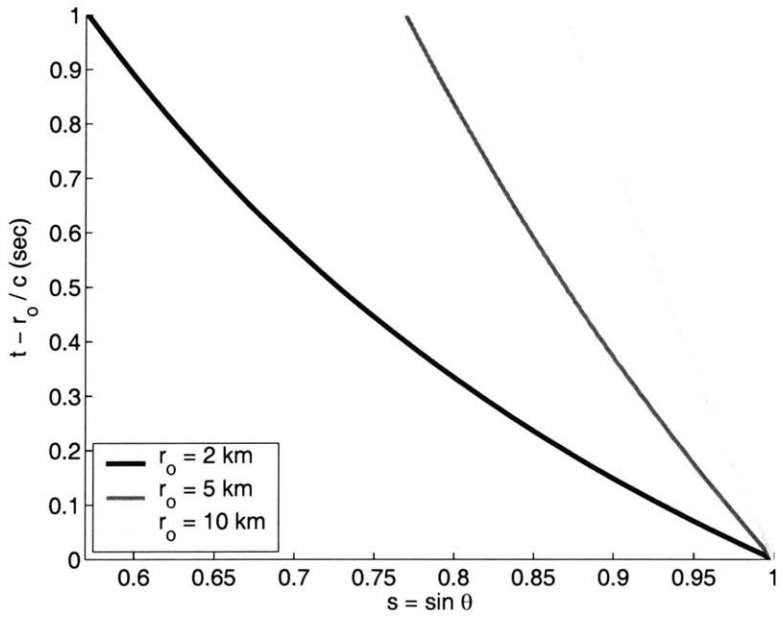

Figure 2-4: The beam-time migration lines $\tilde{s}_n(t)$ as a function of reduced travel time $t - r_o/c$ and array scan angle θ for various source ranges over the full 0 to 80-Hz frequency band shown in Fig. 2-3. The sound speed c is 1500 m/s and source bearing θ_o is $\pi/2$. It can be seen that all the $\tilde{s}_n(t)$ merge to a single beamformer migration line $\tilde{s}(t)$.

given by Eq. (2.8), which completely determines the peak beam-time migration in an ideal waveguide. If the source signal occupies the entire 30 to 50-Hz band, the $\tilde{s}_n(t)$ for individual modes overlap to form the continuous $\tilde{s}(t)$, as shown in Fig. 2-5 (c).

We define an array invariant χ_h for a horizontal linear receiver array as

$$\chi_h \equiv \frac{d\tilde{s}^{-1}(t)}{dt} = \frac{c}{r_o \sin\theta_o}, \tag{2.9}$$

For fixed source bearing, Eq. (2.9) is independent of source frequency band, mode number, source depth, receiver depth, and waveguide depth. Also, Eq. (2.9) is valid for both pressure release and rigid boundary ideal waveguides.

Source range can now be estimated using

$$\hat{r}_o = \frac{c}{\hat{\chi}_h \sin\hat{\theta}_o}, \tag{2.10}$$

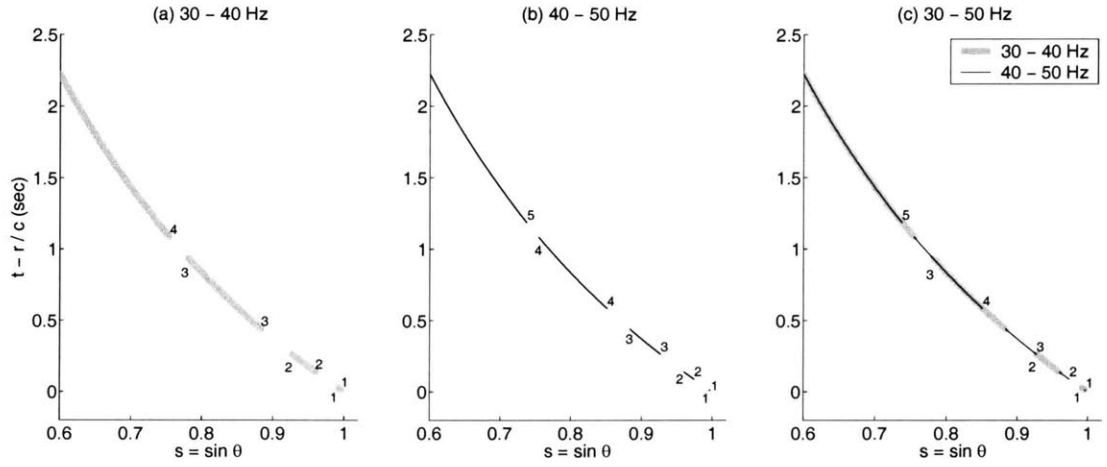

Figure 2-5: (a): The beam-time migration lines $\tilde{s}_n(t)$ for modes in the 30 to 40-Hz band shown in Fig. 2-3 as a function of reduced travel time $t - r_o/c$ and array scan angle θ for a source at $r_o = 5$ km and $\theta_o = \pi/2$. The beam-time migration lines $\tilde{s}_n(t)$ appear as discrete line segments. The beginning and end of each $\tilde{s}_n(t)$ segment is marked by mode number n. (b): The same as (a), but for modes in the 40 to 50-Hz band. As group velocity and elevation angle of a given mode changes, $\tilde{s}_n(t)$ for that mode migrates to a different location in the beam-time plot. This migration is constrained to occur within the $\tilde{s}(t)$ curve given by Eq. (2.8). (c): The same as (a), but for modes in the 30 to 50-Hz band. As the frequency band of the source increases, $\tilde{s}_n(t)$ for the individual modes overlap to form the continuous $\tilde{s}(t)$.

based on direct measurements of the array invariant $\hat{\chi}_h$ and source bearing $\hat{\theta}_o$ obtained from beam-time intensity data. Since Eq. (2.10) is a unique one-to-one mapping of $\hat{r}_o$ from $\hat{\chi}_h$ for fixed $\hat{\theta}_o$, range inversion using the array invariant does not suffer from ambiguity, as is common in MFP.

The array invariant method differs significantly from the waveguide invariant method in that the array invariant does not rely on modal interference. Application of the waveguide invariant is not possible, for example, if there is only one mode propagating in a waveguide. The array invariant, however, is still applicable if the solitary mode causes sufficient dispersion in the source band, as can be seen in Eq. (2.8) and Fig. 2-4. In most practical applications, the combined dispersion of multiple modes is needed for robust source localization as will be shown in Sec. 2.2.

2.1.3 Array invariant for horizontal arrays in stratified waveguides

For general horizontally stratified waveguides, the relationship between group velocity and horizontal wavenumber is

$$[v_{gn}]^{-1} = \frac{1}{2\pi}\frac{d}{df}\sqrt{k^2(z) - k_{zn}^2(z)},$$

which leads to the relation

$$v_{gn} = \frac{c(z)\sin\phi_n(z)}{1 + \frac{c(z)}{2\pi}\cos\phi_n(z)\frac{dk_{zn}(z)}{df}} \tag{2.11}$$

between group velocity and modal elevation angle. By substituting Eq. (2.11) into Eq. (2.6), the peak beam-time migration line $\tilde{s}_n(t)$ for a given mode can be written explicitly as

$$\tilde{s}_n(z,t) = \sin\tilde{\phi}_n(z,t)\sin\theta_o = \frac{r_o}{c(z)t}\sin\theta_o\left\{1 + \frac{c(z)}{2\pi}\cos\tilde{\phi}_n(z)\left[\frac{dk_{zn}(z)}{df}\right]_{f=\tilde{f}}\right\}. \tag{2.12}$$

The second term in the bracket in Eq. (2.12) is the correction term for the beam-former migration when there is variation in sound speed structure versus depth. This correction term for the n^{th} mode is negligible when

$$\left|\frac{1}{2\pi}\left[\frac{dk_{zn}(z)}{df}\right]_{f=\tilde{f}}\right| \ll \left|c(z)\cos\tilde{\phi}_n(z)\right|^{-1}, \tag{2.13}$$

as can be seen in Eq. (2.12). It will be shown in Sec. 2.2 that most of the modes propagating in shallow-water waveguides satisfy Eq. (2.13) since change of the vertical wavenumber versus frequency is typically negligible for frequencies not near modal cut-off. We refer to modes that do not satisfy Eq. (2.13) as waterborne modes. This terminology for waterborne modes is similar to that used by Ref. [146]. While Eq. (2.13) is not satisfied near modal cut-off frequencies, modal contribution near cut-off are negligible since the corresponding modal amplitudes decay rapidly as r_o

increases [130].

Equation (2.12) is then independent of mode number, and can be approximated as

$$\tilde{s}(z,t) \simeq \frac{r_o}{c(z)t} \sin\theta_o, \tag{2.14}$$

where the departure from Eq. (2.8) is that sound speed at the receiver depends on receiver depth.

An array invariant for a general horizontally stratified waveguide is then defined as

$$\chi_h \equiv \frac{d\tilde{s}^{-1}(z,t)}{dt} \simeq \frac{c(z)}{r_o \sin\theta_o}, \tag{2.15}$$

where source range can again be estimated from Eq. (2.10) but with $c(z)$ substituted for c. The sound speed dependence of Eq. (2.15) is not an impediment since the sound speed at receiver depth can be readily measured by Expendable Bathythermographs (XBT). If such measurements are not available, $c(z) = 1490$ m/s can be used for range estimation, which leads to only 3% error for the typical range of sound speeds, roughly 1440 to 1540 m/s, encountered in continental shelf waveguides [134].

An array invariant can also be defined in another way. In practical shallow-water waveguides, the maximum extent of the exact beam-time migration line $\tilde{s}_n(z,t)$ along the beam-time migration line for non-waterborne mode $\tilde{s}(z,t)$ is limited by the time of the latest modal arrival, which is bounded by the minimum group velocity at the Airy phase. This maximum extent is typically sufficiently small that $d\tilde{s}(z,t)/dt$ can be expanded around $t = r_o/c(z)$, and only the zeroth order term

$$\chi_l \equiv \frac{d\tilde{s}(z,t)}{dt} \simeq -\frac{c(z)}{r_o} \sin\theta_o \tag{2.16}$$

need be retained. Equation (2.16) defines an array invariant χ_l that is more convenient for practical use, and is a good approximation unless the seafloor is impenetrable. It will be used for source range estimation in Sec. 2.2 and Sec. 2.3.

2.1.4 Array invariant for vertical arrays in stratified waveguides

The array invariant method can also be used to instantaneously estimate source range from vertical line array measurements. The sound speed across the aperture of the array is taken to be approximately constant. The geometry is shown in Fig. 2-1 (b). The beamformed pressure of the vertical array as a function of array scan angle ϕ is

$$\begin{aligned} P_{B,v}(s_v, f) &= 4\pi Q(f) \frac{i}{\sqrt{8\pi}\rho(z_o)} e^{-i\pi/4} \sum_n u_n(z_o) \frac{e^{ik_{rn}r_o}}{\sqrt{k_{rn}r_o}} \\ &\times \left[N_n^+ B(s_v - s_{v,n}) + N_n^- B(s_v + s_{v,n}) \right], \end{aligned} \tag{2.17}$$

where $s_v = \cos\phi$, $s_{v,n} = \cos\phi_n$. Here N_n^+ and N_n^- are the plane-wave amplitudes of the n^{th} mode that satisfy $u_n(z) = N_n^+ e^{ik_{zn}z} + N_n^- e^{-ik_{zn}z}$ at the receiver depths z spanned by the array. For evanescent modes, $s_{v,n}$ does not lie in real space since $\cos\phi_n = i\sinh\phi_n'$. The time-domain complex beamformed pressure is approximated as

$$\begin{aligned} \tilde{P}_{B,v+}(s_v, t) \simeq \frac{4\pi i}{\sqrt{8\pi}\rho(z_o)} e^{-i\pi/4} \sum_n |Q(\tilde{f})| \tilde{u}_n(z_o) \frac{e^{i\tilde{k}_{rn}r_o}}{\sqrt{\tilde{k}_{rn}r_o}} \\ \left[\tilde{N}_n^+ \tilde{B}(s_v - \tilde{s}_{v,n}) + \tilde{N}_n^- \tilde{B}(s_v + \tilde{s}_{v,n}) \right] F_n(\tilde{f}) \end{aligned}$$

by the stationary phase method, where $\tilde{N}_n^+, \tilde{N}_n^-, \tilde{s}_{v,n}$ are the corresponding values of $N_n^+, N_n^-, s_{v,n}$ at the frequencies $\tilde{f}$ that satisfy Eq. (2.5).

For an ideal waveguide, group velocity and elevation angle are related by $v_{gn} = c\sqrt{1 - \cos^2\phi_n}$, which can be obtained from Eq. (2.7). The beam-time migration line for a vertical array in an ideal waveguide then obeys

$$\pm\tilde{s}_{v,n}(t) \equiv \pm\tilde{s}_v(t) = \pm\sqrt{1 - \left(\frac{r_o}{ct}\right)^2}, \tag{2.18}$$

and the migration lines $\tilde{s}_{v,n}(t)$ for all the modes merge to a single line $\tilde{s}_v(t)$. The signs specify whether the migration is vertically up or down. This is due to the symmetry

of up and down-going plane-wave components of the modes when the sound speed across the array aperture is constant.

An array invariant χ_v for vertical arrays can be defined as

$$\chi_v \equiv \frac{d}{dt}\left[1 - \tilde{s}_v^2(t)\right]^{-1/2} = \frac{c}{r_o}, \tag{2.19}$$

using Eq. (2.18). Source range can then be estimated as $\hat{r}_o = c/\hat{\chi}_v$, after measuring $\hat{\chi}_v$ from the migration of $\tilde{s}_v(t)$ in the given beam-time intensity data set. Linearization of $d\tilde{s}_v(t)/dt$ using a Taylor series expansion is not appropriate for vertical arrays since the zeroth order term of $d\tilde{s}_v(t)/dt$ at $t = r_o/c$ is not finite.

The array invariant approach for vertical arrays can be applied in a general horizontally stratified waveguide when the sound speed $c(z)$ is constant across the aperture of the array. Using Eq. (2.11) and relation (2.13), the beam-time migration line in this scenario is

$$\pm\tilde{s}_{v,n}(z,t) \equiv \pm\tilde{s}_v(z,t) \simeq \pm\sqrt{1 - \left(\frac{r_o}{c(z)t}\right)^2}, \tag{2.20}$$

from which the array invariant becomes

$$\chi_v \equiv \frac{d}{dt}\left[1 - \tilde{s}_v^2(z,t)\right]^{-1/2} \simeq \frac{c(z)}{r_o}, \tag{2.21}$$

so that source range can be estimated as $\hat{r}_o = c(z)/\hat{\chi}_v$.

Equations (2.20) and (2.21) are also good approximations if the sound speed is not constant along the array aperture in general horizontally stratified waveguides so long as the variation of $k_{zn}(z)$ along the aperture of an array satisfies

$$|k_{zn}(z)(z - z_c) - k_{zn}(z_c)(z - z_c)| < \frac{\pi}{4}, \tag{2.22}$$

where z_c is the center depth of an array. The worst case would then occur at either end of the array for waves propagating parallel to the z-axis. Equation (2.22), with the approximation $1/c(z) = 1/(c(z_c)+\Delta c(z)) \simeq c^{-1}(z_c)(1-\Delta c(z)/c(z_c))$ where $\Delta c(z)$ is the sound speed difference at z_c and depths z spanned by the array, leads to a more

practical condition

$$|\Delta c(z)| < \frac{c(z_c)}{2L/(\lambda(z_c)/2)} \tag{2.23}$$

for the sound speed variation along the array aperture for source range estimation using Eq. (2.21), where $\lambda(z_c) = k(z_c)/2\pi$ and L is the array aperture. For a typical vertical array aperture of $L = 64\lambda(z_c)/2$ and $c(z_c) = 1490$ m/s, Eq. (2.23) requires that the relatively benign condition $|\Delta c(z)| < 11$ m/s must be satisfied for Eqs. (2.20) and (2.21) to be good approximations.

2.1.5 Array invariant for planar arrays in stratified waveguides

The beam-time migration line for planar receiver arrays is obtained by further decomposing $u_n(z)$ in Eq. (2.2) into up and down-going wave components, as was done in Eq. (2.17). It is given as a 3-D parametric line in the t, s, and s_v domain, the path of which is given by Eqs. (2.8) and (2.18) as a function of t. Both $\hat{\chi}_h$ and $\hat{\chi}_v$ can be estimated from the given beam-time intensity data set by observing the projection of the beam-time migration onto s and s_v domain.

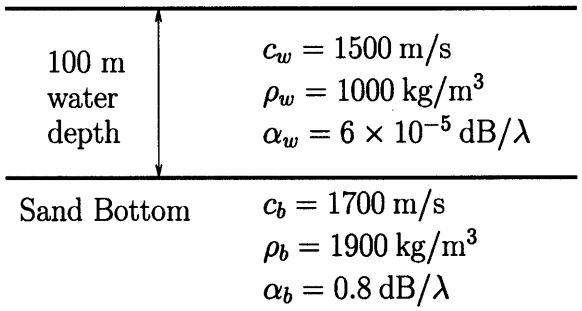

Figure 2-6: The Pekeris waveguide with sand bottom, where c_w, ρ_w, and α_w are the sound speed, density, and attenuation of the water column, and c_b, ρ_b, and α_b are those of the sea-bottom.

2.2 Illustrative examples by simulation

2.2.1 Horizontal array

Instantaneous source range estimation by the array invariant method is illustrated by a number of examples involving typical continental shelf environments and array configurations. The first example employs a horizontal receiving array in a Pekeris waveguide. The environmental parameters are shown in Fig. 2-6. The detection geometry is defined by $z = 30$ m, $z_o = 50$ m, $r_o = 5$ km, and $\theta_o = 60°$. The source signal is impulsive in the time-domain and bandlimited to 390 to 440 Hz by a Tukey filter [52]. The source level is 219 dB *re* 1 μPa at 1 m. The array aperture L is 94.5 m, and is tapered by a Hann window. The source, receiver, and geoacoustic parameters of the seabed are chosen for consistency with the field experiment described in Sec. 2.3.

The acoustic field from the impulsive source is measured as a time-series on each hydrophone sensor of the horizontal array. The hydrophone time-series data are converted to beam-time data by standard time-domain beamforming. Only the beam-time sound pressure level $L_{bt}(s,t) = 20 \log |P_B(s,t)/1\mu\text{Pa}|$, which forms a 2-D image as shown in Fig. 2-7 (a), is necessary for range estimation by the array invariant method.

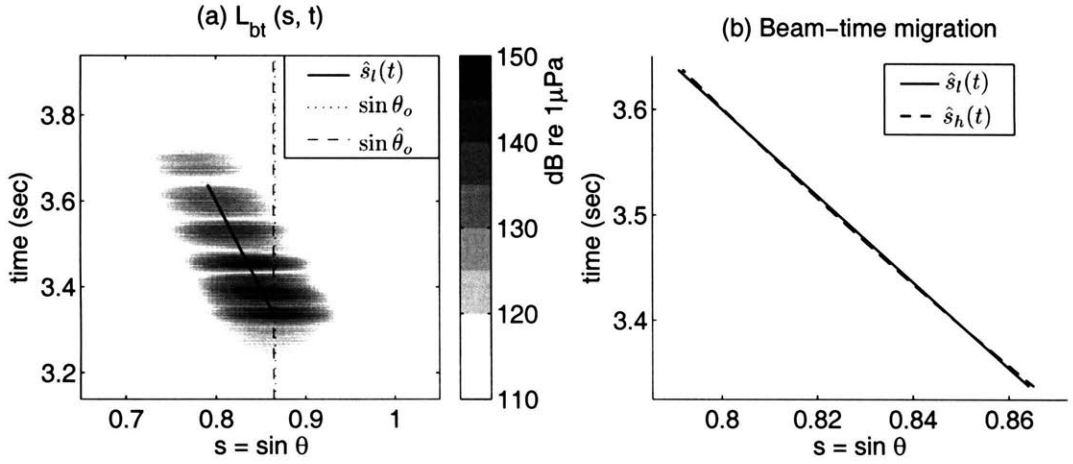

Figure 2-7: (a): Beam-time image $L_{bt}(s,t)$ with true source range $r_o = 5$ km and bearing $\theta_o = 60°$ in the Pekeris sand waveguide. The dotted and dashed vertical lines are at $\sin\theta_o$ and $\sin\hat{\theta}_o$, respectively, where $\hat{\theta}_o$ is the scan angle of the array corresponding to the global maximum of the $L_{bt}(s,t)$ data. The black solid line is the linear least squares fit $\hat{s}_l(t)$ of peak intensity angle versus time using Eq. (2.26). (b): The black solid line is the same $\hat{s}_l(t)$ as shown in Fig. 2-7 (a), and the black dashed line is the linear least squares fit $\hat{s}_h(t)$ using Eq. (2.28). The two least squares fits are nearly identical to each other.

The source range estimate

$$\hat{r}_o = -\frac{c(z)}{\hat{\chi}_l}\sin\hat{\theta}_o \tag{2.24}$$

is then a function of the estimates $\hat{\theta}_o$ and $\hat{\chi}_l$ based on the $L_{bt}(s,t)$ data. As noted in Sec. 2.1.3 the assumption $c(z) = 1490$ m/s is employed if no local sound speed measurements are available.

The source bearing estimate $\hat{\theta}_o$ is taken as the scan angle that corresponds to the global maximum of the beam-time sound pressure level data $L_{bt}(s,t)$. This is typically a good approximation in any continental shelf environment because (1) the global maximum is dominated by contributions from the earliest arrivals corresponding to the lowest order modes, which typically suffer the least attenuation and dispersion, and (2) these modes typically satisfy $\sin\phi_n \simeq 1$ so that the global maximum occurs at $\sin\phi_n \sin\theta_o \simeq \sin\theta_o$, as can be seen from Eq. (2.6). The location of the global maximum is found by an automated exhaustive search through the $L_{bt}(s,t)$ data,

leading to the estimate $\hat{\theta}_o = 59.8°$, which is consistent with the value obtained by inspection of Fig. 2-7 (a), and is within a fraction of a degree of the true bearing.

The array invariant χ_l is estimated from the data by first finding

$$s_{\max}(t) = \arg\max_s L_{bt}(s,t)$$

by an automated peak detection algorithm. A least squares estimate of $\hat{\chi}_l$ is then found under the linear approximation

$$\hat{s}_l(t) = \hat{\chi}_l t + d_l \tag{2.25}$$

from Eq. (2.16), where d_l is a constant intercept. By this approach, the array invariant estimate $\hat{\chi}_l$ would explicitly be the first element of the vector

$$[\hat{\chi}_l \quad d_l]^T = (\mathbf{T}^T\mathbf{T})^{-1}\mathbf{T}^T\mathbf{S_l}, \tag{2.26}$$

where $\mathbf{S_l} = [s_{\max}(t_1),\ s_{\max}(t_2),\ \cdots,\ s_{\max}(t_N)]^T$, $\mathbf{T} = \left[(t_1,\ t_2,\ \cdots, t_N)^T \quad \mathbf{1}^T\right]$, $t_j = t_1 + (j-1)\Delta t_s$, Δt_s is the sample spacing in time, and $\mathbf{1}$ is an $1 \times N$ matrix given by $\mathbf{1} = [1,\ 1,\ \cdots, 1]$. Other methods of estimation could be used such as the maximum likelihood or the Radon transform method. If the received field undergoes circular complex Gaussian fluctuations due to transmission through a random waveguide, or due to a random source, the least squares estimate of the log transformed beam-time intensity data is approximately the maximum likelihood estimator [77, 78].

The linear least squares fit $\hat{s}_l(t)$ of Eq. (2.25) is overlain on the $L_{bt}(s,t)$ data in Fig. 2-7 (a). The slope of the fitted line is the array invariant estimate, $\hat{\chi}_l = -0.244$. The corresponding source range estimate is then $\hat{r}_o \simeq 5.3\,\text{km}$, from Eq. (2.24), which is within 6% of the true range $r_o = 5\,\text{km}$.

A slightly more accurate source range estimate can be obtained from

$$\hat{r}_o = \frac{c(z)}{\hat{\chi}_h \sin\hat{\theta}_o}, \tag{2.27}$$

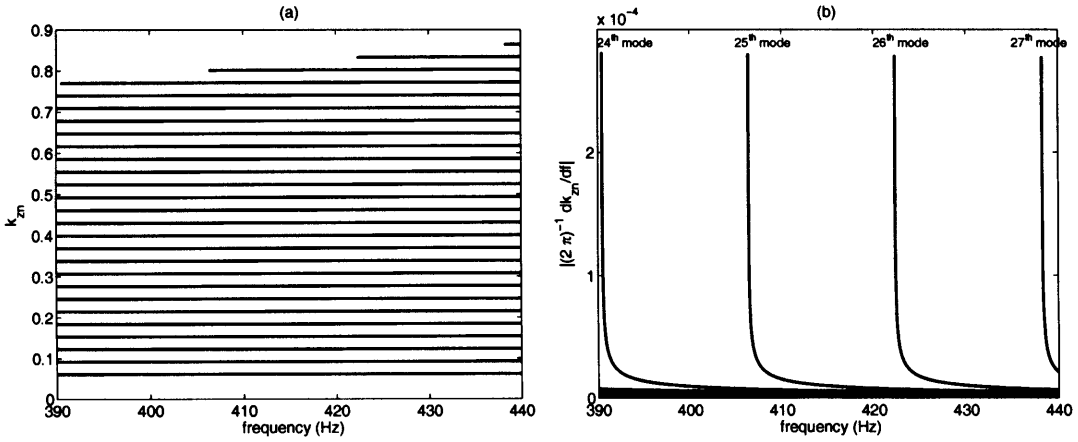

Figure 2-8: (a): Vertical wavenumber k_{zn} versus frequency for modes in the Pekeris sand waveguide of Fig. 2-6. Each horizontal line corresponds to a specific mode. Higher order modes have higher wavenumbers. (b): Frequency derivatives of k_{zn}. This figure shows that k_{zn} is effectively a constant function of frequency so that relation (2.13) is satisfied for the Pekeris waveguide except near mode cut-off.

where a least squares estimate of $\hat{\chi}_h$ is found under the approximation $\hat{s}_h^{-1}(t) = \hat{\chi}_h t + d_h$ from Eq. (2.15), with

$$[\hat{\chi}_h \quad d_h]^T = (\mathbf{T}^T\mathbf{T})^{-1}\mathbf{T}^T\mathbf{S_h}, \tag{2.28}$$

$\mathbf{S_h} = [s_{\max}^{-1}(t_1),\ s_{\max}^{-1}(t_2),\ \cdots,\ s_{\max}^{-1}(t_N)]^T$, and d_h as a constant intercept. The resulting least squares fit is shown in Fig. 2-7 (b), where $\hat{\chi}_h = 0.355$. The estimate of source range is then $\hat{r}_o \simeq 4.9\,\text{km}$, from Eq. (2.27), which is within 2% of the true range.

In these examples, we do not use knowledge of the environment to estimate source range. This is necessary to show that the array invariant method can be used for range estimation simply by use of Eqs. (2.24), (2.27), and incoherent beam-time data $L_{bt}(s,t)$.

The array invariant method works because relation (2.13) is satisfied in the given Pekeris waveguide environment as can be seen in Fig. 2-8, where the vertical wavenumber of the 27 propagating modes and their frequency derivatives are plotted. The vertical wavenumbers are nearly constant except near modal cutoff frequencies. Relation (2.13) is then satisfied for all modes except near cutoff, as can be seen in Fig. 2-8 (b). The components near cutoff, however, do not contribute to the acoustic pressure

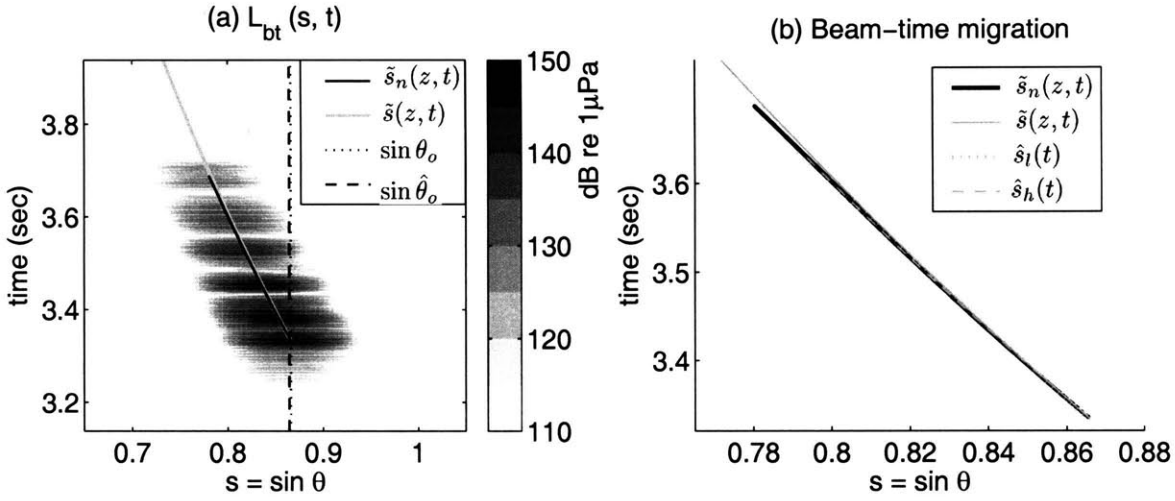

Figure 2-9: (a): Beam-time image $L_{bt}(s,t)$ identical to that in Fig. 2-7. The black solid line is the exact beam-time migration line $\tilde{s}_n(z,t)$ given in Eq. (2.12), for modes up to $n = 23$. The last 4 modes with mode cut-off in the 390 to 440 Hz band, as shown in Fig. 2-8, are neglected. The gray solid line is the beam-time migration line for non-waterborne modes $\tilde{s}(z,t)$ from Eq. (2.14). (b): The black and gray solid lines are the detailed shapes of the same $\tilde{s}_n(z,t)$ and $\tilde{s}(z,t)$ shown in Fig. 2-9 (a). The two least squares fits $\hat{s}_l(t)$ and $\hat{s}_h(t)$ in Fig. 2-7, overlain as gray dashed and dotted lines, show good agreement with the exact beam-time migration line $\tilde{s}_n(z,t)$.

as noted in Sec. 2.1.3, and can be neglected.

The array invariant method also works because the exact beam-time migration line $\tilde{s}_n(z,t)$ is well approximated by the least squares fits. The exact beam-time migration line $\tilde{s}_n(z,t)$, calculated using Eq. (2.12), is shown in Fig. 2-9 (a) as a black line. The temporal extent of $\tilde{s}_n(z,t)$ is limited by the time of the latest modal arrival in the source band, as discussed in Sec. 2.1.3. The detailed shape of $\tilde{s}_n(z,t)$ is plotted in Fig. 2-9 (b), which shows that $\tilde{s}_n(z,t)$ can be well approximated by the least squares fits given in Eqs. (2.26) and (2.28).

2.2.2 Vertical array

Here we show that source range can be instantaneously estimated using the array invariant for vertical arrays with a Pekeris waveguide example. The environmental parameters are shown in Fig. 2-6. The detection geometry is defined by $z_c = 50$ m, $z_o = 50$ m, and $r_o = 5$ km. The source signal is impulsive in the time-domain and

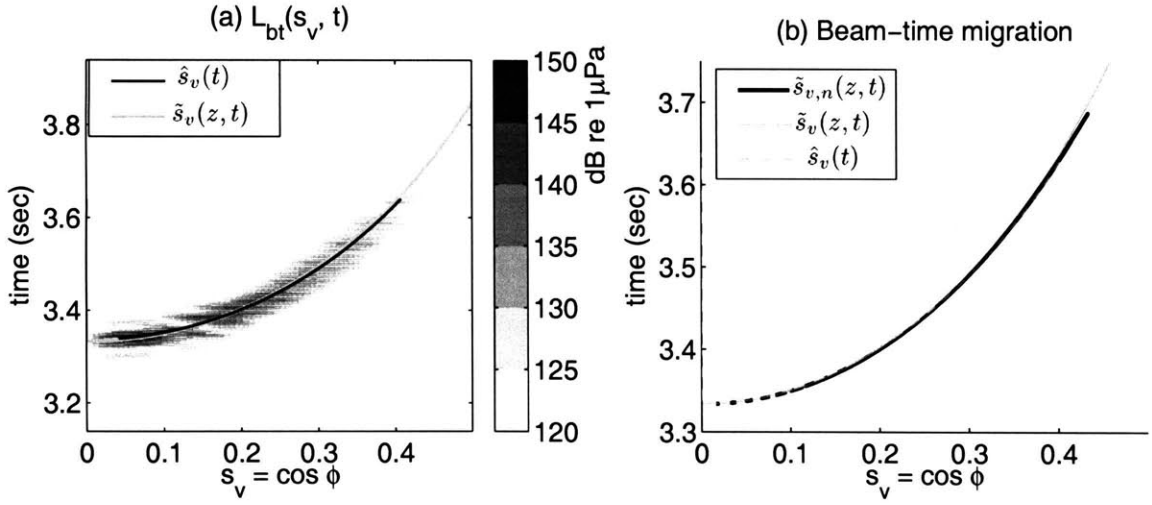

Figure 2-10: (a): Beam-time image $L_{bt}(s_v, t)$ for $r_o = 5$ km in the Pekeris sand waveguide. The black solid line is the linear least squares fit $\hat{s}_v(t)$ of peak intensity versus time calculated using Eq. (2.30). The gray solid line is the beam-time migration line for non-waterborne modes, $\tilde{s}_v(z,t)$, in Eq. (2.18). (b): The black solid line is the exact beam-time migration line $\tilde{s}_{v,n}(z,t)$. The gray solid and dashed lines are $\tilde{s}_v(z,t)$ and $\hat{s}_v(t)$ in Fig. 2-10 (a), respectively. It can be seen that the exact beam-time migration line $\tilde{s}_{v,n}(z,t)$ can be well approximated by the least squares fit $\hat{s}_v(t)$.

bandlimited in 390 to 440 Hz by a Tukey filter. The source level is 219 dB *re* 1 μPa at 1 m. The array aperture L is 94.5 m, and is tapered by a Hann window.

The acoustic field from the impulsive source is measured as a time-series on each element of the vertical array. The time-series data are converted to beam-time data by standard time-domain beamforming. The beam-time sound pressure level $L_{bt}(s_v, t) = 20 \log |P_B(s_v, t)/1\mu\text{Pa}|$ is shown in Fig. 2-10 (a). The $L_{bt}(s_v, t)$ data is symmetric with respect to array broadside, where $s_v = 0$, since each mode is composed of an up and a down-going plane wave component with equal amplitude in the water column. Only $L_{bt}(s_v > 0, t)$ is shown in Fig. 2-10 (a). Resolution of lower order modes is significantly better for the vertical array than the horizontal array since equivalent plane waves are incident near broadside in the former [147].

Source range can be estimated from

$$\hat{r}_o = \frac{c(z)}{\hat{\chi}_v}, \tag{2.29}$$

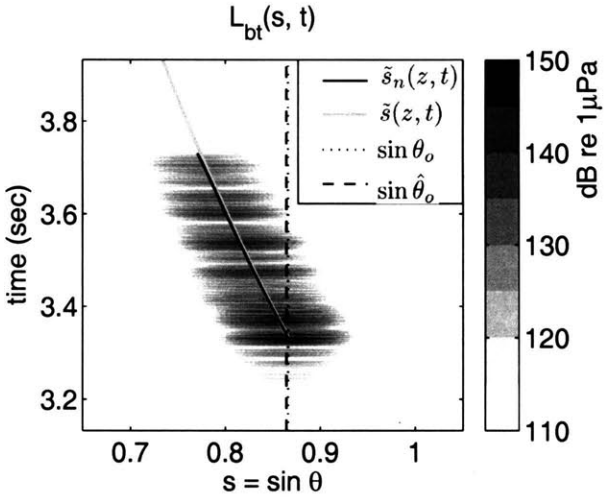

Figure 2-11: The same as Fig. 2-9 (a), but for the 150-m deep Pekeris sand waveguide. The exact beam-time migration line $\tilde{s}_n(z,t)$ is plotted for the first 36 modes of the 41 propagating modes. It can be seen by comparison of Fig. 2-9 (a) and Fig. 2-11 that the exact beam-time migration line $\tilde{s}_n(z,t)$ in a Pekeris waveguide is invariant over the waveguide depth.

where a least squares estimate of $\hat{\chi}_v$ is found with the approximation $[1-\hat{s}_v^2(t)]^{-1/2} = \hat{\chi}_v t + d_v$ from Eq. (2.21), by

$$[\hat{\chi}_v \quad d_v]^T = (\mathbf{T}^T\mathbf{T})^{-1}\mathbf{T}^T\mathbf{S_v}, \tag{2.30}$$

where $\mathbf{S_v} = \left[(1-s_{\max}^2(t_1))^{-1/2}, (1-s_{\max}^2(t_2))^{-1/2}, \cdots, (1-s_{\max}^2(t_N))^{-1/2}\right]^T$, and d_v is a constant intercept. Since the beam-time intensity is symmetric with respect to the $s_v = 0$ axis, $s_{\max}(t)$ can be found either from

$$s_{\max}(t) = \arg\max_{s_v>0} L_{bt}(s_v, t),$$

or from

$$s_{\max}(t) = \arg\max_{s_v<0} L_{bt}(s_v, t).$$

The resulting least square fit is overlain in Fig. 2-10 (a) as a black line, where $\hat{\chi}_v = 0.312$. The corresponding source range estimate is then $\hat{r}_o \simeq 4.8\,\text{km}$, from Eq. (2.29), which is within 4% of the true range $r_o = 5\,\text{km}$.

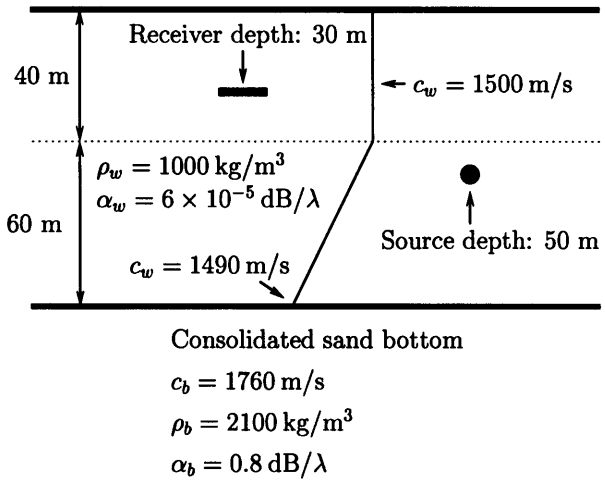

Figure 2-12: Horizontally stratified waveguide with linear sound speed gradient. The sound speed is constant up to 40-m depth, and linearly decreases to 1490-m/s at 100-m depth. The density and attenuation of the water column are the same as those in Fig. 2-6, but the geoacoustic parameters of the sea-bottom are assumed to be different.

2.2.3 Environmental invariance

Here we illustrate the environmental invariance of the range estimation equations (2.24) and (2.27) with some examples. We first note that the array invariants χ_l and χ_h are effectively identical for the 100-m deep Pekeris waveguide of Fig. 2-9, and for the 150-m deep Pekeris waveguide of Fig. 2-11. This is because the migration of $\tilde{s}_n(z,t)$ in response to the given change in waveguide depth occurs only within $\tilde{s}(z,t)$, as discussed in Sec. 2.1. From this example, it can also be deduced that the same invariance holds over frequency. This is because the dispersion relation in a Pekeris waveguide with water depth H effectively depends only on the nondimensional parameter Hf/c_w for fixed ρ_b/ρ_w and c_b/c_w, as shown in Fig. 28 of Ref. [106] and Fig. 4-10 of Ref. [34].

The next example illustrates that array invariants are insensitive to the detailed sound speed profile of the water column and the geoacoustic parameters of the sea-bottom. Figure 2-12 shows an ocean waveguide with a sound speed gradient in the water column. The sound speed changes linearly from 1500-m/s at z =40 m to 1490-m/s at z =100 m. The sea-bottom is assumed to be a consolidated sand bottom with

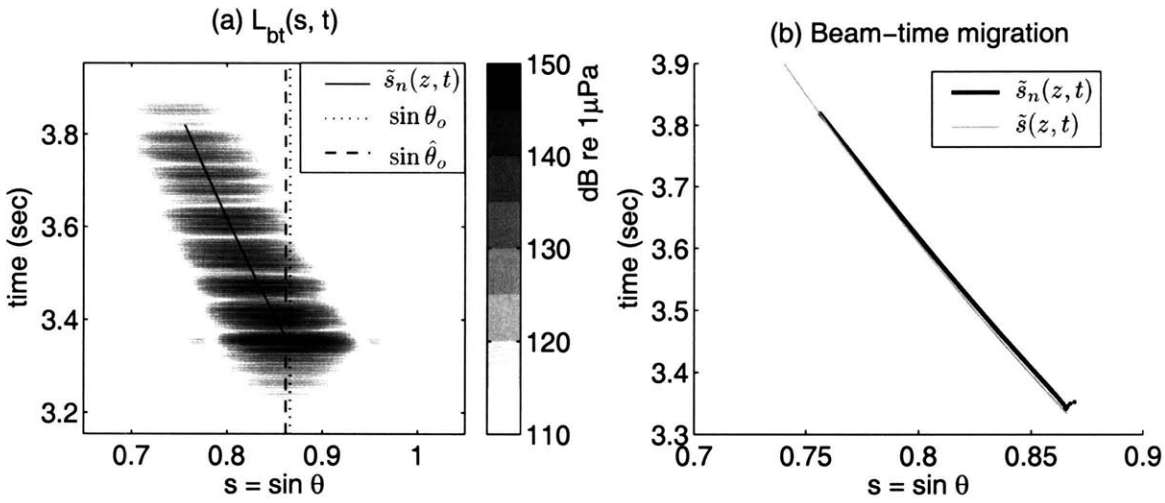

Figure 2-13: Beam-time image $L_{bt}(s,t)$ for $r_o = 5\text{km}$ and $\theta_o = 60°$ in the environment shown in Fig. 2-12. The exact beam-time migration line $\tilde{s}_n(z,t)$ is plotted for the first 27 modes of the 31 propagating modes. The exact beam-time migration line $\tilde{s}_n(z,t)$ is nearly identical to that of the Pekeris waveguide shown in Fig. 2-9, and it effectively spans the entire $\tilde{s}(z,t)$ line.

geoacoustic parameters given in Fig. 2-12. The true source range and bearing with respect to the receiver array are identical to those in Sec. 2.2.1.

The vast majority of modes satisfy relation (2.13), and the exact beam-time migration line $\tilde{s}_n(z,t)$ effectively span the entire $\tilde{s}(z,t)$ line shown in Fig. 2-13. Only the negligible portion of the line $\tilde{s}_n(z,t)$ at its temporal inception arises from waterborne modes that violate relation (2.13), as can be seen from Figs. 2-14 and 2-15. Source range can then be estimated following the same procedure in Sec. 2.2.1, by estimating $\hat{\chi}_l$ or $\hat{\chi}_h$ and using Eqs. (2.26) or (2.28).

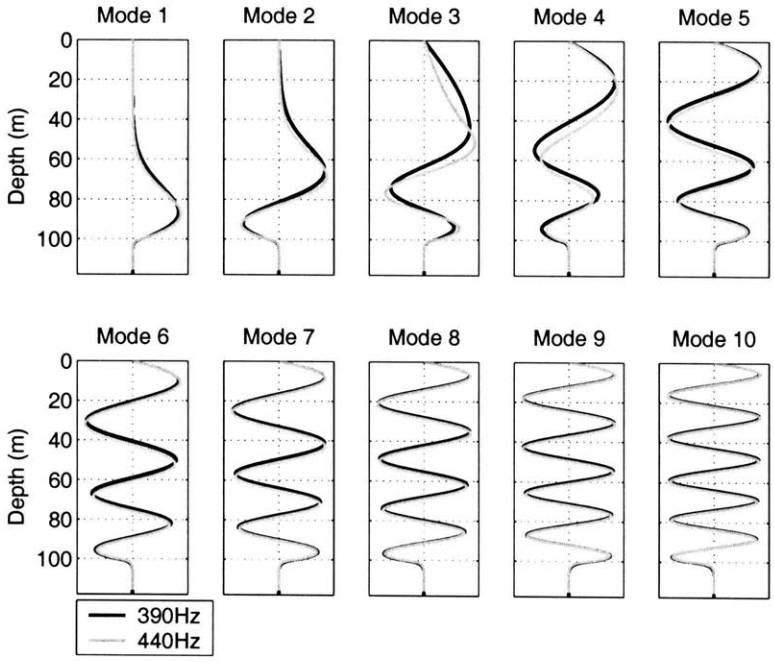

Figure 2-14: Mode shape of the first 10 modes at 390 and 440 Hz, for the environment shown in Fig. 2-12. Only the first 3 modes are waterborne since they are trapped in the refract-bottom-reflect sound speed channel between $z = 40$ m and 100 m shown in Fig. 2-12.

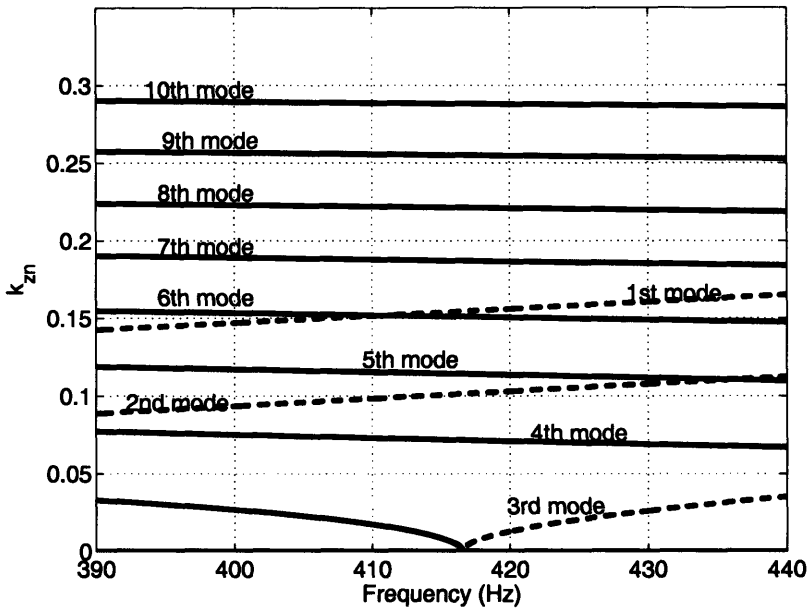

Figure 2-15: Vertical wavenumber k_{zn} of the first 10 modes in the environment shown in Fig. 2-12. The solid lines represent $\mathrm{Re}\{k_{zn}\}$, and the dashed lines represent $\mathrm{Im}\{k_{zn}\}$. Only the first 3 modes are waterborne, and exhibit rapid change of k_{zn} versus frequency.

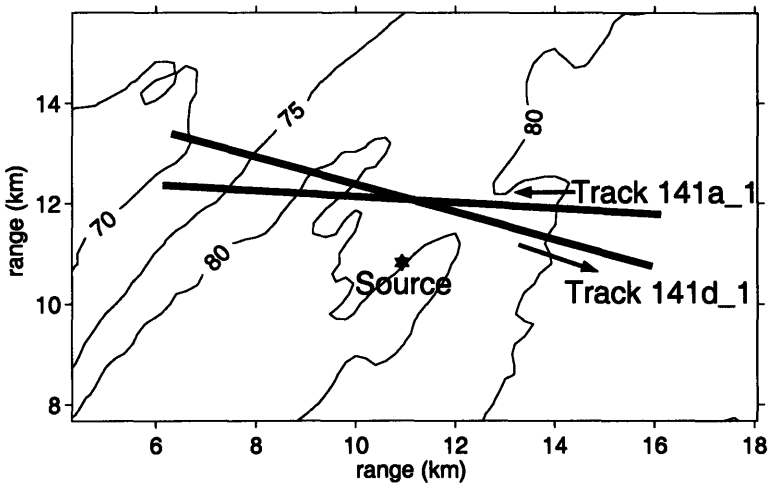

Figure 2-16: The source position and the two receiver ship tracks on May 7, 2003. The source to receiver distance varied from 1 km to 6 km. The depth contour of the sea-bottom in meters is also shown in the figure. The arrows show the heading of the receiver ship along the tracks. The origin of the coordinates in Figs. 2-16 and 2-17 is at 38.955°N and 73.154°W.

2.3 Experimental demonstration of the array invariant

We demonstrate the performance of the array invariant method at range estimation with field data acquired during the Main Acoustic Clutter Experiment (MAE) of 2003 conducted in the New Jersey Strataform area. Water depth typically varied from 70 to 80 m, and source range from 1 to 8 km for the data considered.

2.3.1 Source, receiver geometry and environmental parameters

The MAE was conducted in the New Jersey Strataform area to identify the causes of acoustic clutter in continental shelf environments [79, 111]. Broadband source signals were transmitted from R/V Endeavor. A horizontal linear receiver array was towed along linear tracks by R/V Oceanus. The positions of the source and the tracks used in the present analysis are shown in Figs. 2-16 and 2-17. The positions of both

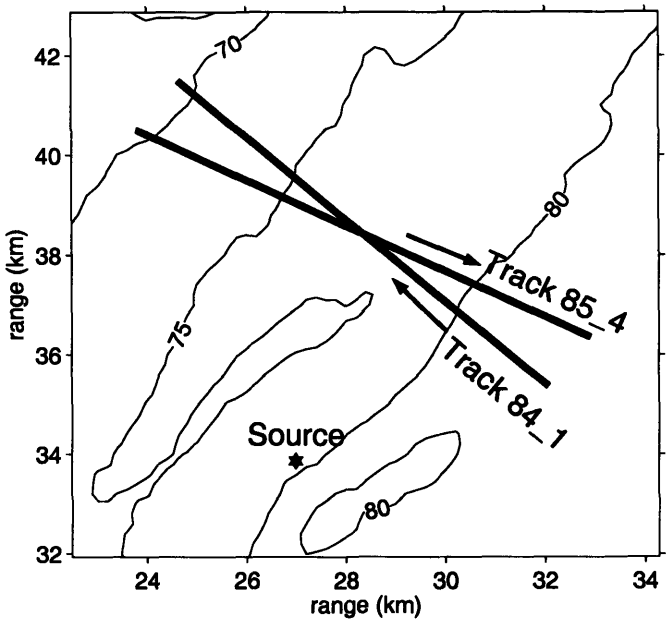

Figure 2-17: The source position and the two receiver ship tracks on May 1, 2003. The source to receiver distance varied from 4 km to 8 km.

research vessels were accurately measured by GPS.

Bathymetry is also plotted in Figs. 2-16 and 2-17. The seafloor has extremely benign slope, typically less than 1°, as can be seen in Fig. 4 of Ref. [111]. The seabed is mostly composed of sand with geoacoustic parameters given in Fig. 2-6 [79, 111]. Two or three XBT's were deployed per track from R/V Oceanus. The sound speed profiles measured by the XBT's are shown in Fig. 2-18.

The receiver was a horizontal line array with aperture $L = 94.5$m for the frequency band of the present analysis. Receiver array depth typically varied from 35 to 45 m for the tracks considered here. The source was a 7-element vertical line array with a 10-m aperture with center depth at 38.1 m. As will be shown later in this section, this vertical source array significantly suppressed the amplitudes of the higher order modes by generating a narrow vertical beam of sound with roughly 6° 3-dB beamwidth. The source transmitted 1-second duration linear frequency modulated (LFM) signals in the 390 to 440-Hz band every 50 seconds, roughly 100 transmissions per track [79]. The signal measured by the receiving array was tapered by a Hann

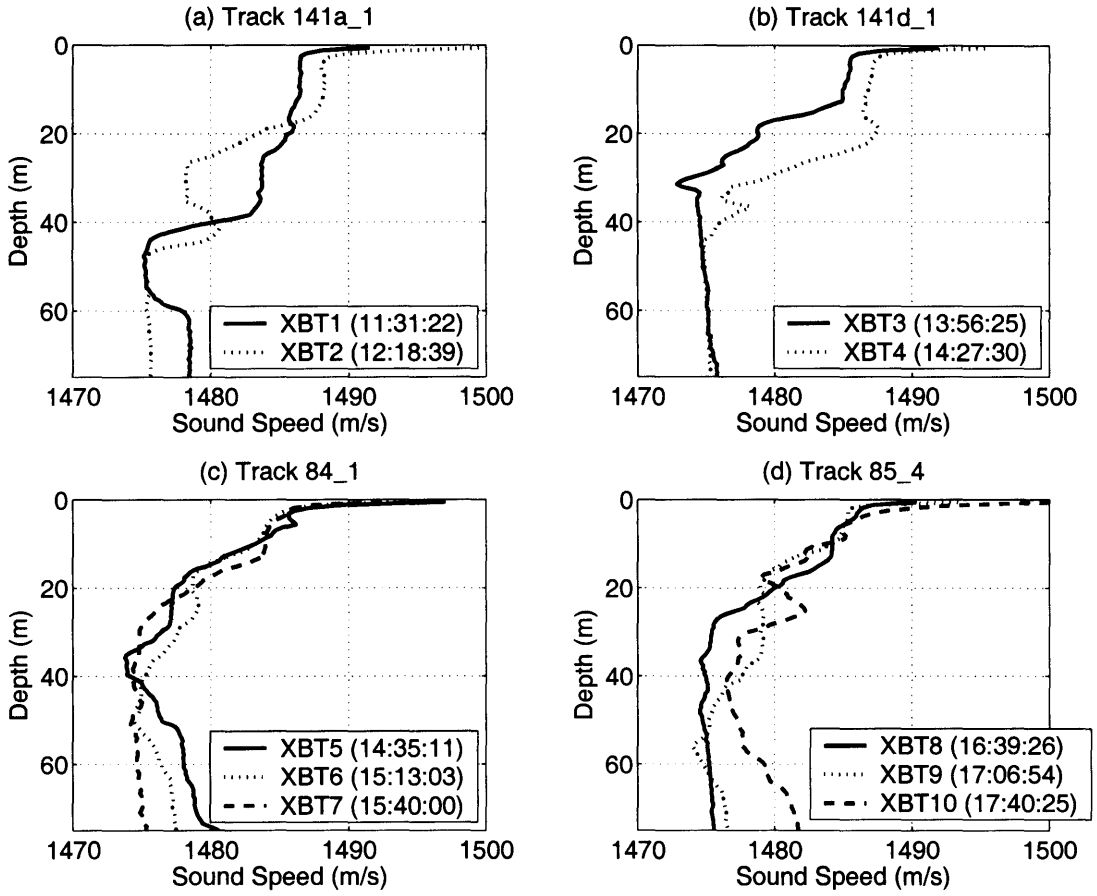

Figure 2-18: Sound speed profiles measured by XBT's during the MAE 2003. Two XBT's were deployed for tracks 141a_1 and 141d_1 (Figs. (a) and (b)), and three XBT's were deployed for tracks 84_1 and 85_4 (Figs. (c) and (d)). The Greenwich Mean Time of the deployment are shown in the parentheses.

window, beamformed, and then matched-filtered with a replica signal. As shown in Appendix A, the array invariant derived for impulsive sources can also be applied to non-impulsive sources if the received field is phase conjugated by matched-filtering. A more general formulation that can treat arbitrary broadband signals that are not necessarily impulsive is possible [73].

2.3.2 Instantaneous range estimation by the array invariant method

We show that source range can be instantaneously and accurately estimated using the array invariant method from field data. The measured beam-time sound pressure level data $L_{bt}(s,t)$, obtained after time-domain beamforming and matched filtering of the acoustic field received on the horizontal array for a source transmissions from Track 141d_1, is imaged in Fig. 2-19 (a). The range and bearing of the source with respect to receiver coordinates are $r_o = 3.6\,\text{km}$ and $\theta_o = -65°$ by GPS measurement. The linear least squares fit of the beam-time migration line $\hat{s}_l(t)$, calculated using Eq. (2.26), is overlain on Fig. 2-19 (a). The slope of the fitted line is the array invariant estimate, $\hat{\chi}_l = 0.339$. The source range r_o is then estimated as $\hat{r}_o = -c(z)\sin\hat{\theta}_o/\hat{\chi}_l \simeq 4.1\,\text{km}$ from Eq. (2.24). This is within 14% of the true range, which is sufficient for many practical applications.

A corresponding simulation is shown in Fig. 2-19 (b). The simulated $\tilde{s}_n(z,t)$, overlain in Fig. 2-19 (b), shows good agreement with the least squares fit of the beam-time migration line $\hat{s}_l(t)$ in Fig. 2-19 (a). Figure 2-20 shows that vertical wavenumber is effectively a constant function of frequency so that relation (2.13) is satisfied for the MAE waveguide, which implies that the array invariant method should work well as shown in the example in Fig. 2-19.

We show that source range can be consistently and robustly estimated using the array invariant method with experimental field data. Source range was estimated 241 times for ranges between 1 to 8 km over the period of 6 hours using MAE data. High correlation was found between source range estimates using the array invariant method and ranges measured by GPS. The range estimates $\hat{r}_o$ using the array invariant method are shown in Fig. 2-21 along with the GPS measured ranges r_o for tracks 141a_1, 141d_1, 84_1, and 85_4. Only ping transmissions that have $20° < |\hat{\theta}_o| < 75°$ were used in range estimation since the array invariant for a horizontal array is insensitive to r_o at broadside incidence, and since the endfire resolution of a horizontal linear array is significantly worse than the near-broadside resolution.

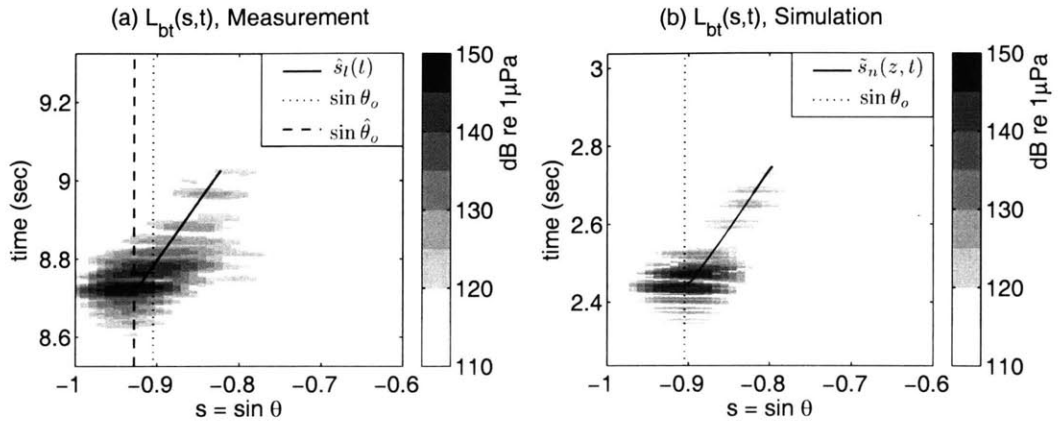

Figure 2-19: (a): The beam-time sound pressure level image $L_{bt}(s,t)$ measured during the MAE 2003. The dotted vertical line is at $\sin\theta_o$, and the dashed vertical line is at $\sin\hat{\theta}_o$, where $\theta_o = -65°$ and $\hat{\theta}_o = -68°$. The slanted line is the linear least squares fit of peak beam-time migration. The receiver depth is 39.7 m. (b): Simulation of the measurement shown in Fig. (a) using the sound speed profile in Fig. 2-18 (b) XBT3. The positions of $\sin\theta_o$ and $\sin\hat{\theta}_o$ are nearly identical. The slant line is $\tilde{s}_n(z,t)$ up to the 20^{th} mode.

Figure 2-22 shows range estimates $\hat{r}_o$ versus GPS measured ranges r_o for all four tracks. The solid line in Fig. 2-22 is the linear regression of $\hat{r}_o$ with respect to r_o. The regression coefficient and the correlation coefficient of 0.946 and 0.835, respectively, are high and indicate that the data have significantly supported the array invariant range estimation model.

The root mean square (RMS) error of all range estimates determined by the array invariant method is 25% of the source range. The accuracy of this particular experimental configuration shows that the array invariant is of extreme practical value.

Even greater accuracy can be achieved for similar measurement scenarios if the source is omnidirectional. The vertical linear source array used in this experiment significantly degraded performance by suppressing higher order modes, especially at long ranges. This is not typical of mobile sources that are detected and tracked in operational systems. Comparison of simulations in Fig. 2-9 and Fig. 2-19 (b) shows that the amplitudes of the higher order modes are significantly reduced by the beampattern of the source. This is especially noticeable since $r_o = 5$ km in

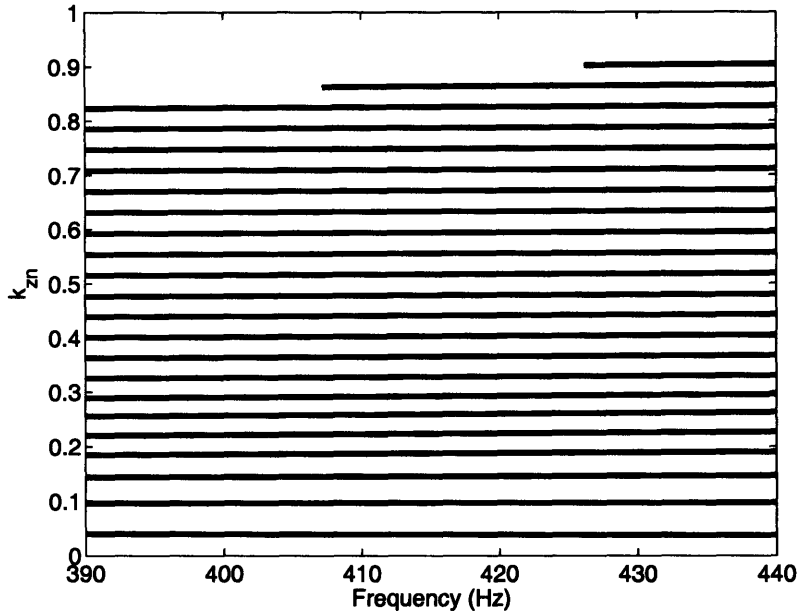

Figure 2-20: Vertical wavenumbers k_{zn} at $z = 39.7$ m calculated using the sound speed profile in Fig. 2-18 (b) XBT3. This figure shows that relation (2.13) is satisfied for the MAE waveguide so that the array invariant method should be applicable. This is because the vertical wavenumber is effectively a constant function of frequency.

Fig. 2-9, whereas $r_o = 3.6$ km in Fig. 2-19 (b). This also appears in the experimental measurement in Fig. 2-19 (a) where peak amplitude decays rapidly with increasing arrival time.

The length of the receiver array used in the MAE was roughly $64\lambda/2$, half the length of many standard arrays. Using a more typical $128\lambda/2$ aperture array would increase the range resolution by a factor of 2, since the range resolution of the array invariant method is roughly proportional to receiving array beamwidth.

Uncertainties in array position, tilt, and shape can also introduce range estimation error. Our numerical simulations show that a 1 degree tilt in both the horizontal and vertical, which was typical in the MAE [79, 111], can cause roughly a 10% error in the current source range estimates.

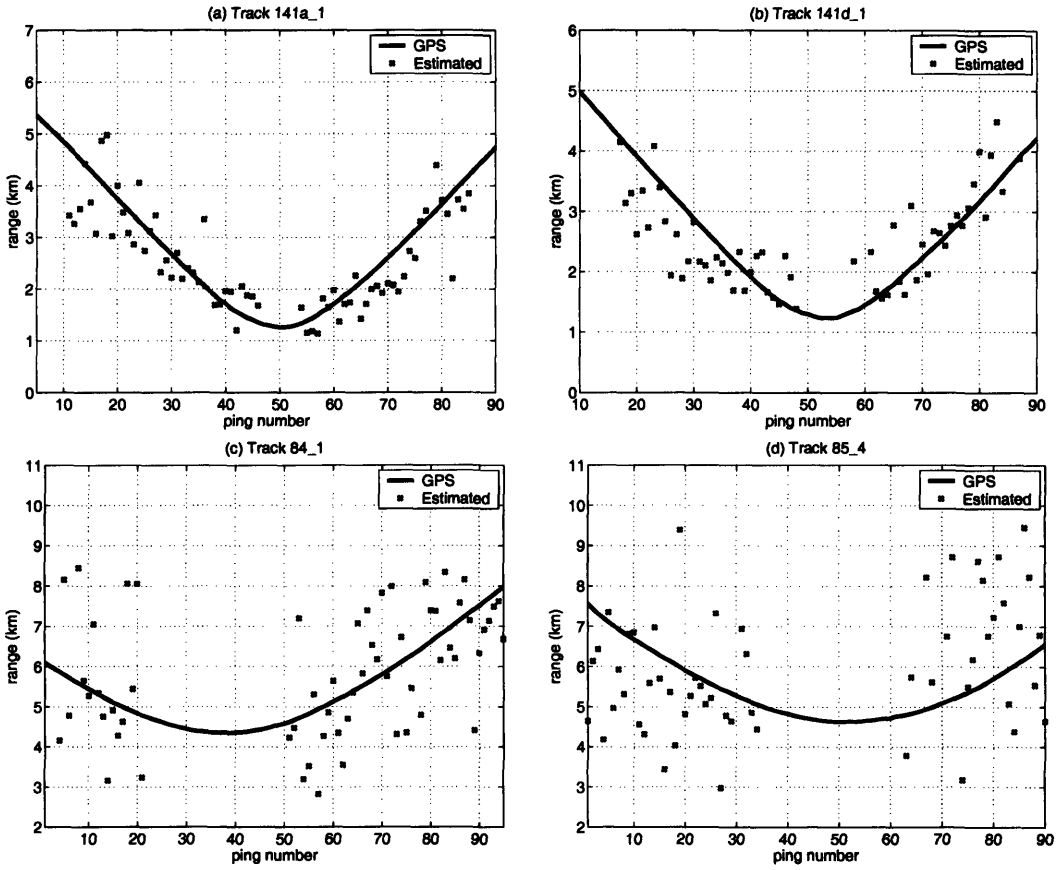

Figure 2-21: Experimental range estimates using the array invariant method. The solid lines show r_o measured by GPS. The cross marks show $\hat{r}_o$ estimated by the array invariant method. (a) Track 141a_1: 66 range estimates are shown, and 3 noise-corrupted data are ignored. The RMS error e_{rms} is 0.6 km. (b) Track 141d_1: 58 range estimates are shown, and 4 noise-corrupted data is ignored. The RMS error e_{rms} is 0.6 km. (c) Track 84_1: 61 range estimates are shown, and 8 noise-corrupted data are ignored. The RMS error e_{rms} is 1.4 km. (d) Track 85_4: 56 range estimates are shown, and 6 noise-corrupted data are ignored. The RMS error e_{rms} is 1.7 km.

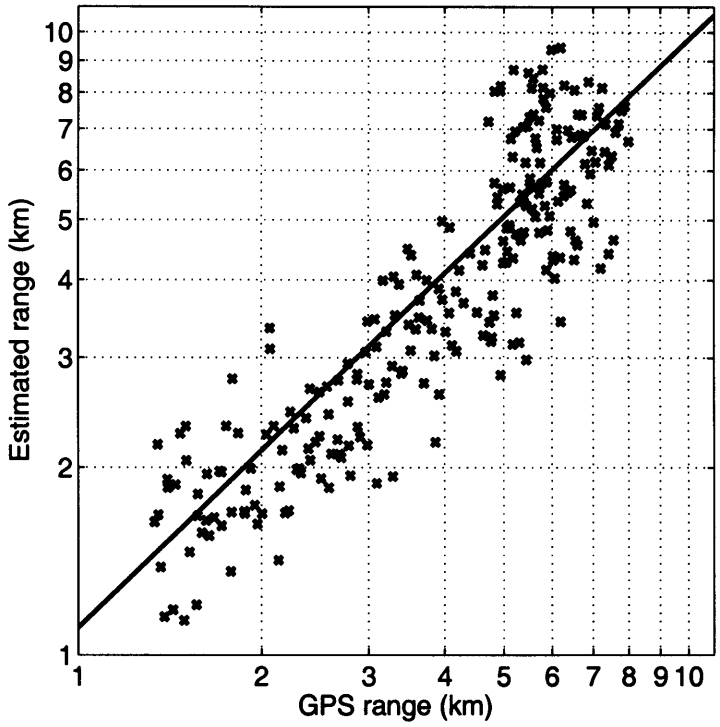

Figure 2-22: Experimental range estimates using the array invariant method. The range estimates $\hat{r}_o$ versus GPS measured ranges r_o for tracks 141a_1, 141d_1, 84_1, and 85_4 plotted in logarithmic scale. The solid line is the linear regression $\hat{r}_o = a + br_o$, where the regression coefficient $b = 0.946$ and the intercept $a = 161$ m. The correlation coefficient is 0.835.

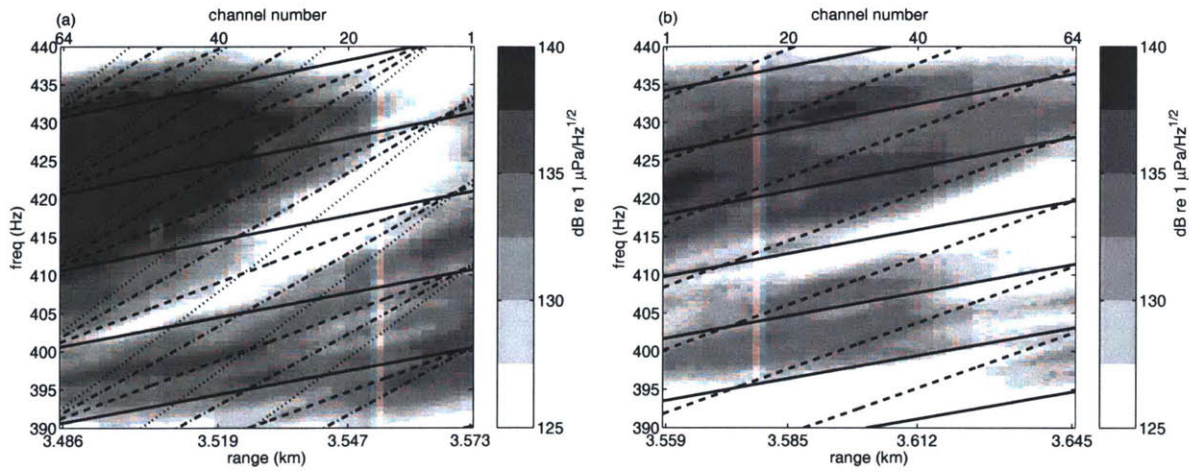

Figure 2-23: Incoherent acoustic intensity measured over the array aperture during the MAE 2003. Figure (a) is one of the measurements from Track 141a_1, and Fig. (b) is the incoherent intensity of the same data shown in Fig. 2-19 from Track 141d_1. The receiver array has 64 channels, the number of which are shown on top of the figures. The range from each channel to the source is shown at the bottom of the figures. The black lines are the interference patterns for $\beta_{mn} = 1$ (—) $\beta_{mn} = 2$ (- - -), $\beta_{mn} = 3$ (- · - ·), and $\beta_{mn} = 4$ (· · ·), respectively, calculated using Eq. (2.31). Variation of β_{mn} from 1 by more than a factor of 2 can be observed.

2.4 Comparison of the array invariant method to other range estimation techniques

It has been suggested that the interference pattern of incoherent acoustic intensity measured as a function of range and frequency can be used for source localization in shallow-water waveguides by the waveguide invariant method, provided that the values of the invariant parameters are known accurately [22, 18]. The waveguide invariant parameter β_{mn} between two propagating modes m and n is defined as

$$\beta_{mn} = -\frac{v_{pm}^{-1} - v_{pn}^{-1}}{v_{gm}^{-1} - v_{gn}^{-1}}. \tag{2.31}$$

For an ideal waveguide with perfectly reflecting boundaries or for a waveguide with an n^2-linear sound speed profile, the waveguide invariant parameters are approximately equal to 1 and -3, respectively. Equation (2.31) shows that the waveguide invariant requires multiple modes in its fundamental definition, whereas the array invariant

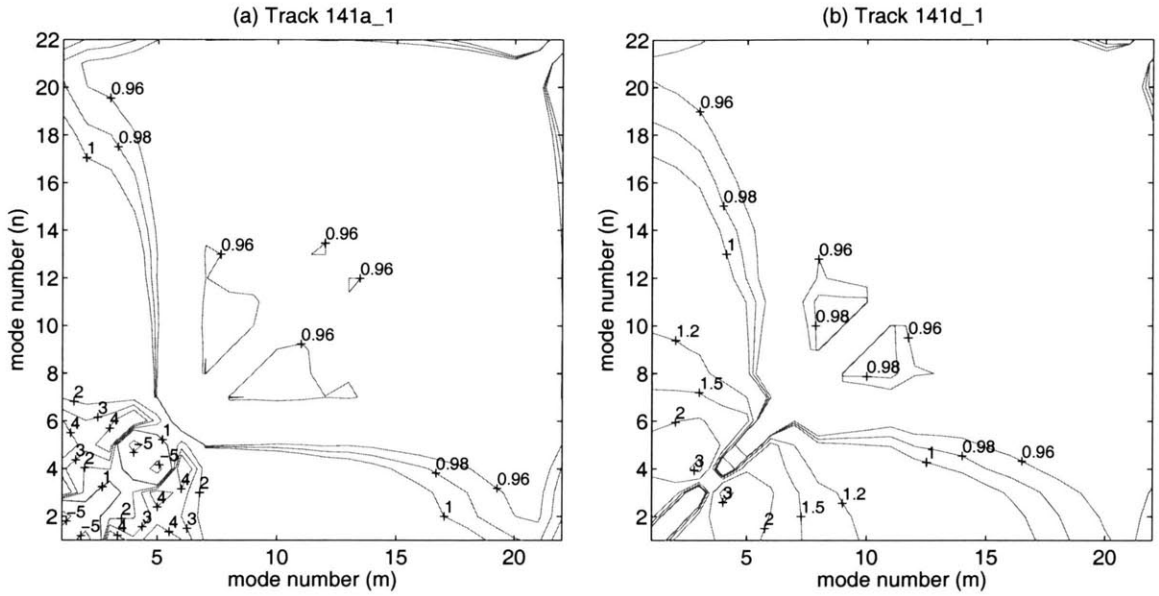

Figure 2-24: (a) Track 141a_1: The waveguide invariant parameters β_{mn} calculated using the sound speed profile in Fig. 2-18 (a) XBT2 at $f = 415$ Hz. (b) Track 141d_1: The waveguide invariant parameters β_{mn} calculated using the sound speed profile in Fig. 2-18 (b) XBT3 at $f = 415$ Hz. It can be seen that roughly a factor of 2 change in β_{mn} has occurred in less than two hours.

does not require multiple modes as discussed in Sec. 2.1.2.

Range estimation using the waveguide invariant can lead to large errors if the distribution of β_{mn} is not known *a priori* since uncertainty in r_o is proportional to uncertainly in β_{mn}. Incoherent intensity interference patterns measured during the Main Acoustic Clutter Experiment and corresponding waveguide invariant parameters are provided in Figs. 2-23 and 2-24, respectively, where it can be seen that β_{mn} can vary from 1 by more than a factor of 2. This variation of β_{mn} will lead to more than a factor of 2 error in range estimates if $\beta_{mn} = 1$ is assumed without *a priori* knowledge of the waveguide invariant parameters. The waveguide invariant parameters also can suffer from large temporal and spatial variation. This is demonstrated in Fig. 2-24, where roughly a factor of 2 change in β_{mn} is shown to have occurred in less than two hours.

Range estimation using MFP techniques also requires accurate knowledge of the environmental parameters. For example, Fig. 9 in Ref. [36] shows that a very common

uncertainty of only ±6-m/s sound speed mismatch in the water column results in intolerable MFP ambiguity in a 100-m deep shallow-water waveguide with a source at 5-km range.

The array invariant, waveguide invariant, and MFP techniques for passive source range estimation all fit into a similar category. This is because they all work even when the source is in the far-field of the receiver since they all rely on the waveguide effects such as modal dispersion or interference. While near-field techniques for source localization, such as focusing or triangulation, may have better range resolution than any of these far-field waveguide techniques, they require an extended aperture or combination of widely separated apertures, which limits their practicality.

2.5 Summary

An array invariant method has been introduced for instantaneous source range estimation in an ocean waveguide. The method exploits the dispersive behavior of guided wave propagation. It has been shown that the array invariant method does not require *a priori* knowledge of the environmental parameters, nor does it require extensive computations. The ability to make simple and accurate range estimates by the array invariant method has been demonstrated with data from the Main Acoustic Clutter Experiment of 2003.

Chapter 3

Simulataneous localization of multiple broadband noise sources in an ocean waveguide using the array invariant

The array invariant method has been introduced in Chap. 2 for range estimation of an impulsive source in an ocean waveguide from passive beam-time intensity data received on arrays with horizontal or vertical aperture. The array invariant method exploits dispersion of acoustic waves inherent in waveguide propagation, and consequent spreading of acoustic waves in time and array scan angle when conventional plane-wave beamforming is applied to data received on an array. The array invariant method has significant advantages over existing source localization methods because it does not require *a priori* knowledge of the wave propagation environment, and the range estimates can be made with little computational effort.

Here we show that the array invariant method can be extended for range and bearing estimation of a broadband random noise source that is not necesarily impulsive in the time domain, while maintaining the advantages of the array invariant method for impulsive source localization. It is shown that the array invariant method can

be used not only for a single source localization, but for simultaneous localization of multiple noise sources in an ocean waveguide without ambiguity.

Localization of multiple sources using the array invariant method has advantages over the conventional triangulation method using two arrays. First, the array invariant method does not require two arrays with sufficient spatial separation, which is a significant advantage when the localization is made from a mobile platform. Second, the array invariant method does not suffer from the ghost source problem typical in the triangulation method when there are multiple sources present [60]. The array invariant method is also advantageous over MFP, where unambiguous source range estimation is nearly impossible even with accurate environmental knowledge when there are unknown number of multiple, spatially stationary sources in an ocean waveguide [25, 49].

The array invariant method for broadband noise source localization is derived in Sec. 3.1. Illustrative examples for localization of a single source and multiple sources in range and bearing are provided in Sec. 3.2.1 and Sec. 3.2.2, respectively.

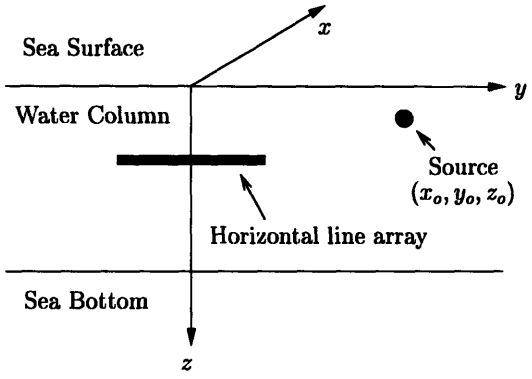

Figure 3-1: The geometry of the coordinate system. The horizontal line array is aligned parallel to the y-axis, and the source is at (x_o, y_o, z_o).

3.1 Theory

The measurement and coordinate geometry is shown in Fig. 1, where a horizontal line array parallel to the y axis is centered at $(0, 0, z)$ and a source is located at (x_o, y_o, z_o). The pressure P_o measured by the sensor at the center of the array can be expressed as a sum of normal modes as

$$P_o(\mathbf{r} = \mathbf{0}, z, f) = \frac{4\pi Q(f)i}{\sqrt{8\pi\rho(z_o)}} e^{-i\pi/4} \sum_n u_n(z_o) u_n(z) \frac{e^{ik_{rn}r_o}}{\sqrt{k_{rn}r_o}}, \tag{3.1}$$

where $\mathbf{r} = x\hat{i}_x + y\hat{i}_y$, $\mathbf{r_o} = x_o\hat{i}_x + y_o\hat{i}_y$, $\hat{i}_x$ and $\hat{i}_y$ are the unit vectors in the x and y directions, $r = |\mathbf{r}|$, $r_o = |\mathbf{r_o}|$, $Q(f)$ is the source spectrum, ρ is the density, k_{rn} is the horizontal wavenumber, and u_n is the mode shape of the nth mode. We assume that the source emitts broadband random noise that is not necesarily impulsive in the time domain.

When the source is in the far-field of the receiver array, the beamformed pressure P_B measured by the array after standard time-delay beamforming is given by

$$P_B(s, f) = \frac{4\pi Q(f)i}{\sqrt{8\pi\rho(z_o)}} e^{-i\pi/4} \sum_n u_n(z_o) u_n(z) \frac{e^{ik_{rn}r_o}}{\sqrt{k_{rn}r_o}} B(s - s_n), \tag{3.2}$$

where $s = \sin\theta$, θ is the array scan angle, $s_n = \sin\phi_n \sin\theta_o$, θ_o is the bearing of the source measured from the x axis, $\sin\phi_n = k_{rn}/k$, k is the wavenumber, and $B(s)$ is

the array beam pattern.

It has been shown in Chap. 2 that the array invariant method derived specifically for an impulsive source in the time domain can be applied to any broadband signals as long as the received pressure field is phase conjugated by the source spectrum. Here we achieve the phase conjugation by cross-correlating the beamformed pressure P_B with the single sensor measurement P_o. The cross-correlated intensity field I_{Bo} of P_o and P_B is then

$$\begin{aligned} I_{Bo}(s,\tau) &= \lim_{T\to\infty}\frac{1}{T}\int_{-T/2}^{T/2} P_B(s,t)P_o(t+\tau)\,dt = \mathcal{F}^{-1}\left\{P_B(s,f)P_o^*(r,f)\right\} \\ &= 2\,\mathrm{Re}\left\{\sum_m\sum_n E_{mn}(s,\tau)\right\}, \end{aligned} \tag{3.3}$$

where E_{mn} is the complex envelope of the cross-correlated intensity field between the mth and the nth mode given by

$$\begin{aligned} E_{mn}(s,\tau) &= \frac{2\pi}{(\rho(z_o))^2}\int_0^\infty |Q(f)|^2 u_m(z_o)u_m(z)u_n(z_o)u_n(z) \\ &\quad \times\frac{B(s-s_m)}{\sqrt{k_{rm}k_{rn}}r_o}e^{ir_o\psi_{mn}}\,df, \end{aligned} \tag{3.4}$$

and $\psi_{mn} = (k_{rm} - k_{rn}) - 2\pi f\tau/r_o$. In Eq. 3.3, the source phase conjugation in I_{Bo} is achieved by the cross correlation of P_o and P_B, and so I_{Bo} depends only on the power spectrum of the source $|Q(f)|^2$ but not on the detailed shape of the source signal in the time domain. This cross-correlation of P_o and P_B, however, also causes unwanted correlation between modes, as can be seen in Eq. 3.4.

We now analyze the structure of E_{mn} in Eq. 3.4 as a function of delay time τ and the array scan angle s. First, when $m = n$,

$$E_{mm}(s,\tau) = \frac{2\pi}{(\rho(z_o))^2}\int_0^\infty |Q(f)|^2\{u_m(z_o)u_m(z)\}^2\frac{B(s-s_m)}{k_{rm}r_o}e^{-i2\pi f\tau}\,df \tag{3.5}$$

is identical to the auto-correlation of the mth mode, except the beampattern $B(s-s_m)$ inside the integral. If the change of the beampattern $B(s-s_m)$ is relatively slow as a function of frequency, E_{mm} is confined only near $\tau \simeq 0$, and the width of E_{mm} in

τ domain is inversely proportional to the bandwidth of the source power spectrum $|Q(f)|^2$.

Second, when $m \neq n$, E_{mn} has a stationary phase point at frequency $f = \tilde{f}$ that satisfies

$$\left[\frac{\partial \psi_{mn}}{\partial f}\right]_{f=\tilde{f}} = \left[\frac{\partial k_{rm}}{\partial f} - \frac{\partial k_{rn}}{\partial f} - \frac{2\pi\tau}{r_o}\right]_{f=\tilde{f}} = 0. \tag{3.6}$$

We define the delay time $\tilde{\tau}_{mn}$ to be the time that satisfies Eq. 3.6,

$$\tilde{\tau}_{mn} \equiv \tau_{mn}(\tilde{f}) = \frac{r_o}{2\pi}\left[\frac{\partial k_{rm}}{\partial f} - \frac{\partial k_{rn}}{\partial f}\right]_{f=\tilde{f}} = r_o\left(v_{gm}^{-1}(\tilde{f}) - v_{gn}^{-1}(\tilde{f})\right). \tag{3.7}$$

From the equation above, it can be seen that $\tilde{\tau}_{mn}$ is the travel time difference between the mth mode and the nth mode at $f = \tilde{f}$. At this stationary phase point $\tau = \tilde{\tau}_{mn}$, the peak of $E_{mn}(s, \tau)$ in the s domain occurs at the array scan angle

$$s(\tilde{\tau}_{mn}) = \sin\phi_m(\tilde{\tau}_{mn}) \sin\theta_o, \tag{3.8}$$

which makes the argument of the beampattern B in Eq. 3.4 to be zero. Equation 3.8 shows that the array scan angle where the peak of E_{mn} occurs depends only on the elevation angle ϕ_m of the mth mode and the source bearing θ_o, however, this elevation angle depends on the travel time difference $\tilde{\tau}_{mn}$ between the mth and the nth mode. To explicitly state this dependence, we define

$$\tilde{s}_{mn} \equiv s(\tilde{\tau}_{mn}) = \sin\phi_m(\tilde{\tau}_{mn}) \sin\theta_o. \tag{3.9}$$

We now analyze migration of $\tilde{s}_{mn}$ in Eq. 3.9 as a function of mode numbers m and n, and the delay time $\tilde{\tau}_{mn}$ in the beam-time domain. This is done by dividing the beam-time domain into two sub-domains where $\tilde{\tau}_{mn} > 0$ and $\tilde{\tau}_{mn} < 0$. It is shown that the migration of $\tilde{s}_{mn}$ when $\tilde{\tau}_{mn} > 0$ reveals the source range r_o, and the migration of $\tilde{s}_{mn}$ when $\tilde{\tau}_{mn} < 0$ reveals the source bearing θ_o.

3.1.1 Case I: $\tilde{\tau}_{mn} > 0$

The case where $\tilde{\tau}_{mn} > 0$ occurs when the group velocity of the nth mode in P_o is faster than that of the mth mode in P_B, as can be seen from Eq. 3.7. We first analyze the structure of E_{mn} for $\tilde{\tau}_{mn} > 0$ in an ideal waveguide with rigid or pressure-release boundaries. We show that the spread of E_{mn} in the s and τ domain is bounded by the beamformer migration line for an impulsive source, defined in Eq. 2.8, from which estimates of the array invariant $\hat{\chi}_h$ and the source range $\hat{r}_o$ can be obtained. We then show that the analysis in an ideal waveguide is approximately valid in a horizontally stratified waveguide, and the source range can be obtained using the same method as in the ideal waveguide case without *a priori* knowledge of the environment.

Ideal waveguide

In an ideal waveguide, the group velocity of the nth mode v_{gn} is related to the elevation angle of the mode ϕ_n by

$$v_{gn} = c \sin \phi_n \tag{3.10}$$

for all frequencies f. Then the travel time difference between two different modes in Eq. 3.7 can be expressed as

$$\tilde{\tau}_{mn} = r_o \left(\frac{1}{\tilde{v}_{gm}} - \frac{1}{\tilde{v}_{gn}} \right) = \frac{r_o}{c} \frac{\sin \tilde{\phi}_n - \sin \tilde{\phi}_m}{\sin \tilde{\phi}_m \sin \tilde{\phi}_n}, \tag{3.11}$$

which can be rewritten as

$$\sin \tilde{\phi}_m = \frac{r_o \sin \tilde{\phi}_n}{c\tilde{\tau}_{mn} \sin \tilde{\phi}_n + r_o}, \tag{3.12}$$

where $\tilde{v}_{gm} = v_{gm}(\tilde{f})$, $\tilde{v}_{gn} = v_{gn}(\tilde{f})$, $\sin \tilde{\phi}_m = \sin \phi_m(\tilde{f})$, and $\sin \tilde{\phi}_n = \sin \phi_n(\tilde{f})$. Using Eq. 3.12, $\tilde{s}_{mn}$ in Eq. 3.9 can be expressed as

$$\tilde{s}_{mn} = \frac{r_o \sin \tilde{\phi}_n}{c\tilde{\tau}_{mn} \sin \tilde{\phi}_n + r_o} \sin \theta_o. \tag{3.13}$$

If $\sin \tilde{\phi}_n$ is approximately constant within the frequency band of the source, the

derivative of $\tilde{s}_{mn}^{-1}$ in Eq. 3.13 with respect to τ_{mn} yields

$$\frac{\partial \tilde{s}_{mn}^{-1}}{\partial \tilde{\tau}_{mn}} \simeq \frac{c \sin \tilde{\phi}_n}{r_o \sin \tilde{\phi}_n \sin \theta_o} = \frac{c}{r_o \sin \theta_o} = \chi_h, \tag{3.14}$$

where χ_h is the array invariant for a horizontal line array in an ideal waveguide, as defined in Eq. 2.9. This is satisfied when (1) the source frequency is much higher than the cut-off frequency of the nth mode so that $\sin \tilde{\phi}_n$ is nearly constant and is close to 1, or (2) the frequency band of the source is sufficiently narrow so that the change of $\sin \tilde{\phi}_n$ within the mode is essentially negligible.

Among the two cases where $\sin \tilde{\phi}_n$ is approximately constant, the first case is of primary interest. If $\sin \tilde{\phi}_n \simeq 1$ within the frequency band of the source, Eq. 3.13 turns into

$$\tilde{s}_{mn} \simeq \frac{r_o}{c\tilde{\tau}_{mn} + r_o} \sin \theta_o = \frac{r_o \sin \theta_o}{c(\tilde{\tau}_{mn} + r_o/c)}. \tag{3.15}$$

If $\sin \tilde{\phi}_n \simeq 1$, the group velocity $\tilde{v}_{gn}$ is approximately equal to the sound speed c, as can be seen in Eq. 3.10. The term $\tilde{\tau}_{mn} + r_o/c = t$ in the denominator of Eq. 3.15 is then approximately equal to the travel time of the mth mode, since $r_o/c \simeq r_o/\tilde{v}_{gn}$ is the travel time of the nth mode, and $\tilde{\tau}_{mn}$ is the travel time difference between the mth and the nth mode. Equation 3.15 is then equivalent to Eq. 2.8 where

$$\tilde{s}(t) = \frac{r_o}{ct} \sin \theta_o \tag{3.16}$$

is the beamformer migration line for an impulsive source in an ideal waveguide, except that Eq. 3.15 is expressed in terms of the reduced travel time $\tilde{\tau}_{mn}$ rather than the total travel time t. It can also be seen in Eq. 3.15 that $\tilde{s}_{mn}(\tilde{\tau}_{mn} \simeq 0) \simeq \sin \theta_o$, so that $\tilde{s}_{mn}$ emerges from the true source bearing $\sin \theta_o$ when τ_{mn} is sufficiently close to zero.

An example of the distribution of the beamformer migration lines for cross-correlated modes $\tilde{s}_{mn}$ in the s and τ domain are shown in Fig. 3-2, for a source in the frequency band from 90 to 100 Hz, located at $r_o = 20$ km and $\theta_o = \pi/2$. Each line segment in Fig. 3-2 shows beam-time migration of $\tilde{s}_{mn}$ for specific mode number m and n overlain on the line segment. The thick gray line in the $\tau > 0$ domain of

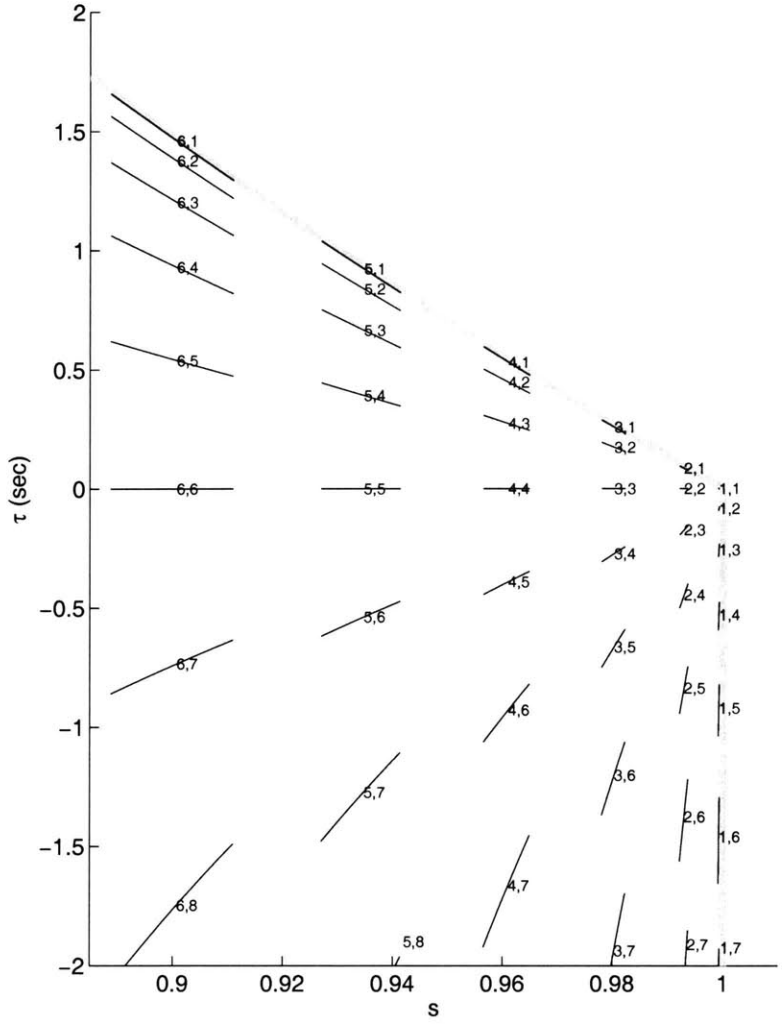

Figure 3-2: The beamformer migration lines $\tilde{s}_{mn}$ of all the cross-correlated modes m and n for a source at $r_o = 20$ km and $\theta_o = \pi/2$, as a function of array scan angle s and delay time τ. The source is assumed to generate broadband signal from 90 to 100 Hz. The migration lines $\tilde{s}_{mn}$ are plotted in black solid lines with corresponding mode numbers marked next to the lines. The thick gray line in $\tau > 0$ is the beamformer migration line for an impulsive source in Eq. 3.16, in terms of the reduced travel time $\tau = t - r_o/c$. The thick gray line in $\tau < 0$ is at the sine of the source bearing $\sin\theta_o = 1$. It can be seen that the beamformer migration lines $\tilde{s}_{mn}$ are bounded by these two thick gray lines.

Fig. 3-2 is the beamformer migration line for an impulsive source in Eq. 3.16 in terms of the reduced travel time $\tau = t - r_o/c$. It can be seen that $\tilde{s}_{mn}$ aligns with this thick gray line when $n = 1$, since the elevation angle of the 1st order mode is close to $\pi/2$, or $\sin\phi_1$ is close to 1, satisfying Eq. 3.15. As mode number n increases for fixed mode number m, the travel time difference $\tilde{\tau}_{mn}$ between the mth and the nth mode decreases, and the beamformer migration lines $\tilde{s}_{mn}$ move closer to the $\tau = 0$ axis, as can be seen in Fig. 3-2. Therefore, the beamformer migration line $\tilde{s}_{m1}$ is the bounding line for all the migration lines $\tilde{s}_{mn}$ for $\tau > 0$. By detecting this bounding line in the cross-correlated intensity field, one can estimate the array invariant χ_h and obtain the source range r_o. In Sec. 3.2, we will present a method to detect this bounding line and to estimate the source range.

Horizontally stratified waveguide

The group velocity of the nth mode in a horizontally stratified waveguide can be expressed as

$$v_{gn} = \frac{c(z)\sin\phi_n(z)}{1 + D_n(z)}, \tag{3.17}$$

where

$$D_n(z) = \frac{c(z)}{2\pi}\cos\phi_n(z)\frac{dk_{zn}(z)}{df} \tag{3.18}$$

is the correction term for the beamformer migration as shown in Eq. 2.11. Using Eq. 3.17, Eq. 3.7 can be expressed as

$$\begin{aligned}\tilde{\tau}_{mn} &= r_o\left[\frac{1}{\tilde{v}_{gm}} - \frac{1}{\tilde{v}_{gn}}\right] = \frac{r_o}{c(z)}\left[\frac{1+\tilde{D}_m(z)}{\sin\tilde{\phi}_m(z)} - \frac{1+\tilde{D}_n(z)}{\sin\tilde{\phi}_n(z)}\right] \\ &= \frac{r_o}{c(z)}\frac{\sin\tilde{\phi}_n(z)[1+\tilde{D}_m(z)] - \sin\tilde{\phi}_m(z)[1+\tilde{D}_n(z)]}{\sin\tilde{\phi}_m(z)\sin\tilde{\phi}_n(z)}.\end{aligned} \tag{3.19}$$

Now, let us assume that there is at least one mode whose cut-off frequency is much lower than the frequency band of the source so that $\sin\tilde{\phi}_n \simeq 1, \cos\tilde{\phi}_n \simeq 0$, and

$\tilde{D}_n(z) \simeq 0$ within the source frequency band. Then $\tilde{\tau}_{mn}$ in Eq. 3.19 simplifies to

$$\tilde{\tau}_{mn} \simeq \frac{r_o}{c(z)} \frac{1 + \tilde{D}_m(z) - \sin\tilde{\phi}_m(z)}{\sin\tilde{\phi}_m(z)}, \tag{3.20}$$

which leads to

$$\sin\tilde{\phi}_m(z) \simeq \frac{r_o[1 + \tilde{D}_m(z)]}{c(z)\tilde{\tau}_{mn} + r_o}. \tag{3.21}$$

By substituting Eq. 3.21 into Eq. 3.9, we obtain

$$\tilde{s}_{mn} = \frac{r_o \sin\theta_o}{c(z)\tilde{\tau}_{mn} + r_o}[1 + \tilde{D}_m(z)]. \tag{3.22}$$

It can be seen from comparison of Eqs. 3.15 and 3.22 that $\tilde{D}_m(z)$ in Eq. 3.22 is the correction term for $\tilde{s}_{mn}$ when there is variation in sound speed structure versus depth. This correction term is negligible for non-waterborne modes in typical shallow-water environments at frequencies higher than modal cut-off frequencies as shown in Chap. 2. Equation 3.22 then turns into the equation for an ideal waveguide in Eq. 3.15, and the array invariant χ_h can be obtained from Eq. 3.22 as

$$\chi_h \equiv \frac{\partial\tilde{s}_{mn}^{-1}}{\partial\tilde{\tau}_{mn}} \simeq \frac{c(z)}{r_o \sin\theta_o}. \tag{3.23}$$

In a horizontally stratified ocean waveguide, the extent of $\tilde{s}_{mn}$ in the τ-domain is finite as is the beam-time migration line for an impulsive source, since the group velocities of the modes are bounded by the minimum group velocity at the Airy phase. Equation 3.22 can then be expanded using the Taylor series at $\tilde{\tau}_{mn} = 0$, and the linearized array invariant χ_l can be defined as

$$\chi_l \equiv \left.\frac{\partial\tilde{s}_{mn}}{\partial\tilde{\tau}_{mn}}\right|_{\tilde{\tau}_{mn}=0} \simeq -\frac{c(z)\sin\theta_o}{r_o}, \tag{3.24}$$

which is convenient for practical use.

3.1.2 Case II: $\tau_{mn} < 0$

The case where $\tilde{\tau}_{mn} < 0$ occurs when the group velocity of the mth mode in P_B is faster than the group velocity of the nth mode in P_o. It is shown that the migraion of $\tilde{s}_{mn}$ in this case is bounded by the bearing of the source. The bearing of the source can then be estimated from this bounding line.

Ideal waveguide

We first assume that there is at least one mode that satisfies $\sin\tilde{\phi}_m \simeq 1$. Then the group velocity of this mode satisfies $v_{gm} \simeq c$ as can be seen from Eq. 3.10. The travel time difference between two different modes is then

$$\tilde{\tau}_{mn} = r_o\left(\frac{1}{v_{gm}} - \frac{1}{v_{gn}}\right) \simeq \frac{r_o}{c}\left(1 - \frac{1}{\sin\tilde{\phi}_n}\right). \tag{3.25}$$

The migraion of $\tilde{s}_{mn}$ is, from Eq. 3.9,

$$\tilde{s}_{mn} = \sin\phi_m(\tilde{\tau}_{mn})\sin\theta_o \simeq \sin\theta_o. \tag{3.26}$$

Equations 3.25 and 3.26 show that the location of $\tilde{s}_{mn}$ in the τ-domain is determined by the elevation angle of the nth mode $\sin\tilde{\phi}_n$, however, the location of $\tilde{s}_{mn}$ in the s-domain is independent of $\sin\tilde{\phi}_n$, and is always at the bearing of the source $\sin\theta_o$. This is shown in Fig. 3-2, where the migration of the first order mode $\tilde{s}_{1n}$ aligns with $\sin\theta_o$ marked by the thick gray line in the $\tau < 0$ domain.

As mode number m increases, $\tilde{s}_{mn}$ migrates to $|\tilde{s}_{mn}| < |\sin\theta_o|$ in the s-domain, as shown in Fig. 3-2, since the elevation angle of the mth mode $\sin\tilde{\phi}_m$ decreases. Therefore, the bearing of the source $\sin\theta_o$ is the bounding line for $\tilde{s}_{mn}$ in the $\tau < 0$ domain.

Horizontally stratified waveguide

We again assume that there is a mode that satisfies $\sin\tilde{\phi}_m \simeq 1$. Then Eq. 3.25 for an ideal waveguide changes to

$$\tilde{\tau}_{mn} = \frac{r_o}{c(z)}\left[1 - \frac{1+\tilde{D}_n(z)}{\sin\tilde{\phi}_n(z)}\right]. \tag{3.27}$$

The migration of $\tilde{s}_{mn}$, however, is still given by

$$\tilde{s}_{mn} = \sin\phi_m(\tilde{\tau}_{mn})\sin\theta_o \simeq \sin\theta_o. \tag{3.28}$$

Equations 3.27 and 3.28 shows that the correction term $\tilde{D}_m(z)$ can change the travel time difference $\tilde{\tau}_{mn}$, and therefore the location of $\tilde{s}_{mn}$ in the τ-domain, but not the location of $\tilde{s}_{mn}$ in the s-domain. Then the migration of $\tilde{s}_{mn}$ in the $\tau < 0$ domain is still bounded by the source bearing $\sin\theta_o$, as was the case in an ideal waveguide.

100 m water depth	$c_w = 1500$ m/s $\rho_w = 1000$ kg/m^3 $\alpha_w = 6 \times 10^{-5}$ dB/λ
Sand Bottom	$c_b = 1700$ m/s $\rho_b = 1900$ kg/m^3 $\alpha_b = 0.8$ dB/λ

Figure 3-3: The Pekeris waveguide with sand bottom, where c_w, ρ_w, and α_w are the sound speed, density, and attenuation of the water column, and c_b, ρ_b, and α_b are those of the sea-bottom.

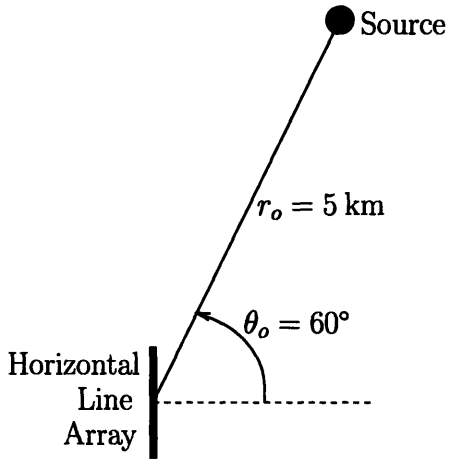

Figure 3-4: Top view of the geometry for the single source localization example. The source is at 60° from the broadside of the horizontal receiving array, and at 5-km range.

3.2 Illustrative Examples

Here we demonstrate that the array invariant method developed in Sec. 3.1 can be used to localize multiple broadband noise sources in an ocean waveguide with examples. We first show that a noise source can be localized in range and bearing without ambiguity using the array invariant method. We then show that the same approach can be used to simultaneously localize multiple noise sources in range and bearing.

3.2.1 Single noise source

We first consider the case of a noise source in a 100-m deep Pekeris waveguide environment with sand bottom shown in Fig. 3-3. The source is located at $r_o = 5$ km and $\theta_o = 60°$ as shown in Fig. 3-4. The source and the receiving array depths are 50 m and 30 m, respectively. The aperture of the receiving array is 150 m. The source power spectral density is assumed to be 0 dB re 1 μPa^2/Hz within the 390 to 440-Hz frequency band.

The cross-correlated intensity field $I_{Bo}(s,\tau)$ in Eq. 3.3 is shown in Fig. 3-5 (a). Two black solid lines are overlain on Fig. 3-5. One line in the $\tau > 0$ domain is the beamformer migration line $\tilde{s}(\tau)$ for ain impulsive source in an ideal waveguide, and the other line in the $\tau < 0$ domain marks the source bearing $\sin\theta_o$. These two lines show that the cross correlated intensity field is bounded by these lines except that the field is smeared by the beampattern of the horizontal receiving line array. The cross correlated beam-time migration lines $\tilde{s}_{mn}(\tau)$ for $I_{Bo}(s,\tau)$ in Fig. 3-5 (a) are shown in Fig. 3-5 (b), which shows that all the cross-correlated beam-time migration lines are indeed bounded by the beamformer migration line Eq. 3.16 when $\tau > 0$, and by the source bearing $\sin\theta_o$ when $\tau < 0$. Given these two bounding lines in the cross-correlated intensity field, we can estimate both source range and bearing without ambiguity.

In order to identify these two bounding lines from Fig. 3-5 (a), we apply an image transform technique similar to the Radon transform [29] to the cross-correlated beam-time image. In this transform, a given image is integrated along a semi-infinite line starting from $(s,0)$ and having an angle ϕ_r from the positive τ-axis in the clockwise direction. More specifically, this transform is defined as

$$\mathcal{I}(s,\phi_r) = \int_0^\infty |I_{Bo}(s + l\sin\phi_r, l\cos\phi_r)|\ dl \tag{3.29}$$

where $\mathcal{I}(s,\phi_r)$ is the instantaneous acoustic intensity in Fig. 3-5(a) integrated along the straight line starting from $(s,0)$ and having a slope $\tan\phi_r$ in the τs-plane. The

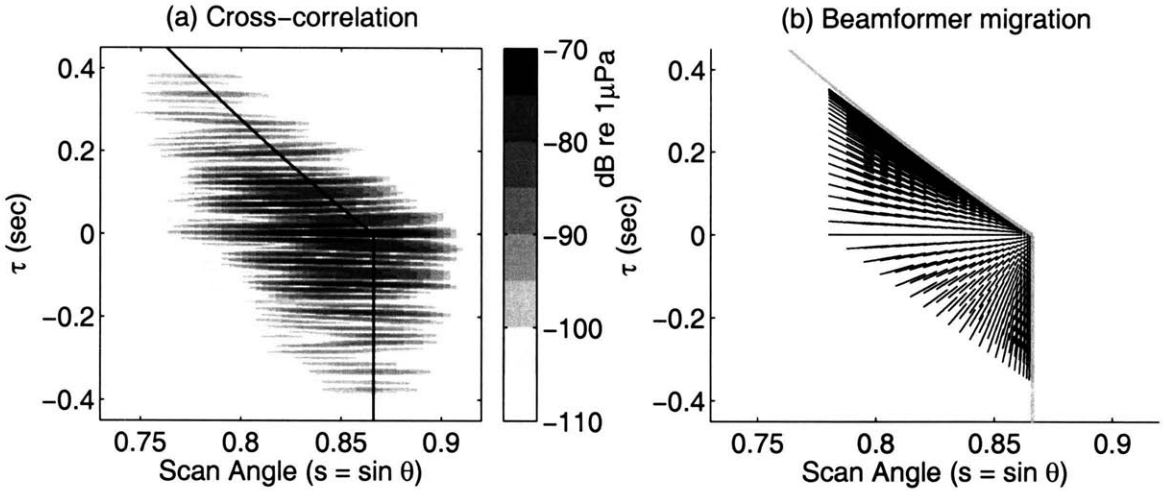

Figure 3-5: (a) The cross-correlated intensity field $I_{Bo}(s, \tau)$ for the source-receiver geometry shown in Fig. 3-4 in the sand-bottom Pekeris waveguide environment in Fig. 3-3. The black solid line overlain in the $\tau > 0$ domain is the beamformer migration line in Eq. 3.16 in terms of the reduced travel time. The black solid line in the $\tau < 0$ domain is at $\sin\theta_o$. (b) The cross-correlated beam-time migration lines $\tilde{s}_{mn}$ for the first 23 modes of the 27 propagating modes. The thick gray lines in the $\tau > 0$ and $\tau < 0$ domain are the same as the black solid lines overlain in Fig. 3-5 (a).

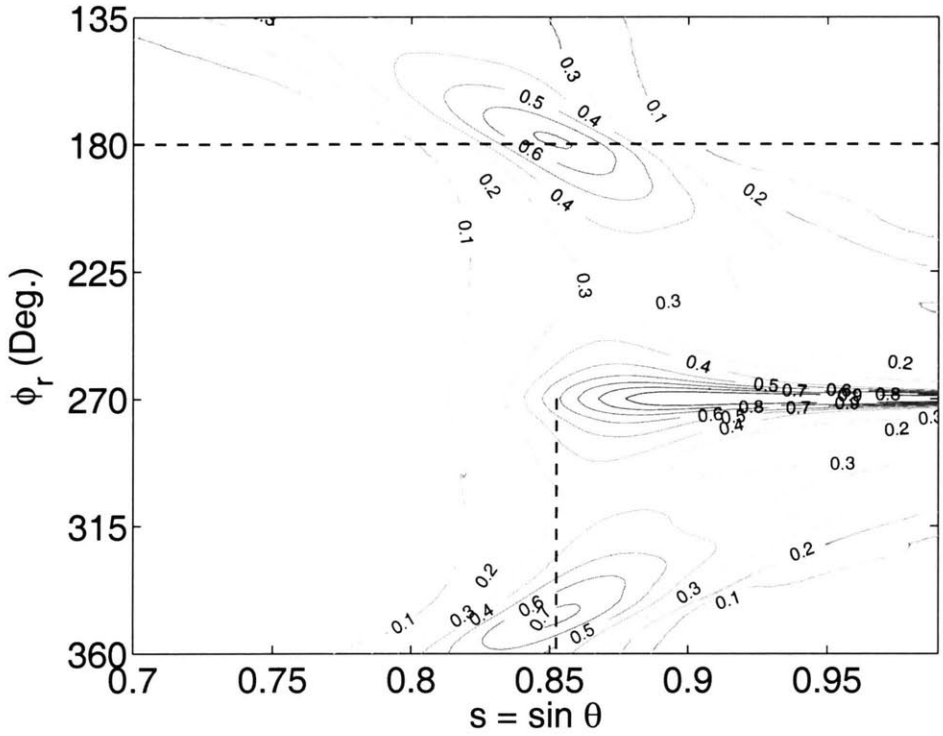

Figure 3-6: The transformed intensity image $\mathcal{I}_n(s, \phi_r)$ of the cross-correlated intensity image in Fig. 3-5 (a). The black dashed lines will be referred to in Figs. 3-7 and 3-8.

transformed image normalized by the maximum value,

$$\mathcal{I}_n(s, \phi_r) = \frac{\mathcal{I}(s, \phi_r)}{\mathcal{I}_{\max}}, \tag{3.30}$$

where $\mathcal{I}_{\max} = \max_{s,\phi_r} \mathcal{I}(s, \phi_r)$, is shown in Fig. 3-6. Now we show that both the range and bearing of the source can be extracted from the transformed intensity field $\mathcal{I}_n(s, \phi_r)$ in Fig. 3-6.

First, the bearing of the source can be estimated from the value of s where the maximum of $\mathcal{I}_n(s, \phi_r = 180°)$ occurs. From Eqs. 3.29 and 3.30,

$$\mathcal{I}_n(s, \phi_r = 180°) = \frac{1}{\mathcal{I}_{\max}} \int_0^\infty |I_{Bo}(s, -l)| \, dl$$

is the integral of the acoustic intensity for specific s along $-\infty < \tau < 0$. From Fig. 3-5, one can see that $\mathcal{I}_n(s, \phi_r = 180°)$ should reach the maximum near the source bearing

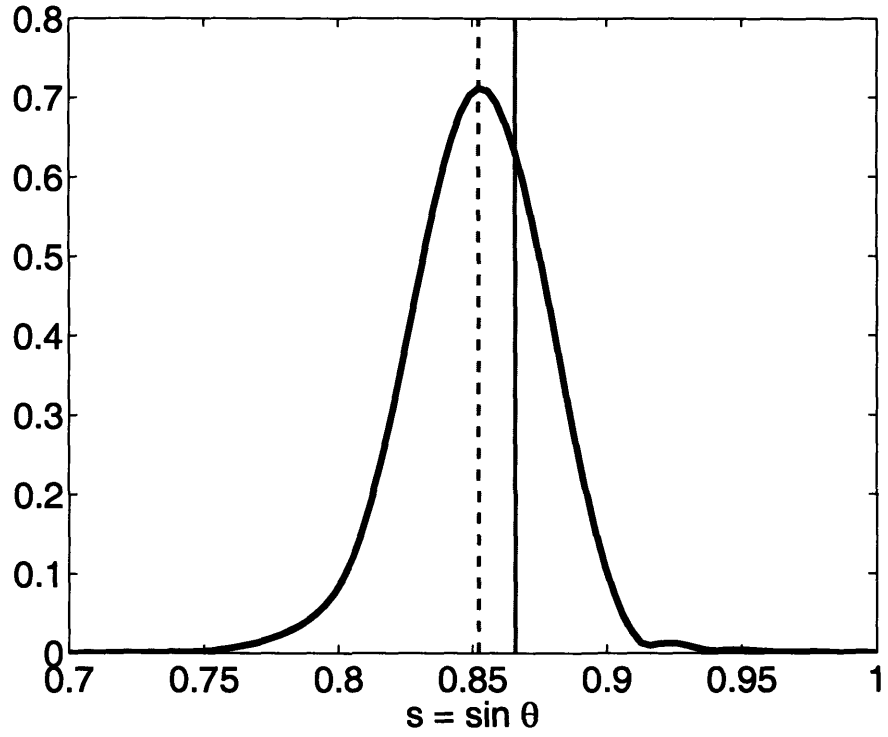

Figure 3-7: Transect of $\mathcal{I}_n(s, \phi_r)$ along the black dashed line following $\phi_r = 180°$ in Fig. 3-6. The peak location of this transect, marked by the vertical dashed line, is the estimate of the source bearing $\hat{s}_o$. The solid dashed line is at the true source bearing $s_o = \sin 60°$.

$\sin\theta_o$, since (1) $I_{Bo}(s, \tau)$ spreads out longest in the τ-domain when $s = \sin\theta_o$, and (2) the cross-correlated beam-time migration lines $\tilde{s}_{mn}$ are concentrated near $s = \sin\theta_o$. A transect of $\mathcal{I}_n(s, \phi_r)$ in Fig. 3-6 along the line where $\phi_r = 180°$ is shown in Fig. 3-7, where the source bearing estimate

$$\hat{s}_o = \sin\hat{\theta}_o \equiv \arg\max_s \mathcal{I}_n(s, \phi_r = 180°)$$

is seen to occur at $\hat{s}_o = 0.853$ or $\hat{\theta}_o = 58.5°$. This is within 3% of the true source bearing $\theta_o = 60°$.

Second, once the bearing of the source has been estimated, the range of the source

can be estimated using

$$\hat{r}_o = -\frac{c(z)\sin\hat{\theta}_o}{\hat{\chi}_l} = -\frac{c(z)\sin\hat{\theta}_o}{\tan\hat{\phi}_r}, \tag{3.31}$$

where

$$\hat{\phi}_r = \arg\max_{\phi_r} \mathcal{I}_n(s = \hat{s}_o, \phi_{r1} < \phi_r < \phi_{r2}),$$

$\phi_{r1} = 270°$ and $\phi_{r2} = 360°$ for $\hat{s}_o > 0$, and $\phi_{r1} = 0°$ and $\phi_{r2} = 90°$ for $\hat{s}_o < 0$. The transformed intensity $\mathcal{I}_n(s = \hat{s}_o, \phi_r)$ is the integral of the cross-correlated intensity $I_{Bo}(\tau, s)$ in Fig. 3-5 (a) along the semi-infinite line that starts from $(\tau, s) = (0, \hat{s}_o)$ with slope $\tan\phi_r$ in the τs-plane. This integral should reach the maximum when $\tan\phi_r = \chi_l$, since the path of the integral is the longest when the integral is performed along the beamformer migration line for an ideal waveguide in Eq. 3.16, marked by the thick gray line in Fig. 3-5 (b). It should reach the maximum there also because the cross-correlated beam-time migration lines $\tilde{s}_{mn}$ are concentrated near the beamformer migration line for an ideal waveguide, as can be seen in Fig. 3-5 (b). A transect of $\mathcal{I}_n(s = \hat{s}_o, 270° < \phi_r < 360°)$ is shown in Fig. 3-8, where the peak of $\mathcal{I}_n$ is seen to occur at $\phi_r = 346.7°$. The range of the source is then estimated to be $\hat{r}_o = 5.4$ km using Eq. 3.31 which is within 10% of the true source bearing.

3.2.2 Multiple uncorrelated noise sources

The approach used for localization of a single source can also be used for localization of multiple uncorrelated random noise sources in an ocean waveguide in both range and bearing. Here we consider the case where there are 3 uncorrelated noise sources S_1, S_2, and S_3, as shown in Fig. 3-9. The source S_1 is at range $r_1 = 8.2$km and bearing $\theta_1 = 45°$. The other two sources S_2 and S_3 are at the same bearing $\theta_2 = \theta_3 = 60°$, and their ranges are $r_2 = 3$ km and $r_3 = 10$ km, respectively. We assume that these three sources have the same source power spectrum of 0 dB re 1 μPa/$\sqrt{\text{Hz}}$ in the 390 to 440 Hz frequency band, but they are uncorrelated with each other so that $\left\langle Q_i(f)Q_j^*(f)\right\rangle = \langle|Q_i|^2(f)\rangle\,\delta_{ij}$, where $Q_i(f)$ is the source spectrum of S_i, and δ_{ij} is the

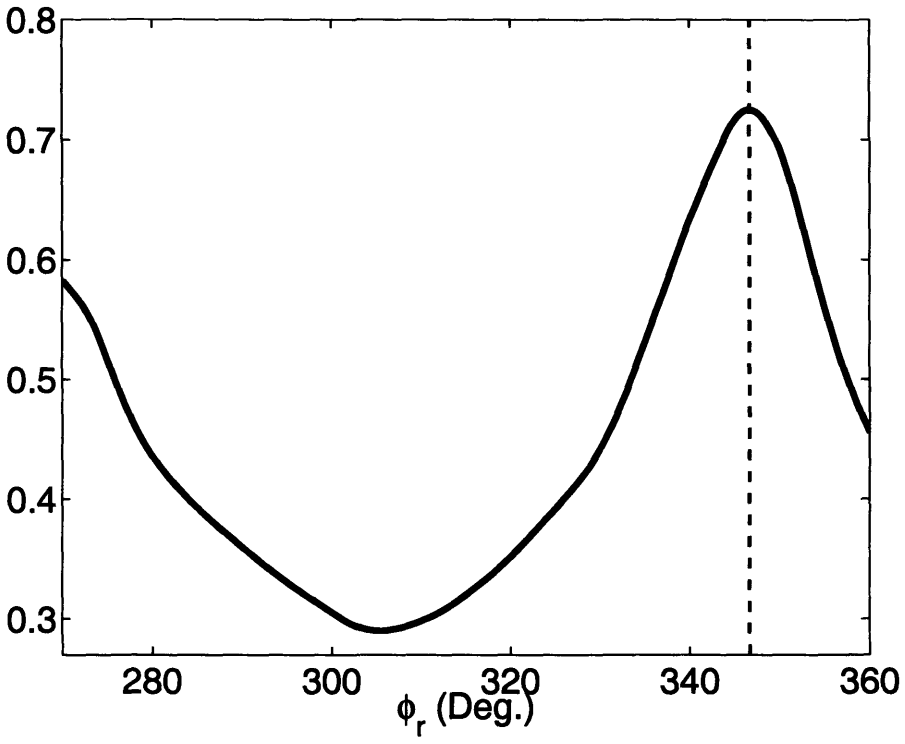

Figure 3-8: Transect of $\mathcal{I}_n(s, \phi_r)$ for $s = \hat{s}_o$ and $270° < \phi_r < 360°$, marked by the black dashed line in Fig. 3-6. The peak of the transect, marked by the vertical dashed line, occurs at $\phi_r = 346.7°$, which can be inverted for the source range of 5.4 km using Eq. 3.31.

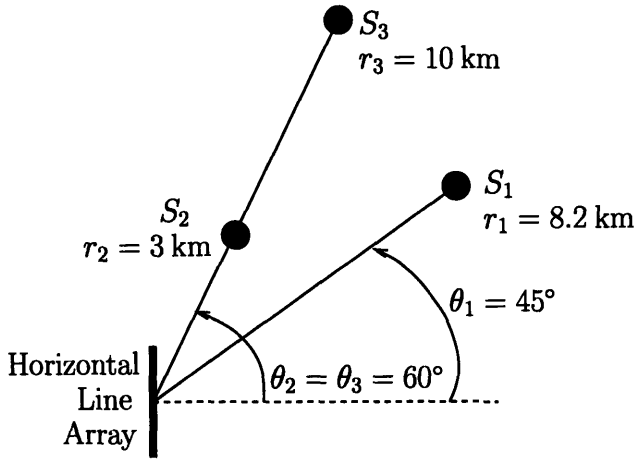

Figure 3-9: Top view of the geometry for the multiple source localization example. All 3 sources are at 30-m depth, and the receiver array depth is 50 m. The receiver array aperture is 150 m.

Kronecker delta. The source and receiver array depths, the receiver array aperture, and the wave propagation environments are identical to those in Sec. 3.2.1.

The cross-correlated intensity field $I_{Bo}(s, \tau)$ for this multiple source scenario is shown in Fig. 3-10. The cross-correlated intensity in Fig. 3-10 exhibits two distict intensity fields when $\tau < 0$, one at the bearing of S_1, and the other at the bearing of S_2 and S_3. When $\tau > 0$, the field for S_2 and S_3 splits into two distinct fields, since their ranges from the receiver array are different. The cross-correlated intensity field for S_1 when $\tau > 0$ shows the same pattern as that of the single source scenario in Sec. 3.2.1.

We now apply the image transform method in Eqs. 3.29 and 3.30 to Fig. 3-10. The transformed image of Fig. 3-10 near $\phi_r = 180°$ is shown in Fig. 3-11, where it can be seen that there are two peaks in $\mathcal{I}_n$ due to two distinct source bearings. The transect of $\mathcal{I}_n$ in Fig. 3-11 along $\phi_r = 180°$ is shown in Fig. 3-12. From this image, we can estimate two bearings of the source to be $\hat{\theta}_1 = 44.5°$ and $\hat{\theta}_2 = 58.8°$, which are within 2% of the true source bearings. The two sources S_2 and S_3 cannot be distinguished in this transect along $\phi_r = 180°$, since the bearings of the two sources are identical.

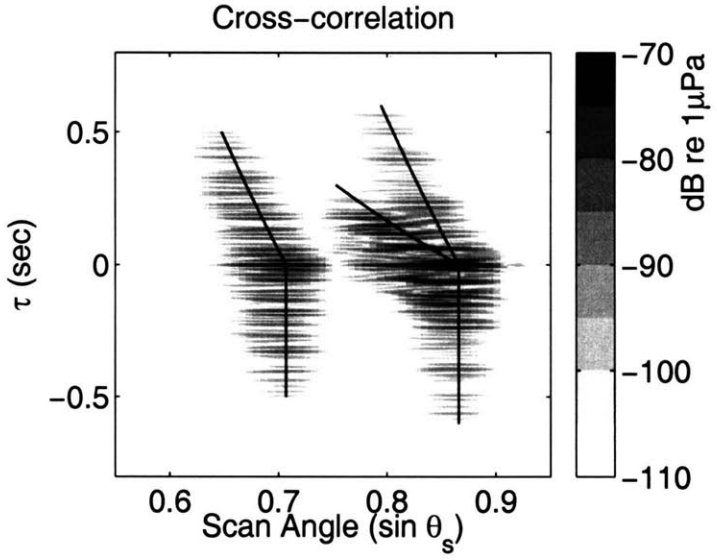

Figure 3-10: The cross-correlated intensity field $I_{Bo}(s, \tau)$ for the source-receiver geometry shown in Fig. 3-9. The two black solid lines overlain in the $\tau < 0$ domain marks $\sin\theta_1$ and $\sin\theta_2$, respectively. The three black solid lines in the $\tau > 0$ domain are the beamformer migration lines in Eq. 3.16 for sources S_1, S_2, and S_3, in terms of the reduced travel time.

Once the bearings of the sources are estimated, the range of the sources r_i can be estimated from $\mathcal{I}_n(\hat{s}_i, \phi_r)$ for each estimated source bearing $\hat{s}_i$. The transformed image $\mathcal{I}_n(s, \phi_r)$ for $310° < \phi_r < 360°$ is shown in Fig.3-13, where three distinct peaks in $\mathcal{I}_n$ due to three sources in the waveguide can be observed.

Transect of Fig. 3-13 along $\hat{s}_1 = \sin\hat{\theta}_1$ is shown in Fig. 3-14. From the angle ϕ_r where the peak of $\mathcal{I}_n(\hat{s}_1, \phi_r)$ occurs, we can estimate the source range to be $\hat{r}_1 = 9\,\text{km}$ using Eq. 3.31, which is within 10% of the true source range r_1. The ranges of the other two sources S_2 and S_3 can be estimated from $\mathcal{I}_n(\hat{s} = \hat{s}_2, \phi_r)$ shown in Fig. 3-15, where it can be seen that there are two distinct peaks due to S_2 and S_3 located at different ϕ_r. The estimated source range of S_2 from this figure is $\hat{r}_2 = 3\,\text{km}$, which is the same as the true source range of S_2. The estimated source range of S_3 is $\hat{r}_3 = 11\,\text{km}$. This is within 10% of the true source range.

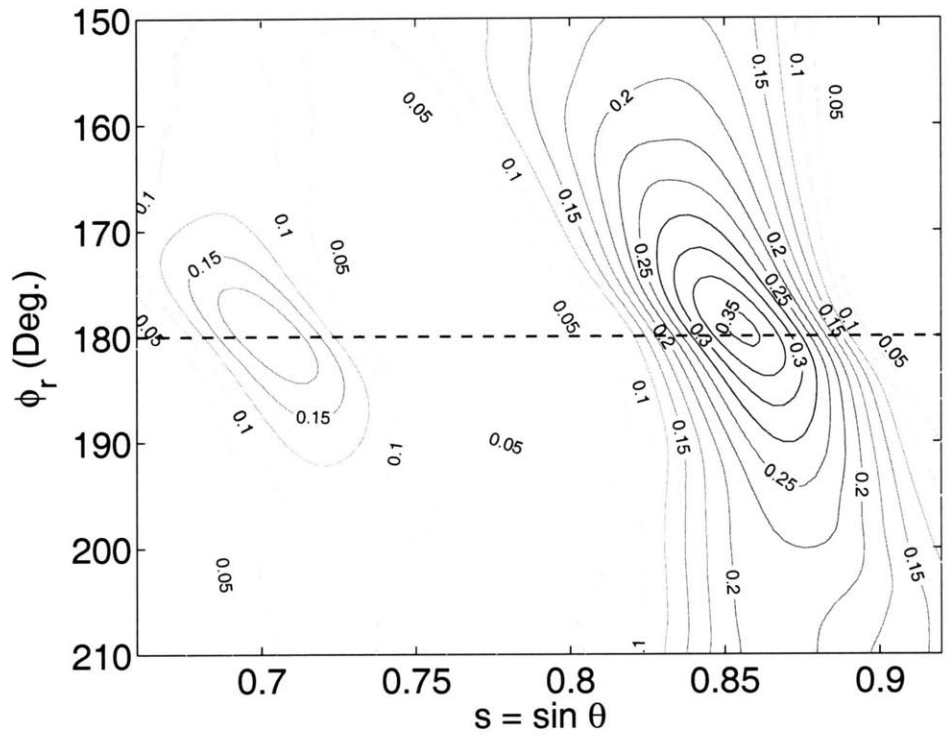

Figure 3-11: The transformed intensity image $\mathcal{I}_n(s, \phi_r)$ of the cross-correlated intensity image in Fig. 3-10 near $\phi_r = 180°$. Two peaks along the $\phi_r = 180°$ radial, marked by the black dashed line, due to two different source bearings are seen.

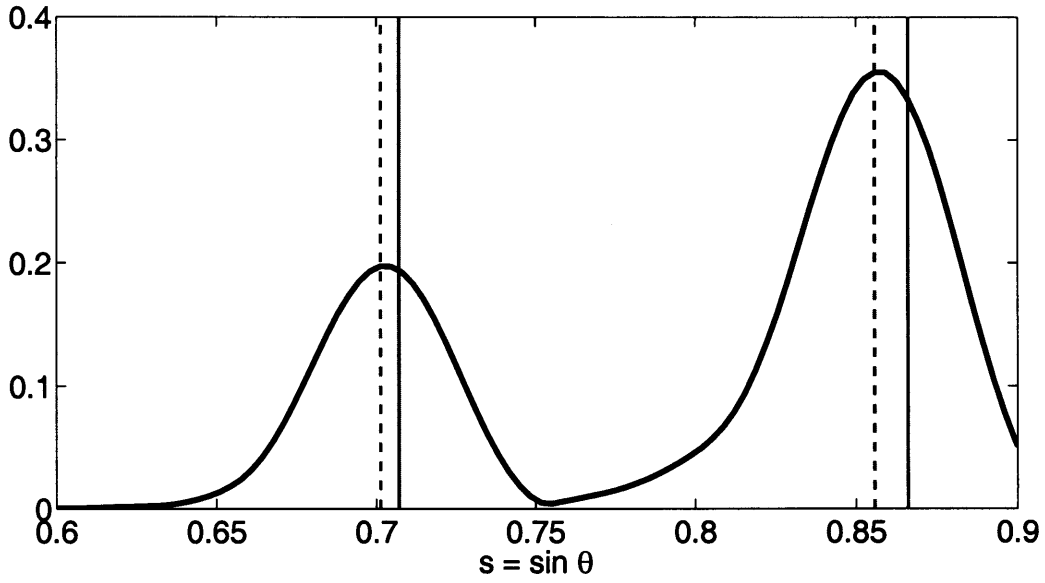

Figure 3-12: Transect of $\mathcal{I}_n(s, \phi_r)$ in Fig. 3-10 along the black dashed line following $\phi_r = 180°$. The locations of the two peaks in this transect, marked by the vertical dashed line, are the estimate of the source bearings $\hat{s}_1 = 44.5°$ and $\hat{s}_2 = 58.3°$. The solid dashed lines are at the true source bearings $s_1 = \sin 45°$ and $s_2 = \sin 60°$.

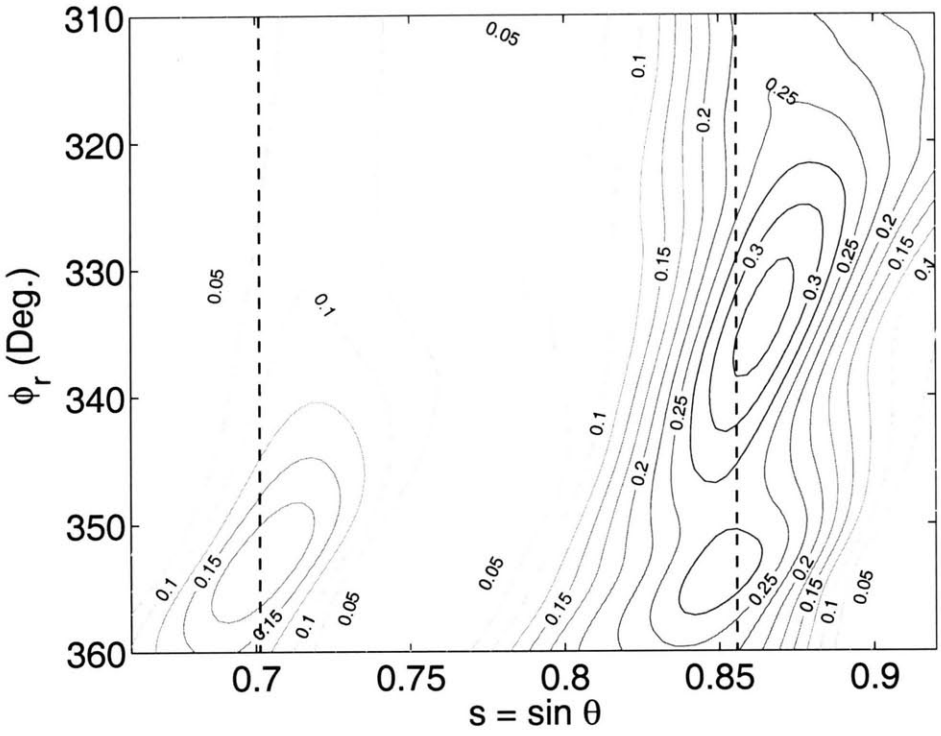

Figure 3-13: The transformed intensity image $\mathcal{I}_n(s, \phi_r)$ of the cross-correlated intensity image in Fig. 3-10 for $310° < \phi_r < 360°$. Two dashed vertical lines are at $\hat{s}_1$ and $\hat{s}_2$, respectively. A peak along $\hat{s}_1$ and two peaks along $\hat{s}_2$ correspond to S_1, S_2, and S_3, respectively.

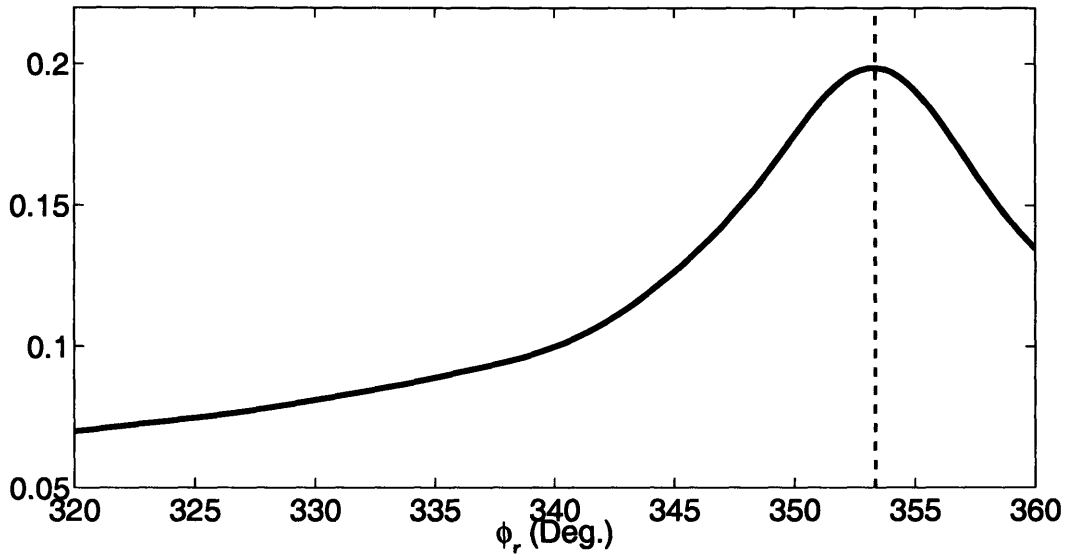

Figure 3-14: Transect of $\mathcal{I}_n(s, \phi_r)$ in Fig. 3-13 along $\hat{s}_1$. The peak of this transect is at $\phi_r = 353.3°$, which corresponds to the estimated range of $\hat{r}_1 = 9$ km.

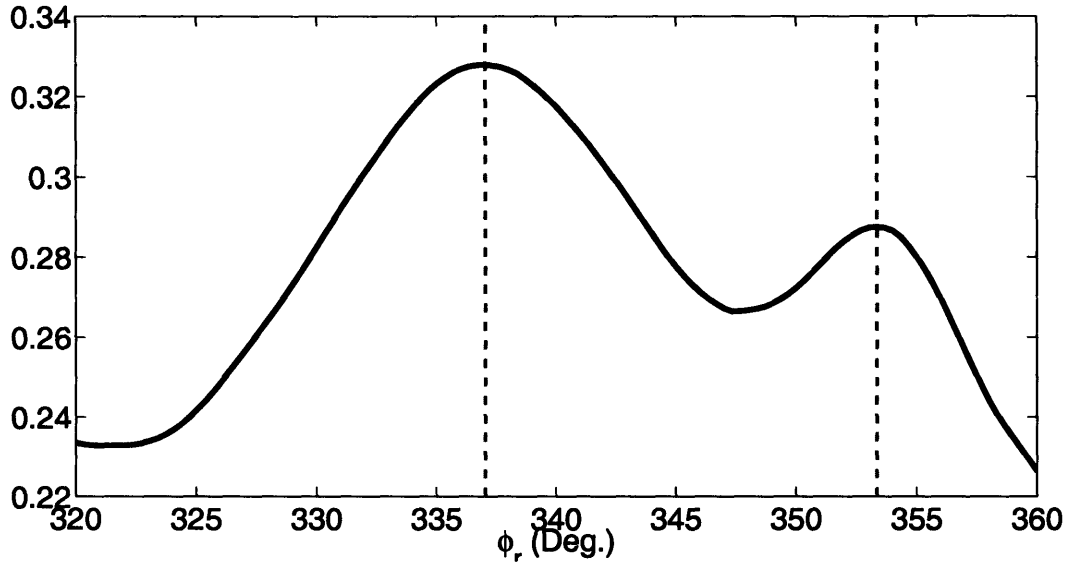

Figure 3-15: Transect of $\mathcal{I}_n(s, \phi_r)$ in Fig. 3-13 along $\hat{s}_2$. The first peak at $\phi_r = 337°$ is due to S_2, corresponds to to the estimated range of $\hat{r}_2 = 3$ km. The second peak due to S_3 is at $\phi_r = 353.3°$. The source range of S_3 is estimated to be $\hat{r}_3 = 11$ km.

3.3 Summary

The array invariant method introduced in Chap. 2 for the localization of an impulsive source in an ocean waveguide has been extended to localization of a broadband noise source in range and bearing. It has been demonstrated that the array invariant method, which exploits waveguide dispersion, can be used to simultaneously localize multiple noise sources in an ocean waveguide without requiring *a priori* knowledge of the wave propagation environment.

Chapter 4

Probing Europa's interior with natural sound sources

Our goal is to show how Europa's interior structure may be revealed by relatively simple and robust seismo-acoustic echo-sounding techniques using natural sources of opportunity. Echo sounding is the traditional and most widely used tool to chart the depth and composition of terrestrial oceans and sub-ocean layers [86]. It employs an active acoustic source and passive receiver to measure the arrival time and amplitude of reflections from the layers to be charted. Our Europan strategy differs from the terrestrial one in that the primary source of sound is not controlled. Rather, it is proposed to arise from ice cracking events and impacts hypothesized to occur regularly on Europa's surface. A single passive geophone on Europa's surface may then be used to estimate (1) its range from a natural source event by analysis of direct compressional and shear wave arrivals in the ice, and (2) the thickness of the ice shell and depth of the ocean by travel time analysis of specular reflections from the corresponding internal strata. The technique, however, requires the ice-crack or impact event of opportunity to be sufficiently energetic for its reflections to stand above the ambient noise generated by other more distant or less energetic events.

To help quantitatively explore the issues involved in echo-sounding, and other seismo-acoustic techniques for probing Europa's interior, our analysis proceeds together with the development of a full-field seismo-acoustic model for Europa. This

includes analysis of ice-cracking and impact source events, seismo-acoustic propagation in Europa's stratified environment, and Europan ambient noise. Here we follow the common convention of referring to both compressional and shear wave disturbances in solids, such as Europa's outer ice shell and interior mantle, as "seismic waves," and compressional waves in fluids, such as Europa's potential ocean, as "acoustic waves." By this convention, waves that propagate from ice to water or vice-versa, for example, are referred to as "seismo-acoustic waves."

Our interest in this problem stems from the significant amount of evidence collected by the Galileo Probe in the past decade to support the possibility that an ocean of liquid water may lie beneath Europa's exterior icy surface. Induced magnetic field measurements Khurana *et al.* [62] suggest the existence of a conducting layer beneath the ice surface that is at least a few kilometers thick and likely corresponds to a liquid ocean of salty water. Various researchers have argued that many of the morphological features that characterize Europa's icy surface can best be explained by the presence of an ocean of liquid water below [105]. This is put in context by the conclusion of Anderson *et al.* [4] that the total thickness of ice and potentially liquid water on Europa's surface is between 80 to 170 km, based on gravity data. Together these observations provide compelling but inconclusive evidence for a subsurface Europan ocean leaving the thickness of the outer ice shell and the depth of the potential ocean poorly constrained.

A variety of techniques have been proposed to measure the thickness of Europa's outer ice shell. They involve measurement of crater morphology [118], tidal gravity [46, 4, 145], laser altimetry [26], ice-penetrating radar reflections [23, 90], and ice-bourne seismic wave interference and dispersion [68]. All but the last have the advantage of being achievable by either fly-by or orbital rather than landing missions. While each may indicate the presence of an ocean, none are sensitive to its thickness [26].

Only two techniques are currently available to remotely determine the thickness of a deep ocean layer on Europa. The first involves extensive magnetometer measurements by a low flying orbiter [62, 66, 65]. These measurements, however, cannot

determine the location of the ocean layer or its structure. The other is the echo-sounding technique under discussion, the primary advantage of which is its ability to determine the absolute interior structure of both the ice and potential ocean layers. A potential disadvantage is that it requires a landing mission.

The first Europan landing mission will likely carry only a single triaxial geophone capable of measuring seismo-acoustic displacements in three spatial dimensions at a single point on Europa's surface. Besides echo-sounding, listening for audible signs of life, and potentially inferring and categorizing dynamical processes of the ice by their acoustic signatures, an initial task for this sensor could be to determine the overall level of seismo-acoustic activity on Europa by time series and spectral analysis. Correlations could be made of ambient noise versus environmental stress level to determine whether noise levels respond directly to orbital eccentricities. Such an analysis was conducted for the Earth's Arctic Ocean where roughly two meters of nearly continuous pack ice cover an ocean that is typically between $0.1 \sim 5$ km in depth. These terrestrial results show a near perfect correlation between underwater noise level and environmental stresses and moments applied to the ice sheet from wind, current, and drift [80, 81]. Additionaly, in the Antarctic, both the flexural motion of ice shelves and the level of seismicity due to tidally induced ice-fracturing events are correlated with the sea tide [115].

For Europa, Hoppa *et al.* [56] show that environmental stresses due to tidal forces vary significantly over the period of its eccentric 3.5 day orbital period and that these stresses may lead to the near daily formation of cycloidal arcs similar to those observed to extend over hundreds of kilometers on Europa's surface. Based on the maximum tidal surface stress expected by Hoppa *et al.* and basic concepts from fracture mechanics, we show that a given cycloidal arc is likely to be formed as a sequence of hundreds of discrete and temporally disjoint cracking events.

A combination of factors, such as the interplay of diurnal stresses with inhomogeneities in the outer ice shell or its potential asynchronous rotation due to an ocean layer below [75], may lead to "Big Bang" cracking events. These events would be statistically less frequent but much more energetic than those primarily caused by

diurnal stresses in pure ice. Echo returns from Big Bang events would be more likely to stand above the ambient noise and so make echo sounding for Europa's interior structure more practical. We determine the tensile stresses and crack depths necessary to generate Big Bang events. We also show that even small impactors, in the 1 $\sim$ 10 m radius range, fall into the Big Bang category, and that Big Bang events will radiate spectral energy peaking in the roughly 1 to 10 Hz range. This is significant because the corresponding seismo-acoustic wavelengths in ice and water will range from hundreds to thousands of meters. Such long wavelength disturbances suffer minimal attenuation from mechanical relaxation mechanisms in ice and water and are relatively insensitive to shadowing by similarly sized anomalies in the ice or on the seafloor that could severely limit remote sensing techniques that rely on shorter wavelengths.

4.1 Modeling Europa as a Stratified Seismo-Acoustic Medium

We begin our analysis by establishing models for Europa as a stratified medium for seismo-acoustic wave propagation. These models specify compressional wave speed c_p, shear wave speed c_s, compressional wave attenuation α_p, shear wave attenuation α_s and density ρ as a function of depth on Europa.

There are two canonical models of Europa's interior structure. The first is the rigid ice shell model, where heat transport is achieved by conduction throughout a completely brittle and elastic ice-shell [99, 47]. The second is the convective ice shell model, where heat is transported primarily by convection of warm ice at the base that can become buoyant enough to rise toward the surface [105, 85, 31].

Linearized internal temperature profiles for these two models are shown in Fig. 4-1(a). The resulting temperature profiles are used to construct compressional and shear wave speed profiles in the ice by the methods described in Appendix B. The rigid ice shell model is characterized by an almost linear temperature change from the top of the ice shell to the ice-water interface, whereas the convective ice shell model leads to a strong temperature gradient on top and bottom of the ice shell, and a mild temperature gradient in the middle. In the latter, temperature is assumed to increase with depth from an average surface value of 100 K [100, 126] to 250 K in the upper thermal boundary layer, which is assumed to comprise the upper 20% of the ice shell, remain constant for the bulk of ice shell before finally increasing to 260 K in the lower thermal boundary layer, which is assumed to comprise the lower 10% of the ice shell.

The sound speed of sea water is mainly a function of temperature, pressure, and salinity. Several regression equations are available to estimate sound speed from these variables. Here we employ one valid under high pressure [21] to estimate the sound speed profile in a subsurface Europan ocean. This ocean is assumed to have a salinity of roughly 3.5%, similar to terrestrial oceans [62], and a temperature of roughly 273 K, the melting temperature of ice in the terrestrial environment.

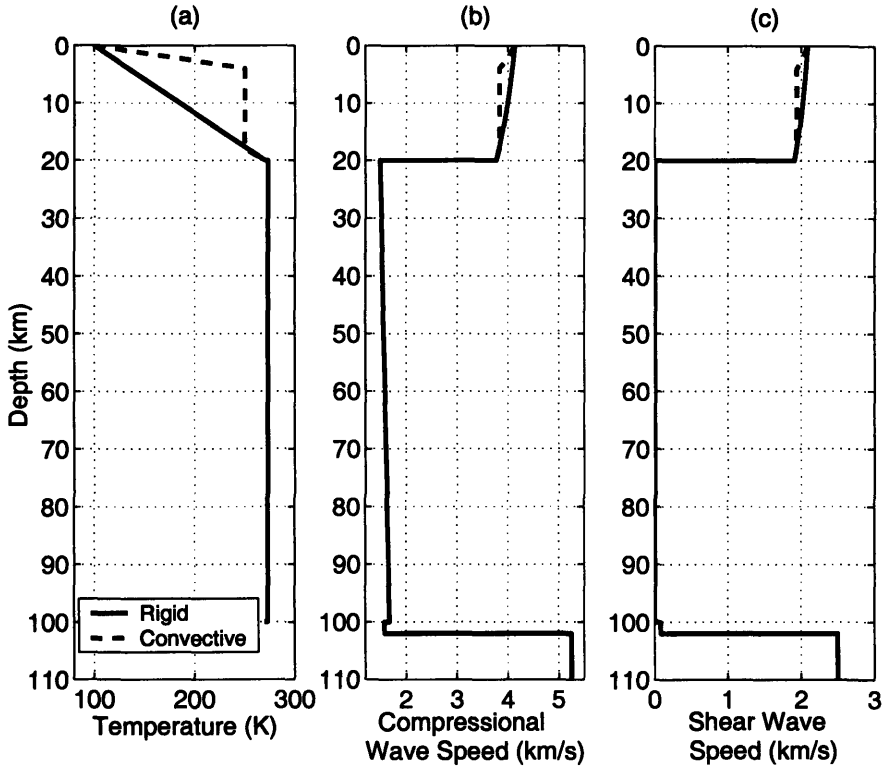

Figure 4-1: Temperature, compressional wave speed, and shear wave speed profiles for 20km thick rigid and convective ice shell models. The solid and dashed lines represent the rigid and convective ice shell models, respectively.

The mantle beneath the ocean is assumed to be comprised of a 2-km of sediment layer overlying a basalt halfspace. The sediment is taken to have sound speed and density similar to water as in terrestrial oceans.

In our subsequent simulations and analysis, we consider four Europan sound speed profiles based upon 5-km rigid, 20-km rigid, 20-km convecting and 50-km convecting ice shell models. The assumed compressional and shear wave speed profiles through the ice, water and mantle are shown in Fig. 4-1(b) and (c) for both 20-km models. Assumed seismo-acoustic parameters of the medium common to all models are shown in Table 4.1.

Attenuation increases significantly with frequency in terrestrial sea ice, water and sediment. The attenuation values shown in Table 4.1, given in standard decibel units per wavelength, are valid in the roughly 1$\sim$4 Hz range of the spectral peak of a

Table 4.1: Seismo-acoustic parameters

Material	c_p (m/s)	c_s (m/s)	α_p (dB/λ)	α_s (dB/λ)	ρ (kg/m^3)
Ice	See Appendix B	See Appendix B	0.24	0.72	930
Water	See Ref. [21]		0.01		1000
Sediment	1575	80	1.00	1.50	1050
Basalt	5250	2500	0.10	0.20	2700

hypothesized Big-Bang ice-quake event used in the simulations to follow. Ice attenuation values are extrapolated to below 200 Hz from the linear trend observed in Arctic Ocean ice [84]. Attenuation due to volumetric absorption in a potential Europan ocean is taken to be similar to that in terrestrial seawater, which is relatively insignificant in the low frequency range of interest in the present study [134]. Attenuations in the sediment and basalt assumed for the mantle also follow terrestrial analogs which are far more significant than that found in seawater.

A schematic of Europa as a stratified seismo-acoustic medium is given in Fig. 4-2 for a convective ice shell. In the rigid ice shell, the upper thermal boundary layer would continue to the ice-ocean interface, eliminating the other two ice layers shown.

4.2 Source Mechanisms and Characteristics

Our primary interest is in source events that are both energetic enough and frequent enough for the proposed echo-sounding technique to be feasible within the period of a roughly week to month long Europan landing mission. Source events of opportunity must have sufficient energy for their echo returns from the ice-water and water-mantle interfaces to stand above the accumulated ambient noise of other more distant or weaker sources. We proceed by first estimating the seismo-acoustic energy spectrum of ice-cracking sources and then impact sources.

4.2.1 Ice-Cracking

Surface cracking events are expected to occur in the brittle, elastic layer of Europa's outer ice shell in response to tensile stresses arising from a diverse set of mechanisms.

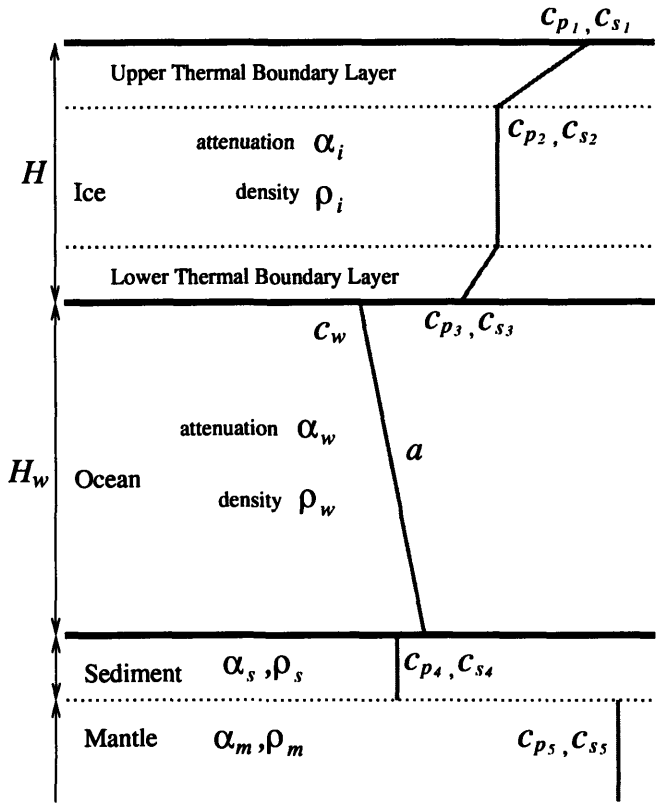

Figure 4-2: Schematic diagram of the full Europa model for a convective ice shell. In the wave speed profile, c_p, c_s are compressional and shear wave speeds in elastic media, c_w is the acoustic wave speed in the ocean, a is the sound speed gradient in the ocean. H and H_w are the thicknesses of the ice shell and subsurface ocean. α and ρ are the attenuation and density of the media.

We show that the source time dependence and energy spectrum can be estimated from crack depth. Expected crack depths can in turn be estimated from the imposed tensile stress.

The maximum depth h of a surface crack is estimated to occur where tensile stress σ is balanced by the pressure due to the gravitational overburden of the ice shell [27, 141, 142, 93],

$$\sigma \sim \rho_i g h \tag{4.1}$$

where $g = 1.3\,\mathrm{m/s^2}$ is the gravitational acceleration on Europa's surface.

Europa's roughly 3.5 day eccentric Jovian orbit is expected to lead to a significant diurnally varying tidal stress, with maximum values ranging from 40 kPa [56] to 100

kPa [75] if a sub-surface ocean of at least a few kilometers thickness is present. Over much longer time scales of roughly 10 Myr, the nonsynchronous rotation of an outer ice shell decoupled from the mantle by a subsurface ocean could lead to maximum tensile stresses as large as 8 MPa [75].

The flexural strength of terrestrial sea ice was measured as a function of brine volume [140]. Based on this work, we estimate a brine volume of 23% is necessary to crack terrestrial ice with the applied surface stress of 40 kPa computed for Europa by Ref. [56]. This is higher than the terrestrial value which usually varies between 1% to 15%. The flexural strength of ice on Europa's surface is expected to be higher than that on Earth due to Europa's much lower surface temperature. However, by assuming that flexural strength is proportional to Young's modulus and considering Appendix B, the flexural strength will only increase by roughly 20% which still puts the brine volume estimated to be roughly 23% on Europa's surface.

The most frequent type of cracking events, expected to occur daily with the diurnal tide, should then penetrate to roughly 50-m depths, based on the maximum tensile stress given by Ref. [56], or to 150-m depths based upon the analysis of Leith and McKinnon. Less frequent events due to asynchronous rotation can penetrate to depths well beyond 1 km [75]. The interplay between short term diurnal stresses, local ice inhomogeneities and even small asynchronous rotations [42], could lead to a reasonable frequency of local Big-bang cracking events, here defined as those exceeding 150-m depths, over the roughly month long period of a first Europan landing mission.

A detailed derivation of the seismo-acoustic energy spectrum for a tensile crack as a function of depth h is provided in Appendix D.1 where the crack geometry is shown in Fig. 4-3. In this derivation it is conservatively assumed that cracks do not exceed a minimum length of h [2, 35]. The crack width D_0 can be determined by

$$\sigma = E\varepsilon \simeq E\frac{D_0}{h}. \tag{4.2}$$

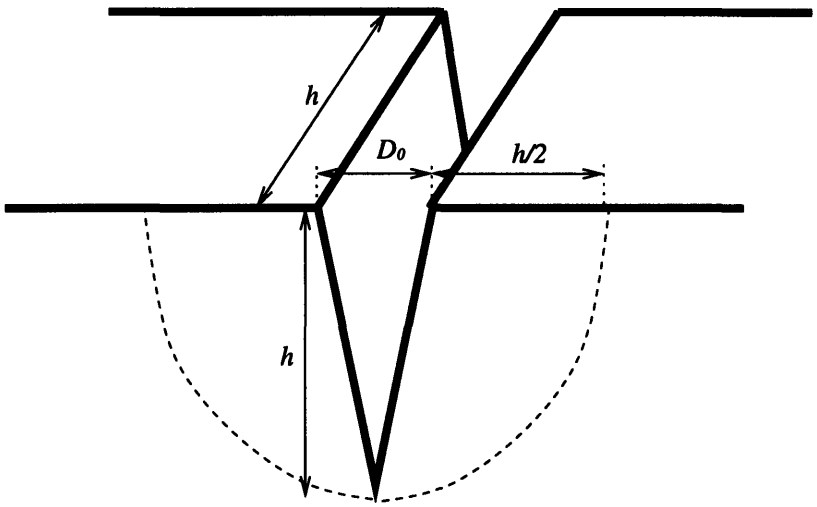

Figure 4-3: The geometry of surface tensile cracks. A crack with depth h propagates until the opening length is h. D_0 is the opening width of a crack. The volume within the dotted line is the regime where the tensile stress is released by the crack.

With the gravitational overburden assumption, we expect

$$D_0 \simeq \frac{\sigma h}{E} \simeq \frac{\rho g h^2}{E}, \tag{4.3}$$

where $E = 10\text{GPa}$ is Young's modulus for pure ice, as given in Appendix B. The pure ice assumption leads to a conservative estimate of the crack opening width. Note, however, that the choice of Young's modulus does not change the relative energy levels between the cracks of various depths, and the signal-to-noise ratio analysis in this paper remains valid.

The crack is also assumed to open as a linear function of time over a period equal to the maximum crack width over the crack propagation speed, as shown in Fig. D-1. The crack propagation speed is taken to be

$$v \simeq 0.9\, c_s, \tag{4.4}$$

following standard models of fracture mechanics [2] and experimental measurements of cracks on ice at terrestrial temperatures [71, 127]. The opening time of the crack

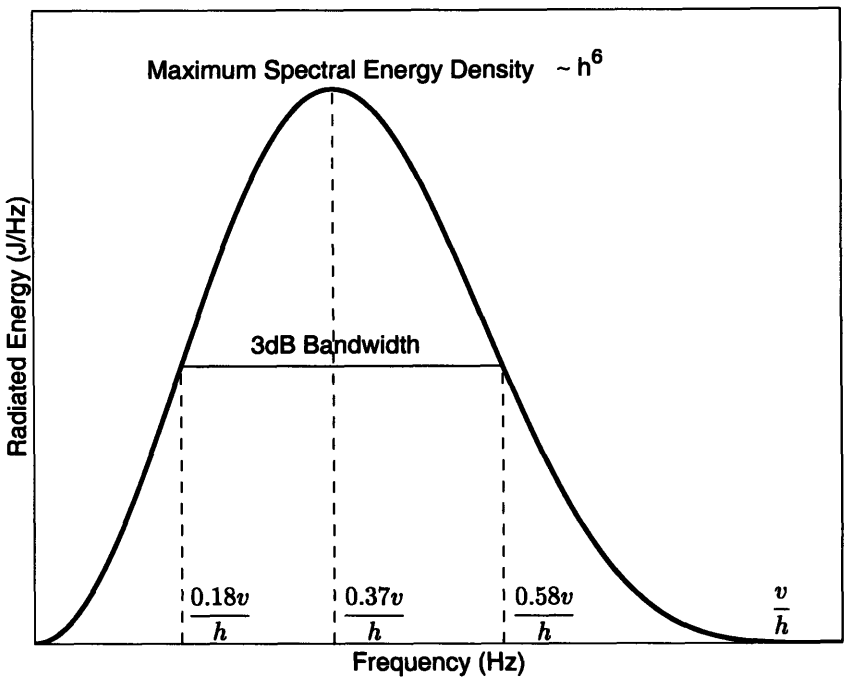

Figure 4-4: The radiated seismo-acoustic energy spectrum $\epsilon(f)$ defined by Eqs. D.9 and D.41 as a function of crack depth h. The amplitude of the spectrum is proportional to h^6, and the peak frequency and bandwidth are inversely proportional to h.

is then directly proportional to the crack depth h.

The source energy spectrum for a general crack of depth h is given in Fig. 4-4, from which it can be seen that the frequency of the peak and 3-dB bandwidth are inversely proportional to crack depth h while the peak energy spectral density grows with a dramatic h^6 proportionality. This is illustrated in Fig. 4-5, where source energy spectral levels are given for various crack depths and it is clear that Big-bang events, with depths exceeding 150-m depths, will be at least 3^6 times more energetic than the nominal 50-m deep cracks expected solely from diurnal tides.

From Eq. 4.3, the opening widths of the cracks will be 0.3 mm and 8 mm for 50-m and 250-m cracks, respectively. Such small-scale surface motions and feature changes will not be readily observable from orbit, but could easily be detected by seismo-acoustic sensors.

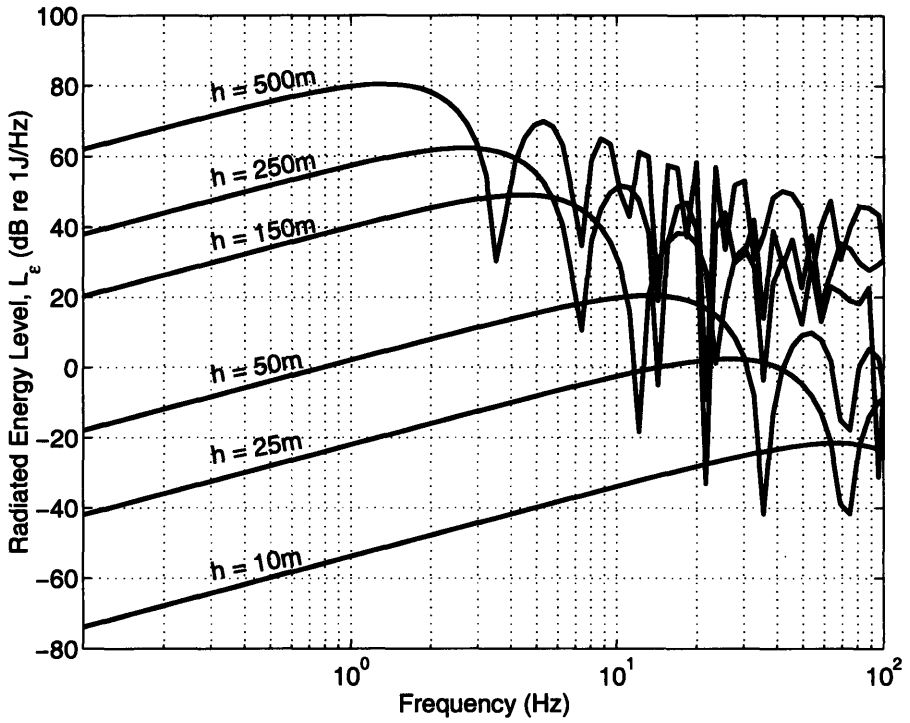

Figure 4-5: The radiated energy level L_ϵ from surface cracks for various crack depths h, as defined in Eq. D.42.

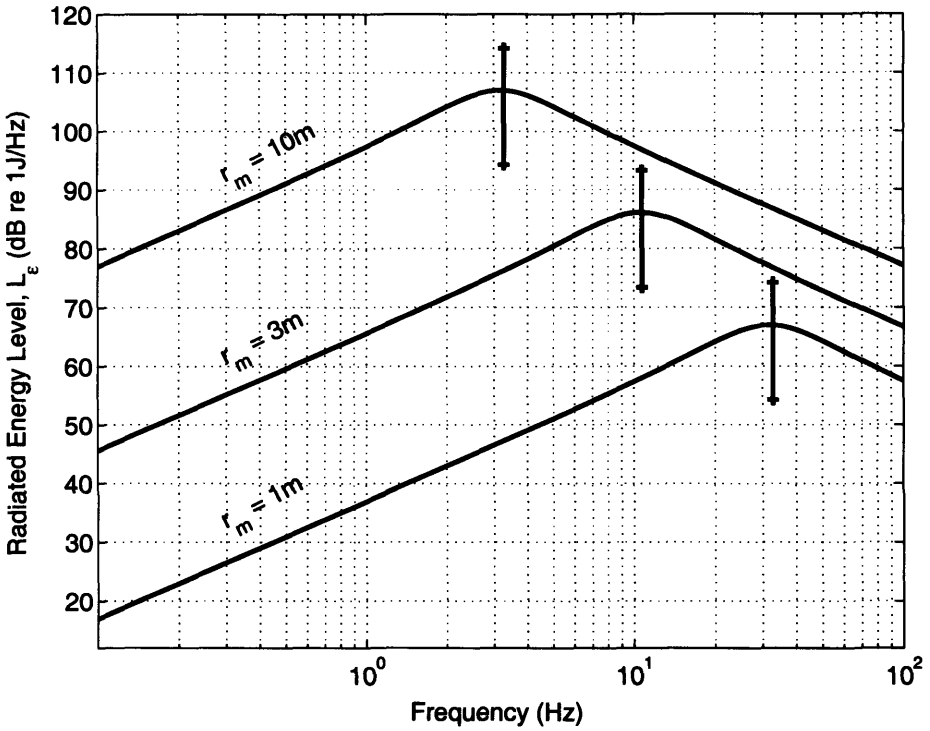

Figure 4-6: The radiated energy level L_ϵ for various radii r_m of impactors, as defined in Eq. D.56. Solid lines represent energy levels of rock impactors with density $\rho = 3\,\mathrm{g/cm^3}$ and impact velocity $v = 20$ km/s. Energy levels of iron meteors with $\rho = 7\,\mathrm{g/cm^3}$ and $v = 30$ km/s, and those of comets with $\rho = 1\,\mathrm{g/cm^3}$ and $v = 8$ km/s are also shown as errorbars in the figure.

4.2.2 Impacts

The rate of small impacts on Europa, for impactors in the 1~10 m radius range, is poorly constrained. A recent model predicts a rate of 0.2 to 16 for such impacts per year over the entire satellite [11] (Personal communication with E. B. Bierhaus). To determine the source energy spectrum for impacts as a function of impactor size, composition and speed, we make use of the impact-explosion analogy discussed in Ref. [88]. A derivation of the radiated energy spectrum using underground explosion phenomenology is given in Appendix D.2.

The radiated energy spectral levels for impactors of various radii are shown in Fig. 4-6, assuming a nominal rock meteor with 3 $\mathrm{g/cm^3}$ density and 20 km/s impact velocity. This energy level will vary within ± 10 dB depending on the seismic efficiency

discussed in Appendix D.2.

Small impacts, then may provide another source of Big-bang events that have energies well above those expected solely from tensile cracks driven by diurnal tides and may be frequent enough to be used as sources of opportunity for echo-sounding.

4.3 Seismo-Acoustic Wave Propagation on Europa

The radiated field from tensile cracks typically have directionality, but here we assume that an omnidirectional source, or a monopole, should best describe the expected or average directionality.

Assuming a time-harmonic acoustic field at frequency f, the equation of motion in horizontally stratified, homogeneous, isotropic elastic media can be expressed in cylindrical coordinates (r, z) as [120, 59]

$$\begin{aligned} \dot{u}_m(r,z,f) &= -i2\pi f S(f)\left[\frac{\partial}{\partial r}G_{\phi,m}(r,z,f) + \frac{\partial^2}{\partial r \partial z}G_{\psi,m}(r,z,f)\right] \\ &\equiv S(f)G_{\dot{u},m}(r,z,f), \end{aligned} \tag{4.5}$$

$$\begin{aligned} \dot{w}_m(r,z,f) &= -i2\pi f S(f)\left[\frac{\partial}{\partial z}G_{\phi,m}(r,z,f) - \frac{1}{r}\frac{\partial}{\partial r}r\frac{\partial}{\partial r}G_{\psi,m}(r,z,f)\right] \\ &\equiv S(f)G_{\dot{w},m}(r,z,f), \end{aligned} \tag{4.6}$$

where $\{\dot{u}_m, \dot{w}_m\}$ are the radial and vertical velocity components, $\{G_{\phi,m}, G_{\psi,m}\}$ are solutions to compressional (P) and shear vertical (SV) displacement potential Helmholtz equations in each layer m with corresponding compressional wave speed $c_{p,m}$ and shear wave speed $c_{s,m}$, and $S(f)$ is the spectral amplitude of volume injection by the source at frequency f.

The solutions are composed of the homogeneous and inhomogeneous solutions of the Helmholtz equations,

$$G_{\phi,m} = \tilde{G}_{\phi,m} + \hat{G}_{\phi,m}, \tag{4.7}$$

$$G_{\psi,m} = \tilde{G}_{\psi,m} + \hat{G}_{\psi,m}. \tag{4.8}$$

The homogeneous solutions satisfy

$$[\nabla^2 + k_m^2]\tilde{G}_{\phi,m}(r,z,f) = 0, \tag{4.9}$$

$$[\nabla^2 + \kappa_m^2]\tilde{G}_{\psi,m}(r,z,f) = 0, \tag{4.10}$$

where $k_m = 2\pi f/c_{p,m}$ and $\kappa_m = 2\pi f/c_{s,m}$ are wavenumbers of compressional and shear waves. The homogeneous solutions can be expressed in the wavenumber domain using integral representations,

$$\tilde{G}_{\phi,m}(r,z,f) = \int_0^\infty [A_m^- e^{-ik_{z,m}z} + A_m^+ e^{ik_{z,m}z}] J_0(k_r r) k_r dk_r, \tag{4.11}$$

$$\tilde{G}_{\psi,m}(r,z,f) = \int_0^\infty [B_m^- e^{-i\kappa_{z,m}z} + B_m^+ e^{i\kappa_{z,m}z}] J_0(k_r r) dk_r, \tag{4.12}$$

where J_0 is the Bessel function of the first kind, k_r is the horizontal wavenumber, and

$$k_{z,m} = \sqrt{k_m^2 - k_r^2}, \tag{4.13}$$

$$\kappa_{z,m} = \sqrt{\kappa_m^2 - k_r^2}, \tag{4.14}$$

are the vertical wavenumbers.

The inhomogeneous Helmholtz equation with a monopole source at $r = 0$, $z = z'$,

$$[\nabla^2 + k_m^2]\hat{G}_{\phi,m}(r,z,z',f) = -\frac{\delta(r)}{2\pi r}\delta(z-z') \tag{4.15}$$

has solution in the form of the integral representation

$$\hat{G}_{\phi,m}(r,z,z',f) = -\frac{1}{4\pi}\int_0^\infty \frac{e^{ik_{z,m}|z-z'|}}{ik_{z,m}} J_0(k_r r) k_r dk_r. \tag{4.16}$$

The inhomogeneous solution for SV component $\hat{G}_{\psi,m}$ is zero, since an omnidirectional source does not excite SV component.

Two-dimensional simulations including radial and vertical components are sufficient since out-of-plane motion does not occur for the assumed monopole source. A stable numerical solution in the frequency domain is obtained by wavenumber integration [120, 63]. The time domain solution and synthetic seismograms are then obtained by Fourier synthesis.

In this section, we investigate wave propagation in Europa through transmission loss, time-range, and synthetic seismogram analysis.

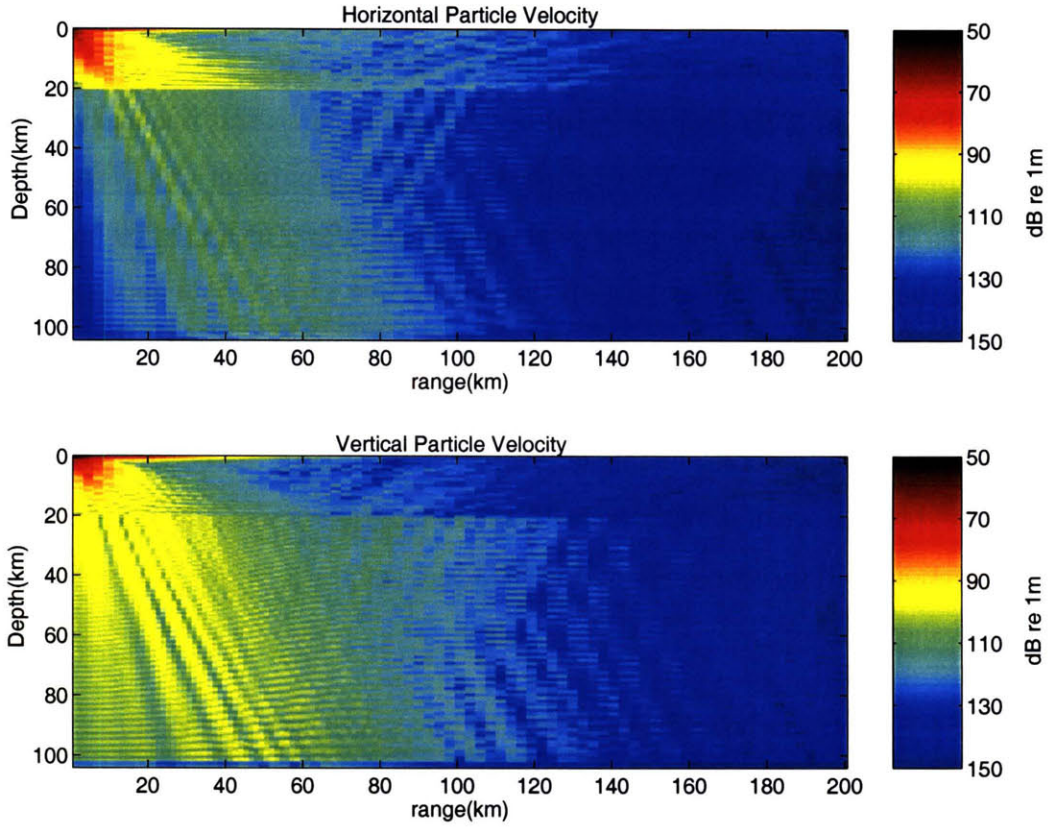

Figure 4-7: Transmission loss plots of the horizontal particle velocity $\mathrm{TL}_{\dot{u}}$ (top) and vertical particle velocity $\mathrm{TL}_{\dot{w}}$ (bottom) as defined in Eq. 4.17, when the source is located 50-m below the surface.

4.3.1 Transmission Loss

Transmission loss is a measure of the acoustic field level as a function of position, and is calculated in the frequency domain for a time-harmonic source via

$$\begin{aligned} \mathrm{TL}_{\dot{u}}(\mathbf{r},\mathbf{r}') &= -20\log_{10}\frac{|\dot{u}(\mathbf{r},\mathbf{r}')|}{|\dot{\mathbf{v}}_{\mathbf{0}}(\mathbf{r}')|} \quad \text{dB re } r_{ref}, \\ \mathrm{TL}_{\dot{w}}(\mathbf{r},\mathbf{r}') &= -20\log_{10}\frac{|\dot{w}(\mathbf{r},\mathbf{r}')|}{|\dot{\mathbf{v}}_{\mathbf{0}}(\mathbf{r}')|} \quad \text{dB re } r_{ref}, \end{aligned} \tag{4.17}$$

where $\dot{u}(\mathbf{r},\mathbf{r}')$ and $\dot{w}(\mathbf{r},\mathbf{r}')$ are the horizontal and vertical velocity fields at point $\mathbf{r}$ for a source at point $\mathbf{r}'$, and $\dot{\mathbf{v}}_{\mathbf{0}}(\mathbf{r}')$ is the velocity produced at a distance of r_{ref} = 1-m from the same source in an infinite, homogeneous medium with density $\rho(\mathbf{r}')$ and compressional wave speed $c_p(\mathbf{r}')$.

The magnitudes of the vertical and horizontal particle velocities of an ice source 50-m below the ice-vacuum interface in the 20-km convecting ice shell model are shown in Fig. 4-7 at 2 Hz frequency, corresponding to the central frequency typical in a Big Bang source event. This figure shows the transmission and reflection of acoustic waves from the ice-water and water-mantle interfaces at up to 200-km range. Fringes in the source radiation pattern due to the free surface boundary condition at the ice-vacuum interface are visible as are modal interference patterns in the ice layer. These patterns are a function of frequency, and are not readily observable for a typical broadband ice-crack or impact source. As expected, the horizontal particle velocity field in the ocean directly beneath the source is very weak due to the almost total reflection of the shear wave at the ice-water interface, which cannot support horizontal shear.

Figure 4-7 illustrates how efficiently seismic waves propagate through the ice shell as do acoustic waves through the subsurface ocean, and how a geophone located at the top of the ice shell will be able to detect multiple reflections from the ice-water interface as well as the water-mantle interface.

The Rayleigh wave is a surface wave that travels at roughly 90 % of the medium shear speed for a homogeneous halfspace, and suffers only cylindrical spreading in horizontal range but is attenuated exponentially with depth from the surface it travels on. It will be strongly excited on the ice-vacuum interface by sources of shallow depth, such as surface cracking events, impacts and the near-surface source of the given example. It can be seen in Fig. 4-7 as a strong vertical velocity field trapped near the surface. Characteristic differences between the Rayleigh wave and direct compressional wave arrivals will prove to be useful in determining the range of surface sources of opportunity. The frequency-dependent characteristics of a Rayleigh wave may also be used as another possible tool to probe the interior structure of the ice shell, and will be described in Sec. 4.6.4.6.2. If the wavelength of the Rayleigh wave is long compared to the thickness of the ice shell, it will propagate as a flexural wave on a thin plate.

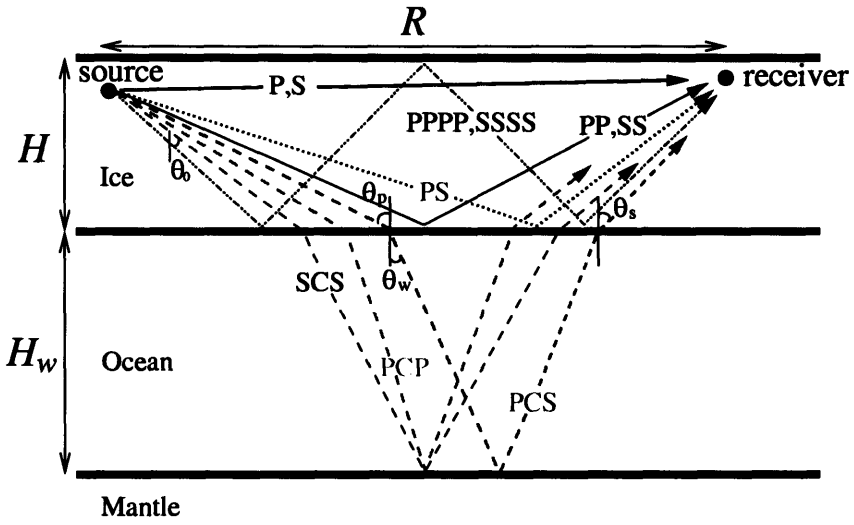

Figure 4-8: Nomenclature of acoustic rays. PP, PS, SS waves are single reflections from the ice-water interface, and PPPP, SSSS waves are double reflections from the ice-water interface. PCP, PCS, and SCS waves are the reflections from the water-mantle interface. Sound speeds in ice layer and ocean layer are assumed constant in this figure.

4.3.2 Nomenclature of Acoustic Rays

The analysis of seismo-acoustic wave propagation from a source to receiver can be intuitively understood by applying ray theory which is valid when the wavelength is small compared to variations in the medium. Rays are defined as a family of curves that are perpendicular to the wavefronts emanating from the source, and are obtained by solving the eikonal equation [18, 39, 86].

In order to describe the various seismo-acoustic rays propagating in ice and water layers, a nomenclature is adopted where P represents a compressional wave in the ice shell, S a shear wave in the ice shell, and where C is an acoustic wave in the subsurface ocean that includes reflection from water-mantle interface. Following this convention, appropriate letters are added consecutively when an acoustic ray reflects from or transmits through a given environmental interface. A PS wave, for example, is a compressional wave that departs from the source, reflects as a shear wave at the ice-water interface and arrives at the receiver. A PCS wave is a compressional wave that transmits through the ice-water interface, reflects from the water-mantle interface,

returns to the bottom of the ice shell, and transmits back into the ice as a shear wave. It should be noted that SP and PS waves arrive at a receiver simultaneously since their ray paths are symmetric. Also, an S wave from a source to a receiver on the ice-vacuum surface is a Rayleigh wave.

Some labelled ray geometries are shown in Fig. 4-8. A ray path follows a straight line in an iso-speed medium. However, if the sound speed in the medium varies along the ray path, the ray must satisfy Snell's law where reflection and transmission will occur at the boundary between iso-speed layers, and a continuous bending of a ray path, or refraction, will occur given a continuous sound speed gradient. For a horizontally stratified medium where sound speed varies only in the z-direction, the radius of curvature r_c of a refracting ray is

$$r_c = \frac{c_0}{\sin\theta_0}\left|\frac{dc}{dz}\right|^{-1}, \tag{4.18}$$

where θ_0 is the incident angle at some fixed depth as in Fig. 4-8 and c_0 is the sound speed at the same depth. For the 20-km convective ice shell model, the minimum radius of curvature of a compressional wave in upper thermal boundary layer regime is 51 km, which is not perceptible in Fig. 4-7. Refracted propagation of sound is a common feature in terrestrial oceans. In mid-latitudes deep sound channels typically form due to thermal heating above and increasing pressure below. These enable sound waves to propagate for thousands of kilometers without ever interacting with the sea surface or bottom [134]. Without more evidence, however, it is difficult to speculate on what sound speed profiles may exist in a potential Europan ocean.

The travel time from a source to receiver depends on the ray path. Travel time differences between ray paths can be used to infer Europa's interior structure. The range between a surface source event and a surface geophone can be obtained from direct P and S wave arrivals given the compressional and shear wave speeds in ice, which can be estimated with reasonable accuracy based on *a priori* information (See Appendix B). With the additional travel time measurement of a single ice-water reflection, such as PP, PS, or SS, the thickness of the ice shell can be estimated. If

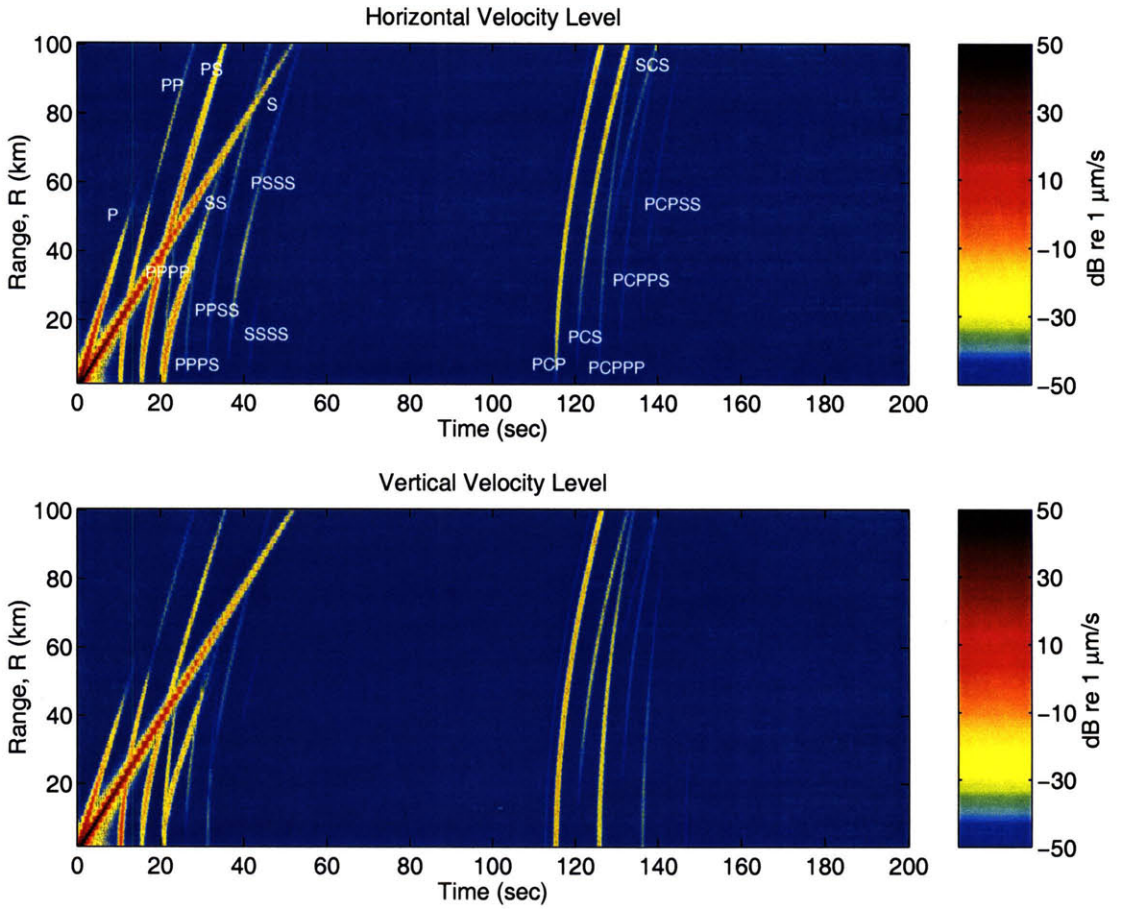

Figure 4-9: Time-range plot for the 20-km convective ice shell model. Colors represent the horizontal velocity level $L_{\dot{u}}$ (top) and vertical velocity level $L_{\dot{w}}$ (bottom), as defined in Eqs. D.18 and D.19.

more than one of these reflected paths are used, the sound speed in ice can also be experimentally estimated to improve upon the *a priori* information. Once the range of the source and the ice shell thickness are obtained, the depth of a subsurface ocean can be estimated by the reflections from the water-mantle interface, using any of the PCP, PCS, or SCS ray paths. The use of this kind of travel time analysis to infer Europa's interior structure will be discussed in more detail in Sec. 4.4

4.3.3 Synthetic Seismograms for a Big Bang Event

Here we study the amplitude and arrival-time structure of a Big Bang surface source event as measured by a triaxial geophone on Europa's surface for the four stratified

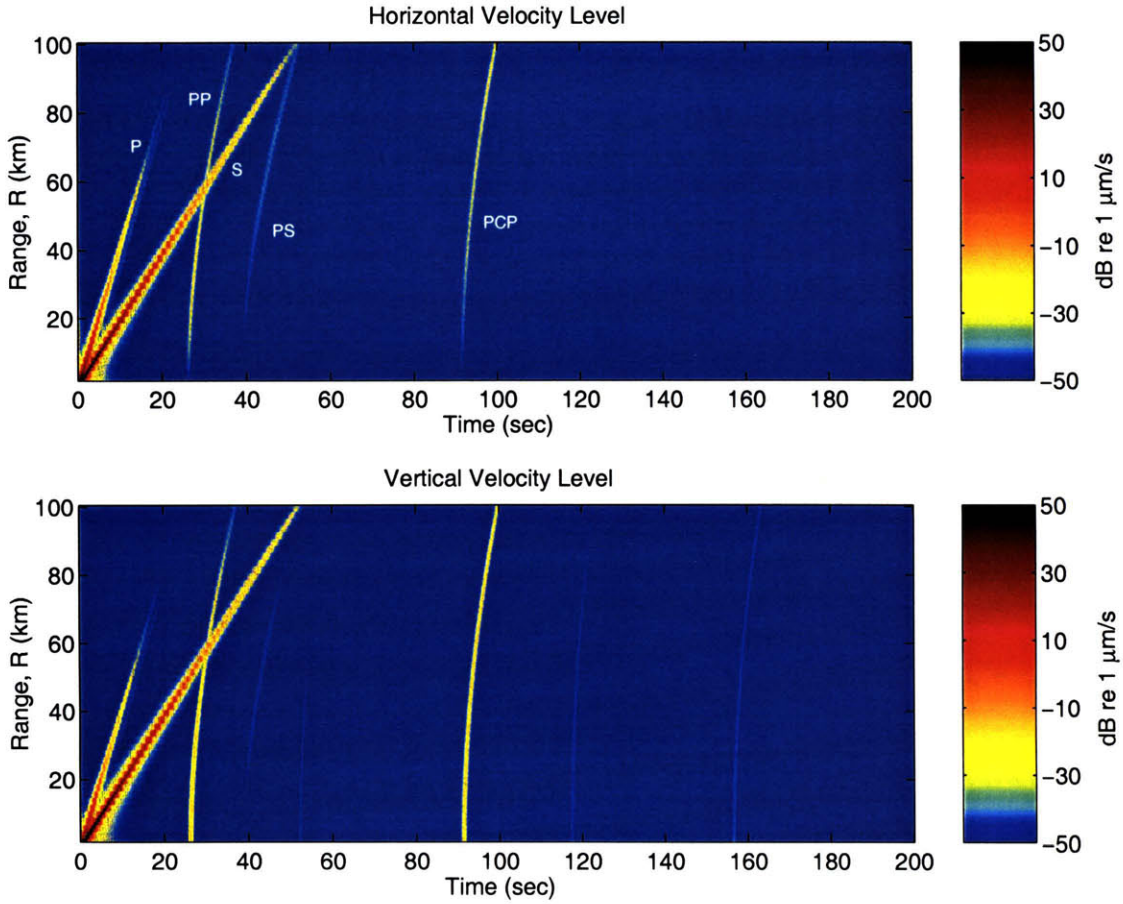

Figure 4-10: Time-range plot for the 50-km convective ice shell model.

models of Europa described in Sec. 4.1. First we consider the arrival time and amplitude structure as a function of range between the surface source and receiver by identifying the direct arrivals and reflections from various internal strata. Then we look in more detail at the type of amplitude and arrival time measurements that may be made at specific ranges. The analysis proceeds by solving the full-field seismo-acoustic wave equations of Eqs. 4.5 to 4.16 for a Big Bang source with a spectral peak in the $1 \sim 4$ Hz range. The source is here modeled as a monopole at 50-m depth and the receiver as a triaxial geophone at 1-m depth beneath the ice-vacuum surface. The finite bandwidth of the radiation is computed by Fourier synthesis. The resulting simulations are referred to as synthetic seismograms when they show amplitude versus time, and time-range plots when they show amplitude versus time and range. All simulations in this section have been performed for $h = 250$-m cracks or equivalently

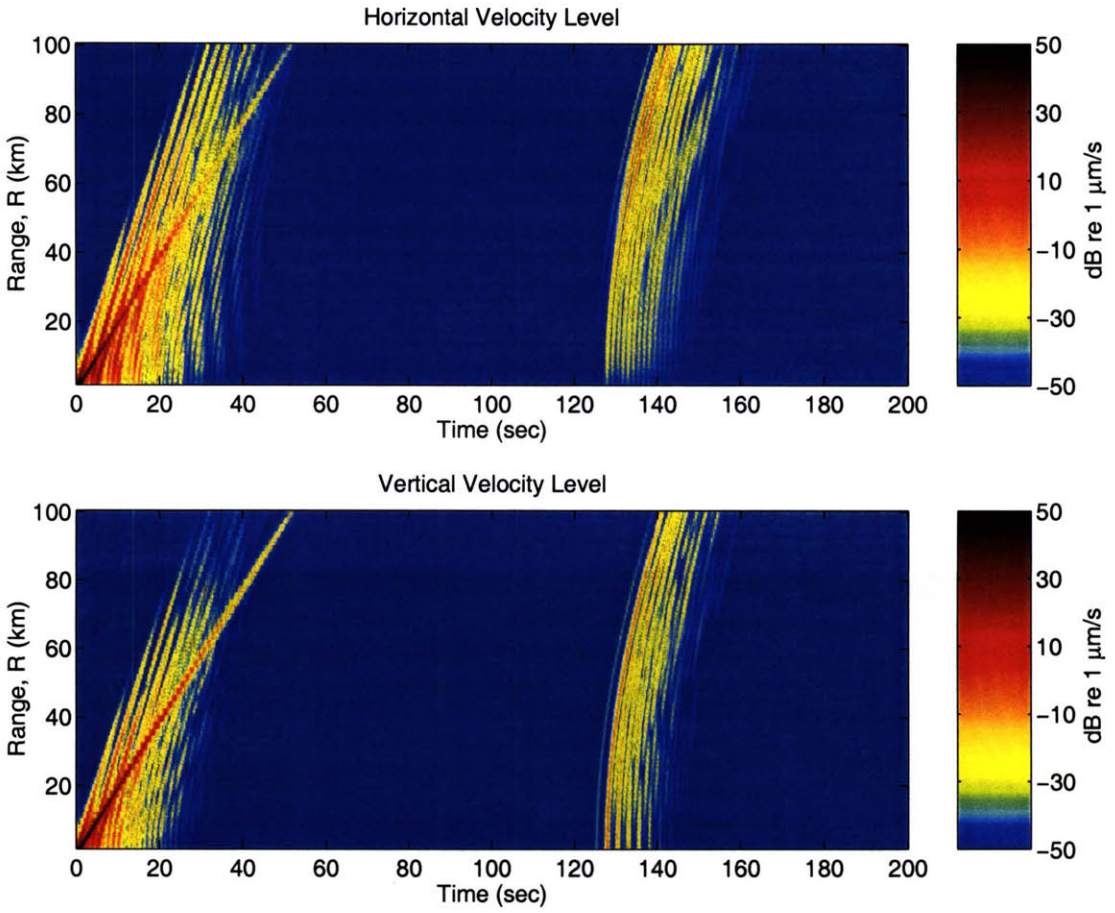

Figure 4-11: Time-range plot for the 5-km rigid ice shell model.

an impactor of roughly 10-m radius. These figures can be scaled for various crack depths h and impactor volume injections s_0 using Figs. 4-5 and 4-6, as explained in Appendix D (Eqs. D.30 to D.33).

Time-range plots are shown in Figs. 4-9 and 4-10 for the convective ice shell model, and Figs. 4-11 and 4-12 for the rigid ice shell model. In each figure, two lines consistently depart without curvature from the origin. These are the direct P wave and Rayleigh wave arrivals in the ice. The Rayleigh wave has the highest amplitude since it propagates as a trapped wave on the ice-vacuum surface.

Arrivals due to multiply reflected paths from the ice-water interface and the water-mantle interface are also readily observed. The travel time differences between the multiple reflections are closely related to the thickness of the ice shell. In the thin ice shell model (Fig. 4-11), the spacing between the multiple reflections is not much

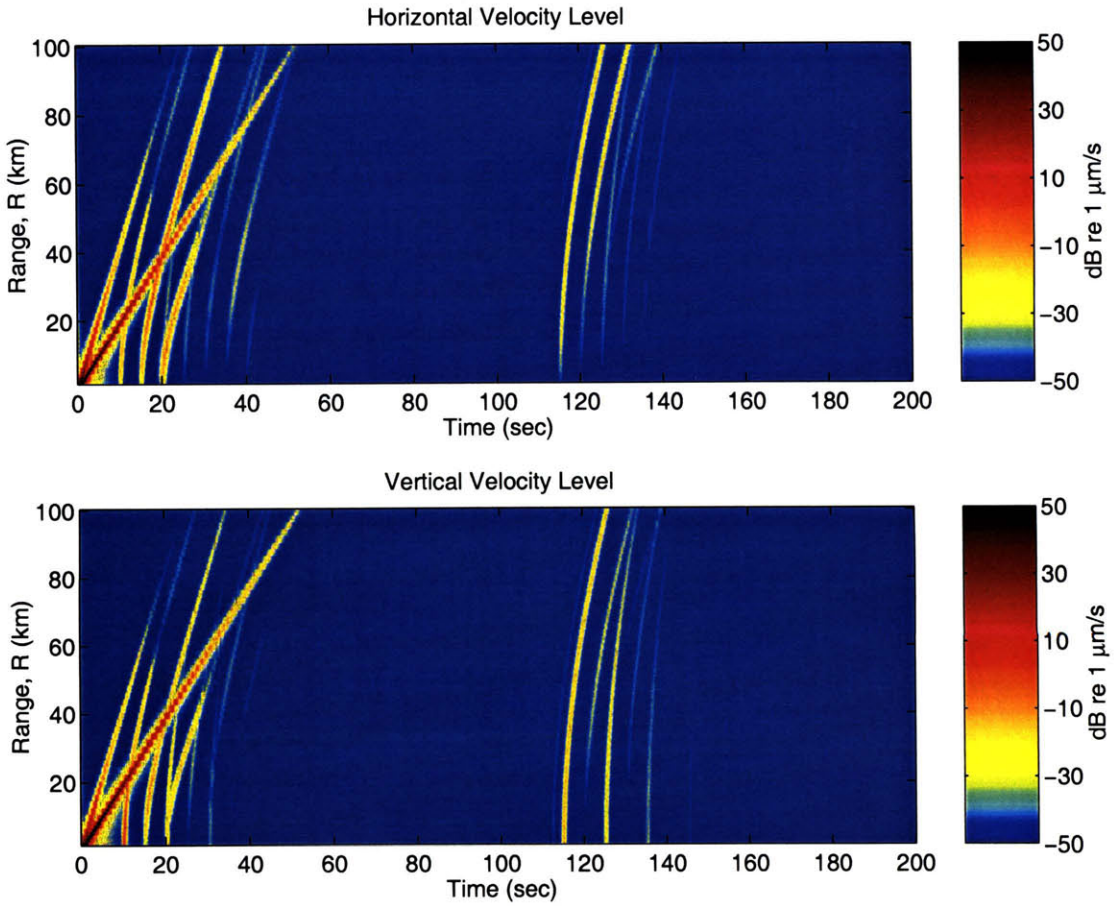

Figure 4-12: Time-range plot for the 20-km rigid ice shell model.

greater than the duration of the source event. This leads to one group of closely spaced arrivals reflected from the ice-water interface and another closely spaced group from the water-mantle interface. As the thickness of the ice shell increases, these multiple reflections separate more in the time domain as can be seen in Figs. 4-9, 4-10, and 4-12.

Inspection of the various scenarios indicates that the overall pattern of arrivals and amplitudes is very sensitive to the structure of Europa's ice-water layer, in particular, the absolute thicknesses and depths of the ice shell and ocean, as expected from basic echo-sounding principles. The pattern, however, is not very sensitive to the differences in internal temperature of the rigid versus convecting ice models, as can be seen by comparing Figs. 4-9 and 4-12. Other techniques involving seismo-acoustic tomography may be better suited to estimating the temperature structure.

4.3.4 Synthetic Seismograms

Detailed characteristics of the time series measured by a surface geophone can be better observed in synthetic seismograms. We present illustrative examples for the 20-km convective ice shell model. Figures 4-13 and 4-14 present a scenario where the seismometer is located at short range (2-km) from the source, while Figs. 4-15 and 4-16 present a longer range (50-km) scenario. In both scenarios, a sufficiently diverse set of prominent and well separated arrivals are found to enable the source range, as well as the thickness of Europa's ice shell and ocean layer to be determined by echo sounding.

For the case of a short source-receiver separation, as in Fig. 4-13, both the direct P and S waves arrive so near in time that they cannot be distinguished. The P wave is in fact overwhelmed by the S wave, which is effectively the Rayleigh wave due to the proximity of the source and receiver to the free surface. All subsequent arrivals can be easily distinguished from each other since they are well separated in time. The first arrivals are multiple reflections from the ice-water interface. For such a short source-receiver separation, waves returning from the water arrive at near normal incidence to the ice-water interface in the present geometry, and so lead to very weak SV transmission into the ice. This explains the relative abundance of prominent and well separated arrivals from the mantle in vertical velocity and the paucity of such arrivals in horizontal velocity at the geophone in Fig. 4-14.

For the case of a much longer source-receiver separation, as in Fig. 4-15, the direct P and S (again, the Rayleigh wave), as well as multiple reflections from ice-water and water-mantle interfaces are well separated in the time domain.

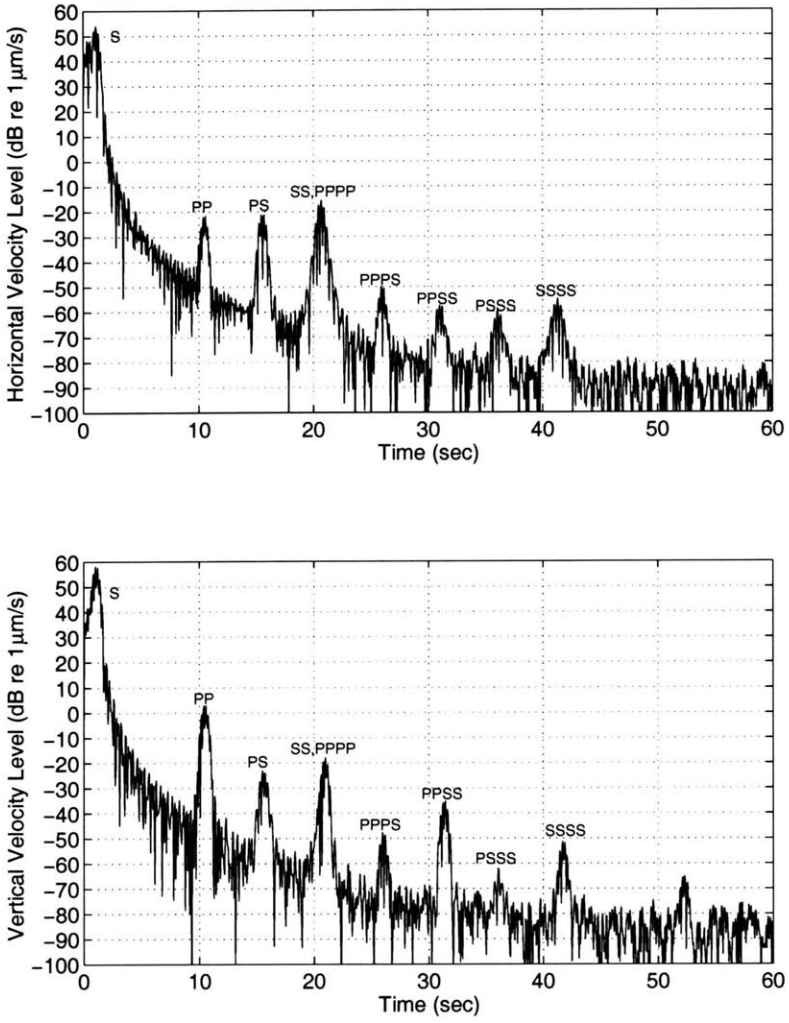

Figure 4-13: Ice-water reflections at 2-km range for the 20-km convective ice shell model. The top figure shows the horizontal velocity level $L_{\dot{u}}$ and the bottom figure shows the vertical velocity level $L_{\dot{w}}$, as defined in Eqs. D.18 and D.19. The regular spacing between the reflections can be directly related to the thickness of the ice shell. Direct P wave and Rayleigh wave arrivals are not well separated for this short range propagation.

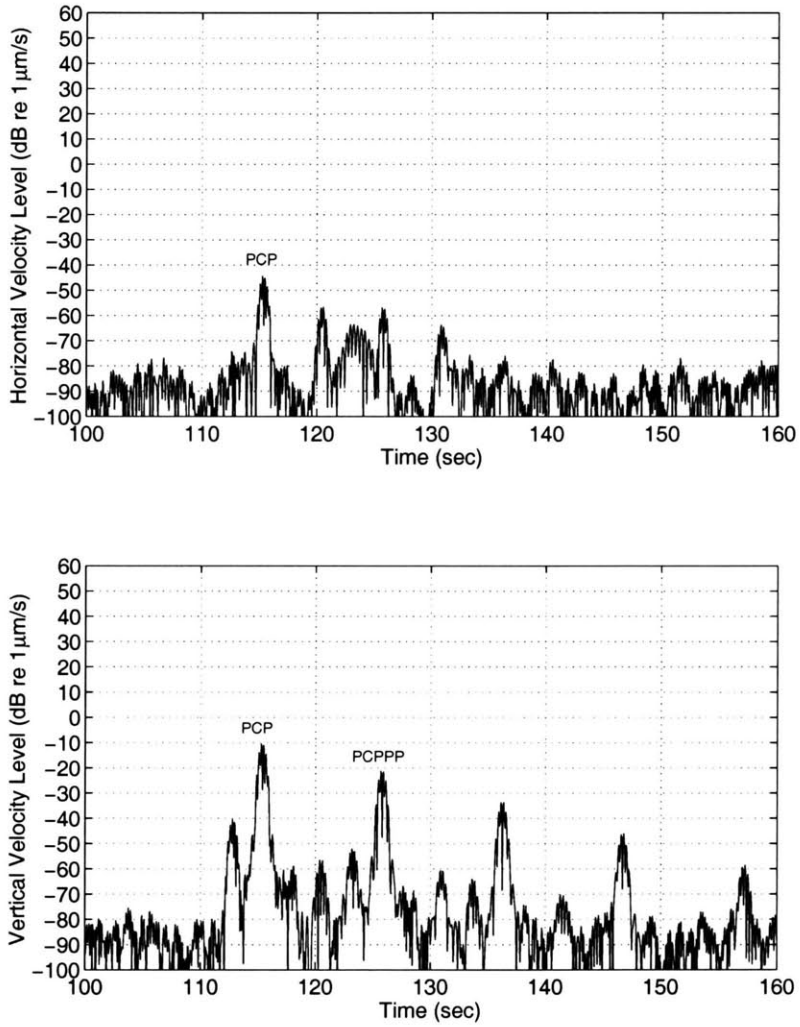

Figure 4-14: Bottom reflections at 2-km range for the 20-km convective ice shell model. The bottom reflections for short range propagation are mostly compressional wave reflections, and are more prominent in the vertical particle velocity components. The weak precursor before the PCP reflection is the reflection from the sediment layer overlying the basalt halfspace.

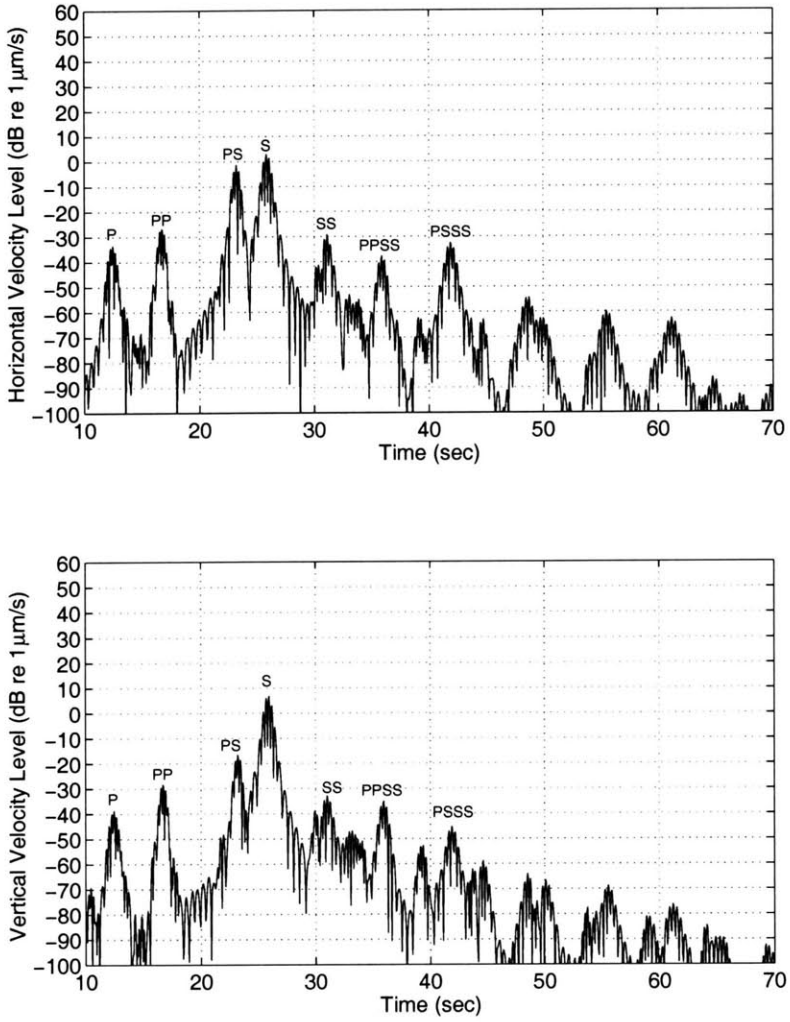

Figure 4-15: Ice-water reflections at 50-km range for the 20-km convective ice shell model. Travel time differences between the direct P wave and the Rayleigh wave can be inverted for the range between the source and receiver, and multiple reflections from the ice-water interface can be inverted for the thickness of the ice shell.

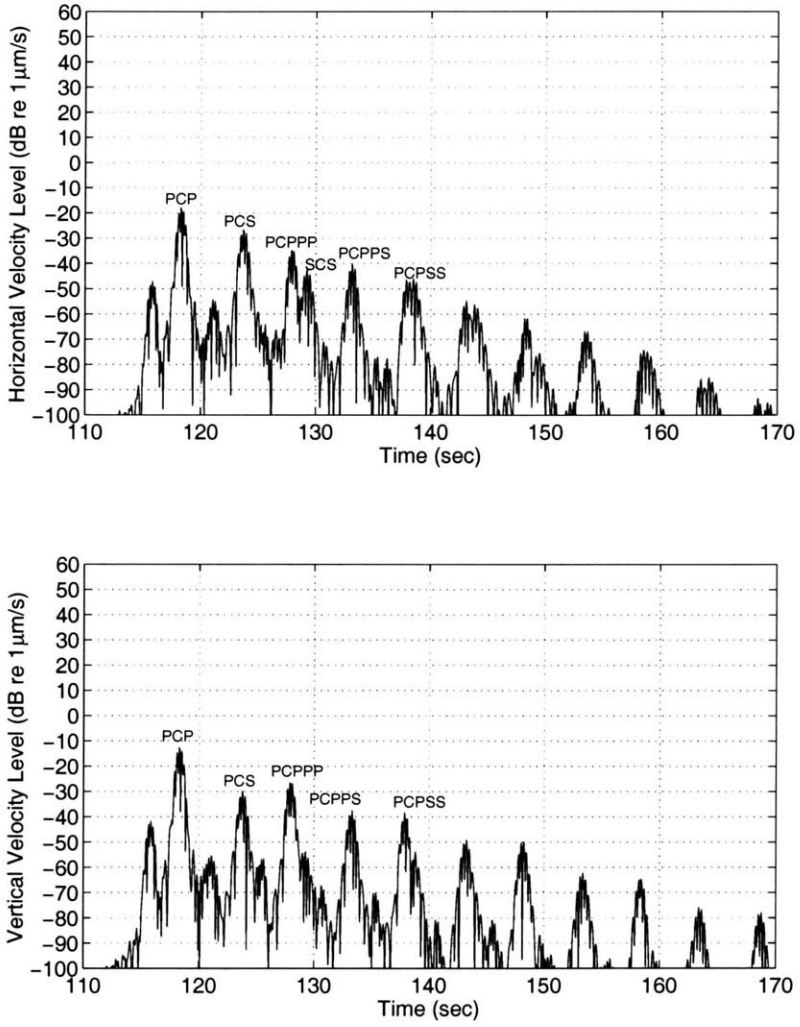

Figure 4-16: Bottom reflections at 50-km range for the 20-km convective ice shell model. For long range propagation, bottom reflections are prominent in both the horizontal and vertical particle velocity components.

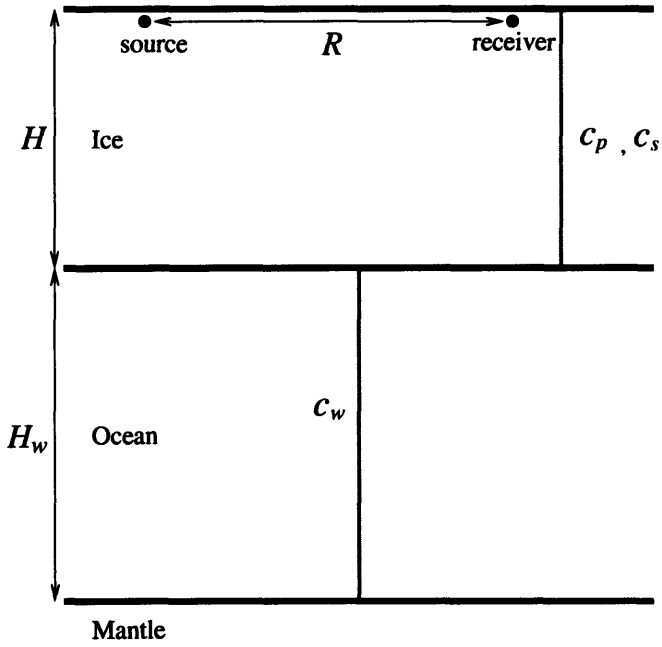

Figure 4-17: Schematic diagram of the simplified Europa model used for the parameter inversion. R is the range between the source and seismometer. The ice shell and ocean are simplified into iso-speed layers.

4.4 Inferring Europa's Interior Structure by Travel Time Analysis

4.4.1 Simplified Europa Model

In the previous section, we showed that the arrival time structure of seismo-acoustic waves is far more sensitive to ice shell thickness and ocean depth than to the temperature variations in the ice shell associated with the various rigid and convecting models examined. The seismo-acoustic parameters most important to the measured arrival-time structure, namely the thickness of the ice shell and the depth of a subsurface ocean, can then be estimated by matching measured travel times with those derived from a simplified Europan model. The simplified model drops parameters of Fig. 4-2 that do not have a first order effect in the arrival time structure. This leaves the six parameters shown in Fig. 4-17 at the top of the hierarchy. Dropped parameters, low in the hierarchy for the present echo-sounding technique, may be far

more important in other inversion schemes.

The simplified Europa model employs an iso-speed ice shell. This is justified to first order for a number of reasons. Although Europa's ice layer may undergo a drastic change in temperature with depth, from roughly 100 K to 273 K, the corresponding variations of c_p and c_s do not exceed 5%, as shown in Appendix B, except where the temperature reaches a few degrees of the melting point. This, however, occurs only over a small portion of the lower thermal boundary in the ice shell, as shown in Fig. 4-1. While the ice in this region undergoes changes in its molecular behavior, the change in sound speed is less than 10%. The overall error associated with the iso-speed assumption will then be less than 10%. In the simplified Europa model, we may further assume that $\xi \equiv c_p/c_s = 2$, which is a typical value for ice (Fig. B-1 (c)).

4.4.2 General Nondimensionalized Travel Time Curves

Under the assumption of an iso-speed ice shell, following the simplified Europan model, the general surface source-to-receiver travel time of ice-water reflected paths can be determined as a function of two nondimensional parameters ξ and R/H, as shown in Appendix C. The travel time curves become functions of only one nondimensional parameter R/H, if we assume the typical value $\xi = 2$. Nondimensional travel time curves for the simplified Europa model are plotted in Fig. 4-18 where the travel time for paths including up to double reflections from the ice-water interface are shown. This figure can be used to analyze arrivals from ice-water reflections in Figs. 4-9 to 4-12.

Similarly, the general source-to-receiver travel time of paths involving water-mantle reflections can also be determined in terms of the additional nondimensional parameters $\xi_w \equiv c_p/c_w$, the ratio between the compressional wave speed in ice and water, and H_w/H, the ratio between the ocean depth and the ice shell thickness, assuming an iso-speed water column. This is also shown in Appendix C. Nondimensional travel time curves for these paths are also plotted in Fig. 4-18, assuming $H_w/H = 4$ and $\xi_w = 4/1.5$.

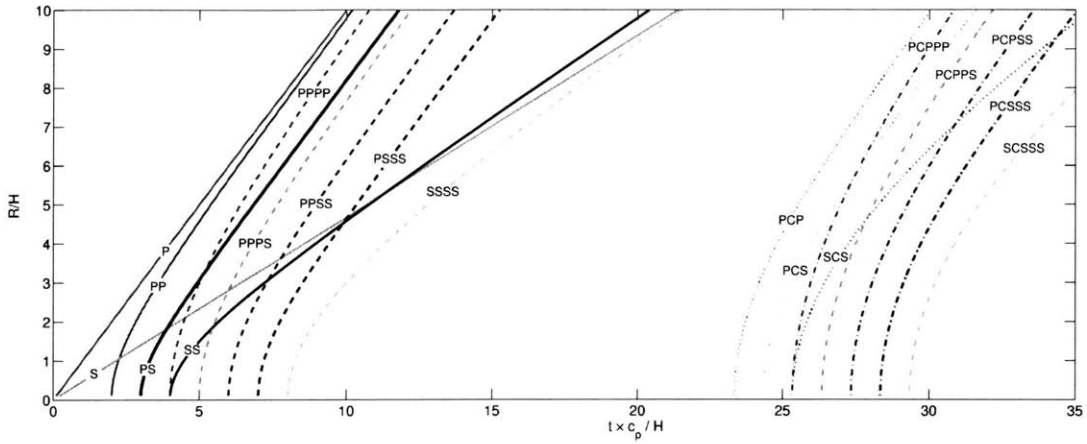

Figure 4-18: Nondimensionalized travel time curves for direct paths, ice-water reflections, and water-mantle reflections. It is assumed that $H_w/H = 4$ and $\xi_w = 4/1.5$ for bottom reflections. This figure can be directly compared to Figs. 4-9 and 4-12.

4.4.3 Estimating Interior Structure

The range between the source and receiver can be determined with a single triaxial geophone on Europa's surface without knowledge of the ice thickness by measuring the travel time difference between the direct P wave and the Rayleigh wave. The Rayleigh wave can be easily identified by its high amplitude and retrograde particle motion where vertical and horizontal components are 90° out of phase.

To also estimate the thickness of the ice shell, at least one reflection from the ice-water interface must also be identified. The PP wave arrival can be readily identified since it arrives the soonest after the direct P wave except when R/H is less than one, as shown in Fig. 4-18. Even in this case, however, the PP wave can be easily identified, since, besides the direct P wave, the Rayleigh wave is the only wave that can arrive before it.

If, for example, we measure the travel time differences $t_s - t_p \equiv \Delta_s$, and $t_{pp} - t_p \equiv \Delta_{pp}$, where t_p, t_s, and t_{pp} are the travel times of the direct P, the Rayleigh, and PP waves,

$$\Delta_s = \left(\frac{1}{0.93\, c_s} - \frac{1}{c_p}\right) R = \frac{1}{c_p}\left(\frac{\xi}{0.93} - 1\right) R, \tag{4.19}$$

$$\Delta_{pp} = \frac{1}{c_p}\left(\sqrt{4H^2 + R^2} - R\right), \tag{4.20}$$

and R/c_p and H/c_p are uniquely determined by,

$$\frac{R}{c_p} = \frac{\Delta_s}{\xi/0.93 - 1}, \tag{4.21}$$

and

$$\frac{H}{c_p} = \frac{1}{2}\left[\Delta_{pp}\left\{\Delta_{pp} + \frac{2\Delta_s}{\xi/0.93 - 1}\right\}\right]^{1/2}. \tag{4.22}$$

This result shows that if the compressional wave speed in the ice is uncertain, but the ratio between the compressional and shear speed in ice is known, the error in the range and thickness estimates will be linearly related to the error in compressional wave speed. Based on the analysis presented in Appendix A, the sound speed in ice can be estimated to within roughly 10%. The range of the source and the thickness of the ice shell can then also be estimated within 10% of error given the travel times of the direct P, the Rayleigh, and PP waves. Estimates of R, H, c_p and c_s can be refined by analyzing arrivals from other paths. Similarly, the ocean thickness H_w and average sound speed c_w can be determined by using Fig. 4-18 to analyze arrivals from paths reflecting from the water-mantle interface.

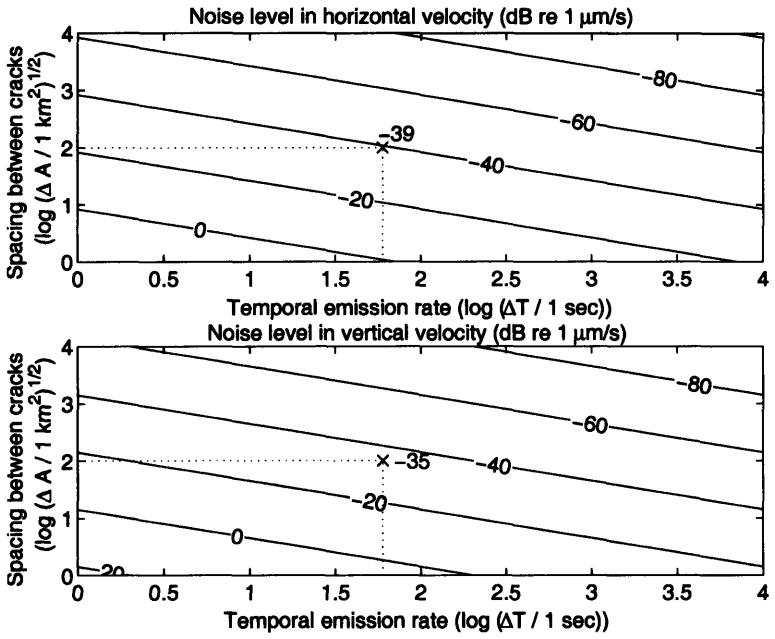

Figure 4-19: Ambient noise levels in the horizontal velocity $NL_{\dot{u}}$ and vertical velocity $NL_{\dot{w}}$, as defined in Eqs. 4.23 and 4.24, for the 20km convective ice shell model as a function of spatial densities and temporal emission rates of the surface cracks. The reference ambient noise levels assuming $\Delta T = 60$ seconds and $\Delta A = 100$ km^2 are marked in the figure.

4.5 Europan Ambient Noise

As noted in the introduction and in Sec. 4.2.1, there is a possibility that ice cracking events on Europa may occur so frequently in space and time that their accumulated effect may lead to difficulties for the proposed echo-sounding technique. Here we attempt to quantify the characteristics of a Big Bang event necessary for it to serve as a source of opportunity in echo sounding given an estimate of the accumulated noise received at a surface geophone. We do so by first developing a Europan noise model in terms of the spatial and temporal frequency and source spectra of the expected noise sources.

4.5.1 Estimation of ambient noise level

In order to calculate the ambient noise level, an ocean acoustic noise modeling technique [70] is adapted for Europa. The basic assumption is that the noise arises from an infinite sheet of monopole sources just below Europa's ice-vacuum boundary at depth z'. The sources are assumed to be spatially and temporally uncorrelated and to have the same expected source cross-spectral densities.

The mean-square horizontal and vertical particle velocities of the ambient noise measured by a geophone at depth z resulting from these uncorrelated sources are respectively

$$\left\langle |N_{\dot{u}}|^2 \right\rangle = \frac{\pi}{(\Delta T)(\Delta A)} \int_{-\infty}^{\infty} \left\langle |S(f)|^2 \right\rangle \int_0^{\infty} |g_{\dot{u}}(k_r, z, z')|^2 \, k_r \, dk_r \, df, \tag{4.23}$$

$$\left\langle |N_{\dot{w}}|^2 \right\rangle = \frac{2\pi}{(\Delta T)(\Delta A)} \int_{-\infty}^{\infty} \left\langle |S(f)|^2 \right\rangle \int_0^{\infty} |g_{\dot{w}}(k_r, z, z')|^2 \, k_r \, dk_r \, df, \tag{4.24}$$

where $1/\Delta T$ and $1/\Delta A$ are temporal and spatial densities of noise sources, $\langle |S(f)|^2 \rangle$ is the expectation of the magnitude squared of source spectrum of a given source, and $g_{\dot{u}}(k_r, z, z')$ and $g_{\dot{w}}(k_r, z, z')$ are the integral representations of the horizontal and vertical particle velocities in the wavenumber domain, which are defined in terms of Hankel transform of Eqs. 4.5 and 4.6,

$$g_{\dot{u},\dot{w}}(k_r, z, z') = \int_0^{\infty} G_{\dot{u},\dot{w}}(r, z, z') J_0(k_r r) r \, dr. \tag{4.25}$$

The variance of the vertical particle velocity is the same as the scalar result given in [144]. The horizontal component is for one out of two horizontal directions spanned by the geophone and so is smaller by a factor of 2. The ambient noise levels in decibels are defined by

$$\mathrm{NL}_{\dot{u}} = 10 \log \frac{\langle |N_{\dot{u}}|^2 \rangle}{\dot{u}_{ref}^2} \quad \text{dB re } \dot{u}_{ref}, \tag{4.26}$$

$$\mathrm{NL}_{\dot{w}} = 10 \log \frac{\langle |N_{\dot{w}}|^2 \rangle}{\dot{w}_{ref}^2} \quad \text{dB re } \dot{w}_{ref}, \tag{4.27}$$

where $\dot{u}_{ref} = \dot{w}_{ref} = 1\ \mu$m/s.

Equations 4.23 and 4.24 are used to compute the general ambient noise levels measured by a geophone at 1-m below the ice-vacuum interface for the 20-km convective shell model as a function of temporal and spatial source density. The results are shown in Fig. 4-19 for noise sources at $z' = 50$-m depth in the 1~4 Hz band, the same depth and band used for the Big Bang synthetic seismograms of Section 3. This noise table is for $h = 50$-m ambient cracks, but can be scaled for other crack depths h by following the procedures described in Appendix D.

The ambient noise levels of Fig. 4-19 can be compared directly with the signal levels of 250-m cracks for the 20-km convective shell model (Figs. 4-9, 4-13, 4-14, 4-15, and 4-16). The noise levels can even be compared with the signal levels in Figs. 4-10, 4-11, and 4-12 because ambient noise level does not vary significantly as a function of ice shell thickness, since it is dominated by the Rayleigh wave, which is trapped on the ice-vacuum interface and so is relatively insensitive to the ice shell thickness H when its wavelength is small compared to H.

Such comparisons still require knowledge of the spatial and temporal densities of the noise sources. These can be estimated for diurnal tidally driven tensile cracks by noting that a cycloidal feature will extend at a speed of roughly 3.5 km/hr, following the location of maximum tensile stress [56]. The propagation speed of a tensile crack, however, is the much larger $v \simeq 0.9\ c_s$, as noted in Sec. 4.2.1. The cycloidal features then are apparently comprised by a sequence of discrete and temporally disjoint cracking events. If we assume that each tidally driven crack, of nominal depth $h = 50$-m extends for a minimum length of $h = 50$-m, as discussed in Sec. 4.2.1, we arrive at a rate of roughly 1 tensile crack per minute along a given cycloidal feature. A consistent estimate of the spatial separation between cracking events would be the roughly 100-km scale of a cycloidal feature [56]. As can be observed in Fig. 4-19, the ambient noise level reaches -35 dB re $1\,\mu$m/s for 100-km crack spacing and 1 discrete emission per minute.

If the source of opportunity and ambient noise sources have the same depth of $h =$ 50-m, the expected energy of each noise source equals that of the signal. In this case,

the amplitudes of the time-range plots and synthetic seismograms in Sec. 4.3.3 should be decreased by 56-dB, as can be determined from Eqs. D.30 and D.31 of Appendix D. Comparison with the time-range plots and synthetic seismograms of Sec. 4.3.3, after subtracting 56-dB to go from an h=250-m to an h=50-m deep crack, shows that the reflections from the ice-water and water-mantle interfaces will be buried by the ambient noise for this scenario. The situation changes if the source of opportunity is far more energetic than an expected noise event, as is the case for a Big Bang source event.

4.5.2 Estimation of signal to noise ratio

It was shown in Sec. 4.2.1 that the peak of the energy spectral density for a surface crack is proportional to h^6, while both the bandwidth and frequency of the spectral peak are inversely proportional to the crack depth h. Smaller cracks will then not only radiate less energy, they will also spread this energy over a broader and higher frequency spectrum. Larger cracks, on the other hand, will radiate more energy over smaller bandwidths at lower frequencies, as shown in Fig. 4-4. This would make it advisable to low-pass filter geophone time series data to the band of a Big Bang source of opportunity, if this source was due to a much deeper and less frequent cracking event than those comprising the expected noise. If the Big Bang is 5 times deeper than the ambient cracks, for example, the radiated energy within the bandwidth of the Big Bang will be approximately 56-dB greater than that radiated by an ambient crack. This will in turn increase the signal-to-noise ratio of the time series by 56-dB. In this case, it will be possible to robustly detect multiple Big Bang reflections from the ice-water interface and water-mantle interface above the noise for nominal 50-m deep noise cracks of 100-km spacing and 1 per minute rate, as is illustrated in Fig. 4-20 for a 250-m deep Big Bang crack.

According to Ref. [98], unfractured ice subject to a fixed tensile stress will develop a distribution of surface fractures that occur at a rate inversely proportional to the maximum depth of the crack h. Larger cracks will be less frequent and so less likely radiate seismo-acoustic waves that overlap. Larger cracks will also release stress over

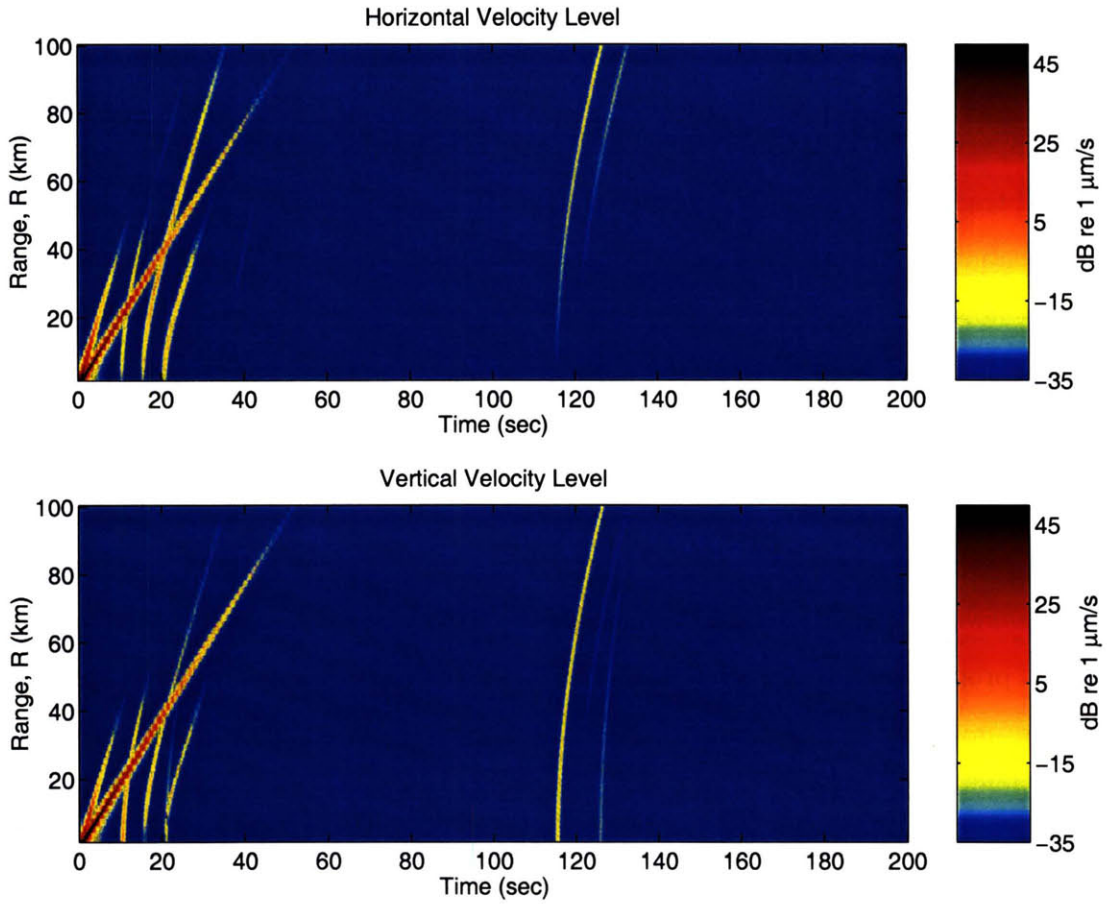

Figure 4-20: Time-range plot for a Big Bang event that can stand above the reference ambient noise level of -35 dB re 1μm/s.

larger areas and so prevent other cracks from developing nearby.

Small impacts are another potential source of Big Bang events that usually have much higher energy spectral levels than surface cracks, as can be seen by comparing Fig. 4-5 and Fig. 4-6. Given the impact rate mentioned in Sec. 4.2.2, the probability of at least one impactor within 100km of the seismometer is 0.1 to 10% assuming a 4 month operational period. While such an impact is not highly likely, the signal-to-noise ratio would be large and the reflections could be easily resolved. Smaller impacts may be much more frequent and still energetic enough to serve as Big Bang events, but their rates are difficult to resolve with current observational methods.

Our signal-to-noise-ratio analysis is based on the worst-case scenario of maximum diurnal stress, where all surface cracks are assumed to actively radiate seismo-acoustic

waves once every minute. Cracking will become less frequent after Europa passes the perigee. The ambient noise level will then decrease, enabling echo-sounding with a surface crack of shallower depth h. Since impactors are totally independent of surface cracking noise, they may strike Europa at low-tide when surface cracks are dormant, achieving the maximum signal to noise ratio.

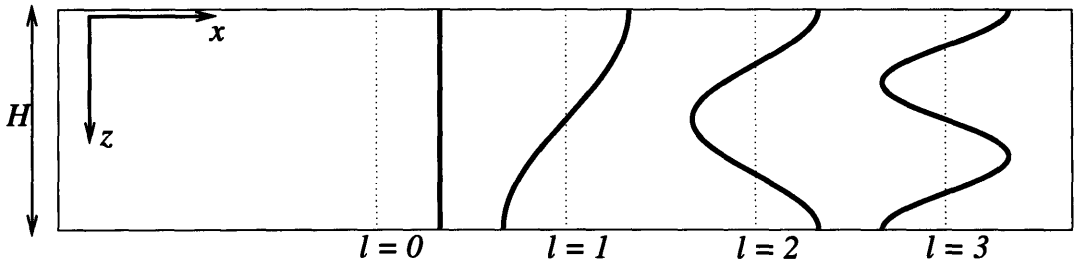

Figure 4-21: Love wave geometry and mode shapes for an elastic plate surrounded by fluid media.

4.6 Inferring Interior Properties of Europa with Love and Rayleigh Waves

Love waves are effectively propagating SH modes trapped by the boundaries of an elastic waveguide, while Rayleigh waves are interface waves that travel along an elastic surface that involve both compressional and SV wave potentials. The theory of these waves in horizontally stratified media is well developed (see, e.g., Refs. [17, 89]). Here we discuss the possibility of using the frequency dependent characteristics of these waves to infer interior properties of Europa.

4.6.1 Dispersion of the Love wave

If an elastic medium is surrounded by a vacuum or fluid media that does not support shear, as in the case of an ice sheet floating on an ocean, the Love wave will propagate like a free wave in a plate.

Considering the geometry in Fig. 4-21, the particle displacement in the y direction $v = v(x, z)$ satisfies the Helmholtz equation

$$\left[\nabla^2 + \kappa^2\right] v(x, z) = 0. \tag{4.28}$$

Since vacuum or fluid media cannot sustain shear stress, boundary conditions are

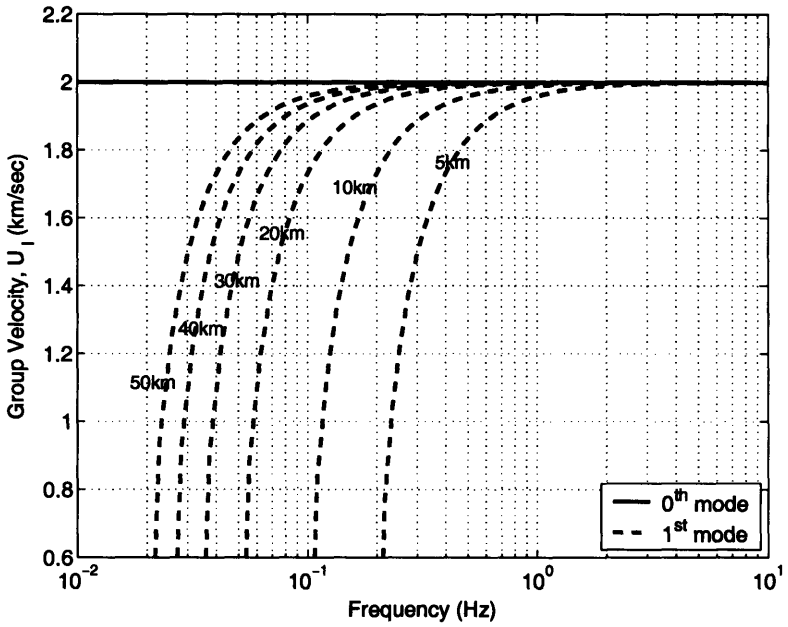

Figure 4-22: Love wave dispersion curves for various ice shell thicknesses assuming an iso-speed ice shell with a shear wave speed $c_s = 2$km/s, overlying a subsurface ocean. The 0^{th} order mode has a constant group velocity that is independent of the ice shell thickness.

expressed as

$$\mu \frac{\partial v}{\partial z}\bigg|_{z=0} = \mu \frac{\partial v}{\partial z}\bigg|_{z=H} = 0, \tag{4.29}$$

where μ is the shear modulus of the elastic medium. The solution is of the form

$$v = V(z)e^{i(\kappa_x x - \omega t)}, \tag{4.30}$$

where κ_x is the horizontal wavenumber in the x direction, and ω is the angular frequency. Equation 4.28 is satisfied by setting

$$V(z) = A\cos\kappa_{z,l} z, \quad l = 0, 1, 2, \cdots, \tag{4.31}$$

where $\kappa_{z,l}^2 = \kappa^2 - \kappa_{x,l}^2$. The boundary conditions are satisfied when

$$\kappa_{z,l} H = \left[\kappa^2 - \kappa_{x,l}^2\right]^{1/2} H = \pi l, \quad l = 0, 1, 2, \cdots. \tag{4.32}$$

The even numbered and odd numbered solutions in Eq. 4.31 represent symmetric and antisymmetric normal modes in the plate respectively. Some of the mode shapes are shown in Fig. 4-21. It can be shown that the group velocity of each mode is

$$U_l = c_s \left[1 - \left(\frac{\pi l}{\kappa H}\right)^2\right]^{1/2}, \qquad l = 0, 1, \cdots, l_{\max}. \tag{4.33}$$

The maximum number of normal modes $l_{\max}$ for a given frequency is

$$l_{\max} = \text{integer part of } \left(\frac{\kappa H}{\pi}\right), \tag{4.34}$$

with the cut-off frequency of each mode is given as

$$f_{c,l} = \frac{c_s l}{2H}. \tag{4.35}$$

It is important to note that there is a zeroth-order mode that is non-dispersive, insensitive to the thickness, and has no cut-off frequency, which can be obtained by setting $l = 0$ in Eq. 4.33 and 4.35. This characteristic of zeroth-order mode is also shown in Fig. 4-22.

This derivation shows that Love waves in a free or fluid loaded plate have group velocities that are inversely proportional to frequency so that the lower frequency components propagate slower than the higher ones. This dispersive characteristic is shown for the group velocity of the 1^{st} mode for various ice shell thicknesses in Fig. 4-22.

If the ice shell overlies another elastic medium with faster shear wave speed such as Europa's mantle, however, at the low frequency end the dispersion relationship will be reversed with the lower frequency components arriving faster than the higher frequency components. This is a common effect also observed in ocean acoustic waveguides [106, 39]. In this case, it can be shown that the group velocity and cut-off

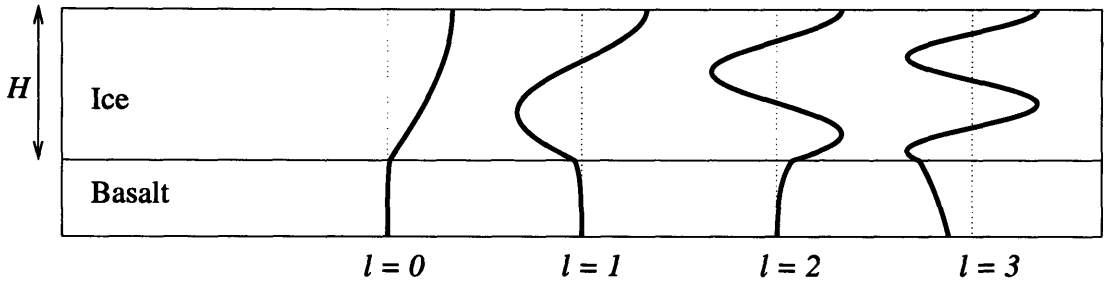

Figure 4-23: Love wave geometry and mode shapes assuming an ice shell overlying basalt halfspace.

frequency of each mode is given by

$$U_l = \frac{\kappa_{x,l}\left[\frac{H\sqrt{\kappa_{x,l}^2-\kappa_b^2}}{\cos^2\left(H\sqrt{\kappa^2-\kappa_{x,l}^2}\right)} + \frac{\mu_b}{\mu}\left\{1+\frac{\kappa_{x,l}^2-\kappa_b^2}{\sqrt{\kappa^2-\kappa_{x,l}^2}}\right\}\right]}{\frac{\kappa}{c_s}\frac{H\sqrt{\kappa_{x,l}^2-\kappa_b^2}}{\cos^2\left(H\sqrt{\kappa^2-\kappa_{x,l}^2}\right)} + \frac{\mu_b}{\mu}\left[\frac{\kappa_b}{c_{sb}}+\frac{\kappa}{c_s}\frac{\kappa_{x,l}^2-\kappa_b^2}{\sqrt{\kappa^2-\kappa_{x,l}^2}}\right]}, \tag{4.36}$$

$$f_{c,l} = \frac{l}{2H}\frac{c_s c_{sb}}{\sqrt{c_{sb}^2-c_s^2}}, \tag{4.37}$$

where $\kappa_{x,l}$ is the wavenumber of l^{th} mode in x direction, and μ_b, c_{sb}, κ_b are the shear modulus, shear wave speed, and shear wavenumber in the elastic medium underlying the ice shell, respectively. The mode shapes and dispersion curves for various ice shell thicknesses assuming an ice shell overlying basalt halfspace are shown in Figs. 4-23 and 4-24, respectively.

Kovach and Chyba [68] have argued that it may be possible to verify the existence of a subsurface ocean on Europa by finding a way to measure the presence or absence of this reversal. Since the Love wave is trapped within the ice shell, it cannot be used to determine the depth of a potential ocean layer below. Kovach and Chyba have also suggested that it may be possible to determine the thickness of the ice layer by measuring the frequency dependence or dispersion in the group velocity of the first Love wave mode.

Since Love waves are modal decompositions of the SH wave, they will likely require source-receiver ranges greatly in excess of the ice sheet thickness to be observed. Group velocity analysis, however, requires the source range, which can be estimated

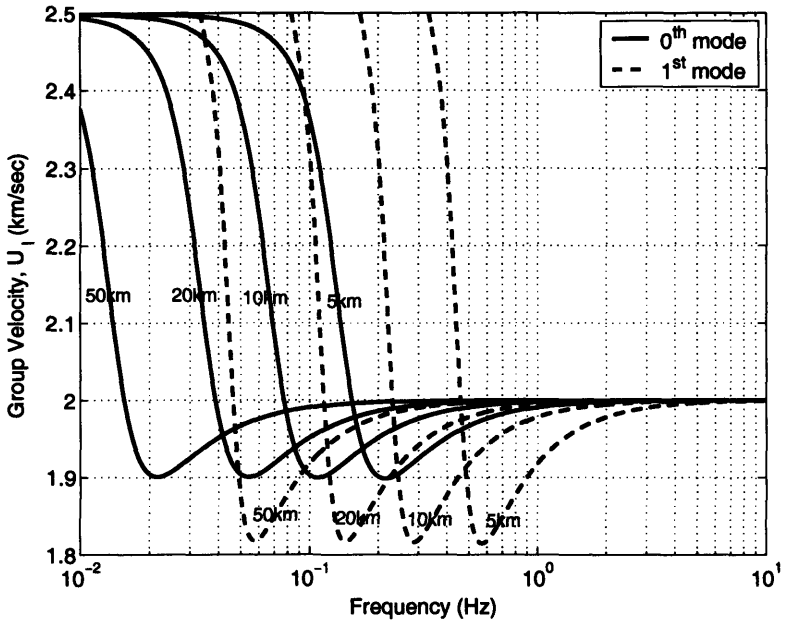

Figure 4-24: Love wave dispersion curves for the 0^{th} and 1^{st} order modes in the case where ice shell is overlying a basalt halfspace.

by measuring the direct P wave arrival for sufficiently energetic sources or multiple reflections from the ice-water interface. Use of the latter, however, would require the ice thickness be determined by echo-sounding, which defeats much of the purpose in Love wave dispersion analysis.

Since the Love wave has a zeroth order mode that is non-dispersive if an ocean is present and has no cut-off, a potentially significant component of any Love wave arrival may never exhibit the sought after frequency dependence or cut-off. Additionally, many modes higher than the 1^{st} can be easily excited by the broadband surface sources described in Sec. 4.2.4.2.1 as shown in Fig. 4-25 for the fluid-loaded scenario. Different order modes from different frequencies must then somehow be separated to avoid ambiguities in the estimation of the group-speed frequency dependence of a given mode. Such separation will be difficult to obtain with a single sensor and an uncontrolled source.

A measurement of reduced Love wave levels in the low frequency regimes near modal cut-offs could then easily be due to the lower source energy spectra expected

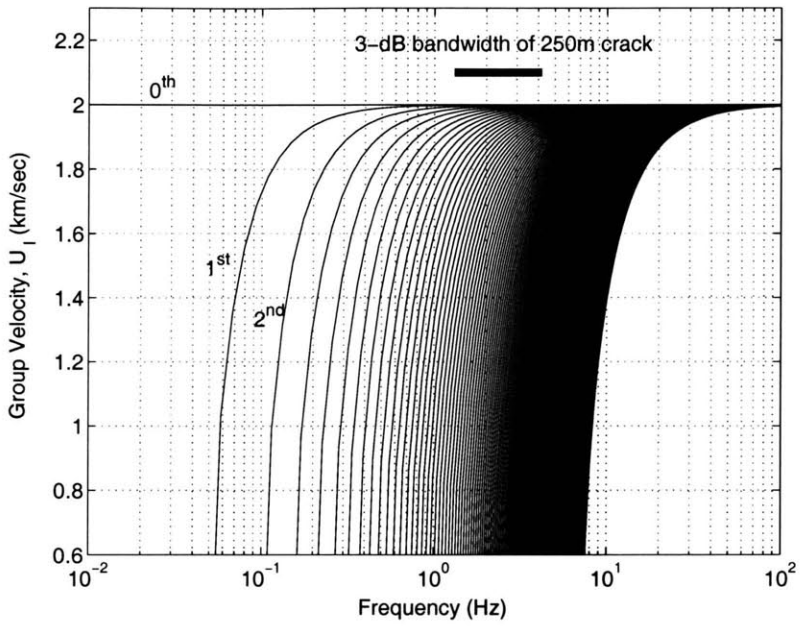

Figure 4-25: Love wave dispersion curve for the 20-km fluid-loaded iso-speed ice shell up to the 144^{th} mode. The mode number runs from left to right. For reference, the 3-dB bandwidth of a 250-m deep crack is shown as a thick horizontal line.

in these regimes from the analysis of Sec. 4.2.1 rather than modal cut-off effects. Comparisons with P wave and SV wave spectra from the same source event could help to reduce this ambiguity, but would not necessarily resolve it even below the cut-off frequency of the 1^{st} mode due to the existence of the 0^{th} order Love wave mode that is non-dispersive in the fluid-loaded scenario and has no cut-off. Some of these issues may be resolvable for very distant sources given well separated arrivals for the different Love wave modes.

4.6.2 Estimating the Upper Ice Shell Temperature Gradient by Rayleigh Wave Dispersion

It may be possible to estimate the temperature gradient in the upper thermal boundary layer of the ice shell by measuring dispersion of the Rayleigh wave. As noted earlier, the Rayleigh wave is a special kind of surface wave that propagates as a trapped wave on the boundary between the vacuum and the elastic medium. Since

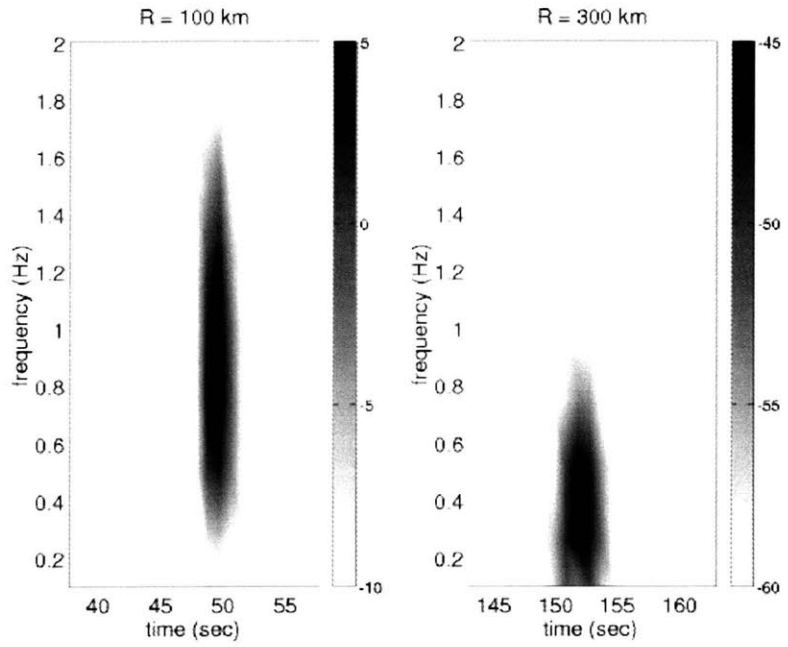

Figure 4-26: Spectrograms of the Rayleigh wave for the 20km rigid ice shell model. No prominent dispersion is observed in the spectrogram.

it's propagation speed is slower than the shear speed in ice, it cannot propagate downward but rather decays exponentially with depth as an "evanescent wave" in the ice. This decay is often referred to as an evanescent tail that reaches down into the elastic medium. Since the length of evanescent tail is dependent on frequency, different frequency components of the Rayleigh wave will probe different depths. The Rayleigh waves at different frequencies, probing different depths, will then disperse in time if the shear speed of the ice changes with depth. A strong sound speed gradient in the ice shell, as in the convective ice shell model, will then force Rayleigh waves to disperse over time. Measurement of this dispersion may reveal the internal sound speed profile of the ice shell, from which the temperature profile may be inferred. Contrary to the problems encountered with Love waves, a broader source spectrum gives better resolution in measuring the dispersion of Rayleigh waves since the Rayleigh wave is a single wave type rather than a set of propagating modes.

Figures 4-26 and 4-27 show the arrival structure of the Rayleigh wave from a Big Bang source as a function of time and frequency for two distinct ranges in the

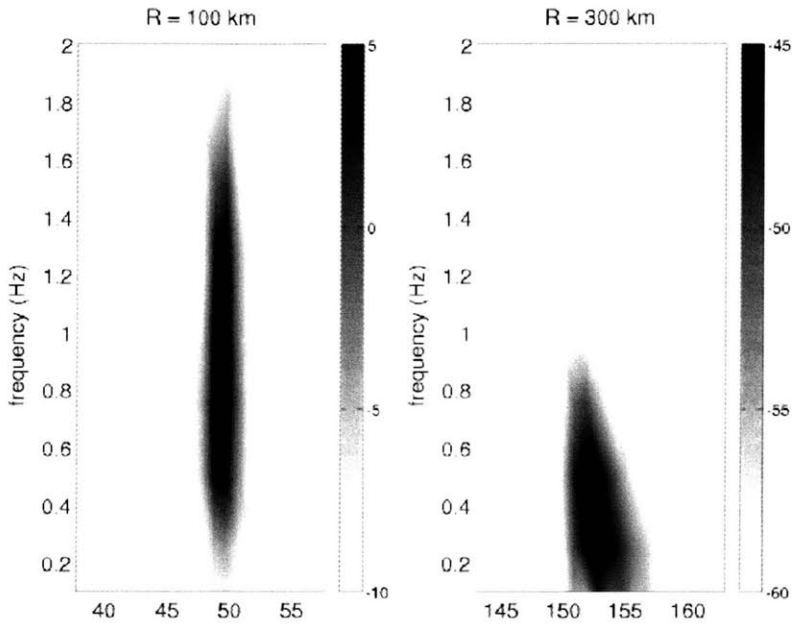

Figure 4-27: Spectrograms of the Rayleigh wave for the 20km convective ice shell model. Dispersion in the low frequency components are observed as a slower arrival in the time series.

20km rigid and convective ice shell models. If there is no prominent change in the sound speed in the ice shell, all the different frequency components of the Rayleigh wave travel with the same speed, making a straight vertical line in the spectrogram as in Fig. 4-26. If there is a very strong sound speed gradient near the surface, however, as expected in the convective ice shell model, the longer evanescent tails of the low frequency components begin to be affected by the partial-melt regime, making the low frequency components propagate more slowly than the high frequency components. This can be observed in Fig. 4-27, where there is a 0.2-km/s variation in shear wave speed across the upper thermal boundary layer in the convective ice shell model. This leads to the roughly 5 second travel time difference observed between the Rayleigh wave's high and low frequency components at 300-km, indicating that the temperature gradient of the upper thermal boundary layer may be inferred by Rayleigh wave dispersion measurements.

The actual measurement of Rayleigh wave dispersion has some similar practical

constraints as those encountered for the Love wave measurement. The range from source to receiver and original energy spectrum of the source must be known. These, however, may be reasonably estimated by measuring the direct P wave arrival time and energy spectrum, as is necessary in echo sounding. To sample deep into the ice shell, very long wavelengths and consequently very low frequency components must be strongly excited. These require large cracking events. Frequency components less than 0.5Hz, for example, would need to be strongly excited for the 20km ice shell model. Also, since the sound speed in ice does not change drastically with temperature, as shown in Appendix B, long-range propagation, well in excess of 100 km, is necessary to clearly resolve the dispersion. For example, a 0.2-km/s variation in the shear wave speed across the upper thermal boundary layer in the convective ice shell model will lead to an approximately 5 second travel time difference between the high and low frequency components at 300 km. So as in both the echo sounding and Love wave techniques, extremely energetic events are required, and as in the Love wave technique the source of opportunity must be very distant for the Rayleigh wave dispersion technique to be feasible.

4.7 Summary

A method to probe the interior structure of Europa by echo-sounding with natural sources of opportunity is presented. To evaluate its feasibility, estimates are made of (1) the frequency of occurrence and energy spectra expected of typical Europan seismo-acoustic sources, (2) the travel time and amplitude structure of arrivals from these sources at a distant receiver after propagation through Europa's ice and potential water layers, and (3) ambient noise on Europa.

We find that a single passive tri-axial geophone planted on Europa's surface should make it possible to estimate the thickness of Europa's ice shell as well as the depth of a potential subsurface ocean by exploiting natural ice cracking events and impactors as seismo-acoustic sources of opportunity. These natural sources are expected to radiate low frequency seismo-acoustic waves that are well suited for efficient propagation deep into the interior of Europa. Our analysis shows that "Big Bang" source events are likely to occur within the period of a landing mission that have returns from the bases of the ice and ocean layers of sufficient magnitude to stand above the accumulated ambient noise of less energetic but more frequent surficial cracking events.

Chapter 5

Mechanics of tidally driven fractures in Europa's ice shell

Among Europa's surface features, cycloidal cracks are probably the most important for proving the existence of a subsurface liquid ocean. This is because (1) there is strong evidence that they are caused by tidally induced stress [47, 56], and (2) this stress likely only approaches the ice failure strength if an ocean is present.

There are a number of outstanding issues, however, in quantitatively explaining cycloidal cracks. First, current estimates of the pure diurnal tidal stress necessary to cause cycloidal cracks even in the presence of an ocean range between 40 to 120 kPa based on kinematic fits to observed cycloid geometry [56, 57, 28]. This range is well below the typical stress known to cause tensile failure in natural terrestrial ice [138, 136]. Second, models of ridge formation suggest that cycloidal cracks penetrate through the entire brittle-ice layer [56, 104, 43], but current models limit the depth of tidally induced surface cracks to be less than 100 m even in the presence of a Europan ocean [27, 56, 74, 43]. These penetration depths are more than an order of magnitude shallower than even the minimum current estimates of Europa's brittle layer thickness, which are in excess of 1 km [99, 47, 104, 31]. Third, the 3-km/h crack propagation speed determined by [56] is three orders of magnitude lower than the roughly 2-km/s speed at which cracks are known to propagate in ice [38].

The purpose of this paper is to quantitatively address these issues in a unified

manner. To do this, a fracture mechanics model is developed for the initiation and propagation of a crack through an ice layer of finite thickness in the presence of gravitational overburden and porosity. It is found that surface cracks can penetrate through Europa's entire brittle layer, roughly a few kilometers, at the tidal stress thresholds found to be consistent with observed cycloid geometry in current kinematic models, if a liquid ocean is present under Europa's ice shell. Such penetration depths are found to be extremely implausible in the absence of a liquid ocean because tidal stress levels are too low.

For crack initiation, it is shown that Europa's ice shell may be highly porous and salt-rich by use of terrestrial models and measurements [138, 136] as well as Earth-based radar-wave backscattering data from Europa [12]. This implies that the strength of Europa's outer ice shell may be sufficiently low to make the crack initiation strengths of 40 to 220 kPa arrived at by [56, 57] and [28] highly plausible, even though they are much lower than those typically measured for terrestrial ice.

For crack propagation, a model is developed for the stress intensity factor at a crack tip in an ice shell with finite thickness, gravitational overburden, and depth-dependent porosity. This leads to the conclusion that cycloids are generated as a sequence of discrete and near instantaneous fracture events, each of which penetrates through the entire brittle layer with horizontal length on the order of the brittle layer thickness. This mechanism yields an apparent propagation speed that is consistent with the 3 km/h crack propagation speed necessary to generate cycloids in current kinematic models [56, 57, 41]. Total penetration would also provide paths for the emergence of water or ductile ice to form the observed ridges. Another implication of this model is that the level of seismic activity should be higher by orders of magnitude in the presence rather than absence of an ocean.

Both terrestrial sea ice measurements and radar backscattering data from Europa strongly suggest that Europa's ice is highly porous and the size of vacuous pores or salt pockets is on the order of a millimeter. Since the latter is at least three orders of magnitude smaller than the ice-penetrating radar wavelength, our calculations show that porosity-induced scattering should not be significant. This differs substantially

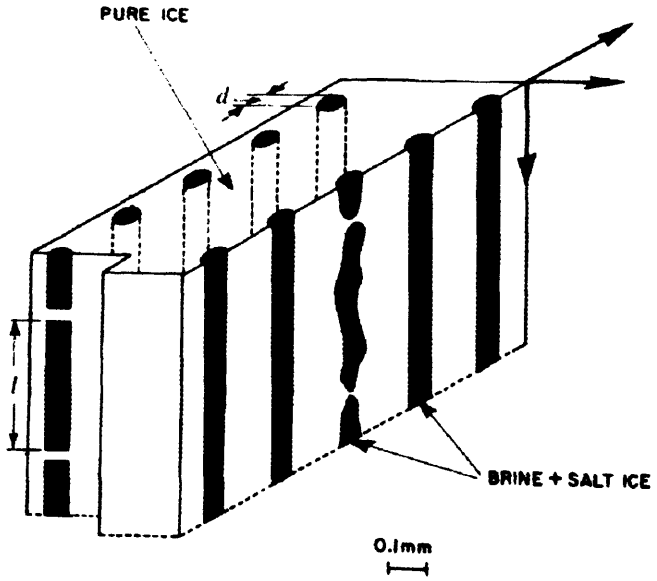

Figure 5-1: The geometry of brine pockets in natural terrestrial sea ice (Adapted from [138]). Brine pockets generate cylindrical cavities with diameter d and length l.

from what has been predicted by [33], who arbitrarily assumed meter-scale spherical pores. Besides pores, fractures might constitute another class of void scatterers. Fractures, however, should only cause noticeable scattering if the surface normal of the fault exceeds the critical angle, typically 32° for electro-magnetic waves incident from ice to vacuum and fracture opening widths are at least of radar-wavelength scale, which will likely be on the order of 1 m [23, 14]. It is not yet clear if plausible mechanisms exist for maintaining such critically large opening widths.

5.1 Fracture initiation based on ice porosity

In current kinematic models for cycloidal cracks, the crack initiation threshold has been found to range from 40 to 120 kPa in the absence of stress accumulated by nonsynchronous rotation, if an ocean is present [47, 56, 57, 48, 8, 28]. The typical strength of naturally occurring terrestrial ice, however, is roughly 500 kPa [138, 136], which is roughly an order of magnitude larger than these crack initiation thresholds. Europa's ice shell would then require significantly lower strength for the current

Table 5.1: Ice porosity of Galilean satellites estimated using 3.5-cm and 13-cm radar-wave observations (Modified from Ref. [12]).

Wavelength	Europa	Ganymede	Callisto
3.5 cm	33 %	2 %	2 %
13 cm	94 %	5 %	7 %

kinematic cycloidal crack models to be feasible.

This discrepancy can potentially be explained by examining the relationship between porosity and ice strength. The existence of pores and brine pockets in natural terrestrial sea ice has been known to decrease its strength significantly. Brine pockets generate cylindrical cavities in naturally grown ice, as shown in Fig. 5-1. Average values of the diameter d and the length l of the cylindrical pores in terrestrial ice are 0.07 mm and 0.23 mm, respectively [3]. These cavities lead to a local magnification of stress near the cavities and a consequent decrease in the overall strength of the ice. Weeks and Assur [138] have derived a semi-empirical relationship for the dependence of ice strength on porosity or brine content based on Arctic glacier and sea ice data assuming cylindrical cavities,

$$\sigma_f = \begin{cases} 6.86 \times 10^5 \left[1 - \left(\frac{v_b}{0.202}\right)^{1/2}\right] \text{ Pa} & \text{for } \sqrt{v_b} < 0.35, \\ 1.96 \times 10^5 \text{ Pa} & \text{for } \sqrt{v_b} > 0.35, \end{cases} \tag{5.1}$$

where σ_f is the tensile strength of ice, and the dimensionless v_b is the fraction of volume occupied by pores, or the porosity. Vaudrey [136] has derived a similar semi-empirical relationship independently from Antarctic glacier data, and has suggested that

$$\sigma_f = 9.59 \times 10^5 \left[1 - \left(\frac{v_b}{0.249}\right)^{1/2}\right] \text{ Pa}. \tag{5.2}$$

These curves make it possible to quantitatively estimate the porosity necessary to obtain a given tensile strength. Given this, it may be determined if porosities corresponding to the crack initiation thresholds given in current kinematic models fall within a plausible range.

One may independently estimate the porosity of Europa's outer ice shell from Earth-based radar backscattering data. Black *et al.* [12] have investigated the effect of porosity on the measured radar reflectivity from Europa assuming spherical pores. The porosity of ice in their model can be obtained using

$$v_b = \int_{r_o}^{r_m} \frac{4\pi}{3} K r^{3-\beta}\, dr, \tag{5.3}$$

where r is the radius of the pores, and r_o and r_m are the minimum and the maximum radius of the pores. The constant K in Eq. 5.3 is given as

$$K = \frac{\tau_o}{l_i^o\,[1 - e^{-\gamma}]} \left[\int_{r_o}^{r_m} r^{-\beta} C(r)\, dr\right]^{-1}. \tag{5.4}$$

The physical explanations and the best-fit values of the parameters β, τ_o, γ and l_i^o in Eqs. 5.3 and 5.4 are given in Table II and IV of Ref. [12]. The mean radius of the pores obtained from their best-fit values is 0.16 mm, which shows good agreement with the typical pore size in terrestrial ice previously discussed. Since most of the pores in their model are much smaller than the wavelengths of Earth-based radar, the detailed geometry of the pores is insignificant in the scattering model.

The resulting porosity estimates v_b for three icy satellites of Jupiter are shown in Table 5.1 for only the 3.5 cm and 13 cm radar observations since backscattering at 70 cm did not have sufficient signal-to-noise ratio [13] to be used for porosity estimation. It can be seen from Table 5.1 that Europa's porosity estimates are both variable and high compared to terrestrial levels, while those of Ganymede and Callisto are significantly lower and well in the terrestrial range.

The semi-empirical models of Refs. [138] and [136], shown in Fig. 5-2, begin with high tensile strength at the lowest porosities found in Antarctic and Arctic glaciers. Tensile strength monotonically decreases with increasing porosity until both models converge at the relatively high terrestrial porosities found in Arctic sea ice. Europa's porosity, as estimated from Earth-based radar backscatter data, exceeds the maximum levels found in natural terrestrial ice. The porosities expected for Ganymede and Callisto from similar radar backscatter data put them in the porosity range of

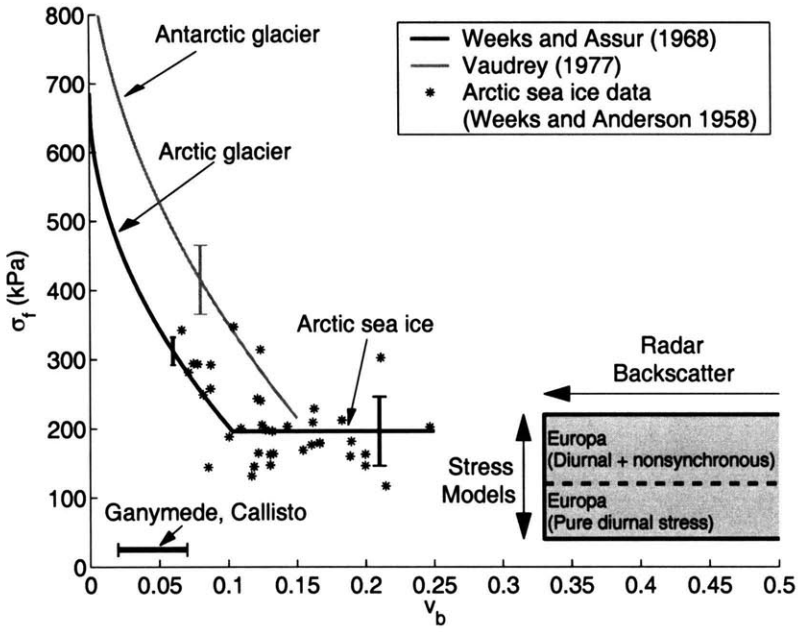

Figure 5-2: Tensile strength σ_f of natural terrestrial ice as a function of porosity v_b. The shaded regime spans Europa's likely porosity range based on radar backscatter (Table 5.1) and the stress threshold range for cycloid formation from current kinematic models [57, 28]. The likely porosity (Table 5.1) and the stress ranges on Ganymede and Callisto [92] are also shown. The strength of clear lake ice typically varies from 600 to 750 kPa [139].

terrestrial glaciers.

The terrestrial ice strength curves of Fig. 5-2 show that the mean tensile strength of natural ice reaches a minimum value of 196 ± 50 kPa in the range $0.15 \leq v_b \leq 0.25$. No data exists beyond $v_b > 0.25$. A single extreme data point at 90 kPa for $v_b = 0.24$ (Fig. 9 of Ref. [122]) indicates that occasionally lower strengths do occur. This may be used as a lower bound on tensile strengths for porosity $v_b \leq 0.25$. The maximum 220 kPa combined tidal and nonsynchronous stress threshold for cycloidal crack formation [28] is consistent with crack initiation on Europa even if its porosity values fall within or exceed the upper range of those measured on Earth. Given this same range of porosities and the 90 kPa lower bound for tensile strength, it is possible that cracks occasionally initiate on Europa even under pure diurnal tidal forcing, with corresponding stress thresholds of 40 to 120 kPa [56, 28]. It is reasonable

to expect that as porosity increases above the values measured for terrestrial ice, the corresponding tensile strength will decrease. In this case, crack initiation on Europa becomes even more likely for the 40 to 220 kPa range of stress thresholds currently expected for cycloid formation. The upper limit allows for the addition of some nonsynchronous rotation stress [47, 28]. In the absence of an ocean all tidally induced stress levels decrease by an order of magnitude, making it far less likely for cracks to initiate on Europa's surface.

The striking differences in surface geomorphology between Jupiter's three icy moons may be due to the differences in ice porosity. Tidal deformation and consequently tidal stress levels are roughly an order of magnitude lower on Ganymede and Callisto than on Europa [92], as shown in Fig. 5-2. Given this and the fact that estimates from Earth-based radar backscattering data find the porosities of their outer shells to be much lower than Europa's, it seems implausible for tidally induced surface cracks to form regularly even if they have subsurface oceans. This can be seen in Fig. 5-2 where the failure stresses are at least an order of magnitude higher than the applied stresses on Ganymede and Callisto. This is consistent with the observation of no cycloidal surface fractures on Callisto [45] or Ganymede [107].

Pore closure due to gravitational overburden may lead to increasing ice strength with depth on Europa. The porosity of the ice shell versus depth can be estimated using the methods of Ref. [97], as shown in Fig. 5-3, where it is seen that high porosity may persist in the upper half of the brittle layer and approaches zero in the lower half of the layer. Together with Fig. 5-2, this indicates that tidally driven cracks on Europa are much more likely to initiate from the weaker outer surface of the ice shell rather than from the stronger base of the shell. Bottom-initiated cracks are also unlikely because of the high gravitational overburden pressure and ductility of warm ice at the base [27]. This is also consistent with terrestrial observation by Neave and Savage [95] that, among more than 1000 ice cracking event samples in a roughly 300 m thick glacier, none originated at depths greater than 60 m.

One may then conclude that the combination of semi-empirical ice strength models and porosity estimates based on radar backscatter data from Europa suggests

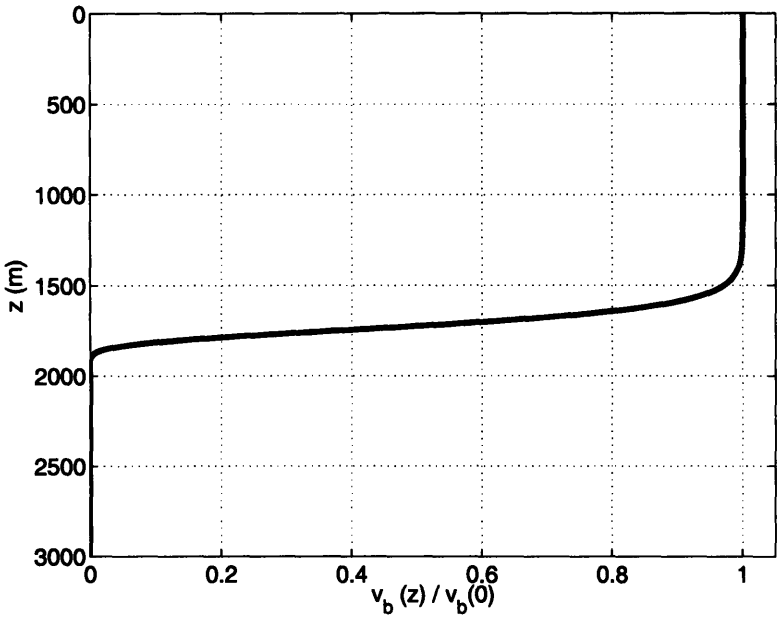

Figure 5-3: Porosity profile versus depth z normalized by the surface porosity $v_b(0)$. The thickness of the brittle layer is assumed to be 3 km (Adapted from Ref. [97]).

that cracks should at least occasionally initiate on Europa's surface under pure tidal stress for the thresholds given in current kinematic models for cycloids. Initiation would be more likely for the thresholds obtained under a combination of tidal and nonsynchronous stress [28], or in concert with additional isotropic stress [96]. Similar evidence suggests that it is unlikely for tidally induced surface cracks to form regularly on Ganymede and Callisto.

5.2 Fracture propagation

In the previous section, it was found that cracks can initiate on Europa's surface under currently hypothesized tensile stress levels, and with much higher probability if there is a liquid ocean present below its ice shell. Here we show that surface generated cracks on Europa may penetrate through the upper brittle layer of ice if the brittle layer is a few kilometers thick and if it is effectively decoupled from water or near-inviscid ductile ice below. We then argue that any given cycloidal arc on Europa's surface

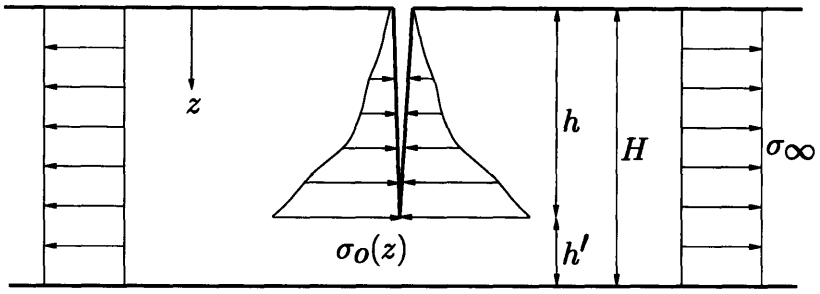

Figure 5-4: Stresses applied to a surface crack with depth h in a brittle ice layer of thickness H, where σ_∞ is the local far-field tensile stress. The gravitational overburden stress $\sigma_o(z)$ on the crack walls is given in Eq. F.1.

was likely formed as a sequence of concatenated cracks that penetrated through the entire brittle layer, so that the crack propagation speed determined by Refs. [56, 57] must then be an apparent speed.

5.2.1 Stress intensity factor as a function of crack depth in a finite ice shell

When a tensile stress field is applied to an elastic medium, cracks develop to release stress locally if the applied stress exceeds the medium's failure strength in tension. The direction of crack propagation is normal to the direction of applied tensile stress. On Europa, the elastic medium is also under the effect of gravitational overburden which exerts a linearly increasing compressive stress along the depth of the medium. This overburden stress suppresses crack propagation in the depth direction [27, 56, 43].

The maximum penetration depth h of a surface-generated crack under the combination of a far-field tensile stress σ_∞ and a gravitational overburden compressive stress σ_o occurs roughly where these two opposing stresses cancel. A schematic diagram of crack geometry and stress distribution is shown in Fig. 5-4. The entire load from tensile stress σ_∞ is concentrated in the unfractured medium $h' = H - h$ below the crack since the fractured medium above cannot support tension. Here H is the thickness of either the entire ice shell which would be thin and brittle [99, 47], or the upper brittle layer that is effectively decoupled from the ductile layer below [104, 31].

The tensile stress at the crack tip then increases nonlinearly as the crack grows in depth toward the lower boundary of the medium. The overburden compressive stress at the crack tip increases linearly as a function of h since the gravity force is a body force acting locally on the surface exposed by the fracture. A difference in depth dependence between tensile stress from far-field tidal forcing and compressive stress from overburden at the crack tip in the process of crack growth has been suggested in Ref. [75] and implied in Ref. [116].

The stress intensity factor $K_{I,t}$ at the crack tip in an ice sheet due to far-field tensile stress σ_∞ is [6, 128]

$$K_{I,t}(\sigma_\infty, H, h) = \sigma_\infty \sqrt{\pi h}\, F\left(\frac{h}{H}\right), \tag{5.5}$$

where

$$F\left(\frac{h}{H}\right) = \sqrt{\frac{2H}{\pi h}\tan\frac{\pi h}{2H}}\ \frac{0.752 + 2.02\left(\frac{h}{H}\right) + 0.37\left(1 - \sin\frac{\pi h}{2H}\right)^3}{\cos\frac{\pi h}{2H}} \tag{5.6}$$

is a nonlinear function of the ratio of crack depth to the ice shell thickness h/H, with geometry shown in Fig. 5-4. The stress intensity factor $K_{I,t}$ approaches infinity as h/H approaches 1, as shown in Eqs. 5.5 and 5.6, due to the concentration of far-field tensile stress in the regime h' below the crack. As h/H approaches 0, Eq. 5.5 approaches the stress intensity factor obtained under the assumption that Europa's ice shell behaves as an infinite halfspace [143, 125, 27],

$$K_{I,t}(\sigma_\infty, h) \simeq 1.122\sigma_\infty \sqrt{\pi h}. \tag{5.7}$$

The stress intensify factor $K_{I,o}$ due to compressive stress from gravitational overburden is approximated as [143, 53, 125]

$$\begin{aligned} K_{I,o}(h, h_p, v_b) \simeq\ & -0.683\rho_i(1 - v_b)gh\sqrt{\pi h} \\ & -u(h - h_p)\frac{2h\sqrt{h}}{\sqrt{\pi}}\rho_i v_b g \int_{\mathrm{asin}(h_p/h)}^{\pi/2} \left(\sin\theta - \frac{h_p}{h}\right)\left[1.3 - 0.3\left(\sin\theta\right)^{5/4}\right] d\theta, \end{aligned} \tag{5.8}$$

where ice density ρ_i is 920 kg/m^3, gravitational acceleration g is 1.32 m/sec^2, and

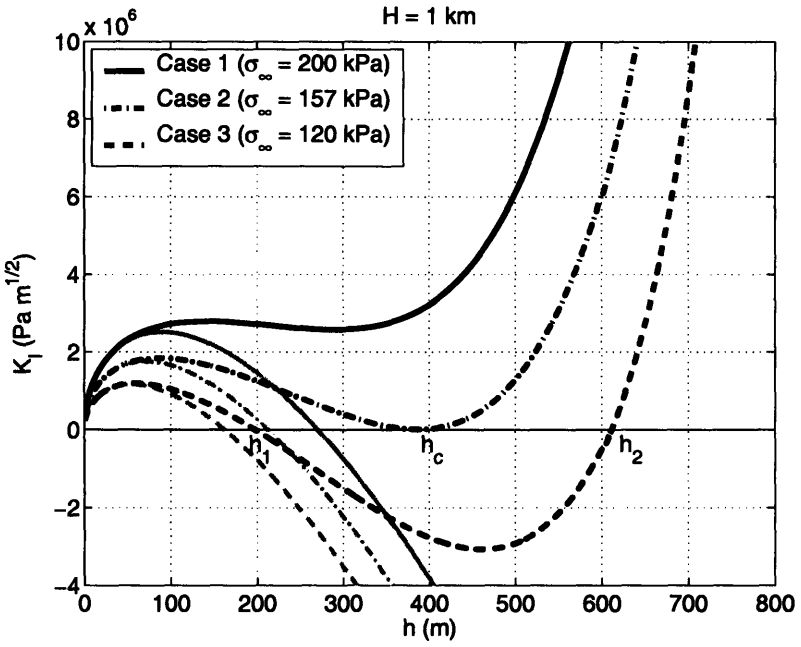

Figure 5-5: The total stress intensity factor K_I for $H = 1$ km. Cases 1, 2, and 3 represent the no solution, 1 solution, and 2 solution cases in Eq. 5.9. The gray lines show the total stress intensity factors for corresponding cases when an infinite halfspace model is employed. The porosity of ice v_b is assumed to be zero.

$u(h)$ is a unit step function. The compression from overburden acts locally on the crack with effectively no influence from the lower boundary. We assume that porosity persists up to the depth h_p from the surface, where the depth of the porous layer h_p is taken to be roughly one half the thickness of the brittle layer based on the model of Ref. [97], as shown in Fig. 5-3.

5.2.2 Crack penetration depth

A surface-generated crack stops propagating at the depth where the stress intensity factor due to tension is balanced by the stress intensity factor due to overburden stress,

$$K_I(\sigma_\infty, H, h, h_p, v_b) = K_{I,t}(\sigma_\infty, H, h) + K_{I,o}(h, h_p, v_b) = 0. \tag{5.9}$$

If K_I is greater than zero, the crack propagates in depth to release the stress at the crack tip until K_I reaches zero. A negative stress intensity factor only has physical

meaning in the sense that the crack cannot reach a depth where $K_I < 0$ since compression due to gravitational overburden overwhelms far-field tension at that depth. To find the depth of a tidally driven crack on Europa, Eq. 5.9 needs to be solved for h given H and σ_∞.

The stress intensity factor as a function of crack penetration depth h for an $H =$ 1 km layer and a halfspace is illustrated in Fig. 5-5. If the fracture process is modeled under the assumption that the ice shell behaves as a halfspace, only a single solution is obtained. Crack penetration is then always limited to very shallow depths of roughly 200 m for pure diurnal tensile stress level of roughly 40 to 120 kPa [56, 28].

By including the finite thickness of the brittle ice layer in the fracture modeling, three possible forms of outcome must be considered, as illustrated in Fig. 5-5. In the first case, there is no mathematical solution to Eq. 5.9. This occurs when the far-field tensile stress σ_∞ is large enough that K_I in Eq. 5.9 is always positive for $0 \leq h \leq H$. A surface-generated crack then penetrates rapidly through the entire brittle ice layer because the stress intensity factor at the crack tip always exceeds zero regardless of the crack depth h. In the second case, only one solution to Eq. 5.9 occurs. This occurs at critical depth $h = h_c$, but the solution is unstable. Given a minor overshoot of the crack tip beyond h_c [38], the stress intensity factor will become positive, where total penetration through the brittle ice layer will again occur. The far-field stress for the one solution case is the minimum required for total penetration through the entire layer H. This stress, defined as the critical stress σ_c, is a function of the layer thickness H. In the third case, the far-field stress is less than σ_c, and Eq. 5.9 has two solutions h_1 and h_2, where $0 < h_1 < h_2 < H$, as shown in Fig. 5-5. Given the exact deterministic equations 5.5 and 5.8, the crack would only reach the shallower depth h_1 and stop. The shallower depth is similar to what one would obtain in the halfspace formulation. It is interesting that the depth scale of this shallower solution, given tidal forcing in the presence of an ocean, is similar to the 100-m-scale topographic variations on Europa's surface. It is also interesting that the expected pattern of stress relief due to these shallower surface cracks from tidal forcing is similar to the striated structure observed in many areas on Europa's surface.

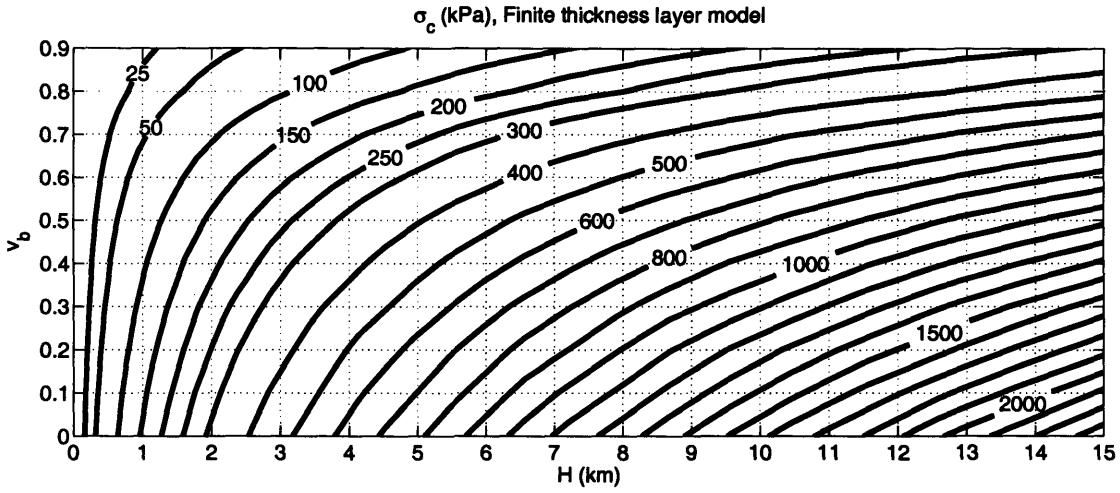

Figure 5-6: The critical stress σ_c for total penetration through the brittle layer of thickness H and porosity v_b. The thickness of the porous layer h_p in Eq. 5.8 is assumed to be $H/2$ based on Ref. [97] and Fig. 5-3.

Simple order of magnitude calculations of crack penetration depths in a finite-thickness ice shell without involving the stress intensity factor theory are given in Appendix E. It can be seen in Appendix E that the solusions obtained from the order of magnitude calculations also show the same behavior in that there are three possible cases of solutions and the critical crack depth occurs at roughly half the ice shell thickness.

The stress required for a crack to penetrate through the entire brittle layer H is shown in Fig. 5-6 as a function of ice porosity v_b and layer thickness H. We consider reasonable values for Europa's near-surface porosity to be within the 0.3 to 0.5 range. Current estimates of the far-field tidal stress necessary to match the geometry of observed cycloidal cracks range from 40 kPa for diurnal stress only [56] to 220 kPa for diurnal combined with nonsynchronous rotation stress [28] if Europa possesses a liquid subsurface ocean. Within these bounds, surface generated cracks will penetrate through the entire brittle layer if its thickness does not exceed roughly 3 km. This limit on conductive layer thickness is consistent with those obtained based on thermal convection models [31]. Nonsynchronous stresses might be on the order of 500 to 1000 kPa, and could then lead to penetration through a significantly thicker brittle layer, on the order of 6 to 13 km. The resulting fractures, however, are not

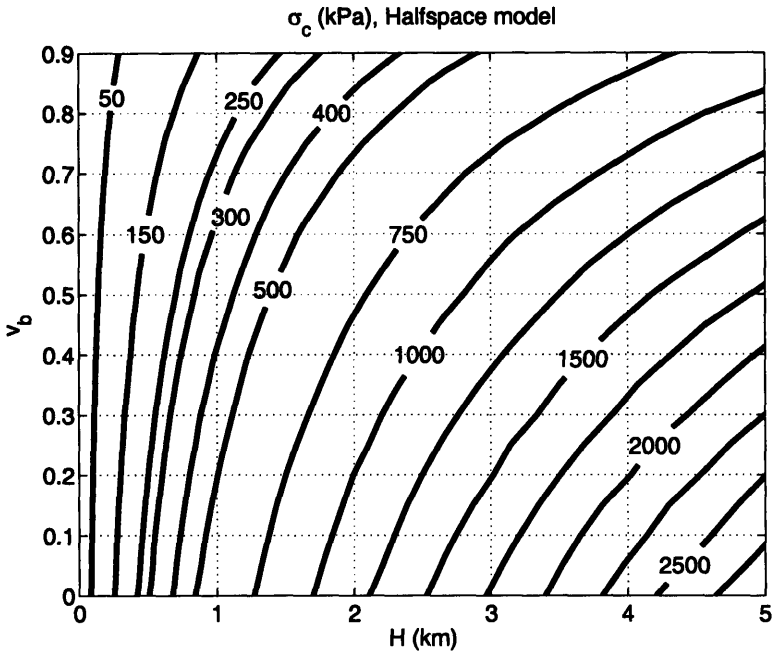

Figure 5-7: The same as Fig. 5-6, but when Europa's brittle ice layer is assumed to be an infinite halfspace.

expected to be cycloidal because the total stress is dominated by the nonsynchronous stress components rather than the diurnal components [55, 28].

If the halfspace fracture model is employed, crack penetration depths are roughly a factor of 4 to 5 smaller within the same porosity and stress bounds, as shown in Fig. 5-7. These depths would not be consistent with cycloidal crack penetration through the entire brittle layer, based on most current estimates of its thickness.

From this fracture model and our current knowledge of the tidally induced stresses on Europa, we can draw the conclusion that the brittle layer should be less than a few kilometers in thickness, and should be mechanically decoupled by water or weak convective ice below. We can also draw the conclusion that Europa should likely have an ocean of liquid water below its ice sheet. This can be inferred from Fig. 5-6, where the maximum outer layer thicknesses corresponding to full crack penetration would have to be less than an unreasonably small 100 m to fracture in response to the order of magnitude smaller tidal stress expected if Europa has no ocean [91]. Brittle layer thicknesses of less than 100 m are highly implausible because they do not even exceed

the standard deviation of Europa's surface elevation [108, 37, 97].

5.2.3 Horizontal region of stress relief

The minimum length of a crack and region of stress relief in response to tension is on the order of the crack depth h when a surface crack develops in an elastic halfspace [98, 51]. If total penetration of a crack through the medium occurs, however, the region of stress relief is no longer limited by the crack depth, but is roughly proportional to the length of the crack [129]. So as a crack extends in length, the region of stress relief, within which other long and deep cracks do not form, increases proportionally.

The minimum length of a crack that penetrates through the entire brittle layer would then be on the order of 1 to 3 km for pure diurnal tidal stress based on the findings of Sec. 5.2.2. Suppose, from a fully penetrating crack's initiation point up to some length at least one crack depth away in range, tidally induced stress exceeds the mean critical stress σ_c by an amount much larger than the critical stress standard deviation. The probability that the crack will exceed this length should then decrease rapidly because there is insufficient stress to maintain its propagation [98].

We believe that this is very likely the situation on Europa because (1) the spatial rate of change of tidal stress on Europa's surface is on the order of 1 kPa over a kilometer scale [28], and (2) the corresponding stress change over the minimum length of a fully penetrating crack, roughly 1 to 3 km, is many times larger than the expected critical stress standard deviation, as shown in Appendix F.

5.2.4 Discrete fracture model for cycloidal crack propagation

Stress relief by fracture is nearly instantaneous because cracks in ice are expected to propagate at the 2-km/s Rayleigh wave speed, which is approximately 90% of the shear wave speed [38, 2]. Since this is three orders of magnitude larger than the roughly 3 km/h crack propagation speed [56, 41], an additional physical mechanism must be considered to explain cycloid formation.

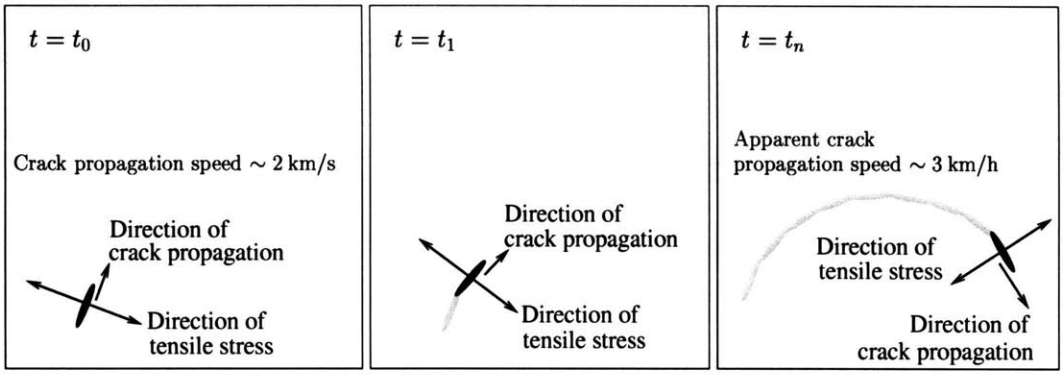

Figure 5-8: Cycloidal crack formation under a temporally and spatially varying tensile stress field. A single crack penetrates through the entire brittle layer at time $t = t_0$ normal to the direction of maximum tensile stress over a fraction of a cycloidal arc. The crack forms "instantaneously" at roughly the Rayleigh speed. At a later time t_1, the fully penetrating crack reinitiates "instantaneously" in a slightly different direction when the threshold stress advects to the crack's former end tip. As the process continues, a series of discrete, temporally discontinuous, concatenated fractures through the entire brittle layer will form a cycloidal arc propagating at an *apparent* speed that is orders of magnitude slower than the Rayleigh speed, where t_n is the time of the n^{th} discrete fracture. The cycloidal arc ceases to propagate when Europa moves so far from pericenter that the applied tensile stress tensor falls below the critical stress.

The stress field due to tidal forcing propagates with a speed that is orders of magnitude lower than the crack propagation speed since it is synchronized with the tidal bulge that slowly moves across Europa's surface. A crack that has penetrated through the entire brittle layer by the model of Sec. 5.2.2 and Sec. 5.2.3 will not continue to propagate horizontally until the applied tidal stress field advected to the end tip of the crack reaches the critical stress.

Assuming the original crack extended in a direction normal to the direction of the maximum tensile principal stress at its space-time initiation point, the crack will extend in a new normal direction when it reinitiates at its former end tip because the direction of the maximum principal stress changes in time and space as a result of tidal forcing [47, 28]. This reinitiated crack will again penetrate the entire brittle layer and propagate in range a distance roughly equal to the brittle layer thickness, wait for the threshold stress to move to the new end tip, and start the process all over. As

the process continues, the series of discrete, temporally discontinuous, concatenated fractures through the entire brittle layer will form a cycloidal arc propagating at an *apparent* speed that is orders of magnitude slower than the Rayleigh speed. This *apparent* speed equals the rate of change of the tidally induced critical stress for total penetration of a crack through the brittle layer, varies with time and space, but should be within the range of 2 to 5 km/h found in the fits of Refs. [56, 57, 8, 48, 41] for pure diurnal stresses. A schematic diagram of cycloidal crack formation in this scenario is shown in Fig. 5-8. The use of these fitted speeds may not be practical for predicting new cycloids if the actual stress in the ice somehow begins to exceed the critical stress over an extended region. Fractures could then rapidly propagate near the Rayleigh speed across the extended region.

As noted in Sec. 5.2.3, stress will be relieved near the cycloidal arc over a proportionally larger region as it progresses. This will suppress development of other tidally induced cracks within a radius equaling roughly an arc length. This is consistent with observed cycloidal geometries (Fig. 3 of Ref. [56]), where it can be seen that the distance between the observable cycloids is roughly the length of a cycloidal arc.

As discussed in Ref. [56], the cycloidal arc ends as Europa moves sufficiently far from pericenter. On the next day, a new tensile crack forms at this end, where stress concentration is largest, when the applied stress field again reaches the critical stress, σ_c. This initiates a new cycloidal arc linked to the end point of the previous one. Since the direction of the applied stress field changes drastically during the period of inactivity, the cycloid will exhibit a sharp cusp where the end of the old arc and the beginning of the new one meet.

Analogous observations have been made in terrestrial ice. Neave and Savage [95] have shown that a sequence of more than 20 consecutive 10-m long tensile fractures formed a several-hundred-meter long crevasse near the surface of an Arctic glacier. They have shown that the apparent propagation speed of the crevasse was 28 m/s, orders of magnitude smaller than the Rayleigh wave speed in ice. On Europa, a similar number of consecutive concatenated fractures form a cycloidal arc in our present model. Each discrete fracture in the cycloid penetrates through the entire

brittle layer at roughly the Rayleigh speed. For the expected roughly 1 to 3 km brittle layer thickness, the penetration depths of these tensile fractures are equivalent to those that lead to the break up of Antarctic ice shelves, after accounting for the difference between the gravitational constants of Earth and Europa. Since the maximum instantaneous opening width of any initial tensile fracture should be on the order of a centimeter, while that of a full cycloid should be on the order of a meter [129], it is unlikely for extensive secondary fracturing and normal faulting to occur immediately.

5.3 Surface seismic activity based on the fracture mechanics model

The fracture initiation and propagation model in Sec. 5.1 and Sec. 5.2 has significant implications for surface seismic measurements on Europa. The fracture initiation model in Sec. 5.1 implies that the level of seismic activity should be higher by orders of magnitude in the presence of an ocean. High correlation is expected between the level of seismic activity and the tidal period in the presence but not in the absence of an ocean. This is because (1) tidal stresses are probably far too low to induce cracks in the absence of an ocean, and (2) surface cracks should form regularly during the tidal cycle if an ocean is present.

The level of seismicity and the frequency spectrum of the ambient noise would also significantly change depending on whether a subsurface ocean is present on Europa. In the absence of a subsurface ocean, the tidal stress levels would decrease by an order of magnitude compared to the stress level in the presence of an ocean, and surface cracks would not initiate. Even if cracking events occur rarely, the crack depths would be limited by roughly 10 m due to low tidal stress level. The frequency the seismic events from these very shallow cracks would be relatively high, with center frequency at roughly 50 Hz.

In the presence of a subsurface ocean, however, many shallow surface cracks with

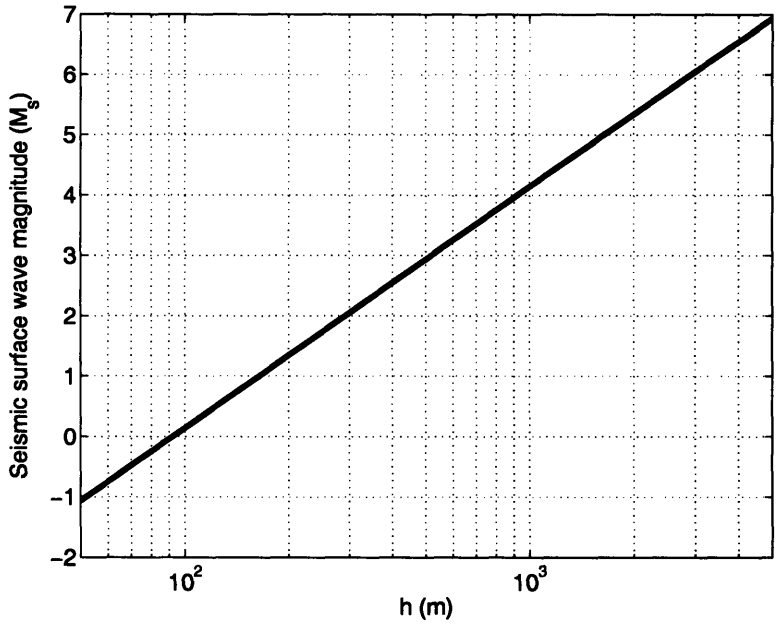

Figure 5-9: Seismic surface wave magnitude level M_s as a function of crack depth h. For roughly 200-m deep crack, $M_s \simeq 1$ and the velocity field measured by a geophone is roughly 1 μm/s for a geophone at 50 km from the crack. For roughly 2-km deep crack, $M_s \simeq 5$ and the velocity field is roughly 1 mm/s for a geophone at 50 km from the crack.

roughly 100 m depth would initiate, since the tidal stress level on Europa's surface would be sufficient to initiate the cracks. High ambient seismic noise level with roughly 1 μm/s rms velocity is then expected, and the ambient noise would be highly correlated with tidal period. The center frequency of the seismic noise would be lower by an order of magnitude in the presence of an ocean, since the crack depth increases by an order of magnitude. The center frequency of the noise would then be at roughly 5 Hz.

Besides roughly 100-m deep cracks, frequent "Big-Bang" cracks would occur if a subsurface ocean is present. The cracks associated with cycloids that fully penetrate the brittle layer should be at least 10^6 times more energetic than the shallow, roughly 100-m deep, surface cracks discussed in Sec. 5.2.2. The former should also have center frequencies an order of magnitude lower than those of the latter. These will improve the signal-to-noise ratio for the type of seismic profiling discussed in Chap. 4

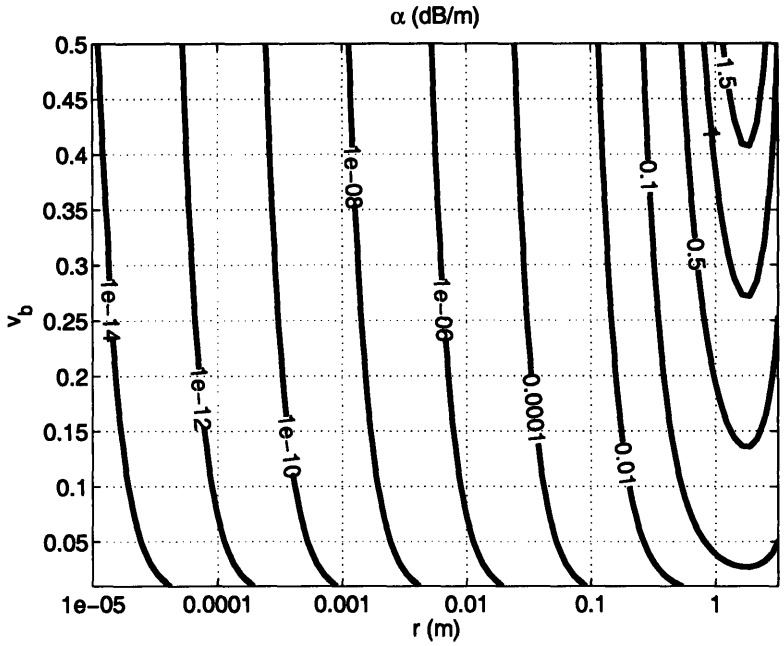

Figure 5-10: Attenuation coefficient α from Eq. 5.10 as a function of porosity v_b and pore radius r, using exact Mie theory for scattering cross section C.

if fully penetrating cracks are used as sources of opportunity. The seismic surface wave magnitude M_s is shown in Fig. 5-9 as a function of crack depth h, where it can be seen that M_s for a few kilometers deep cracks would be as large as 5. Since fully penetrating cracks are expected to occur on the order of once an hour for any given cycloid, the probability of unwanted overlap between different source signals and their multiple reflections is not high. Furthermore, the center frequencies of the seismic events from the "Big-Bang" cracks may enable us to constrain the thickness of the brittle ice layer, since the center frequency is inversely proportional to the crack depth, which is limited by the brittle layer thickness.

5.4 Ice-penetrating radar scattering loss

It has been proposed that Europa's potential subsurface ocean could be detected by ice-penetrating radar [23, 90]. The main challenge to radar sounding on Europa lies in accrued absorption due to warm or dirty ice [23, 90], and scattering due to ice surface

roughness and volume inhomogeneities [44, 14]. As shown in Sec. 5.1, Europa's ice shell may be highly porous, and as shown in Sec. 5.2, it may also be highly fractured. These inhomogeneities together with surface roughness will lead to scattering losses, the significance of which can be quantitatively assessed. Eluszkiewicz [33] considered scattering losses from porosity on Europa. He arbitrarily assumed a pore radius of roughly 1 m, which is orders of magnitude larger than both that estimated from Earth-based radar measurements by Black *et al.* [12], and terrestrial ice rheology models as noted in Sec. 5.1. We show that this overestimation of pore size leads to a corresponding overestimation of transmission loss due to scattering by orders of magnitude.

The attenuation coefficient α of the mean electro-magnetic field transmitted through a medium with inhomogeneities is [113, 135]

$$\alpha = (10 \log e)\, NC \quad \text{dB/m}, \tag{5.10}$$

where N is the expected number density of scatterers per volume, and C is the expected scattering cross section of a given inhomogeneity. The scattering optical depth in Eq. (1) of Ref. [33] is related to α in Eq. 5.10 by

$$\tau_s^{\text{void}} = \alpha L / (10 \log e) = \frac{v_b}{4\pi r^3/3} Q(r) \pi r^2 L, \tag{5.11}$$

if the scatterers are arbitrarily assumed to be spherical as in Ref. [33], where L is the thickness of the scattering layer.

In general, the scattering cross section for spherical scatterers needs to be calculated using Mie theory, as in Fig. 5-10. The expression for the scattering cross section, however, can be simplified using the Rayleigh scattering formula for $kr \ll 1$, or for $r \ll 0.5$ m at 50 MHz frequency,

$$C(r) \simeq \frac{8\pi}{3} k^4 r^6 \left| \frac{1 - n_i^2}{1 + 2n_i^2} \right|^2, \tag{5.12}$$

where k is the wavenumber of the electro-magnetic waves, and $n_i \simeq 1.8$ is the refrac-

tive index of ice [50]. Then Eq. 5.10 can be simplified to [113]

$$\alpha \simeq (20 \log e)\ v_b\, k^4\, r^3 \left| \frac{1 - n_i^2}{1 + 2n_i^2} \right|^2 \quad \text{dB/m}. \tag{5.13}$$

As can be seen from Eq. 5.13, attenuation by pores is linearly proportional to porosity v_b and the third power of pore radius r. Radar wave attenuation then increases dramatically with pore radius. The strong dependence of attenuation on scatterer size and distribution has long been demonstrated both theoretically and experimentally [132, 112]. Since the pore size on Europa is expected to be on the millimeter scale, as discussed in Sec. 5.1, the attenuation coefficient α is approximately 10^{-6} dB/km for $v_b = 0.3$, as shown in Fig. 5-10. Assuming a 20 km thick ice shell, and conservatively assuming constant porosity from the surface to the bottom of Europa's ice shell, the two-way attenuation loss due to pores is then a negligible 10^{-4} dB. Arbitrarily assuming the meter-scale pores of Ref. [33] rather than the expected millimeter-scale pores leads to an extremely high attenuation loss of 100 dB/km, which is not observed in terrestrial ice-penetrating radar where total attenuation losses are only a few dB/km for cold ice [50]. Even if pore closure by gravitational compaction is taken into account, Eluszkiewicz's meter-scale pore radius assumption still leads to an unprecedented 300 dB two-way transmission loss, for example, through a brittle layer of 3 km thickness. Since the loss for the expected millimeter scale pores is orders of magnitude less than the absorption loss due to warm ice or dirty ice [23], ice-penetrating radar detectability will likely be far more challenged by absorption loss, rather than scattering loss due to pores.

For scattering from rough surfaces and fractured ice, a somewhat more accurate and in this case perhaps more insightful approach than that given in Eq. 5.10 would be to consider two-way transmission through a series of M layers. This would have a loss in the mean field due to scattering of [113]

$$L_s = \sum_{j=0}^{1} \sum_{i=0}^{M} 20 \log(1 - m_i^j), \tag{5.14}$$

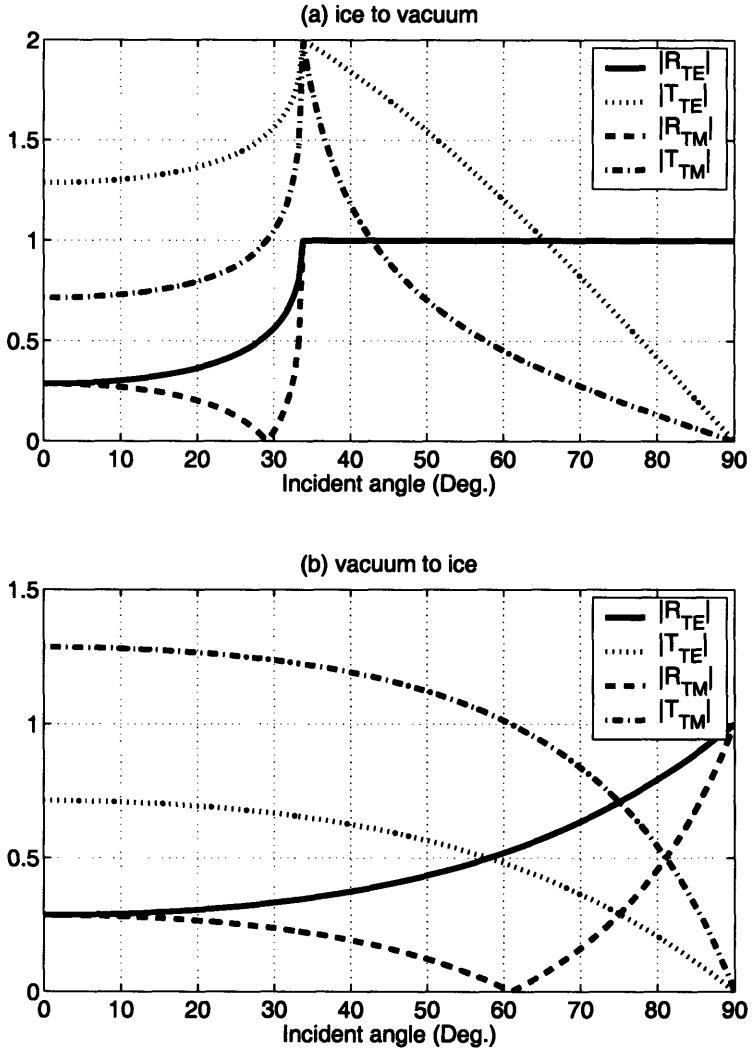

Figure 5-11: Magnitude of reflection and transmission coefficients for a transverse electric (R_{TE}, T_{TE}) and a transverse magnetic (R_{TM}, T_{TM}) plane wave as a function of incident angle [17, 67]. Propagation from (a) ice to vacuum interface, and (b) vacuum to ice interface. Total reflection occurs for incident angles greater than the 32° critical angle as can be seen in Fig. (a), where the magnitude of the reflection coefficients become unity.

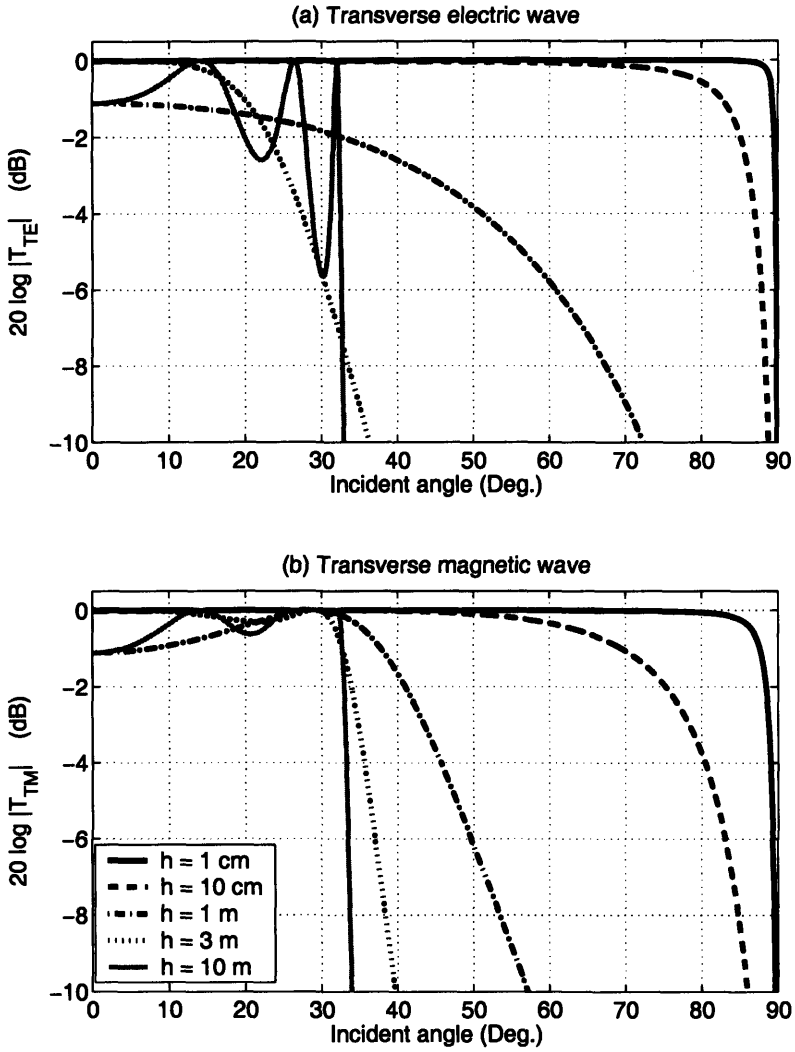

Figure 5-12: Transmission coefficient of a transverse electric and a transverse magnetic plane wave through ice with a vacuum layer of thickness h. Even when the incident angle is below the critical angle, an evanescent component "tunnels" through the vacuum layer if its thickness is much smaller than the wavelength. The wavelength of the ice-penetrating radar waves is approximately 3 m at 50 MHz operating frequency. Transmission loss in dB per fracture is the negative of $20 \log |T_{TE}|$ or $20 \log |T_{TM}|$.

where the effective transmission coefficient $1 - m_i^j$ for the i^{th} layer has negative reflection coefficient

$$m_i^j = \frac{N_i \, dz_i \, C_i^j}{2}, \tag{5.15}$$

and N_i is the number of scatterers per unit volume, dz_i is the layer thickness, and C_i^j is the expected scattering cross section for inhomogeneities in the i^{th} layer for a downward-directed wave ($j = 0$) and an upward-directed wave ($j = 1$).

Let us first consider a simple first-order estimate of the scattering loss from Europa's rough outer ice-vacuum boundary, the $i = 0$ layer. Assume that some fraction χ of the surface is inclined so that the angle between the local vertically directed incident plane wave and surface normal is greater than the critical angle, typically 32° for electro-magnetic waves incident from ice to vacuum (See Fig. 5-11). Occlusion would not occur for a downward-directed plane wave from vacuum to ice making m_0^0 roughly zero, but it would occur for an upward-directed plane wave from ice to vacuum on the way back to the receiver making $m_0^1 = \chi$, as shown in Fig. 5-11. A total scattering loss in dB of $20 \log(1 - \chi)$ would be expected due to occlusion for this layer. Based on Europa's surface topography [108, 37, 97], a reasonable upper bound is roughly $\chi = 1/2$. This yields a total two-way loss of roughly 6 dB specifically for rough surface scattering, which is not a significant radar design impediment.

The expected scattering cross section C_i of fractures buried in the ice shell can be used to estimate radar attenuation due to scattering. While the opening width of a 100-km long cycloidal crack with total penetration through the brittle layer is expected to be on the order of a meter, based on linear elastic theory [129], these fractures will likely be filled by infiltration of liquid water or convective ice from below the layer and should not cause significant scattering. Shallow surface cracks that do not penetrate through the brittle layer are expected to be confined to the upper half of the brittle layer as shown in Sec. 5.2.4, and to have opening widths on the order of a millimeter to a centimeter [98, 74]. Since the tidally induced fractures considered so far are vertical, let us assume some mechanism exists by which the fracture plane is geologically rotated so that they will potentially affect ice-penetrating radar, such

as the tectonic model of Ref. [83].

Fractures should only cause noticeable transmission loss if (1) the angle between the surface normal and the direction of the incident waves exceeds the critical angle, and (2) the fracture opening widths are at least on the order of the wavelength to negate any significant tunneling of evanescent waves. This can be seen by inspection of Fig. 5-12, which shows transmission coefficients through ice with a planar vacuum layer of thickness h, or equivalently transmission loss in dB for an extended fracture, as a function of the incident angle and layer or fracture thickness. Current Earth-based radar measurements show far greater scattering cross sections for Europa for wavelengths at the centimeter rather than meter scale [101, 12, 13]. This is consistent with our findings that tidally driven cracks that do not penetrate through the entire brittle layer have opening widths that probably do not exceed the centimeter scale and may be a significant source of radar scattering at these but not longer wavelengths, and that cracks that penetrate through the brittle layer should likely be filled in. Given this, there seems to be no compelling reason at the present time to expect the m_i^j for $i = 1, \cdots, M$ to be substantially different from zero for the meter-scale wavelengths of ice-penetrating radar missions under consideration for Europa [23, 14]. This is consistent with terrestrial ice-penetrating radar scenarios in the Antarctic [50]. It is not yet clear what mechanisms could be responsible for meter-scale or larger voids based on our current understanding of tidally driven fractures on Europa. Consequently, it is not yet clear whether any *scattering* mechanisms exist to significantly limit radar penetration of Europa's ice shell.

5.5 Summary

We find that surface cracks generated in response to a tidally induced stress field may penetrate through the entire brittle layer of Europa's ice shell, regardless of whether it lies directly above water or effectively inviscid warm ice, if a subsurface ocean exists. Such penetration is found to be unlikely in the absence of an ocean because tidal stresses are then too low to induce deep cracks. A cycloidal crack would then

form as a sequence of near instantaneous discrete failures, each extending in range on the order of the brittle layer thickness. Tidal forcing would link these fractures with an apparent speed corresponding to the low crack propagation speed derived by Ref. [56]. We have shown that ice-penetrating radar scattering losses due to porosity are likely to be negligible since pores are expected to be extremely small compared to the wavelength. While fractures with opening widths of at least the wavelength scale may affect ice-penetrating radar, it seems unlikely that such openings could remain sufficiently void and occur with sufficient spatial frequency to significantly limit radar penetration. We have also shown that the level of seismic activity should be higher by orders of magnitude if an ocean is present on Europa.

Chapter 6

Conclusion

The array invariant method has been developed for instantaneous and simultaneous localization of multiple broadband noise sources in an ocean waveguide without *a priori* knowledge of the environmental parameters. The method exploits the waveguide dispersion inherent in ocean acoustic wave propagation. The array invariant method has been developed for localization of an impulsive source in Chap. 2, and then expanded for multiple broadband noise sources in Chap. 3. Experimental demonstration of the array invariant method has been provided in Chap. 2 with data from the Main Acoustic Clutter Experiment 2003.

Source range estimation and environmental parameter inversion using echo-sounding techniques has been discussed in Chap. 4, and applied to Jovian icy satellite Europa. We have shown that a single passive tri-axial seismic sensor on Europa's surface may make it possible to estimate Europa's interior structure by exploiting natural ice cracking events and impactors as seismo-acoustic sources of opportunity. Our analysis shows that "Big Bang" source events are likely to occur within the period of a landing mission that have returns from the bases of the ice and ocean layers of sufficient magnitude to stand above the accumulated ambient noise of less energetic but more frequent surficial cracking events.

Mechanics of tidally driven fractures and formation of cycloidal cracks have been physically explained in Chap. 5. We have found that surface cracks generated in response to a tidally induced stress field may penetrate through the entire brittle

layer of Europa's ice shell only if a subsurface ocean exists. The cracks associated with cycloids that fully penetrate the brittle layer should be sufficiently energetic to improve the signal-to-noise ratio for the type of seismic profiling discussed in Chap. 4, if fully penetrating cracks are used as sources of opportunity. Scattering loss of ice-penetrating radar through Europa's porous ice has been calculated. It has been shown that the scattering loss from pores and buried fractures would not be a significant radar design impediment.

Appendix A

Stationary phase approximation applied to array beamforming in a waveguide

The method of stationary phase has long been used in guided wave propagation problems to obtain the time-domain response at a receiver [34, 89], and to obtain the time-domain solution of the scattered field [82, 110] by a broadband source. The stationary phase approximation used here is explicitly given in Appendix A.1, and applied to beamforming in a waveguide in Appendix A.2.

A.1 General stationary phase approximation

Let

$$I(x) = \int_a^b g(f) e^{ix\psi(f)}\, df, \tag{A.1}$$

and let $\psi(f)$ satisfy

$$\psi^{(\nu)}(\tilde{f}) \neq 0$$

and

$$\psi^{(1)}(\tilde{f}) = \psi^{(2)}(\tilde{f}) = \cdots = \psi^{(\nu-1)}(\tilde{f}) = 0$$

at $f = \tilde{f}$, where $\psi^{(\nu)}(f)$ is the ν^{th} derivative of $\psi(f)$ with respect to f for positive integer ν. Then $\psi(f)$ can be expanded into the Taylor series as

$$\psi(f) \simeq \psi(\tilde{f}) + \frac{\psi^{(\nu)}(\tilde{f})}{\nu!}(f - \tilde{f})^{\nu}$$

near $f = \tilde{f}$, and Eq. (A.1) can be approximated as

$$I(x) \simeq \begin{cases} 2g(\tilde{f})e^{ix\psi(\tilde{f})+\text{sgn}(\psi^{(\nu)}(\tilde{f}))i\pi/2\nu}\left[\frac{\nu!}{x|\psi^{(\nu)}(\tilde{f})|}\right]^{1/\nu}\frac{\Gamma(1/\nu)}{\nu} & \text{if } \nu \text{ is even,} \\ 2g(\tilde{f})e^{ix\psi(\tilde{f})}\left[\frac{\nu!}{x|\psi^{(\nu)}(\tilde{f})|}\right]^{1/\nu}\frac{\Gamma(1/\nu)}{\nu}\cos\left(\frac{\pi}{2\nu}\right) & \text{if } \nu \text{ is odd,} \end{cases} \tag{A.2}$$

for $x \gg 1$ [9]. Solutions for the special cases of $\nu = 2$ and $\nu = 3$ can be found in Ref. [89]. The error term introduced by the approximation in Eq. (A.2) vanishes at a rate of $1/x$ and therefore is negligible for sufficiently large x [9].

A.2 Application of the stationary phase approximation for array beamforming

The complex beamformed pressure $P_{B+}(s,t)$ of Eq. (2.3) can be rewritten as

$$P_{B+}(s,t) = \frac{4\pi i}{\sqrt{8\pi\rho(z_o)}}e^{-i\pi/4}\sum_n \int_0^\infty |Q(f)|u_n(z_o)u_n(z) \times \frac{B(s-s_n)}{\sqrt{k_{rn}r_o}}e^{ir_o\psi_n(f)}\,df, \tag{A.3}$$

where

$$\psi_n(f) = k_{rn} - \frac{2\pi ft - \angle Q(f)}{r_o}, \tag{A.4}$$

and $|Q(f)|$ and $\angle Q(f)$ are the magnitude and phase of $Q(f)$. Then $\psi_n'(f)$ is zero at the frequency f that satisfies

$$t = \frac{r_o}{v_{gn}(\tilde{f})} + \frac{1}{2\pi}\frac{d}{df}\angle Q(f)\Big|_{f=\tilde{f}}, \tag{A.5}$$

where $\tilde{f}$ is the dominant frequency component that arrives at the receiver array at time t.

The first term in the right-hand side of Eq. (A.5) is the travel time of the n^{th} mode at $f = \tilde{f}$. The second term is the relative phase shift of the source spectrum, or the relative source time delay of the frequency component $\tilde{f}$. For example, for a source signal $q(t) = \delta(t - t_o)$, its Fourier transform is $Q(f) = e^{i2\pi f t_o}$, and

$$\frac{1}{2\pi}\frac{d}{df}\angle Q(f) = t_o.$$

The equation above shows that the relative source time delay is a constant t_o for all the frequency components of $q(t) = \delta(t - t_o)$. For an LFM signal

$$q(t) = \Pi\left(\frac{t}{T}\right) e^{i2\pi f_c t} e^{i2\pi B_w t^2/2T}, \tag{A.6}$$

where

$$\Pi(t) = \begin{cases} 1 & -\frac{1}{2} < t < \frac{1}{2}, \\ 0 & \text{otherwise}, \end{cases} \tag{A.7}$$

f_c is the center frequency, T is the time duration, and B_w is the bandwidth of $q(t)$, the Fourier transform of Eq. (A.6) is given by [102, 103, 16]

$$Q(f) \simeq \sqrt{\frac{iT}{B_w}}\ \Pi\left(\frac{f - f_c}{B_w}\right) e^{i2\pi(f-f_c)^2 T/2B_w}. \tag{A.8}$$

The source signal $q(t)$ has the initial frequency $f_1 = f_c - B_w/2$ at $t = -T/2$, and the final frequency $f_2 = f_c + B_w/2$ at $t = T/2$, as can be seen in Eq. (A.6). The Fourier transform $Q(f)$ in Eq. (A.8) shows that the source spectrum is non-zeros only when $f_1 < f < f_2$. The relative time delay of different frequency components of $q(t)$ in Eq. (A.6) is then

$$\frac{1}{2\pi}\frac{d}{df}\angle Q(f) = \frac{T}{B_w}(f - f_c) = \frac{T}{B_w}\left(f - f_1 - \frac{B_w}{2}\right). \tag{A.9}$$

At the initial and the final frequencies f_1 and f_2, the relative time delays are

$$\frac{1}{2\pi}\frac{d}{df}\angle Q(f)\Big|_{f=f_1} = -\frac{T}{2},$$

and

$$\frac{1}{2\pi}\frac{d}{df}\angle Q(f)\Big|_{f=f_2} = \frac{T}{2},$$

respectively. The relative time delay increases linearly with frequency f when $f_1 < f < f_2$, as can be seen in Eq. (A.9). This is consistent with the behavior of the LFM signal $q(t)$ in Eq. (A.6).

The stationary phase approximation of Eq. (A.3) is then

$$P_{B+}(s,t) \simeq \frac{4\pi i}{\sqrt{8\pi}\rho(z_o)} e^{-i\pi/4} \sum_n |Q(\tilde{f})| \tilde{u}_n(z_o)\tilde{u}_n(z) \frac{\tilde{B}(s-\tilde{s}_n)}{\sqrt{\tilde{k}_{rn} r_o}} F_n(\tilde{f}), \quad \text{(A.10)}$$

where

$$F_n(\tilde{f}) = \begin{cases} e^{i\left[\tilde{k}_{rn}r_o - \left\{2\pi\tilde{f}t - \angle Q(\tilde{f})\right\}/r_o + \mathrm{sgn}\left(\psi_n''(\tilde{f})\right)\pi/4\right]} \left[\frac{2\pi}{r_o|\psi_n''(\tilde{f})|}\right]^{1/2} & \text{if } \psi_n''(\tilde{f}) \neq 0, \\ e^{i\left[\tilde{k}_{rn}r_o - \left\{2\pi\tilde{f}t - \angle Q(\tilde{f})\right\}/r_o\right]} \left[\frac{6}{r_o|\psi_n'''(\tilde{f})|}\right]^{1/3} \frac{\Gamma(1/3)}{3} & \text{if } \psi_n''(\tilde{f}) = 0. \end{cases} \quad \text{(A.11)}$$

The phase term of the source spectrum in Eq. (A.3) can be eliminated when the time duration of the source is much smaller than the time spread of the source due to waveguide dispersion so that the relative phase difference is negligible. Equation (A.3) then simplifies to

$$P_{B+}(s,t) \simeq \frac{4\pi i}{\sqrt{8\pi}\rho(z_o)} e^{-i\pi/4} \sum_n |Q(\tilde{f})| \tilde{u}_n(z_o)\tilde{u}_n(z) \frac{\tilde{B}(s-\tilde{s}_n)}{\sqrt{\tilde{k}_{rn} r_o}} F_n(\tilde{f}) \quad \text{(A.12)}$$

for $Q(f) = |Q(f)|$, where

$$F_n(\tilde{f}) = \begin{cases} e^{i\left(\tilde{k}_{rn}r_0 - 2\pi\tilde{f}t\right) - i\mathrm{sgn}\left(\tilde{v}'_{gn}\right)\pi/4}\sqrt{\frac{(\tilde{v}_{gn})^2}{r_o|\tilde{v}'_{gn}|}} & \text{if } \tilde{v}'_{gn} \neq 0, \\ \\ e^{i\left(\tilde{k}_{rn}r_0 - 2\pi\tilde{f}t\right)}\left[\frac{3(\tilde{v}_{gn})^2}{\pi r_o|\tilde{v}''_{gn}|}\right]^{1/3}\frac{\Gamma(1/3)}{3} & \text{if } \tilde{v}'_{gn} = 0. \end{cases} \tag{A.13}$$

Similar results can be obtained if the received field is matched filtered with the transmitted signal. The matched filter output P_M of the beamformed field P_B is

$$\begin{aligned} P_M(s,t) &= 2\,\mathrm{Re}\left\{K\int_0^\infty P_B(s,f)Q^*(f)e^{-i2\pi ft}\,df\right\} \\ &= 2\,\mathrm{Re}\left\{P_{M+}(s,t)\right\}, \end{aligned} \tag{A.14}$$

where

$$K = \left[\int_{-\infty}^{\infty}|Q(f)|^2\,df\right]^{-1/2}.$$

Again using the method of stationary phase,

$$P_{M+}(s,t) \simeq \frac{4\pi Ki}{\sqrt{8\pi}\rho(z_o)}e^{-i\pi/4}\sum_n |Q(\tilde{f})|^2\tilde{u}_n(z_o)\tilde{u}_n(z)\frac{\tilde{B}(s-\tilde{s}_n)}{\sqrt{\tilde{k}_{rn}r_o}}F_n(\tilde{f}), \tag{A.15}$$

where $\tilde{f}$ satisfies Eq. (2.5). The function $F_n(\tilde{f})$ in Eq. (A.15) is identical to that for impulsive sources given in Eq. (A.13).

Appendix B

Acoustic Properties of Ice

Europa has an average surface temperature of roughly 100K, a value much lower than is found in natural terrestrial ice. To estimate the seismo-acoustic properties of Europan ice, we resort to theory, extrapolation from laboratory data obtained at extreme temperatures, and data from Arctic field experiments. While this approach should provide reasonable estimates, within roughly 10%, further investigation of the seismo-acoustic properties of ice at extremely low temperature and high pressure would be beneficial.

B.1 Seismo-acoustic wave speed

Several *in situ* and laboratory measurements of the dependence of compressional and shear wave speeds on temperature have been made in ice.

Proctor [109] measured wave speeds for temperatures between 60K and 100K in

Table B.1: Elastic compliance constants C_{ij} of ice.

C_{ij}	A_0 (10^4 bar)	A_1 (bar / K)	A_2 (10^{-2} bar / K^2)
C_{11}	17.10±0.0006	-47±1	-29.2±0.3
C_{33}	18.21±0.01	-42±2	-32.2±0.7
C_{44}	3.62±0.01	9±3	-15.5±0.5
C_{12}	8.51±0.10	21±23	-39±13
C_{13}	7.13±0.04	-43±10	3±2

pure ice, and suggested

$$C_{ij} = A_0 + A_1 T + A_2 T^2 \tag{B.1}$$

for the elastic compliance constants C_{ij}, where T is temperature in Kelvin and the values of A_0, A_1 and A_2 provided in Table B.1. Given the elastic compliance constants, the average sound speed in hexagonal systems such as ice can be calculated by the method of Anderson [5]. The results are shown in Fig. B-1 along with several *in situ* measurements [114, 61, 84] assuming the density of ice $\rho_i = 930\text{kg/m}^3$. In Fig. B-1, the Voigt and Reuss approximations represent the upper and lower bounds of the elastic constants, while the Hill approximation is the arithmetic mean of these two. Anderson [5] suggested the Hill approximation as an average sound speed for hexagonal systems. Figure B-1, however, shows that *in situ* measurements agree better with the Reuss approximation. It appears that the porosity in sea ice induced by air bubbles or brine cells significantly lowers the elastic constants of sea ice with respect to pure crystaline ice. Mellor [87] also pointed out that Young's modulus in ice varies significantly with porosity. Noting that the magnetic signature of Europa suggests a salty ocean with salinity comparable to that of the Earth [62], we conclude that the Reuss approximation using Proctor's elastic compliance constant equations will best estimate the sound speed profiles in the Europa's ice shell, and employ this approximation to construct the wave speed profiles in Fig. 4-1.

There are several measurements suggesting a strong change in compressional and shear wave speed at temperatures near the melting point of ice [58, 76]. This effect can be also observed in Fig. B-1. Since the regime near the melting point in Europa's ice shell occupies only a small portion of the total ice shell (Fig. 4-1), we ignore this effect in the compressional and shear speed profiles, since the error introduced in echo sounding will likely be negligible.

It is significant that the total change in speed, for compressional and shear waves in ice, over temperature is small compared to the speed at any given temperature. The compressional wave speed, for example, ranges from 3.7 km/s to 4.1 km/s over Europa's ice shell temperature range of 100K to 270K, exhibiting only a 5% variation

about the mean compressional wave speed of 3.9 km/s. Similarly mild variation is observed in the shear wave speed. The ratio of the compressional to shear wave speed ξ, moreover, is a very weak function of temperature, and has a typical value of 2 in both the Reuss approximation and the *in situ* measurement data, as shown in Fig. B-1 (c).

The dependence of compressional and shear wave speed with pressure in ice has been primarily determined by laboratory experiments with pure polycrystalline ice [123, 40]. These experiments show only 1% change of wave speed in the pressure range between 0 bar to 1 kbar, the expected pressure range in the Europan ice shell. We expect that pressure variation will have a negligible effect on compressional and shear wave propagation speeds in the Europan ice shell.

The elastic properties such as Young's modulus E and Poisson's ratio ν can be obtained from the wave speeds assuming an isotropic medium,

$$E = \rho_i c_s^2 \frac{3\xi^2 - 4}{\xi^2 - 1}, \tag{B.2}$$

$$\nu = \frac{1}{2}\frac{\xi^2 - 2}{\xi^2 - 1}. \tag{B.3}$$

The wave speed curves in Fig. B-1 suggest that the Young's modulus of ice can vary from 9 GPa to 11 GPa in the temperature regime of Europa, and Poisson's ratio $\nu = 0.333$. In this paper, we used $E = 10$ GPa as an average value over the ice shell.

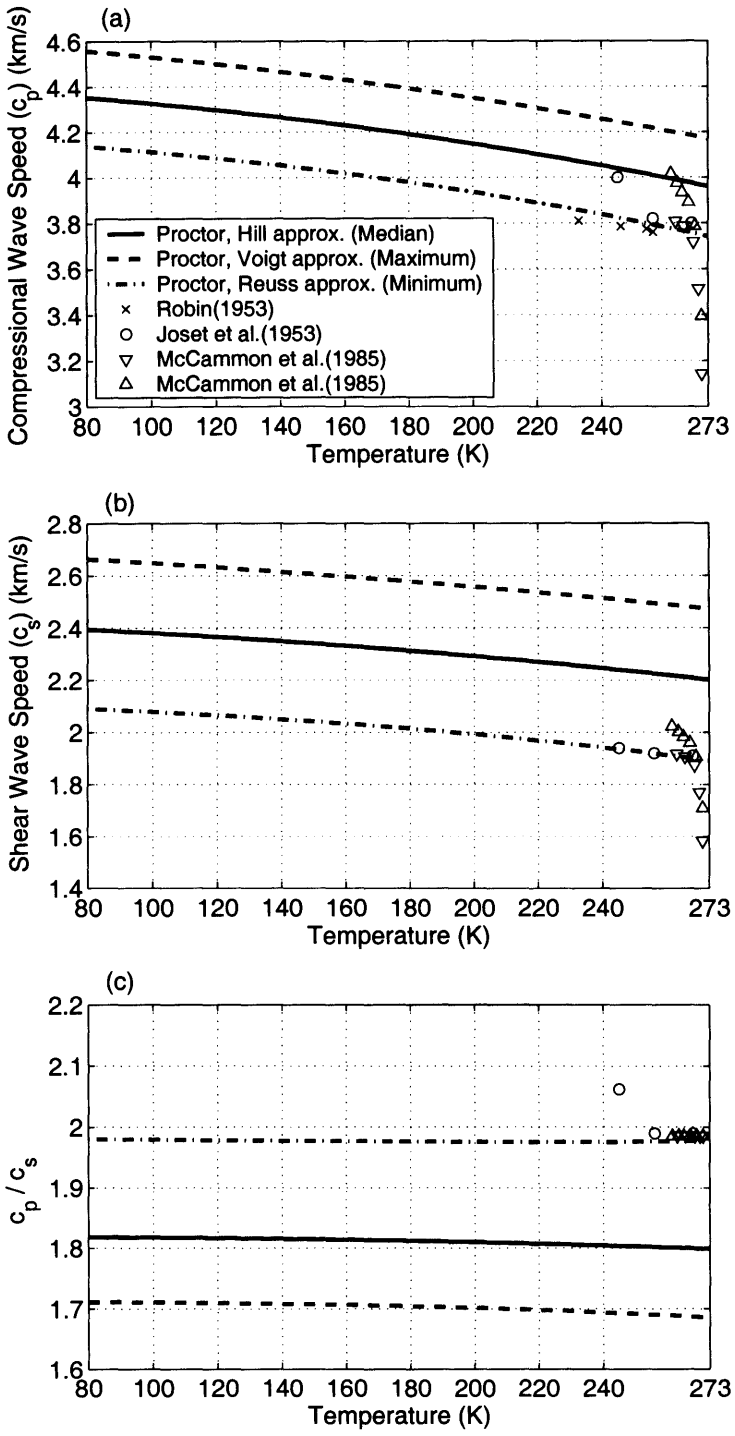

Figure B-1: Compressional, shear wave speeds and the ratio as a function of temperature.

Appendix C

Nondimensionalization of the travel time curves

Assuming an iso-speed ice shell, the time-range plots in Sec. 4.3.3 can be nondimensionalized by dimensionless parameters $t\,c_p/H$, R/H, and ξ. Furthermore, we can assume that $\xi = 2$, as mentioned in Appendix B. In this case, the nondimensionalized travel times $t\,c_p/H$ of all the direct waves and ice-water reflections can be expressed using only one parameter R/H to generate the nondimensional travel time curve in Fig. 4-18.

Nondimensionalization of water-mantle reflections assuming iso-speed ocean can also be achieved by introducing additional nondimensional parameters H_w/H and c_p/c_w.

C.1 Nondimensionalization of Direct Paths

The travel times of the direct P wave and the Rayleigh wave are

$$t_p = \frac{R}{c_p}, \tag{C.1}$$

$$t_s = \frac{R}{0.93\,c_s}. \tag{C.2}$$

The propagation speed of Rayleigh wave is 0.93 c_s when $\xi = 2$.

These equations can be nondimensionalized by multiplying c_p/H to both sides of Eqs. C.1 and C.2:

$$\frac{t_p\, c_p}{H} = \frac{R}{H}, \tag{C.3}$$

$$\frac{t_s\, c_p}{H} = \frac{\xi}{0.93}\frac{R}{H}. \tag{C.4}$$

C.2 Nondimensionalization of multiple reflections from the environmental interfaces

Let t_{ray} to be a travel time of a specific acoustic ray following the ray nomenclature in Sec. 4.3.2, and let

n_p = number of occurrences of P in ray nomenclature,

n_s = number of occurrences of S in ray nomenclature,

n_c = number of occurrences of C in ray nomenclature.

For example, for PSSCP ray path, $n_p = 2$, $n_s = 2$, $n_c = 1$. Then it can be shown that the nondimensionalized travel time of each ray is given by

$$\frac{t_{ray}\, c_p}{H} = \frac{n_p}{\cos\theta_p} + \frac{n_s}{\cos\theta_s}\xi + \frac{2n_c}{\cos\theta_w}\frac{H_w}{H}\xi_w, \tag{C.5}$$

where θ_p, θ_s, and θ_w satisfy

$$n_p \tan\theta_p + n_s \tan\theta_s + 2n_c\frac{H_w}{H}\tan\theta_w = \frac{R}{H}, \tag{C.6}$$

$$\sin\theta_p = \xi \sin\theta_s = \xi_w \sin\theta_w. \tag{C.7}$$

Eq. C.6 is derived from the source, receiver, and waveguide geometry. An acoustic ray must satisfy Snell's law along the ray path as given in Eq. C.7. The terms on the right hand side of Eq. C.5 represents the travel time of the compressional wave

and shear wave in the ice shell, and the travel time of the acoustic wave in the ocean, respectively.

Appendix D

Radiated energy spectra, transmission loss, and scaling laws

Here we first derive the equations that relate the radiated energy level, source level, and particle velocity level from a monopole or pure volume injection source in an infinite homogeneous medium and then generalize these results to a waveguide.

Assuming an omnidirectional volume injection source at the center of a spherical coordinate system (r_s, θ, φ), the inhomogeneous wave equation in the time domain is

$$\nabla^2\phi(r_s,t) - \frac{1}{c_p^2}\frac{\partial^2\phi(r_s,t)}{\partial t^2} = -s(t)\delta(\mathbf{r_s}), \tag{D.1}$$

where $\delta(\mathbf{r_s})$ is 3-Dimensional delta function, and $s(t)$ is volume injection amplitude in the time domain. The solution to Eq. D.1 in an infinite homogeneous medium with no boundaries is that obtained by d'Alembert

$$\phi(r_s,t) = \frac{s(t-r_s/c_p)}{4\pi r_s}, \tag{D.2}$$

and the radial displacement component is

$$u_{r_s}(r_s,t) = \frac{\partial\phi(r_s,t)}{\partial r_s} = -\frac{1}{4\pi}\left[\frac{s(t-r_s/c_p)}{r_s^2} + \frac{\dot{s}(t-r_s/c_p)}{r_s c_p}\right]. \tag{D.3}$$

The first term in the bracket is a near field term proportional to $1/r_s^2$, and the second

term is a radiating displacement component. By considering the radiating component only, the radial particle velocity is

$$\dot{u}_{r_s}(r_s,t) = -\frac{\ddot{s}(t - r_s/c_p)}{4\pi r_s c_p}. \tag{D.4}$$

Given the particle velocity, the total radiated energy E_T from the source is the integral of the energy flux over an area enclosing the source and over time,

$$\begin{aligned} E_T &= \rho c_p \int_{-\infty}^{\infty}\int_0^{2\pi}\int_0^{\pi} |\dot{u}_{r_s}(r_s,t)|^2 r_s^2 \sin\theta \, d\theta \, d\varphi \, dt \\ &= 4\pi r_s^2 \rho c_p \int_{-\infty}^{\infty} |\dot{u}_{r_s}(r_s,t)|^2 \, dt. \end{aligned} \tag{D.5}$$

The radiated energy spectrum is defined using Parseval's identity,

$$\epsilon(f) = 8\pi r_s^2 \rho c_p |\dot{u}_{r_s}(r_s,f)|^2. \tag{D.6}$$

From Eq. D.4, the radial particle velocity in the frequency domain is

$$\dot{u}_{r_s}(r_s,f) = \frac{(2\pi f)^2}{4\pi r_s c_p} S(f) e^{-i2\pi f r_s/c_p}, \tag{D.7}$$

where the source spectrum $S(f)$ is the Fourier transform of the source volume $s(t)$. From Eqs. D.6 and D.7,

$$\epsilon(f) = \frac{8\pi^3 \rho f^4}{c_p} |S(f)|^2. \tag{D.8}$$

Taking the log of both sides of Eq. D.8,

$$20\log\frac{|S(f)|}{S_{ref}} = 10\log\frac{\epsilon(f)}{\epsilon_{ref}} - 40\log\frac{f}{f_{ref}} + 10\log\frac{c_p \epsilon_{ref}}{8\pi^3 \rho S_{ref}^2 f_{ref}^4}, \tag{D.9}$$

where $S_{ref} = 1\ \mathrm{m^3/Hz}$, $\epsilon_{ref} = 1\ \mathrm{J/Hz}$, and $f_{ref} = 1\ \mathrm{Hz}$. For ice with $c_p = 4\ \mathrm{km/s}$ and $\rho = 930\ \mathrm{kg/m^3}$, Eq (C9) becomes

$$L_s = L_\epsilon - 40\log\frac{f}{f_{ref}} - 18, \tag{D.10}$$

where L_s is the source level in dB re 1 m^3/Hz, and L_ϵ is the radiated energy level in dB re 1 J/Hz. The relationship between the radiated energy and velocity can be obtained by substituting Eq. D.7 into Eq. D.9.

$$10\log\frac{\epsilon(f)}{\epsilon_{ref}} = 20\log\frac{|\dot{u}_{r_s}(r_s,f)|}{\dot{u}_{ref}} + 10\log\frac{8\pi\rho c_p r_{ref}^2 \dot{u}_{ref}^2}{\epsilon_{ref}} + 20\log\frac{r}{r_{ref}}, \tag{D.11}$$

where $\dot{u}_{ref} = 1\ \mu\text{m s}^{-1}\text{Hz}^{-1}$, and $r_{ref} = 1$ m. The last term on the right hand side of the equation is the transmission loss

$$\text{TL} = -20\log\frac{r_s}{r_{ref}}, \tag{D.12}$$

which takes the spherical spreading loss in free space into account. Equation D.11 then becomes

$$L_{\dot{u}_{r_s}} = L_\epsilon + \text{TL} - 20, \tag{D.13}$$

where $L_{\dot{u}_{r_s}}$ is the velocity level in dB re 1 $\mu\text{m s}^{-1}\text{Hz}^{-1}$, so that the radiated energy level and the velocity level are directly related.

This result can be generalized for a waveguide by rewriting Eqs. 4.5 and 4.6 as

$$\dot{u}_m(r,z,f) = \frac{(2\pi f)^2 S(f)}{4\pi c_p}\left[\frac{4\pi c_p}{(2\pi f)^2} G_{\dot{u},m}(r,z,f)\right], \tag{D.14}$$

$$\dot{w}_m(r,z,f) = \frac{(2\pi f)^2 S(f)}{4\pi c_p}\left[\frac{4\pi c_p}{(2\pi f)^2} G_{\dot{w},m}(r,z,f)\right]. \tag{D.15}$$

Using Eq. D.8, we have

$$|\dot{u}_m(r,z,f)|^2 = \frac{\epsilon(f)}{8\pi\rho c_p}\left|\frac{4\pi c_p}{(2\pi f)^2} G_{\dot{u},m}(r,z,f)\right|^2, \tag{D.16}$$

$$|\dot{w}_m(r,z,f)|^2 = \frac{\epsilon(f)}{8\pi\rho c_p}\left|\frac{4\pi c_p}{(2\pi f)^2} G_{\dot{w},m}(r,z,f)\right|^2. \tag{D.17}$$

Equations relating received velocity level to source energy level and transmission loss similar to Eq. D.13 can be obtained by taking the log of both sides of the previous

two equations,

$$L_{\dot{u}} = L_{\epsilon} + \mathrm{TL}_{\dot{u}} - 20, \tag{D.18}$$

$$L_{\dot{w}} = L_{\epsilon} + \mathrm{TL}_{\dot{w}} - 20, \tag{D.19}$$

where $L_{\dot{u}}$ and $L_{\dot{w}}$ are horizontal and vertical velocity levels in dB re 1 μm s^{-1} Hz^{-1}. The transmission losses in the horizontal and vertical particle velocities are given by

$$\mathrm{TL}_{\dot{u}} = -20 \log \left[\left| \frac{4\pi c_p}{(2\pi f)^2} G_{\dot{u},m}(r, z, f) \right|^{-1} / r_{ref} \right], \tag{D.20}$$

$$\mathrm{TL}_{\dot{w}} = -20 \log \left[\left| \frac{4\pi c_p}{(2\pi f)^2} G_{\dot{w},m}(r, z, f) \right|^{-1} / r_{ref} \right]. \tag{D.21}$$

which are identical to Eq. 4.17 for $r_{ref} = 1$ m.

In general, this relationship is valid in the frequency domain only, since, in the time domain, each frequency response is weighted by the source spectrum and synthesized by the Fourier integral,

$$\dot{u}(r, z, t) = \int_{-\infty}^{\infty} S(f) G_{\dot{u}}(r, z, f) e^{-i2\pi f t} df. \tag{D.22}$$

The source spectrum in a given frequency band $f_1 < f < f_2$ can be expressed as

$$S(f) \simeq A(\chi) \tilde{S}(f), \tag{D.23}$$

if the source spectrum retains the same shape $\tilde{S}(f)$ with varying amplitude A that is a function of the source parameter χ. The velocity in time domain after filtering can be expressed as

$$\dot{u}(r, z, t) \simeq A(\chi) \int_{f_1}^{f_2} \tilde{S}(f) G_{\dot{u}}(r, z, f) e^{-i2\pi f t} df. \tag{D.24}$$

By taking the log of both sides,

$$L_{\dot{u}}(\chi) \simeq L_A(\chi) + \tilde{L}_{\dot{u}}, \tag{D.25}$$

where

$$L_A(\chi) = 10 \log A^2(\chi), \tag{D.26}$$

$$\tilde{L}_{\dot{u}} = 10 \log \left| \int_{f_1}^{f_2} \tilde{S}(f) G_{\dot{u}}(r, z, f) e^{-i2\pi f t} df \right|^2 . \tag{D.27}$$

Equation D.25 shows that velocity level $L_{\dot{u}}(\chi_1)$ can be scaled to velocity level $L_{\dot{u}}(\chi_2)$ by

$$L_{\dot{u}}(\chi_2) \simeq L_{\dot{u}}(\chi_1) + [L_A(\chi_2) - L_A(\chi_1)]. \tag{D.28}$$

Furthermore, substitution of Eq. D.23 into Eq. D.8 shows that

$$L_A(\chi_2) - L_A(\chi_1) = L_\epsilon(\chi_2) - L_\epsilon(\chi_1). \tag{D.29}$$

Therefore, Eq. D.28 can be changed to

$$L_{\dot{u}}(\chi_2) \simeq L_{\dot{u}}(\chi_1) + [L_\epsilon(\chi_2) - L_\epsilon(\chi_1)], \tag{D.30}$$

where the velocity level is simply expressed in terms of the change in source energy level.

For surface cracks $\chi = h$, and for impactors $\chi = s_0$, where s_0 is the permanent volume injection by an impactor as defined in Appendix D.2. The differences between the energy spectra can either be obtained from Figs. 4-5 and 4-6, or

$$L_\epsilon(h_1) - L_\epsilon(h_2) = 80 \log \frac{h_1}{h_2}, \quad h \leq 250\text{-m} \tag{D.31}$$

for surface cracks, and

$$L_\epsilon(s_{0,1}) - L_\epsilon(s_{0,2}) = 20 \log \frac{s_{0,1}}{s_{0,2}}, \quad r_m \leq 10\text{-m} \tag{D.32}$$

for impactors when $f \leq 4$ Hz, as shown in Appendices D.1 and D.2. Equation D.32 can also be expressed in terms of the impactor radius r_m,

$$L_\epsilon(r_{m,1}) - L_\epsilon(r_{m,2}) = 60 \log \frac{r_{m,1}}{r_{m,2}}, \quad r_m \leq 10\text{-m}, \tag{D.33}$$

given the density ρ_m and the impact velocity v_m of an impactor.

The ambient noise levels in Eqs. 4.26 and 4.27 can also be scaled by source energy level

$$\left\langle |S(f)|^2 \mid \chi \right\rangle = A^2(\chi) \left\langle |\tilde{S}(f)|^2 \right\rangle, \tag{D.34}$$

based on Eq. D.23. Then using Eqs. 4.23 and 4.26, we have

$$\mathrm{NL}_{\dot{u}}(\chi_2) \simeq \mathrm{NL}_{\dot{u}}(\chi_1) + [L_\epsilon(\chi_2) - L_\epsilon(\chi_1)], \tag{D.35}$$

so that the velocity level and the noise level can be scaled by the same term for a given change in source energy level.

D.1 Radiated energy spectra from tensile cracks

The radiated energy spectra for tensile cracks can be estimated in a spherical coordinate system (r_s, θ, φ) with corresponding particle velocity components $\dot{u}_{r_s}$, $\dot{u}_\theta$, $\dot{u}_\varphi$ [54]. Assuming that the radial velocity is compressional and the other components are due to shear,

$$\begin{aligned}
\epsilon_{c_p}(f) &= 2\rho c_p \int_0^{2\pi} \int_0^{\pi} |\dot{u}_{r_s}(f)|^2 r_s^2 \sin\theta d\theta d\varphi, \\
\epsilon_{c_s}(f) &= 2\rho c_s \int_0^{2\pi} \int_0^{\pi} \left(|\dot{u}_\theta(f)|^2 + |\dot{u}_\varphi(f)|^2 \right) r_s^2 \sin\theta d\theta d\varphi,
\end{aligned} \tag{D.36}$$

where

$$\begin{aligned}
4\pi c_s r_s \dot{u}_{r_s} &= \frac{c_s}{c_p} I_{c_p} \left[1 - 2\left(\frac{c_s}{c_p}\right)^2 + 2\left(\frac{c_s}{c_p}\right)^2 \sin^2\theta \sin^2\varphi \right], \\
4\pi c_s r_s \dot{u}_\theta &= I_{c_s} \sin 2\theta \sin^2\varphi, \\
4\pi c_s r_s \dot{u}_\varphi &= I_{c_s} \sin\theta \sin 2\varphi,
\end{aligned} \tag{D.37}$$

$$I_{c_p}(t) = D_0 h \int_0^h \ddot{D}\left(\tau_p - \frac{\eta}{v}\right) d\eta,$$

$$
\begin{aligned}
I_{c_s}(t) &= D_0 h \int_0^h \ddot{D}\left(\tau_s - \frac{\eta}{v}\right) d\eta, \\
\tau_p &= t - \frac{d}{c_p}, \\
\tau_s &= t - \frac{d}{c_s},
\end{aligned} \tag{D.38}
$$

and d is the distance from the instantaneous opening position of the propagating crack to the receiver position. Since $d \gg h$ we take d to be a time-invariant constant measured from the center of the completed crack. This assumption is consistent with monopole radiation, which is expected on average, and enables analytic evaluation of $I_{c_{p,s}}$.

The total radiated energy spectrum $\epsilon(f)$ is the sum of the compressional wave energy spectrum $\epsilon_{c_p}(f)$ and the shear wave energy spectrum $\epsilon_{c_s}(f)$. $D(t)$ is the source shape function that satisfies the initial and final conditions

$$
\begin{aligned}
D(t) &= 0, \quad t < 0, \\
D(t) &\to 1, \quad t \to \infty.
\end{aligned} \tag{D.39}
$$

We use the Haskell source model characterized by a ramp function as shown in Fig. D-1. The relative change of the energy spectrum as a function of crack depth is independent of this choice.

We also assume that the crack opening time τ is the same as the crack propagation time $T = h/v$. Under these assumptions,

$$
\begin{aligned}
I_{c_{p,s}}(f) &= i\frac{2D_0h^2}{T}\mathrm{sinc}(Tf)\sin(\pi Tf)e^{-i2\pi f(d/c_{p,s}+T)} \\
|I_{c_{p,s}}(f)| &\equiv |I(f)| = \frac{2D_0h^2}{T}|\mathrm{sinc}(Tf)\sin(\pi Tf)|, \\
\epsilon_{c_p}(f) &= |I(f)|^2 \frac{2\pi\rho c_p}{(4\pi c_s)^2\xi^2}\left(4 - \frac{14}{3\xi^2}\right), \\
\epsilon_{c_s}(f) &= |I(f)|^2 \frac{2\pi\rho c_s}{(4\pi c_s)^2}\frac{37}{15},
\end{aligned} \tag{D.40}
$$

where $\mathrm{sinc}\,(x) = \sin(\pi x)/(\pi x)$.

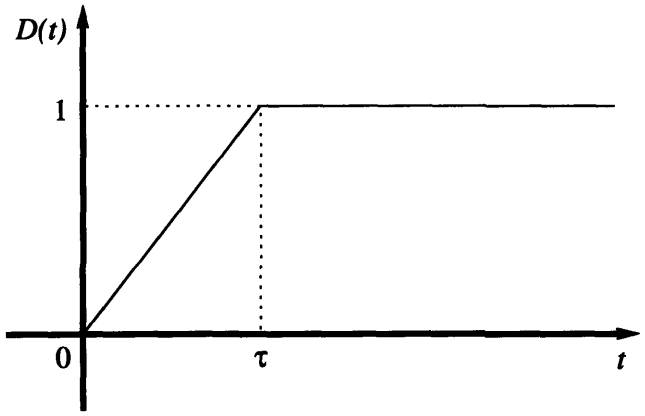

Figure D-1: The source shape function $D(t)$ for Haskell source model. τ is the opening time of a surface crack.

We employ an equivalent volume injection source that has the same total radiated energy spectrum as a tensile crack by assuming

$$S(f) = i\frac{2D_0h^2}{T}\text{sinc}(Tf)\sin(\pi Tf)e^{-i2\pi fT} \times \left[\frac{\xi}{64\pi^4f^4}\left\{\frac{1}{\xi}\left(4-\frac{14}{3\xi^2}\right)+\frac{37}{15}\right\}\right]^{1/2}. \quad \text{(D.41)}$$

Since $\epsilon(f)$ is proportional to $|I(f)|^2$, the overall behavior of the source spectrum can be understood by analyzing the behavior of $|I(f)|^2$, where $\rho I(f)$ is the Fourier transform of the rate of change of mass outflow from the source.

The frequency dependent characteristics of $|I(f)|^2$ are determined by $\text{sinc}^2(Tf)\sin^2(\pi Tf)$, and its behavior with the 3-dB bandwidth is plotted in Fig. 4-4. Given the surface crack depth, the radiated energy level is

$$L_\epsilon = 10\log\frac{\epsilon(f)}{\epsilon_{ref}} \sim 20\log|\text{sinc}\,(Tf)| + 20\log|\sin(\pi Tf)|, \quad \text{(D.42)}$$

where the symbol $\sim$ indicates "proportional to."

For frequencies below the 3-dB bandwidth, $\text{sinc}\,(Tf) \simeq 1$, $\sin(\pi Tf) \simeq \pi Tf$, so that

$$L_\epsilon \sim 20\log(\pi Tf), \quad \text{(D.43)}$$

which characterizes an energy spectrum that increases by 20 dB/decade.

For frequencies above the 3-dB bandwidth, $\mathrm{sinc}\,(Tf) \sim (\pi T f)^{-1}$, so that

$$L_\epsilon \sim -20\log(\pi T f), \tag{D.44}$$

which characterizes an energy spectrum with rapid sinusoidal oscillation and a trend that falls off by 20 dB/decade.

The amplitude of the energy spectrum depends on the crack depth. By taking Eq. 4.3 into account, the peak of the energy spectral density

$$\epsilon(f)_{max} \sim |I(f)|^2_{max} \sim \frac{D_0^2 h^4}{T^2} \sim D_0^2 h^2 \sim h^6,$$

follows a sixth power law in h so that the maximum energy level is

$$L_{\epsilon,max} \sim 60\log\frac{h}{h_{ref}}, \tag{D.45}$$

where h_{ref}=1 m. But this peak value varies with frequency as a function of crack depth h, as shown in Fig. 4-5.

The energy spectra for frequencies below the 3-dB bandwidth show greater differences across h than those found by comparing the spectral peaks since

$$\epsilon(f) \sim \frac{D_0^2 h^4}{T^2}|\mathrm{sinc}\,(Tf)\sin(\pi T f)|^2 \sim D_0^2 h^4 \sim h^8$$

leads to an eighth power law in h and the corresponding energy level functionality

$$L_\epsilon \sim 80\log\frac{h}{h_{ref}}, \tag{D.46}$$

from which Eq. D.31 can be obtained.

When $f < 1/T$ the source spectrum can also be approximated as

$$S(f) \simeq 2\pi i D_0 h^2 f\left[\frac{\xi}{64\pi^4 f^4}\left\{\frac{1}{\xi}\left(4-\frac{14}{3\xi^2}\right)+\frac{37}{15}\right\}\right]^{1/2}, \tag{D.47}$$

so that the amplitude of the source spectrum in Eq. D.23 can be approximated as

$$A(h) = D_0 h^2 \sim h^4,$$

which explicitly shows its dependence on crack depth.

D.2 Radiated energy spectra from impactors

To estimate the radiated energy spectrum of an impactor, we base our estimation on the impact-explosion analogy.

Given the kinetic energy E_K of an impactor, the seismic efficiency of the impact is defined as

$$\eta_s = \frac{E_S}{E_K}, \tag{D.48}$$

where E_S is the total radiated seismic energy. The seismic efficiency typically varies from 10^{-3} to 10^{-5} with the most commonly accepted value of 10^{-4} [121, 88].

In underground explosions of spherical radiation, permanent volume injection is related to the total radiated seismic energy by

$$E_S = \frac{\pi^2 \rho f_c^3 s_0^2}{2c_s}, \tag{D.49}$$

where s_0 is the permanent volume injection measured in the elastic regime from the explosion. The corner frequency f_c is given by

$$f_c = \frac{c_s}{\pi R_e} \tag{D.50}$$

in the model employed by Denny and Johnson [30]. It is worth noting that the corner frequencies in both surface cracks and impactors are proportional to the ratio of the wave speed in the medium and the characteristic length of the seismo-acoustic source. When the impact velocity of the impactor onto a rocky target is larger than a few

kilometers per second, the elastic radius R_e can be assumed as

$$R_e \simeq 20\, r_m, \tag{D.51}$$

where r_m is the radius of an impactor [1, 88].

The permanent volume injection from an impactor can be estimated using Eqs. D.48~D.51,

$$s_0 = \left[\frac{2c_s E_S}{\pi^2 \rho f_c^3}\right]^{1/2} = \left[\frac{1.2 \times 10^4 \times \eta_s \rho_m v_m^2}{\rho c_s^2}\right]^{1/2} V_m, \tag{D.52}$$

where ρ_m, v_m, and V_m are the density, impact velocity, and volume of the impactor.

The source spectrum and the total radiated energy spectrum are given by [30]

$$S(f) = \frac{s_0 f_c^2}{i2\pi f[(f_c^2 - f^2) + 2if_c f/\xi]} = \frac{s_0}{i2\pi f\left[\left\{1 - \left(\frac{f}{f_c}\right)^2\right\} + i\frac{2f}{\xi f_c}\right]}, \tag{D.53}$$

$$\epsilon(f) = \frac{2\pi\rho}{c_p} \frac{s_0^2 f^2}{\left\{1 - \left(\frac{f}{f_c}\right)^2\right\}^2 + \left(\frac{2f}{\xi f_c}\right)^2}. \tag{D.54}$$

As can be observed in Eq. D.54, the energy spectral density at the corner frequency, slightly above the frequency of the peak, is

$$\epsilon(f_c) \sim s_0^2 f_c^2 \sim r_m^4,$$

which shows a fourth power law in r_m that leads to the energy level dependence

$$L_{\epsilon, f_c} \sim 40 \log(r_m / r_{m,ref}), \tag{D.55}$$

given ρ_m and v_m for the impactor, where $r_{m,ref}$ = 1-m. Since $\epsilon(f) \sim f^2$ if $f \ll f_c$, and $\epsilon(f) \sim f^{-2}$ if $f \gg f_c$, the slope of the energy spectrum follows the same laws as surface cracks above and below the 3-dB bandwidth.

For f below the 3-dB bandwidth,

$$S(f) \simeq \frac{s_0}{i2\pi f} \sim r_m^3,$$

so that the source amplitude function in Eq. D.23 can be expressed as $A(s_0) = s_0$. The radiated energy spectrum can then be approximated as

$$\epsilon(f) \simeq \frac{2\pi\rho}{c_p} s_0^2 f^2 \sim r_m^6,$$

with energy spectral level following the dependence

$$L_\epsilon = 10 \log \frac{\epsilon(f)}{\epsilon_{ref}} \sim 20 \log \frac{s_0}{s_{0,ref}} \sim 60 \log \frac{r_m}{r_{m,ref}}, \tag{D.56}$$

where $s_{0,ref} = 1\ \mathrm{m}^3$. The difference between the energy spectral levels for various impactors can be determined by Eqs. D.32 and D.33.

The radiated energy levels for impactors of various radii are given in Fig. 4-6, assuming $\rho_m = 3\,\mathrm{g/cm}^3$ and $v_m = 20\,\mathrm{km/s}$. The seismic efficiency was assumed to be 10^{-4}. The radiated energy spectrum can vary by $\pm$ 10 dB due to the uncertainty in the seismic efficiency.

Appendix E

Alternative derivations of crack penetration depth in a finite-thickness layer under far-field tension and gravitational overburden

Here we present two simple order of magnitude calculations to determine crack penetration depth in a finite-thickness layer, such as Europa's ice shell, under far-field tension and gravitational overburden pressure. A rigorous derivation of crack penetration depth is given in Chap. 5.2 using the stress intensity factor theory. The methods presented in this chapter provide further insight into the amplification of far-field tension near the crack and spontaneous crack propagation through the entire ice shell.

The first method involves calculating the amplification of far-field tension below the crack as a function of crack depth h, and comparing this amplified tension with the gravitational compressive stress at the crack tip. When far-field tension σ_∞ is applied to a layer that has a surface crack with depth h, the stress in the medium

below the crack is given by

$$\sigma = \frac{H}{H-h}\sigma_\infty \tag{E.1}$$

from the force balance, and so the tensile stress below the crack is amplified by the factor $H/(H-h)$. This is because the fractured part of the layer cannot sustain any tension. The gravitational stress below the crack, however, is not disturbed by the presence of the crack as far as the crack opening width is sufficiently small [133], and is given by $\rho_i g h$.

The order of magnitude crack depth h can then be obtained by finding the depth where the tensile stress below the crack in Eq. E.1 is balanced by the gravitational overburden,

$$\frac{H}{H-h}\sigma_\infty = \rho_i g h. \tag{E.2}$$

From Eq. E.2, one can obtain two crack depths h_1 and h_2 given by

$$h_{1,2} = \frac{\rho_i g H \pm \sqrt{(\rho_i g H)^2 - 4\rho_i g H \sigma_\infty}}{2\rho_i g}. \tag{E.3}$$

The behavior of the solutions in Eq. E.3 is similar to the behavior of the stress intensity factor solutions shown in Fig. 5-5. Given far-field tension σ_∞ in a layer of thickness H, there are two crack depth solutions h_1 and h_2. The first crack depth h_1 is the depth where a surface generated crack would stop propagating, since the tension below the crack is smaller than the gravitational overburden. The second depth h_2 is the depth where, once a surface generated crack reaches this depth, a crack would propagate spontaneously through the entire layer. The critical crack depth h_c would occur when the far-field tension is given in such a way that the terms inside the square root in Eq. E.3 equals zero, or when the far-field tension is equal to the critical stress

$$\sigma_c = \frac{\rho_i g H}{4}. \tag{E.4}$$

The corresponding critical crack depth is

$$h_c = \frac{H}{2}. \tag{E.5}$$

One can see that the critical depth in Eq. E.5 is roughly 30% larger than the critical depth in Fig. 5-5, and the critical stress in Eq. E.4 is roughly a factor of two larger than the critical stress in Fig. 5-6 for zero porosity. This is because the order of magnitude stress balance formulation does not account for the concentration of stress at the sharp crack tip. This is also consistent with the half-space formula, where the Nye crack depth obtained from simple stress balance between the far-field tension and gravitational overburden is roughly 1.6 times smaller than the rigorous stress intensity factor calculation [125].

The second method for crack depth calculation involves the Byerlee's criteria, where the yield strength of material is assumed to be proportional to the gravitational overburden [20, 117]. In ice, the yield strength in tension is equal to $0.7\rho_i g z$ [15, 117]. The total penetration of surface crack through the entire layer under the Byerlee's criteria occurs when the applied horizontal force on the layer due to far-field tension is larger than or equal to the integrated strength of the uncracked part of the layer below the surface crack, i.e.,

$$H\sigma_\infty \geq \int_h^H 0.7\rho_i g z \, dz. \tag{E.6}$$

In this formula, the cracked part of the layer in the depths $0 < z < h$ does not contribute to the strength of the ice shell, since the cracked part cannot sustain any tension.

The critical stress σ_c required for the total penetration of a surface crack can be obtained from the far-field tension that makes the left-hand side and the right-had side of Eq. E.6 equal to each other. The Byerlee's criteria, however, does not provide a crack penetration depth h as a function of the far-field tension σ_∞. A conservative assumption would be to use the crack penetration depth in the half-space scenario [125],

$$h = 1.64\frac{\sigma_\infty}{\rho_i g}. \tag{E.7}$$

One can then find from Eqs. E.6 and E.7 that the critical stress σ_c and the critical

crack depth h_c are

$$\sigma_c \simeq \frac{\rho_i g H}{3.6} \tag{E.8}$$

and

$$h_c \simeq 0.46H, \tag{E.9}$$

respectively.

The critical stress in Eq. E.8 is roughly a factor of two larger than the critical stress in Fig. 5-6 for zero porosity, and the critical depth in Eq. E.9 is roughly 10% larger than the critical depth in Fig. 5-5. This is because the crack penetration depth in Eq. E.7 is that of half-space scenario, which underestimates the crack penetration depth in a finite-thickness layer. The overall behavior of the solution, however, is similar to that in Chap. 5.2.2 using the stress intensity factor theory and the order of magnitude stress balance calculation presented above, since all these calcuations show that once a crack penetrates roughly half the layer, the crack should propagate spontaneously through the entire layer.

Appendix F

Standard deviation and bias of critical stress in an ice shell with random depth-dependent porosity

We show that the standard deviation and bias of critical stress σ_c due to fluctuation of ice porosity v_b as a function of depth is appreciably smaller than the 1 kPa spatial change of tidal stress expected on Europa's surface over 1 km, roughly the minimum length of a fully penetrating crack. The compressive stress $\sigma_o(z)$ due to gravitational overburden is given by

$$\sigma_o(z) = \int_0^z \rho(z_o) g \, dz_o, \tag{F.1}$$

where $\rho(z)$ is the density of a medium. The stress intensity factor $K_{I,o}$ due to σ_o is [128]

$$K_{I,o}(h) = -\int_0^h f(z)\sigma_o(z) \, dz, \tag{F.2}$$

where

$$f(z) = \frac{2}{\sqrt{\pi h}} \frac{1.3 - 0.3(z/h)^{5/4}}{\sqrt{1-(z/h)^2}}. \tag{F.3}$$

Then the variance of the stress intensity factor in Eq. F.2 is

$$\mathrm{Var}\left(K_{I,o}(h)\right) = \int_0^h \int_0^h f(z) f(z') \, \mathrm{Cov}\left(\sigma_o(z), \sigma_o(z')\right) \, dz \, dz', \tag{F.4}$$

where

$$\mathrm{Cov}\left(\sigma_o(z), \sigma_o(z')\right) = g^2 \int_0^z \int_0^{z'} \mathrm{Cov}\left(\rho(z_o), \rho(z_o')\right)\, dz_o\, dz_o'. \tag{F.5}$$

We take the covariance of density to be

$$\mathrm{Cov}\left(\rho(z_o), \rho(z_o')\right) = z_c \delta(z_o - z_o') \mathrm{Var}\left(\rho(z_o)\right) = z_c \delta(z_o - z_o') \rho_i^2 \mathrm{Var}\left(v_b(z_o)\right), \tag{F.6}$$

where z_c is the correlation length of density versus depth. Fluctuating density contributions to the variance of the stress intensity factor then accumulate incoherently with depth. We take the correlation length z_c to be roughly the pore size, which is expected to be less than 1 mm based on terrestrial values and estimates of Europa's pore size given in Sec. 5.1.

The variance of the stress intensity factor in Eq. F.2 is then

$$\mathrm{Var}\left(K_{I,o}(h)\right) = g^2 z_c \rho_i^2 \mathrm{Var}\left(v_b\right) \int_0^h f(z) \left[\int_0^z z' f(z')\, dz'\right] dz \tag{F.7}$$

using Eqs. F.5 and F.6. Here we have neglected pore closure due to gravitational compaction, and assumed that porosity obeys a stationary random process across depth so that $\mathrm{Var}\left(v_b(z_o)\right) \equiv \mathrm{Var}\left(v_b\right)$. When the mean to standard deviation ratio of critical stress is large, its asymptotic variance becomes [94]

$$\mathrm{Var}\left(\sigma_c\right) = \left(\frac{\partial \sigma_c}{\partial K_{I,o}(h_c)}\right)^2 \mathrm{Var}\left(K_{I,o}(h_c)\right), \tag{F.8}$$

and the bias of the critical stress

$$\mathrm{bias}\left(\sigma_c\right) = \left\langle \sigma_c(v_b) \right\rangle - \sigma_c(v_b) \tag{F.9}$$

is asymptotically

$$\mathrm{bias}\left(\sigma_c\right) = -\frac{1}{2} \frac{\partial^2 \left\langle v_b \right\rangle}{\partial \sigma_c^2} \left(\mathrm{Var}\left(v_b\right)\right)^{-1} \frac{\partial \left\langle v_b \right\rangle}{\partial \sigma_c} \left(\mathrm{Var}\left(\sigma_c\right)\right)^2. \tag{F.10}$$

Our numerical simulations show that the standard deviation of the critical stress

σ_c calculated using Eq. F.8 is roughly 0.1 kPa and the bias is effectively zero for a brittle layer of ice with a few kilometer thickness. Here it is conservatively assumed that $z_c = 1$ mm and v_b follows a uniform distribution from 0 to 1.

Bibliography

[1] T. J. Ahrens and J. D. O'Keefe. Equations of state and impact-induced shock-wave attenuation on the moon. In D. J. Roddy, R. O. Pepin, and R. B. Merrill, editors, *Impact and Explosion Cratering*, pages 639–656. Pergamon Press, New York, 1977.

[2] K. Aki and P. G. Richards. *Quantitative Seismology.* W. H. Freeman, San Francisco, 1980.

[3] D. L. Anderson and W. F. Weeks. A theoretical analysis of sea-ice strength. *Trans. Am. Geophys. Union*, 39:632–640, August 1958.

[4] J. D. Anderson, G. Schubert, R. A. Jacobson, E. L. Lau, W. B. Moore, and W. L. Sjogren. Europa's differentiated internal structure: Inferences from four Galileo encounters. *Science*, 281:2019–2022, September 1998.

[5] O. L. Anderson. A simplified method for calculating the Debye temperature from elastic constant. *J. Phys. Chem. Solids*, 24:909–917, 1963.

[6] T. L. Anderson. *Fracture Mechanics: Fundamentals and Applications.* CRC Press, Boca Raton, 1991.

[7] A. B. Baggeroer, W. A. Kuperman, and H. Schmidt. Matched field processing: Source localization in correlated noise as an optimum parameter estimation problem. *J. Acoust. Soc. Am.*, 83(2):571–587, 1988.

[8] G. D. Bart, R. Greenberg, and G. V. Hoppa. Cycloids and wedges: Global patterns from tidal stresses on Europa. *LPSC XXXIV*, page Abstract #1396, 2003.

[9] C. M. Bender and S. A. Orszag. *Advanced Mathematical Methods for Scientists and Engineers.* McGraw-Hill, New York, 1978.

[10] R. T. Beyer. *Sounds of Our Time: Two Hundred Years of Acoustics.* Springer-Verlag, New York, 1998.

[11] E. B. Bierhaus, C. R. Chapman, W. J. Merline, S. M. Brooks, and E. Asphaug. Pwyll secondaries and other small craters on Europa. *Icarus*, 153:264–276, October 2001.

[12] G. J. Black, D. B. Campbell, and P. D. Nicholson. Icy Galilean satellites: Modeling radar reflectivities as a coherent backscatter effect. *Icarus*, 151:167–180, 2001.

[13] G. J. Black, D. B. Campbell, and S. J. Ostro. Icy Galilean satellites: 70 cm radar results from Arecibo. *Icarus*, 151:160–166, 2001.

[14] D. D. Blankenship, B. C. Edwards, Y. Kim, P. E. Geissler, D. Gurnett, W. T. K. Johnson, W. Kofman, J. C. Moore, D. L. Morse, R. T. Pappalardo, G. Picardi, R. K. Raney, E. R. Rodriguesz, X. M. Shao, J. Weertman, H. A. Zebker, and J. van Zyl. Feasibility study and design concept for an orbiting ice-penetrating radar sounder to characterize in three-dimensions the Europan ice mantle down to (and including) any ice/ocean interface. Technical Report 184, University of Texas, Austin, 1999.

[15] W. F. Brace and D. L. Kohlstedt. Limits on lithospheric stress imposed by laboratory experiments. *J. Geophys. Res.*, 85(B11):6248–6252, 1980.

[16] R. N. Bracewell. *The Fourier Transform and Its Applications.* McGraw-Hill, Boston, 3rd edition, 2000.

[17] L. M. Brekhovskikh. *Waves in Layered Media.* Academic Press, New York, 2nd edition, 1980.

[18] L. M. Brekhovskikh and Y. Lysanov. *Fundamentals of Ocean Acoustics.* Springer-Verlag, New York, 3rd edition, 2003.

[19] H. P. Bucker. Use of calculated sound fields and matched field detection to locate sound sources in shallow water. *J. Acoust. Soc. Am.*, 59:368–373, 1976.

[20] J. Byerlee. Friction of rocks. *Pure Appl. Geophys.*, 116:615–626, 1978.

[21] C.-T. Chen and F. J. Millero. Speed of sound in seawater at high pressures. *J. Acoust. Soc. Am.*, 62:1129–1135, November 1977.

[22] S. D. Chuprov. Interference structure of a sound field in a layered ocean. In L. M. Brekhovskikh and I. B. Andreevoi, editors, *Acoustics of the Ocean: Current Status (in Russian)*, pages 71–91. Nauka, Moscow, 1982.

[23] C. F. Chyba, S. J. Ostro, and B. C. Edwards. Radar detectability of a subsurface ocean on Europa. *Icarus*, 134:292–302, 1998.

[24] C. S. Clay. Array steering in a layered waveguide. *J. Acoust. Soc. Am.*, 33(7):865–870, 1961.

[25] M. D. Collins, L. T. Fialkowski, W. A. Kuperman, and J. S. Perkins. The multi-valued Bartlett processor and source tracking. *J. Acoust. Soc. Am.*, 97:235–241, 1995.

[26] J. F. Cooper, C. B. Phillips, J. R. Green, X. Wu, R. W. Carlson, L. K. Tamppari, R. J. Terrile, R. E. Johnson, J. H. Eraker, and N. C. Makris. Europa exploration: Science and mission priorities. In M. V. Sykes, editor, *The Future of Solar System Exploration, 2003-2013 Community Contributions to the NRC Solar System Exploration Decadal Survey*, volume 272 of *Astronomical Society of the Pacific Conference Series*, pages 217–252. Astronomical Society of the Pacific, California, 2002.

[27] G. D. Crawford and D. J. Stevenson. Gas driven water volcanism and the resurfacing of Europa. *Icarus*, 73:66–79, January 1988.

[28] Z. Crawford, R. T. Pappalardo, A. Barr, D. Gleeson, M. Mullen, F. Nimmo, M. M. Stempel, and J. Wahr. Wavy lineaments on Europa: Fracture propagation into combined nonsynchronous and diurnal stress fields. In *Proc. Lunar Planet Sci. Conf. XXXVI*, 2005. Abstract #2042.

[29] S. R. Deans. Radon and Abel transform. In A. D. Poularikas, editor, *The Transforms and Applications Handbook*, chapter 8. CRC Press, Boca Raton, 2nd edition, 2000.

[30] M. D. Denny and L. R. Johnson. The explosion seismic source function: Models and scaling laws reviewed. In S. R. Taylor, H. J. Patton, and P. G. Richards, editors, *Explosion Source Phenomenology*, number 65 in Geophysical Monograph, pages 1–24. American Geophysical Union, 1991.

[31] F. Deschamps and C. Sotin. Thermal convection in the outer shell of large icy satellites. *J. Geophys. Res.*, 106:5107–5121, March 2001.

[32] G. L. D'Spain and W. A. Kuperman. Application of waveguide invariants to analysis of spectrograms from shallow water environments that vary in range and azimuth. *J. Acoust. Soc. Am.*, 106(5):2454–2468, November 1999.

[33] J. Eluszkiewicz. Dim prospects for radar detection of Europa's ocean. *Icarus*, 170:234–236, 2004.

[34] W. M. Ewing, W. S. Jardetzky, and F. Press. *Elastic Waves in Layered Media.* McGraw-Hill, New York, 1957.

[35] D. M. Farmer and Y. Xie. The sound generated by propagation cracks in sea ice. *J. Acoust. Soc. Am.*, 85:1489–1500, April 1989.

[36] C. Feuillade, D. R. DelBalzo, and M. M. Rowe. Environmental mismatch in shallow-water matched-field processing: Geoacoustic parameter variability. *J. Acoust. Soc. Am.*, 85(6):2354–2364, June 1989.

[37] P. H. Figueredo, F. C. Chuang, J. Rathbun, R. L. Kirk, and R. Greeley. Geology and origin of Europa's mitten feature (Murias Chaos). *J. Geophys. Res.*, 107:10.1029/2001JE001591, 2002.

[38] L. B. Freund. *Dynamic Fracture Mechanics.* Cambridge University Press, New York, 1990.

[39] G. V. Frisk. *Ocean and Seabed Acoustics: A Theory of Wave Propagation.* Prentice Hall, Englewood Cliffs, N.J., 1994.

[40] R. E. Gagnon, H. Kiefte, and M. J. Clouter. Pressure dependence of the elastic constants of ice Ih to 2.8 kbar by Brillouin spectroscopy. *J. Chem. Phys.*, 89:4522–4528, October 1988.

[41] D. Gleeson, Z. Crawford, A. C. Barr, M. Mullen, R. T. Pappalardo, L. M. Prockter, M. M. Stempel, and J. Wahr. Wavy and cycloidal lineament formation on Europa from combined diurnal and nonsynchronous stresses. In *Proc. Lunar Planet Sci. Conf. XXXVI*, 2005. Abstract #2364.

[42] R. Greeley, C. Chyba, J. W. Head, T. McCord, W. B. McKinnon, and R. T. Pappalardo. Geology and geophysics of Europa. In F. Bagenal, W. B. McKinnon, and T. Dowling, editors, *Jupiter: The Planet, Satellite, and Magnetosphere.* submitted, 2003.

[43] R. Greeley, C. Chyba, J. W. Head III, T. McCord, W. B. McKinnon, R. T. Pappalardo, and P. Figueredo. Geology of Europa. In F. Bagenal, T. E. Dowling, and W. B. McKinnon, editors, *Jupiter: The Planet, Satellites & Magnetosphere*, pages 329–362. Cambridge University Press, New York, 2004.

[44] R. Greeley, T. Johnson, and the JIMO Science Definition Team. Report of the NASA Science Definition Team for the Jupiter Icy Moons Orbiter. Technical report, NASA, 2004.

[45] R. Greeley, J. E. Klemaszewski, R. Wagner, and the Galileo Imaging Team. Galileo views of the geology of Callisto. *Planet. Space Sci.*, 48:829–853, 2000.

[46] R. Greenberg. Tides and the biosphere of Europa. *Am. Sci.*, 90:48–55, 2002.

[47] R. Greenberg, P. Geissler, G. Hoppa, B. R. Tufts, D. D. Durda, R. T. Pappalardo, J. W. Head, R. Greeley, R. Sullivan, and M. H. Carr. Tectonic processes on Europa: Tidal stresses, mechanical response, and visible features. *Icarus*, 135:64–78, 1998.

[48] R. Greenberg, G. V. Hoppa, G. Bart, and T. Hurford. Tidal stress patterns on europa. *Celest. Mech. Dyn. Astron.*, 87:171–188, 2003.

[49] M. V. Greening, P. Zakarauskas, and S. Dosso. Matched-field localization for multiple sources in an uncertain environment, with application to Arctic ambient noise. *J. Acoust. Soc. Am.*, 101:3525–3538, 1997.

[50] P. Gudmandsen. Electromagnetic probing of ice. In J. R. Wait, editor, *Electromagnetic Probing in Geophysics*, pages 321–348. The Golem Press, Boulder, 1971.

[51] A. Gudmundsson. Tectonics of the Thingvellir fissure swarm, SW Iceland. *J. Struct. Geol.*, 9:61–69, 1987.

[52] F. J. Harris. On the use of windows for harmonic analysis with the discrete Fourier transform. *Proc. IEEE*, 66(1):51–83, 1978.

[53] R. J. Hartranft and G. C. Sih. Alternating method applied to edge and surface crack problems. In G. C. Sih, editor, *Methods of Analysis and Solutions of Crack Problems*, chapter 4, pages 179–238. Noordhoff International Publishing, Leyden, 1973.

[54] N. A. Haskell. Total energy and energy spectral density of elastic wave radiation from propagating faults. *Bull. Seismol. Soc. Am.*, 54:1811–1841, December 1964.

[55] G. V. Hoppa. *Europa: Effects of rotation and tides on tectonic processes.* PhD thesis, University of Arizona, Tucson, 1998.

[56] G. V. Hoppa, B. R. Tufts, R. Greenberg, and P. E. Geissler. Formation of cycloidal features on Europa. *Science*, 285:1899–1902, 1999.

[57] G. V. Hoppa, B. R. Tufts, R. Greenberg, T. A. Hurford, D. P. O'Brien, and P. E. Geissler. Europa's rate of rotation derived from the tectonic sequence in the Astypalaea region. *Icarus*, 153:208–213, 2001.

[58] K. Hunkins. Seismic studies of sea ice. *J. Geophys. Res.*, 65:3459–3472, October 1960.

[59] F. B. Jensen, W. A. Kuperman, M. B. Porter, and H. Schmidt. *Computational Ocean Acoustics.* AIP series in modern acoustics and signal processing. Springer-Verlag, New York, 1993.

[60] D. H. Johnson and D. E. Dudgeon. *Array Signal Processing.* Prentice Hall, Upper Saddle River, 1993.

[61] A. Joset and J.-J. Holtzscherer. Étude des vitesses de propagation des ondes séismiques sur l'inlandsis du Groenland. *Ann. Geophys.*, 9:330–344, 1953.

[62] K. K. Khurana, M. G. Kivelson, D. J. Stevenson, G. Schubert, C. T. Russell, R. J. Walker, and C. Polanskey. Induced magnetic fields as evidence for subsurface oceans in Europa and Callisto. *Nature*, 395:777–780, October 1998.

[63] J. S. Kim. *Radiation from Directional Seismic Sources in Laterally Stratified Media with Application to Arctic Ice Cracking Noise.* PhD thesis, Massachusetts Institute of Technology, 1989.

[64] L. E. Kinsler, A. R. Frey, A. B. Coppens, and J. V. Sanders. *Fundamentals of Acoustics.* John Wiley & Sons, Inc., New York, 4th edition, 2000.

[65] M. G. Kivelson, K. K. Khurana, C. T. Russel, M. Volwerk, R. J. Walker, and C. Zimmer. Galileo magnetometer measurements: A stronger case for a subsurface ocean at Europa. *Science*, 289:1340–1343, 2000.

[66] M. G. Kivelson, K. K. Khurana, D. J. Stevenson, L. Bennett, S. Joy, C. T. Russell, R. J. Walker, C. Zimmer, and C. Polanskey. Europa and Callisto: induced or intrinsic fields in a periodically varying plasma environment. *J. Geophys. Res.*, 104:4609–4625, 1999.

[67] J. A. Kong. *Electromagnetic Wave Theory.* EMW Publishing, Cambridge, 2000.

[68] R. L. Kovach and C. F. Chyba. Seismic detectability of a subsurface ocean on Europa. *Icarus*, 150:279–287, 2001.

[69] W. A. Kuperman and G. L. D'Spain, editors. *Ocean Acoustic Interference Phenomena and Signal Processing*, New York, 2002. American Insitute of Physics.

[70] W. A. Kuperman and F. Ingenito. Spatial correlation of surface generated noise in a stratified ocean. *J. Acoust. Soc. Am.*, 67:1988–1996, June 1980.

[71] M. A. Lange and T. J. Ahrens. The dynamic tensile strength of ice and ice-silicates mixtures. *J. Geophys. Res.*, 88:1197–1208, February 1983.

[72] S. Lee and N. C. Makris. A new invariant method for instantaneous source range estimation in an ocean waveguide from passive beam-time intensity data. *J. Acoust. Soc. Am.*, 116(4):2646, 2004.

[73] S. Lee and N. C. Makris. Range estimation of broadband noise sources in an ocean waveguide using the array invariant. *J. Acoust. Soc. Am.*, 117(4):2577, 2005.

[74] S. Lee, M. Zanolin, A. M. Thode, R. T. Pappalardo, and N. C. Makris. Probing Europa's interior with natural sound sources. *Icarus*, 165:144–167, 2003.

[75] A. C. Leith and W. B. McKinnon. Is there evidence for polar wander on Europa? *Icarus*, 120:387–398, 1996.

[76] W. Lotze. Schallgeschwindigkeitsmessungen von Eis in Abhängigkeit von Druck und Temperatur. *Z. Geophys.*, 23:243–249, 1957.

[77] N. C. Makris. A foundation for logarithmic measures of fluctuating intensity in pattern recognition. *Opt. Lett.*, 20(19):2012–2014, 1995.

[78] N. C. Makris. The effect of saturated transmission scintillation on ocean acoustic intensity measurements. *J. Acoust. Soc. Am.*, 100(2):769–783, 1996.

[79] N. C. Makris. Main Acoustic Clutter Experiment Cruise Report. Technical report, Office of Naval Research, 2003.

[80] N. C. Makris and I. Dyer. Environmental correlates of pack ice noise. *J. Acoust. Soc. Am.*, 79:1434–1440, May 1986.

[81] N. C. Makris and I. Dyer. Environmental correlates of Arctic ice-edge noise. *J. Acoust. Soc. Am.*, 90:3288–3298, December 1991.

[82] N. C. Makris and P. Ratilal. A unified model for reverberation and submerged object scattering in a stratified ocean waveguide. *J. Acoust. Soc. Am.*, 109(3):909–941, 2001.

[83] M. Manga and A. Sinton. Formation of bands and ridges on Europa by cyclic deformation: Insights from analogue wax experiments. *J. Geophys. Res.*, 109:E09001, doi:10.1029/2004JE002249, 2004.

[84] D. F. McCammon and S. T. McDaniel. The influence of the physical properties of ice on reflectivity. *J. Acoust. Soc. Am.*, 77:499–507, February 1985.

[85] W. B. McKinnon. Convective instability in Europa's floating ice shell. *Geophys. Res. Lett.*, 26:951–954, 1999.

[86] H. Medwin and C. S. Clay. *Fundamentals of Acoustical Oceanography.* Academic Press, Boston, 1998.

[87] M. Mellor. Mechanical behavior of sea ice. Technocal Report CRREL Monograph 83-1, US Army Cold Regions Research & Engineering Laboratory, June 1983.

[88] H. J. Melosh. *Impact Cratering: A Geologic Process.* Oxford University Press, New York, 1989.

[89] J. Miklowitz. *The Theory of Elastic Waves and Waveguides.* North-Holland Publishing Company, Amsterdam, 1978.

[90] J. C. Moore. Models of radar absorption in Europan ice. *Icarus*, 147:292–300, 2000.

[91] W. B. Moore and G. Schubert. The tidal response of Europa. *Icarus*, 147:317–319, 2000.

[92] W. B. Moore and G. Schubert. The tidal response of Ganymede and Callisto with and without liquid water oceans. *Icarus*, 166:223–226, 2003.

[93] O. Muller and M. R. Muller. Near surface magma movements. *Proc. Lunar Planet. Sci. Conf.*, 11:1979–1985, 1980.

[94] E. Naftali and N. C. Makris. Necessary conditions for a maximum likelihood estimate to become asymptotically unbiased and attain the Cramer-Rao Lower Bound. Part I. General approach with an application to time-delay and Doppler shift estimation. *J. Acoust. Soc. Am.*, 110:1917–1930, 2001.

[95] K. G. Neave and J. C. Savage. Icequakes on the Athabasca glacier. *J. Geophys. Res.*, 75:1351–1362, 1970.

[96] F. Nimmo. Stresses generated in cooling viscoelastic ice shell: Application to Europa. *J. Geophys. Res.*, 109:E12001, doi:10.1029/2004JE002347, 2004.

[97] F. Nimmo, R. T. Pappalardo, and B. Giese. On the origins of band topography, Europa. *Icarus*, 166:21–32, 2003.

[98] A. Nur. The origin of tensile fracture lineaments. *J. Struct. Geol.*, 4:31–40, 1982.

[99] G. W. Ojakangas and D. J. Stevenson. Thermal state of an ice shell on Europa. *Icarus*, 81:220–241, 1989.

[100] G. S. Orton, J. R. Spencer, L. D. Travis, T. Z. Martin, and L. K. Tamppari. Galileo photopolarimeter-radiometer observations of Jupiter and the Galilean satellites. *Science*, 274:389–391, October 1996.

[101] S. J. Ostro, D. B. Campbell, R. A. Simpson, R. S. Hudson, J. F. Chandler, K. D. Rosema, I. I. Shapiro, E. M. Standish, R. Winkler, D. K. Yeomans, and R. M. Goldstein. Europa, Ganymede, and Callisto: New radar results from Arecibo and Goldstone. *J. Geophys. Res.*, 97:18227–18244, November 1992.

[102] A. Papoulis. *The Fourier Integral and Its Applications.* McGraw-Hill, New York, 1962.

[103] A. Papoulis. *Signal Analysis.* McGraw-Hill, New York, 1977.

[104] R. T. Pappalardo, M. J. S. Belton, H. H. Breneman, M. H. Carr, C. R. Chapman, G. C. Collins, T. Denk, S. Fagents, P. E. Geissler, B. Giese, R. Greeley, R. Greenberg, J. W. Head, P. Helfenstein, G. Hoppa, S. D. Kadel, K. P. Klaasen, J. E. Klemaszewski, K. Magee, A. S. McEwen, J. M. Moore, W. B. Moore, G. Neukum, C. B. Phillips, L. M. Prockter, G. Schubert, D. A. Senske, R. J. Sullivan, B. R. Tufts, E. P. Turtle, R. Wagner, and K. K. Williams. Does Europa have a subsurface ocean? Evaluation of the geological evidence. *J. Geophys. Res.*, 104:24015–24055, October 1999.

[105] R. T. Pappalardo, J. W. Head, R. Greeley, R. J. Sullivan, C. Pilcher, G. Schubert, W. B. Moore, M. H. Carr, J. M. Moore, M. J. S. Belton, and D. L. Goldsby. Geological evidence for solid-state convection in Europa's ice shell. *Nature*, 391:365–367, January 1998.

[106] C. L. Pekeris. Theory of propagation of explosive sound in shallow water. *Geol. Soc. Am. Mem.*, 27:1–117, 1948.

[107] L. M. Prockter, P. H. Figueredo, R. T. Pappalardo, J. W. Head III, and G. C. Collins. Geology and mapping of dark terrain on Ganymede and implications for grooved terrain formation. *J. Geophys. Res.*, 105:22519–22540, 2000.

[108] L. M. Prockter, J. W. Head III, R. T. Pappalardo, R. J. Sullivan, A. E. Clifton, B. Giese, R. Wagner, and G. Neukum. Morphology of Europan bands at high resolution: A mid-ocean ridge-type rift mechanism. *J. Geophys. Res.*, 107:doi:10.1029/2000JE001458, 2002.

[109] T. M. Proctor, Jr. Low-temperature speed of sound in single-crystal ice. *J. Acoust. Soc. Am.*, 39:972–977, 1966.

[110] P. Ratilal. *Remote sensing of submerged objects and geomorphology in continental shelf waters with acoustic waveguide scattering.* PhD thesis, Massachusetts Institute of Technology, Cambridge, 2002.

[111] P. Ratilal, Y.-S. Lai, D. T. Symonds, L. A. Ruhlmann, J. A. Goff, C. W. Holland, J. R. Preston, E. K. Scheer, M. T. Garr, and N. C. Makris. Long range acoustic imaging of the continental shelf environment: The Acoustic Clutter Reconnaisance Experiment 2001. *J. Acoust. Soc. Am.*, 117(4):1977–1998, 2005.

[112] J. W. S. Rayleigh. *The Theory of Sound*, volume 2. Macmillan, London, 2nd edition, 1896.

[113] J. W. S. Rayleigh. On the transmission of light through an atmosphere containing small particles in suspension, and on the origin of the blue of the sky. *Phil. Mag.*, 47:375–384, 1899.

[114] G. Q. Robin. Measurements of ice thickness in Dronning Maud Land, Antarctica. *Nature*, 171:55–58, January 1953.

[115] G. Q. Robin. Glaciology III, seismic shooting and related investigations. In *Norwegian-British-Swedish Antarctic Expedition, 1949-52, Scientific Results*, volume 5. Norsk Polarinstitut, Oslo, 1958.

[116] D. Sandwell, P. Rosen, W. Moore, and E. Gurrola. Radar interferometry for measuring tidal strains across cracks on Europa. *J. Geophys. Res.*, 109:E11003, doi:10.1029/2004JE002276, 2004.

[117] D. T. Sandwell. Limits on the strength of Europa's icy shell from topographic spectra. In *Workshop on Europa's Icy Shell: Past, Present, and Future*, LPI Contribution No. 1195, pages 78–79. Lunar and Planetary Institute, Houston, 2004.

[118] P. M. Schenk. Thickness constraints on the icy shells of the Galilean satellites from a comparison of crater shapes. *Nature*, 417:419–421, May 2002.

[119] H. Schmidt, A. B. Baggeroer, W. A. Kuperman, and E. K. Sheer. Environmentally tolerant beamforming for high-resolution matched field processing: Deterministic mismatch. *J. Acoust. Soc. Am.*, 88(4):1851–1862, October 1990.

[120] H. Schmidt and G. Tango. Efficient global matrix approach to the computation of synthetic seismograms. *Geophys. J. R. astron. Soc.*, 84:331–359, 1986.

[121] P. H. Schultz and D. E. Gault. Seismic effects from major basin formation on the Moon and Mercury. *The Moon*, 12:159–177, 1975.

[122] J. Schwarz and W. F. Weeks. Engineering properties of sea ice. *J. Glaciol.*, 19:499–531, 1977.

[123] G. H. Shaw. Elastic properites and equation of state of high pressure ice. *J. Chem. Phys.*, 84:5862–5868, May 1986.

[124] G. B. Smith, H. A. Chandler, and C. Feuillade. Performance stability of high-resolution matched-field processors to sound-speed mismatch in a shallow-water environment. *J. Acoust. Soc. Am.*, 93(5):2617–2626, 1993.

[125] R. A. Smith. The application of fracture mechanics to the problems of crevasse penetration. *J. Glaciol.*, 17:223–228, 1976.

[126] J. R. Spencer, L. K. Tamppari, T. Z. Martin, and L. D. Travis. Temperatures on Europa from Galileo photopolarimeter-radiometer: Nighttime thermal anomalies. *Science*, 284:1514–1516, May 1999.

[127] S. T. Stewart and T. J. Ahrens. Correction to the dynamic tensile strength of ice and ice-silicate mixtures (Lange & Ahrens 1983). In *Proc. Lunar Planet. Sci. Conf.*, 30:Abstract #2037, 1999.

[128] H. Tada, P. C. Paris, and G. R. Irwin. *The Stress Analysis of Cracks Handbook.* ASME Press, New York, 3rd edition, 2000.

[129] S. P. Timoshenko and J. N. Goodier. *Theory of Elasticity.* McGraw-Hill, New York, 3rd edition, 1970.

[130] C. T. Tindle. Virtual modes and mode amplitudes near cutoff. *J. Acoust. Soc. Am.*, 66(6):1423–1428, June 1979.

[131] I. Tolstoy and C. S. Clay. *Ocean Acoustics: Theory and Experiment in Underwater Sound.* American institute of Physics, New York, 1987.

[132] J. Tyndall. *Sound.* Longmans, Green, and Co., London, 5th edition, 1893.

[133] F.-J. Ulm and O. Coussy. *Mechanics and Durability of Solids*, volume 1. Prentice Hall, Upper Saddle River, 2003.

[134] R. J. Urick. *Principles of Underwater Sound.* McGraw-Hill, New York, 3rd edition, 1983.

[135] H. C. van de Hulst. *Light Scattering by Small Particles.* Wiley, New York, 1957.

[136] K. D. Vaudrey. Ice engineering - study of related properties of floating sea-ice sheets and summary of elastic and viscoelastic analyses. Technical Report TR-860, Civil Engineering Laboratory, Alexandria, 1977.

[137] Y. Y. Wang, C. S. Clay, and E. C. Shang. Bearing determination in a waveguide. *J. Acoust. Soc. Am.*, 82(1):233–237, 1987.

[138] W. F. Weeks and A. Assur. The mechanical properties of sea ice. In *Ice Pressures against Structures*, pages 25–78. Assoc. Committee on Geotech. Res. of the Natl. Res. Council of Canada, Ottawa, 1968. Proceedings of a Conference held at Laval University, Quebec, 10-11 November 1966, Tech. Memo. No. 92.

[139] W. F. Weeks and A. Assur. Fracture of lake and sea ice. In H. Liebowitz, editor, *Fracture, An Advanced Treatise*, volume 7, pages 879–978. Academic Press, New York, 1972.

[140] W. F. Weeks and G. F. N. Cox. The mechanical properties of sea ice: a status report. *Ocean Sci. Eng.*, 9:135–198, 1984.

[141] J. Weertman. Theory of water filled crevasses in glaciers applied to vertical magma transport beneath oceanic ridges. *J. Geophys. Res.*, 76:1171–1173, 1971.

[142] J. Weertman. Velocity at which liquid filled cracks move in the earth's crust or glaciers. *J. Geophys. Res.*, 76:8544–8553, 1971.

[143] J. Weertman. Can a water-filled crevasse reach the bottom surface of a glacier? In *Symposium on the Hydrology of Glaciers, Cambridge, 7-13 Sept. 1969*, pages 139–145. Glaciological Society, 1973.

[144] J. D. Wilson and N. C. Makris. Ocean acoustic hurricane classification. *J. Acoust. Soc. Am.*, 119:168–181, 2006.

[145] X. Wu, Y. E. Bar-Sever, W. M. Folkner, J. G. Williams, and J. F. Zumberge. Probing Europa's hidden ocean from tidal effects on orbital dynamics. *Geophys. Res. Lett.*, 28:2245–2248, 2001.

[146] T. C. Yang. Beam intensity striations and applications. *J. Acoust. Soc. Am.*, 113(3):1342–1352, March 2003.

[147] M. Zanolin, I. Ingram, A. Thode, and N. C. Makris. Asymptotic accuracy of geoacoustic inversions. *J. Acoust. Soc. Am.*, 116(4):2031–2042, 2004.